Mechanisms of nanogratings formation and erasure in oxide glasses by femtosecond laser direct writing

Qiong Xie

THESE DE DOCTORAT

NNT : 2024UPASF028

université PARIS-SACLAY

Mechanisms of nanogratings formation and erasure in oxide glasses by femtosecond laser direct writing

Mécanismes de formation et effacement des nanoréseaux dans les verres d'oxyde par écriture directe laser femtoseconde

Thèse de doctorat de l'université Paris-Saclay

École doctorale n° 571, Sciences chimiques : molécules, matériaux, instrumentation et biosystèmes (2MIB)
Spécialité de doctorat : Physique
Graduate School : Chimie. Référent : Faculté des sciences d'Orsay

Thèse préparée dans l'unité de recherche **Institut de chimie moléculaire et des matériaux d'Orsay (Université Paris-Saclay, CNRS)**
sous la direction de **Matthieu LANCRY**, Professeur des Universités
et le co-encadrement de **Maxime CAVILLON**, Maître de conférences

Thèse soutenue à Paris-Saclay, le 4 juillet 2024, par

Qiong XIE

Composition du Jury

Membres du jury avec voix délibérative

Marie-Christine SCHERRMANN Professeure des Universités, Université Paris-Saclay	Présidente
Jean-Philippe COLOMBIER Professeur des Universités, Université Jean Monnet Saint-Etienne - CNRS	Rapporteur & Examinateur
Yannick PETIT Maître de conférences (HDR), Université de Bordeaux - CNRS	Rapporteur & Examinateur
Thierry CARDINAL Directeur de recherche, Université de Bordeaux - CNRS	Examinateur
Rudy DESMARCHELIER Ingénieur de recherche, Université Paris Saclay – CEA	Examinateur

université PARIS-SACLAY

ÉCOLE DOCTORALE
Sciences Chimiques : Molécules, Matériaux, Instrumentation et Biosystèmes (2MIB)

Titre : Mécanismes de formation et effacement des nanoréseaux dans les verres d'oxyde par écriture directe laser femtoseconde

Mots clés : verres multi-composants ; traitement laser femtoseconde ; biréfringence ; nanopores.

Résumé : Les nanoréseaux sont les plus petites structures « auto-organisées » jamais créées par la lumière dans le volume d'un matériau transparent. Ils ont été observés pour la première fois en 2003 à l'intérieur d'un verre de silice, et induits au moyen d'une irradiation par laser femtoseconde (fs). Ils ont suscité un grand intérêt ces dernières années en raison de propriétés particulières. Ils sont biréfringents, avec un axe neutre orientable dans l'espace grâce à la polarisation du laser fs. Ils peuvent également induire une biréfringence circulaire et un dichroïsme, présentent une stabilité thermique extraordinaire, et permettent une attaque chimique hautement sélective. En conséquence, ces nanostructures suscitent un intérêt dans des domaines tel quel le stockage optique de données, les dispositifs optiques biréfringents 2D ou 3D, les capteurs en environnement extrême, la microfluidique, etc. Ces nanoréseaux sont constitués d'un assemblage de couches nanoporeuses principalement observées dans la silice et les verres riches en silice. Plusieurs travaux ont pu mettre en évidence l'effet des propriétés physiques du verre (température de ramolissement, diffusivité thermique, etc.) sur leur processus de formation et d'effacement au cours de l'irradiation. En outre, l'importance de comprendre les mécanismes de formation réside dans la capacité de les produire de manière contrôlée, ainsi que d'acquérir une compréhension fondamentale plus approfondie des interactions complexes lumière-matière. Cette compréhension permettrait une généralisation dans tout type de verres optiques. Dans ce contexte, l'objectif de cette thèse est de mettre en évidence le lien entre la composition chimique des verres et la fenêtre d'inscription des nanoréseaux. De plus, nous sommes intéressés à mieux comprendre les mécanismes de formation et d'effacement des nanoréseaux pendant l'irradiation, afin de contrôler les propriétés optiques anisotropes associées à ces transformations (signe, amplitude, orientation, pertes associées). Premièrement, nous discutons de l'impact de la viscosité du verre sur leur existence à l'aide de l'équation de Rayleigh-Plesset. Il est établi que la viscosité est une propriété clé à considérer, et proposons un domaine d'existence des nanoréseaux grâce à une approche basée cette dernière, en faisant une série d'hypothèses sur les conditions de confinement thermique et de pression pendant l'irradiation. L'étude de la fenêtre d'existence dans un paysage taux de répétition - énergie d'impulsion pour un grand nombre de verres d'oxyde (commerciaux et réalisés en laboratoire), valide l'approche proposée, où la fenêtre théorique est bien corrélée à son équivalent expérimental. Ensuite, nous analysons la nanostructure interne des nanoréseaux par des techniques d'imagerie en microscopie électronique à haute résolution, rendant ainsi compte de leur formation à l'intérieur de la silice. Ces investigations à l'échelle nanométrique révèlent que leur structure intrinsèque est composée de nanopores aplatis, façonnés en nanoplans, régulièrement espacés et orientés perpendiculairement à la polarisation du laser. Ces couches nanoporeuses sont organisées par la lumière sous des effets thermomécaniques via un processus de nanocavitation assisté par le plasma. D'après les observations obtenues par des expériences de recuit en conditions isochrones, l'effacement des nanopores créés lors de l'irradiation laser est également fortement lié à la dépendance de la viscosité du verre à la température. Finalement cet effacement peut être prédit pour un processus temps-température quelconque. Ainsi, il devient possible de d'anticiper la durée de vie des nanoréseaux dans différents verres commerciaux, étendant ainsi notre travail bien au-delà de la silice.

Title : Mechanisms of nanogratings formation and erasure in oxide glasses by femtosecond laser direct writing

Keywords : multicomponent glasses; femtosecond laser processing; birefringence; nanopores.

Abstract : Nanogratings are the smallest « self-organized » structures ever created by light inside transparent materials. They were observed for the first time in 2003 inside silica glass and induced by femtosecond (fs) laser irradiation. They have drawn considerable attention over the last decades due to their unique properties. They are birefringent, with a neutral axis orientable in space through light polarization, can induce dichroism or circular birefringence, exhibit excellent thermal stability and a highly selective chemical etching. Consequently, they have shown promises in technological areas including optical data storage, 2D/3D birefringent optical devices, sensing in harsh environment, microfluidic, etc. These nanogratings are composed of nanoporous layers, mostly observed in silica and silicate glasses. A series of works have shed light on the role played by physical glass properties (softening temperature, thermal diffusivity, etc.) on their formation and erasure during the laser writing process. Moreover, the understanding of formation mechanism directly impacts the ability to inscribe nanogratings in a controlled way, as well as improve the fundamental physics and chemistry at play during complex light-matter interaction. This understanding could thus be generalized to all optical glasses, and in this context the main objective of this work is to decipher the relationship between glass composition and nanogratings formation window. Additionally, better control of the anisotropic properties associated to fs laser induced modifications (sign, amplitude, orientation, losses) is possible provided the nanogratings formation and erasure mechanisms are well understood. In this thesis, we first discuss the effect of glass viscosity on nanogratings existence using the Rayleigh-Plesset equation. It is established that viscosity is a key property to consider, and we propose a related approach to determine a theoretical temperature domain of their existence provided a series of assumptions are satisfied (thermal confinement and associated pressure induced). The latter approach is experimentally validated using a large number of oxide glasses (commercial and laboratory ones) by investigating the nanogratings processing window in a repetition rate – pulse energy landscape. Following this work, the internal structuring of the nanogratings inside silica is investigated by high resolution electron microscopy techniques. Observations at the nanoscale reveal that nanoplanes are intrinsically made of regularly spaced nanoplanes, oriented perpendicular to the light polarization, and where oblate nanopores line up to form the nanoplanes. These nanoporous layers are organized by light through thermomecanical solicitations and assisted by a plasma mediated nanocavitation process. Under isochronal thermal annealing experiments, the erasure of nanopores created during the laser irradiation is strongly correlated to the temperature dependence of the glass viscosity. Finally, such an erasure can be predicted for any time-temperature process, provided the hypothesis remains valid. It becomes possible to anticipate and model nanogratings lifetime in many commercial glasses and extending it well beyond silica glass.

CONTENU

ACKNOWLEDGMENT

Foremost, I would like to express my deepest gratitude to my supervisor Prof. Matthieu Lancry. He has been the best supervisor since I started in research. He has been always very nice, helpful and accessible since I enrolled as a PhD student. He leads me on the path of fs laser and matter interaction and let me want to continue doing research in this interesting area. He always helps and inspires me when I struggle on problems. He always gives valuable feedbacks no matter what I ask for. His suggestions of work and life have enriched me. I am such lucky to meet my supervisor. All these let me feel never helpless and make my study progress well. I would like also to extend my sincere thanks to my co-supervisor, Dr. Maxime Cavillon. He is always nice and helpful to me. He helps me solve so many problems. Each discussion with him teaches and inspires me a lot. Without his guides, my study can't go well. And special thanks to Prof. Bertrand Poumellec. "His disturbing" during work teaches me many concepts from the origin and in a pedagogical way. He usually asks me questions that keeps me question myself to make my study clear.

I am also grateful to our colleagues and collaborates for their nice help. Benjamin Sapaly and Dr. Yitao Wang taught me how to use our platform of fs laser direct writing and optical microscopes, and annealing experiments, and gave me lots of help on experiments when I was a beginner in our lab. François Brisset from SP2M-ICMMO helped me on the measurement of SEM. Dr. Jiafeng Lu helps me a lot on the graphs and Matlab coding, and gives me useful suggestions about academic research. Dr. Ruyue Que helps me a lot in life during this journey and make me feel less lonely. Dr. Diego Pugliese and Prof. Davide Janner from Politecnico di Torino helped me on the polish and fabrication of the glass, and the measurement of Raman spectroscopy. To our MAP team members, Dr. Julien Ari, Dr. Elisa Muzi, Dr. Pierre Delullier, Imane Ktafi, Jun Zou, Nadezhda Shchedrina, Jing Kong, Matilde Sosa marti, Sebastien Bourdel, Heng Yao, many thanks for their discussions in our lab and their friendships.

I am grateful to the funding provided by Chinese Scholarship Council and University Paris Saclay.

Finally, I am sincerely thankful to my parents, for their unconditional love and support. To all my friends, Ismail Mkinsi, Selma Leonardi, Dr. Timothée Lauridant, Dr. Shanyu Tang, Dr. Dayi Liu, Dr. Rui Luo, Wei Cao, Donghuang Chen, Bocheng Chen, Mengyuan Li, Chaoyan Yin, Linhua Shen, Qinglin Wang, Tianyue Wei, Liangjian Hu, Qian He, Shuai Luo, etc., for their help and company.

May my work bring some values to the world and thanks all!

Qiong XIE

ICMMO, Orsay, France

April 8, 2024

GENERAL INTRODUCTION

Photonics needs a flexible manufacturing technique: Photonics is currently undergoing a transition toward more integration of optical components as well as a transition toward structured beams [1]. Compact, lightweight components are needed for healthcare, transportation, space applications. Simultaneously, complex shaping of amplitude, phase and polarization are crucial for a fast-growing number of applications and fundamental science (quantum optics, biophotonics, attosecond pulses, laser materials processing). Therefore, next generation photonics needs a manufacturing technique to print "on-demand" any arbitrary optical component for beam shaping. Ideally such optics would be flat, thin, exhibiting low optical losses, high damage threshold and low cost. Conventional light shaping tools have limited capabilities: Spatial Light Modulators are bulky, expensive, provide limited phase change (typ. 3π at 800 nm) and exploit single polarization axis. Diffractive optical elements cannot offer polarization shaping. Space variant metasurfaces [2] enable a full control of the output light field, but lithographic processes are long, multi-steps, require costly and polluting processes while the final nm layer is fragile.

3D direct writing methods for photonics: Recent publications on 3D manufacturing of optics demonstrate the attractiveness of this topic worldwide. Many methods recalled in Ref. [3] allow 3D manufacturing of optical elements. Among these different techniques we find deposition techniques, inkjet printing, stereolithography and 2-photon polymerization (2PP) by a femtosecond laser. However, the optics be produced by these methods have moderate resolution (up to 0.1 µm in 2PP) and with various surface roughness (which can go down to 10 nm in 2PP or inkjet). Among these methods, 2PP or inkjet printing can be used to produce optics of sufficiently high quality for imaging. However, these technologies are still in their beginning and most often carried out by a few startups (PRINTOPTIX, Vadient Optics, Luxexcel, ADDOPTICS). One of the limitations of these technologies is the spectral domain of application limited to the visible domain. 3D printing strategies with chalcogenide infrared glasses are being investigated in the academic context [4, 5] but the level of roughness is currently close to polymer deposition techniques, so that this approach makes it possible to produce preforms used for the final optics by molding. Besides, none of the techniques is capable to control the polarization of light.

Femtosecond laser direct writing (FLDW): Even if the approach of texturing and structuring by a femtosecond laser cannot be strictly considered as a method of 3D manufacturing of optics, the possibility of acting in the volume of an optical plate (of any shape) allows to consider manufacturing optical functions in an area inaccessible to the optical designers. It is a versatile method compatible with a wide range of materials and therefore in several spectral bands, in particular from the visible up to the thermal infrared. It allows both a modification of the material optical properties in volume and a structuring at the surface). This method also makes it possible to foresee

optical materials with very good mechanical properties which are neither machinable by diamond nor moldable. This method is well established in the academic field [6-8]. Of particular interest, fs laser-induced nanogratings can be used to form, in principle, any optics.

Laser-written flat optics is a far-reaching solution. With fs laser pulses, nanogratings can be formed inside most glasses in a multi-pulse laser regime [9]. These structures are subwavelength, periodic (typ. 200-300 nm), and birefringent. A key feature is that their amplitude and direction can be controlled respectively through pulse energy and light polarization direction. Therefore, Femtosecond Laser Direct Writing unfolds large perspectives to fabricate any optical component. It has been exploited to demonstrate fabrication of 3D space variant birefringent optics (vectors beams, microwaveplates arrays) as well as optical elements operating on 3D geometric phase (lens, grating) [2, 10, 11]. In parallel, recent advances in flat optics have challenged the limitations of conventional optics. The phase profile of nearly any optical components including lenses, gratings, prism, vortex phase plates, as well as elements capable of bending light in unusual ways can be designed using the geometric-phase (Pancharatnam-Berry phase). Theoretically any phase pattern can be achieved by means of geometric-phase optics with efficiencies reaching up to 100%. In addition, the possibility to imprint spatially varying anisotropic phase (birefringence) response will enable the shaping of polarization structured (transversal and longitudinal) light beams like cylindrical vector beams or more generally Poincaré beams. However, and despite exciting achievements, their development is hindered by relatively low performances (> 10 h/cm2 writing speed, 70% transmission (can be improved within Type X regime [2], 0.25 rad/µm phase density [10] and 300 nm retardance per layer [12]) mostly resulting from the lack of control of the laser-matter interaction processes. As a result, this technology of 3D FLDW is well studied in the academic environment due to its unambiguous advantages but remains little exploited at an industrial level.

In this context, understanding interaction of matter with femtosecond laser light will enable the evaluation of the industrial potential this new direct writing method has to offer. Some aspects of the light-matter interaction are fundamentally new. The underlying physics is the behavior of electron plasma in the presence of an ionic support and of a light wave. Here, solid and plasma states coexist for a fraction of picosecond. In addition, both, matter and light are in interaction to produce a structured organization of the plasma density. The fundamental problems are to accurately describe the structuration of the plasma of free electrons produced at the end of multiphoton ionization (transition through the gap of the transparent insulator). Here the solid intervenes as a source of electrons. Its microstructure organizes the plasma in coherence with that of the light beam. Then, after the pulse, this electron density distribution is "imprinted" by trapping electrons in the solid, and it can be used as a “source” by the next pulse thus ensuring a memory effect. In this operation, the solid is not destroyed; it remains below the vaporization threshold, it is restructured in the force field created by the laser. We can therefore imagine the orientation of the

material, imprinted oriented nano/microstructures like directionally solidified eutectics. This is a new physics. But for chemistry too, there are new aspects because the processes involve highly excited states, which are largely off equilibrium. It is therefore necessary to question some previous ideas. For example, the knowledge on the effect of impurities, defects states, or easily ionized states, remains highly limited. Force fields and not simply energy fields are also produced. Their control opens the door to a science of material modification by laser. This is the focus of the today work carried out by MAP group at ICMMO.

In particular, one main discovery forms the basis of this PhD thesis. This is the discovery of self-organized nanogratings in SiO_2 (200-400 nm periodicity persisting on mm range, including nanolayers as thin as 10-30 nm), which are in fact the smallest structures ever created by light [13, 14] [8]. From the authors, these nanogratings arise from modulation of the chemical composition (probably oxygen redistribution) and this would be related to stationary density waves in the plasma produced by the coupling between bulk plasmonic waves and light waves. In 2011, our group revealed that nanogratings are in fact an assembly of nanoporous layers due to oxide decomposition [15] that was suggested to come from a "tensile stress" assisted nanocavitation process [16, 17]. These structures, also called Type II modifications in the literature, are at the root of other experimental unusual phenomena like high linear birefringence response (up to -10^{-2}), polarized luminescence, anisotropic light scattering, strong linear "dichroism", negative index changes, chiral optical properties, and extraordinary good thermal stability (until a few 10's hours at 1000°C) [18-20].

These experimental observations left several opened questions that should be addressed to enable reliable applications. How to master such structures and the resulting properties, and consequently how to use them efficiently? The challenge of this PhD thesis was to improve our understanding of the interaction of femtosecond laser with optical glasses, in order to control the overall anisotropic optical properties (sign, amplitude, orientation, losses) in transparent solid materials using a high speed, low cost, ideally environmentally friendly, and sustainable technology for optical applications. As a result, the heart of this thesis work aims to characterize and understand the laser-induced transformations in a wide range of oxide glasses, their types and structural changes. One key interest is to better understand the mechanisms at the root of nanogratings formation and related anisotropic optical properties. Mastering this type of photosensitivity will allow us to correctly assess the potential of FLDW and to fully exploit the strengths of this interaction regime. This will unlock the industrial potential towards reliable applications based on anisotropic linear/circular optical properties.

The first chapter provides a review of the basic knowledge necessary to fully understand this thesis. We will highlight the structure of silica-based oxide glasses, which is the principal material constituting our samples. We shall discuss ultrashort laser pulse propagation in glass as well. Therefore, we will summarize the different

processes of interaction leading to structural changes, associated with the formation of permanent changes in the glass optical properties. Finally, the last part of this chapter will focus on the anisotropic optical properties and nanogratings formation in glasses. In particular, these anisotropic optical properties will be measured and studies throughout this thesis.

Chapter II is dedicated to study the role of the glass composition on the formation of the NGs processing window in different oxide glasses using FLDW. The first part of this chapter depicts a published paper in **Optical Materials** in 2022 [16]. By the investigation of the NGs window in a pulse energy-repetition rate (E_p-RR) landscape inside five different oxide glasses, SiO_2 (SuprasilCG), GeO_2, free/low alkali aluminoborosilicate (Schott glasses AF32 and Borofloat33) and alkali borosilicate (BK7) using the similar laser parameters, we discuss the impact of glass viscosity on the formation of NGs using Rayleigh-plesset (R-P) equation, which is a key property to consider. The domain of the NGs existence is defined using a viscosity argument under thermal and pressure confinement conditions. The experimental windows agree with the arguments developed through this viscosity approach. The second part of this chapter is related to a paper published in **Nanomaterials** in 2022 [21]. The investigated glasses are extended to more glass including commercial ones: aluminoborosilicates (Eagle XG and 7059), Soda-lime, titanium silicate (ULE), in addition to the previously investigated glasses. The E_p-RR landscapes or NGs windows inside these 9 glasses are summarized and compared. The retardance (R) of the NGs is measured by polarized microscopy. Scanning electron microscopy (SEM) is used to confirm the porous nature of the nanolayers composing the NGs. Moreover, the quantitative birefringence values of the NGs can be determined with complementary information of the laser track length from SEM analysis. The alkali or alkali earth content effects on the NGs window and the performance were compared and rationalized. The viscosity approach applies well in this extended glass composition range, and theoretical NGs window is well correlated to the experimental one. The third part of this chapter depicts a published paper in **Optics EXPRESS** in 2023 [22]. We investigate the NGs formation in a series of aluminoborosilicate doped with alkali (Na^+) and alkaline earth (Ca^{2+}) element, named SAN, SAC, and SACN. The NGs possessing windows in the E_p and pulse duration (τ_p) landscape are assessed according to the $(Na_2O + CaO)/Al_2O_3$ and B_2O_3/Al_2O_3 ratios. The effects of the glass chemical composition and its correlation to viscosity is discussed. The last part of this chapter summarizes in a published paper in **Nanoscale Advances** in 2024 [14]. We analyze the internal nanostructure of the NGs and its formation inside silica glass via SEM, scanning transmission electron microscopy (STEM), high-resolution transmission electron microscopy (HRTEM) and atomic force microscopy (AFM) techniques. Through NGs observation under different orientations, it is revealed that oblate nanopores compose the nanolayers, being discontinuous and of a wavy shape. The periodicity of the NGs is investigated, along with the effect of deposited pulse density on it. And based on the findings herein and literature, we discuss formation mechanisms of the NGs in a plasma-mediated nanocavitation process.

Chapter III is dedicated the investigation of thermal stability for self-organized porous NGs imprinted by FLDW in transparent materials is useful for high temperature optical devices application, especially for the designers to predict their working conditions (upper temperature and time). Upon thermal annealing, R or linear birefringence is progressively erased, characteristic of NGs erasure. The first part of this chapter depicts a published paper in **Applied optics** in 2023 [19]. We study the thermal stability of NGs in 8 commercial oxide glasses (Schott BK7, Borofloat 33 and AF32, Corning ULE, Eagle XG and 7059, Heraeus Suprasil CG and Marienfield Superior soda lime, as listed in the second chapter) by monitoring R induced by the NGs and upon isochronal thermal annealing experiments (time step = 30 min). The upper temperature of NGs erasure can be recorded during the evolution of the R as the temperature increase. From the observations gained by annealing experiments, we demonstrate that the collapse of nanopores created during the laser irradiation is also strongly related to the temperature dependence of the glass viscosity. An upper temperature limit to the NGs survival can be deduced based on the thermal process considered (annealing, laser irradiation process etc.). The time and temperature couple must be considered in the erasure of NGs since it is a kinetics problem, and a relationship between the two in a NGs erasure context is established. The second part of this chapter is related to a paper published in **Ceramics International** in 2024 [23]. We propose a procedure to predict the lifespan of NGs composed of nanopores by two main approaches. First, a numerical modeling of optical retardance ageing using the Rayleigh-Plesset equation, and second, exploiting VAREPA (variable reaction pathways) framework feed by simulated ageing data. Finally, we rationalize the predictions in different commercial glasses, extending our work much beyond silica, and obtained theoretical results are then compared to experimental ones. The last part of this chapter depicts **a paper submitted in May 2024** about a modeling NGs erasure at high repetition rate in commercial optical glasses. We exploit a heat diffusion model combined with Rayleigh-Plesset equation to simulate the time-temperature evolution of nanopores along the laser heat cooling profile. Then to establish some objective criteria to determine the energy threshold that results in the collapse of the NGs processing window in the E_p-RR landscapes. And we consider a multiple pulses approach to analyze the heat accumulation at steady state for various repetition rates. Finally, we simulate the maximum deposited energy that leads to the erasure of NGs along the laser cooling profile for a wide range of commercial optical glasses, in comparison to available experimental data.

Chapter IV, we summarize the discovery of NGs in various chemical compositions of optical glasses, from silica and silicates to multicomponent glass compositions including alumino-silicates, heavy oxide glasses, sodium silicates or germanates, and commercial glasses. It depicts a published paper in **Progress in Materials Science** in early 2024 [9]. It includes findings from previous chapters of this dissertation. The optical properties of formed NGs (NGs energy window, R, birefringence) can vary in great proportion with respect to glass composition. The mechanisms NGs formation induced in transparent materials are extensively discussed, along with the effect of

glass composition on characteristic features such as periodicity, nanopore size, filling factors (FF) and correlated "technological performances" such as writing speed, optical losses, retardance amplitude, thermal stability or energy consumption according to oxide glass chemical composition.

Finally, we provide the **conclusion and perspective sections**, which remind our overall investigations NGs formation within a wide range of optical glasses but mostly in oxide glasses. These results could provide a useful roadmap in the fabrication and design of optical glasses to induce NGs with targeted optical properties. These may find some suitable interests for the main identified applications such as birefringent or geometric phase optics, optical data storage, micro/nanofluidic devices and optical fiber sensors.

Chapter I. BACKGROUND AND STATE-OF-THE-ART OF FEMTOSECOND LASER DIRECT WRITING IN TRANSPARENT GLASSES

I.1 INTRODUCTION

First of all, this chapter is the basis background related to my work, which is useful to understand this dissertation. It is beginning with the silica glass, different component oxide glasses and their viscosity property. It is addressed how the femtosecond laser propagate in dielectric. It is presented that the interaction between femtosecond laser and glass, and the different modifications induced by laser in silica. The nanogratings, one of the functional modifications, and the related effects on its formation is addressed. The formation and erasure of the nanogratings and the relation with viscosity are throughout this dissertation.

I.2 OXIDE GLASSES

I.2.1 Silica glass

Since the 1960s, the effects of electron bombardment on glasses have been studied with high-energy sources in the MeV range [24-26]. As early as the 1980s, some authors began to use less energetic electron beams (on the order of few keV) to probe the induced volume changes and optical modifications under irradiation [27-29]. Irrespective of the type of irradiation, these changes are based on structural changes induced by irradiation. Most commercial glasses are silica-based, with other conventional dopants or constituents including OH group. Pure silica glass is composed of an irregular 3D network consisting of disordered tetrahedral SiO_4 units as shown in Fig. I - 1 using atomic resolution STM of silica bilayers [30], and as opposed to its crystalline counterpart.

I.2.1.1 Silica glass structure

There are various possibilities of assembling SiO_4 tetrahedra in three dimensions (3D). However; the most stable configuration is the one for which the Si-Si distance is the longest, which is achieved through an assembly by the vertices. This configurational assembly is found in all forms of crystalline silica: quartz, trydimite, cristobalite and coesite. The intermediate bond angle of the Si-O-Si group gives an average value of 145° [31], which admits a certain dispersion, corresponding to an Si-Si distance of approximately 3.12 Å. The Si-O interatomic distance varies between 1.62 Å and 1.77 Å, and the O-O one is typically situated between 2.50 Å and 2.65 Å [32]. The complete assembly of all the tetrahedra in silica glass thus forms a 3D network presenting only a short-range order, but lacking long range order. This representation of the structure corresponds to the definition of the disordered or random network in the literature.

At a short distance, the order is governed by the coordination of silicon: a silicon atom is surrounded by 4 oxygen atoms forming a tetrahedron and, each oxygen is shared between 2 tetrahedra, to respect the SiO_2 stoichiometry. Silica glass is a special case of disordered systems because it has a medium range order. The latter is due to molecular connectivity. There are always four tetrahedra surrounding a given tetrahedron. However, there is no Euclidean translational symmetry [33]. The correlation length is defined as the number of successive correctly ordered tetrahedra. The free space in the structure allows tetrahedra to rotate. In this case, the correlation length or the degree of polymerization of the glass may vary according to the method of preparation and especially the cooling rate and more generally the thermal history. The structure of a cooled glass is frozen from a so-called fictive temperature T_f as described in details in Ref. [34]. Silica has the same medium-range order as the crystalline form of tridymite and cristobalite. When silica is elaborated under high pressures [35], its specific volume is lower. It then adopts a denser structure, this new configuration approaching that of quartz or coesite. Silica subjected to a very high pressure can also adopt a rutile structure in the form of SiO_6 octahedra, and so called stishovite [36]. Pure silica glass is composed of an irregular 3D network consisting of disordered tetrahedral SiO_4 units as shown in Fig. I - 1 using atomic resolution STM of silica bilayers [30], and as opposed to its crystalline counterpart.

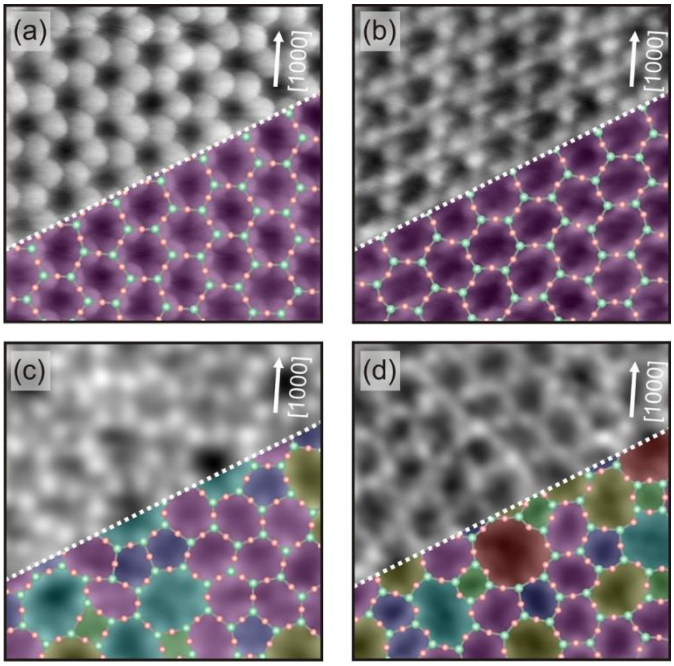

Fig. I - 1 Atomically resolved scanning tunneling microscopy (STM) images of the thin silica bilayers: the crystal structure (a and b) and the disordered silica glass (c and d). Cite from [30].

I.2.1.2 Point defects in silica glasses

A glass can be subjected to a multitude of treatments such as heating, high pressure or laser irradiations and a combination thereof. These treatments will locally modify the

linkage sequence to form point defects. The definition of a defect in the glass is different from the definition given in a crystal. Indeed, in a crystal, any exception in translational symmetry is considered a defect. In a glass, this symmetry of translation does not exist and this definition cannot apply. The notion of defect is then based on the notion of chemical order. An idealized, i.e., perfect, silica glass network can be presented as a sequence of SiO_4 tetrahedral interconnected by common oxygen atoms. Thus, each silicon atom is connected to four oxygen atoms and each oxygen atom must have two Si as nearest neighbors. Any exception in this sequence ≡Si-O-Si≡ can be considered as a defect. Each defect has a structure and properties (absorption, fluorescence, magnetism, etc ...) that are unique to it. In order to better understand and subsequently control the impact of point defects on the properties of silica, it is essential to know their atomic structure. This is usually determined by a combination of experimental techniques from spectroscopy and theoretical calculations of quantum chemistry. The experimental technique that quickly proved to be the most suitable for developing and confirming defect models was the RPE (Electronic Paramagnetic Resonance). Although the RPE is *a priori* only applicable to paramagnetic defects, the absence of RPE signal in the case of a diamagnetic defect can be important information in the search for models. A certain number of absorption bands have thus been identified. Begun several decades ago, the study of point defects is far from over. The structure of many defects, the absorption bands associated with them, or the mechanisms that lead to their appearance or disappearance, are still the subject of many disagreements. For more details on the properties of point defects, we can refer to the works of Griscom [37, 38], Garapon [39], Skuja [40, 41] and Trukhin [42].

I.2.2 Multicomponent oxide glasses

Several models include most of the relevant aspects which are known to lead to glass formation. For example, Zachariasen-Warren network theory is based on coordination number [43, 44]. This theory is strictly applicable to oxide glasses only in its original form, sometimes referred to as the crystallochemical theory. The model known as the 3-D continuous random network deduced from this theory. The basic postulates of this theoty are that i) interatomic forces similar in glass and corresponding crystal; ii) glass is in a slightly higher energy state; iii) nearest neighbor coordination polyhedra similar in glass and crystal; iv) nature of interatomic bonds similar in glass and corresponding crystal. Zachariasen's rules for glass formation are as following: i) Each oxygen atom is linked (bonded) to no more than two glass-forming cations (e.g. Si^{4+}); ii) Oxygen coordination number (CN) around glass-forming cation is small (3 or 4); iii) Cation polyhedra share corners, not edges or faces; iv) The polyhedral structural units form a 3-D continuous random network in which every polyhedron shares at least 3 corners with its neighbors. A_2O_3, AO_2, and A_2O_5 oxides meet the above rules and can be as the good glass former (e.g. Si, Ge, P, B, ect.). No glasses could be formed like A_2O, AO, AO_3, A_2O_7, etc., based on the above rules. These rules didn't consider all modified oxides, non-oxide glasses (e.g. fluoride and metallic glasses) and chain-like glass structures (e.g. metaphosphate glasses). Some oxides were ruled out; such as Al-lime can form

glasses in fact. Network modifiers (alkali, alkaline-earth, transition elements) decrease the network connectivity by forming non-bridging oxygens (NBO), not bridging oxygen (BO), which have high coordination numbers and a random distribution in the glass interstices. As the model developed, cations in the glass were catagorized according to their role in the glass network. Network former can form a glass network alone by strong directional bonding (e.g. Si^{4+}, B^{3+}, P^{5+}, Ge^{4+}, As^{3+}, Be^{2+}, with CN of 3 or 4). Network modifier breaks the linkages between network formers in more ionic bonding (e.g. Na^{+}, K^{+}, Ca^{2+}, Ba^{2+}, with CN ≥ 6). Intermediates (conditional network former) may reinforce (CN = 4) or further loosen the network further (CN 6 to 8) and can substitute to a network former but cannot form a glass on their own (e.g. Al_2O_3, TiO_2, Ga_2O_3, As_2O_3, Sb_2O_3, Bi_2O_3, TeO_2, V_2O_5, MoO_3, WO_3).

In the following chapters, we studied a series of aluminoborosilicate doped with Na^{+} and Ca^{2+}, GeO_2 and many commercial glasses including alkali aluminoborosilicate (Schott glasses AF32 and Borofloat33), borosilicate (BK7), aluminoborosilicates (Eagle XG and 7059), Soda-lime, titanium silicate (ULE).

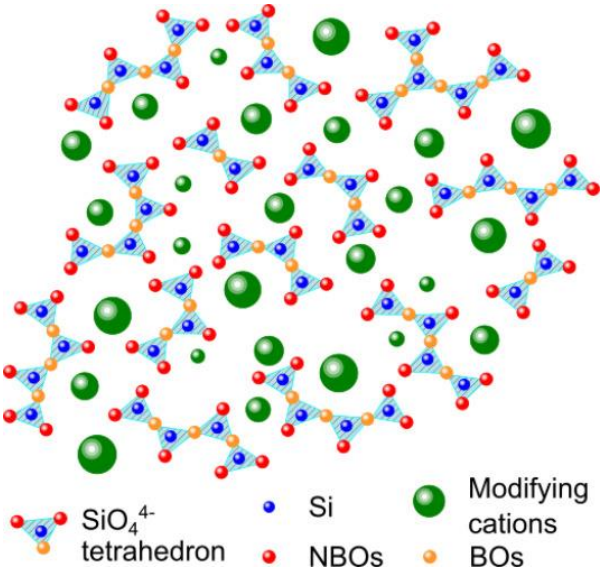

Fig. I - 2 Two-dimensional schematic of the structure of an invert glass. Cite from [45].

I.2.3 Viscosity of glass

Within the framework of this dissertation, glass viscosity, and its temperature dependency, is a key property to comprehend the mechanisms behind the formation, and erasure, of nanogratings. Viscosity (η) is used to measure the inverse of fluidity. In fluid mechanics, viscosity is a measurement of the resistance to shear deformation / stress over time. On an atomic scale, it describes as the motion of atoms/molecules relative to their neighbors [46]. Stated otherwise, viscosity indicates opposition to the flow. It has the dimensions of a pressure multiplied by time. The SI unit for viscosity (η) is Pa·s. The most commonly used unit is also Poise (often abbreviated as "P") or dPa·s in glass industry and 1 Pa·s =10 Poise [47]. Viscosity is a thermally active process, which can be modeled, to some extent, using a typical Arrhenius law. From standardized

experimental measurements and glass manufacturing, viscosity reference points have been defined and shown in Fig. I - 3. These are temperatures at which the viscosity has a specific value, which mark the temperature ranges (especially the so-called annealing point, softening point and working point). The location of these ranges on the temperature scale depends sensitively on the type of glass, such as silica glass, borosilicate glass, soda-lime glass or aluminosilicate glass. For quartz glass and borosilicate glass, the difference between the working point and the annealing point is usually higher (the so-called long glass), while for aluminosilicate glasses, it is usually small (the so-called short glasses). Soda-lime-silicate glass is usually between short glasses and long glasses.

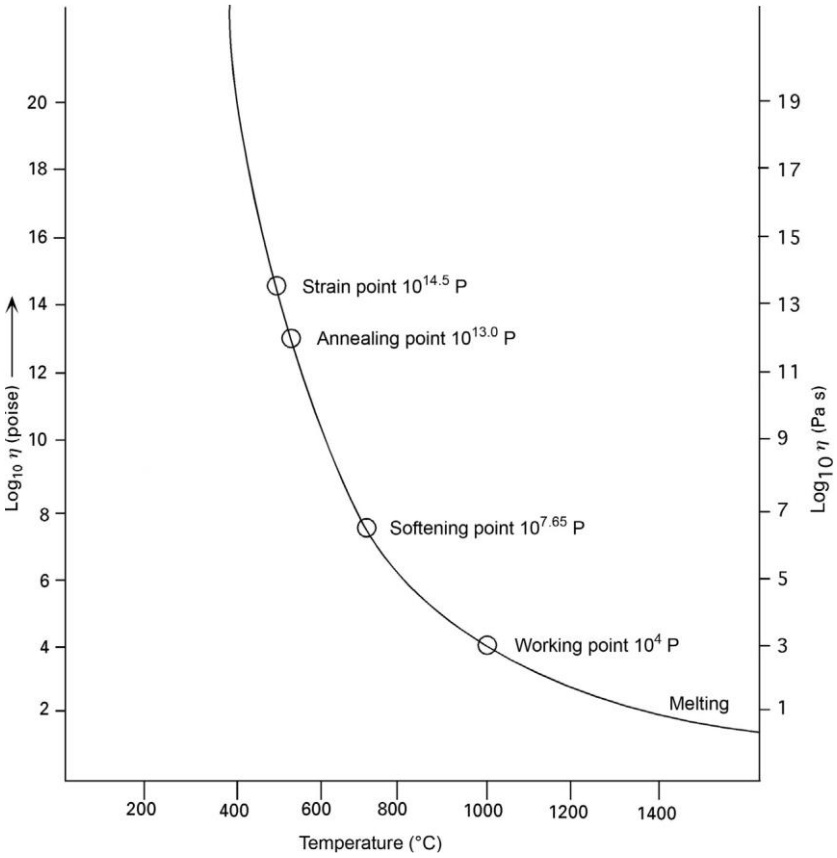

Fig. I - 3 Variation of the viscosity of a common soda lime silicate glass with temperature. Cite from [46].

Several models have been proposed to model the viscosity of glass. A simple exponential equation (Eq. I.1) with constant activation energy of viscosity was used as the basis for the Frenkel-Andrade model, which is the first known model about viscosity [48]. In this model, viscosity was not adequately described at intermediate temperatures between strain and melting points. Actually, the activation energy is distributed.

$$\eta(T) = Ae^{\frac{E_a}{RT}} \quad \text{(Eq. I.1)}$$

An empirical equation (Eq. I.2) was introduced and proposed by Gordon S. Fulcher in 1925 [49] based on analysis of viscosity data for various silicate glass forming systems, which revealed the temperature dependence of viscosity remarkably well with only

three fitting parameters: A, B, and T_0. Its mathematical form was first proposed by Hans Vogel in 1921 [50] and subsequently followed by Tammann and Hesse in 1926 [51] in the context of organic liquids. It is widely known as the Vogel-Fulcher-Tammann (VFT) equation. The VFT equation provides a highly accurate description of viscosity data at intermediate temperatures over wide orders of magnitude.

$$\log(\eta) = A + \frac{B}{T - T_0} \quad \text{(Eq. I.2)}$$

The Adam and Gibbs (AG) equation [52] (Eq. I.3) is derived on the assumption that molecules in a liquid, above the glass transition temperature can explore a wide range of configurational states over time, and when the temperature is raised, higher energy configurational states can be accessed. In contrast, a single configurational state is assumed to exist in glass below the glass transition temperature. Like the VFT equation, the configurational entropy model of AG fits a large number of viscosity data well within intermediate temperature, not accurately over the entire temperature range. When viscosity is high or low, it does not reflect experimental temperature dependence, so increasing deviations from experimental values occur.

$$\ln \eta(T) = A + \frac{B}{T S_{conf}(T)} \quad \text{(Eq. I.3)}$$

where A and B are adjustable constants, and $S_{conf}(T)$ is the configurational entropy. Considering $S_{conf}(T) = \frac{\Delta C_P (T - T_V)}{T}$, where ΔC_p is the relaxational part of the specific heat, and T_V is Vogel temperature.

Viscosity is behaved differently with temperature since activation energy (E_a) of viscosity varies with temperatures in the Avramov and Milchev (AM) model. The AM model is based on the assumption that the height of activation energy barriers varies different in case of the the disordered nature of glass, so the distribution function of the height of activation energy barriers is determined by its entropy. In this respect, viscosity is proposed as a function of system entropy. The equation is:

$$\ln \eta(T) = A + 2.3(13.5 - A)\left(\frac{T_g}{T}\right)^{\alpha} \quad \text{(Eq. I.4)}$$

where T_g is obtained from $ln\,\eta(T_g) = 12.5\ Pa \cdot s$. A is a constant, and α is the Avramov fragility parameter. The higher α is, the less strong a fluid is. So the α value of strong liquids is close to 1.

In the following chapters, the viscosity is important to explain the effects on the formation and erasure of NGs in different glasses by FLDW.

I.3 PROPAGATION OF ULTRASHORT LASER PULSES IN DIELECTRICS

This section lays the foundation of laser pulses propagating inside a dielectric medium, and interacting with it, as well as the definition of the different concepts relating to

femtosecond laser pulses and employed in this thesis.

I.3.1 Basic principles

The equation of propagation of an electromagnetic wave in a dielectric medium is deduced from the Maxwell equations and is written in the following form [53]:

$$\nabla^2\vec{E} - \frac{1}{c^2}\frac{\partial^2\vec{E}}{\partial t^2} = \mu_0\frac{\partial^2\vec{P}}{\partial t^2} \quad \text{(Eq. I.5)}$$

where $\vec{E}$ means the electric field; μ_0 is the magnetic permeability checking the relationship, $\varepsilon_0\mu_0 = \frac{1}{c^2}$ with c is the speed of light in the vacuum and ε_0 is the vacuum electric permittivity; $\vec{P}$ is the polarization. The polarization $\vec{P}$ induced by electric dipoles is a non-linear function of the electric field $\vec{E}$ and can be developed in increasing powers of the electric field [53] in the dipolar approximation as :

$$\vec{P} = \varepsilon_0\left(\chi^{(1)}\vec{E} + \chi^{(2)}\vec{E}^2 + \chi^{(3)}\vec{E}^3 + \cdots\right) \quad \text{(Eq. I.6)}$$

$$\vec{P} = \vec{P}^{(1)} + \vec{P}^{(2)} + \vec{P}^{(3)} + \cdots \quad \text{(Eq. I.7)}$$

$$\vec{P} = \vec{P}_L + \vec{P}_{NL} \quad \text{(Eq. I.8)}$$

where $\chi^{(i)}$ is the susceptibility and $\vec{P}^{(i)}$ is the polarization of order i where according to the classical description of non-linear optics [54-56], the vector polarization is the sum of linear polarization $\vec{P}_L = \vec{P}^{(1)}$ and non-linear polarization$\vec{P}_{NL} = \vec{P}^{(2)} + \vec{P}^{(3)} + \cdots$

In a centrosymmetric medium such as silica glass, the second order susceptibility tensor is identically zero because of the inversion center [53-55, 57]. We thus have:

$$\chi^{(2)} = 0 \quad \text{(Eq. I.9)}$$

By simplifying the expression of the polarization (Eq. I.6) to the third order, we obtain the expression in the case of an isotropic material:

$$\vec{P} = \varepsilon_0\bar{\bar{\chi}}^{(1)}\vec{E} + \varepsilon_0\bar{\bar{\bar{\chi}}}^{(3)}\vec{E}.\vec{E}.\vec{E} \quad \text{(Eq. I.10)}$$

$$\vec{P} = \varepsilon_0\left(\bar{\bar{\chi}}^{(1)} + \bar{\bar{\bar{\chi}}}^{(3)}\vec{E}.\vec{E}\right)\vec{E} \quad \text{(Eq. I.11)}$$

$$\vec{P} = \varepsilon_0\left(n_0^2 - 1 + \frac{3}{4}\chi_{eff}^{(3)}\left|\vec{E}\right|^2\right)\vec{E} \quad \text{(Eq. I.12)}$$

$$\vec{P} = \varepsilon_0\left[n_0^2\left(1 + \frac{3}{4}\frac{\chi_{eff}^{(3)}}{n_0^2}\left|\vec{E}\right|^2\right) - 1\right]\vec{E} \quad \text{(Eq. I.13)}$$

$$\vec{P} = \varepsilon_0(n^2 - 1)\vec{E} \text{ (Eq. I.14)}$$

where $n_0^2 = \chi_{eff}^{(1)} + 1$ is the linear refractive index of the medium and $n = n_0\left(1 +\right.$

$\frac{3}{4}\frac{\chi_{eff}^{(3)}}{n_0^2}\left|\vec{E}\right|^2\Big)^{\frac{1}{2}}$ is the refractive index of the medium. By carrying out the limited development of $(1+x)^a$ at the first order, we get:

$$n \approx n_0\left(1+\frac{3}{4}\frac{\chi_{eff}^{(3)}}{n_0^2}\left|\vec{E}\right|^2\right)^{\frac{1}{2}} = n_0 + \frac{3}{8}\frac{\chi_{eff}^{(3)}}{n_0}\left|\vec{E}\right|^2 = n_0 + \frac{3}{8}\frac{\chi_{eff}^{(3)}}{\varepsilon_0 c n_0^2} I = n_0 + n_2 I$$

(Eq. I.15)

Where $I = \varepsilon_0 c n_0 \left|\vec{E}\right|^2$ is the laser intensity and $n_2 = \frac{3}{8}\frac{\chi_{eff}^{(3)}}{\varepsilon_0 c n_0^2}$ is the non-linear refractive index that leads to the optical Kerr effect developed in the next section. The equation of evolution of the envelope of the electric field is given by the relation [58] :

$$T\frac{\partial E}{\partial z} = \frac{i}{2k_0}\Delta_T E - \frac{ik_0^{"}}{2}\frac{\partial^2 E}{\partial \tau^2} + i\frac{k_0}{n_0}(n_2 I)E \quad \text{(Eq. I.16)}$$

where $T = \left(1+\frac{i}{k_0 v_g}\frac{\partial}{\partial \tau}\right)$ is an operator; $k_0 = \frac{\omega_0}{c} = \frac{2\pi}{\lambda_0}$ is the wave vector in the vacuum ; ω_0 is the central pulsation of the wave; λ_0 is the central wavelength and c is the light speed in the vacuum ; $\Delta_T = \left(\frac{\partial^2}{\partial r^2}+\frac{1}{r}\frac{\partial}{\partial r}\right)$ is the transverse Laplacian of the envelope of the electric field in cylindrical coordinates; $k_0^{"} = \left.\frac{d^2k}{d\omega^2}\right|_{\omega_0}$ is the group velocity dispersion (GVD) ; $\tau = t - \frac{z}{v_g}$ represents the delayed time; with $\frac{i}{2k_0}\Delta_T E$ is the diffraction term in a medium of index n_0 in cylindrical coordinates ; $\frac{ik_0^{"}}{2}\frac{\partial^2 E}{\partial \tau^2}$ is the term of dispersion of the group velocity; $i\frac{k_0}{n_0}(n_2 I)E$ is the term relating to the optical Kerr effect.

I.3.2 Self-focusing by Kerr effect

The self-focusing of light is a process in which the intensity of the beam changes the optical properties of the material, in particular the refractive index. Due to the intensity spatial distribution (for a Gaussian profile), the laser beam induces a variation of index such that the index at the center of the beam is higher than at its periphery. Thus, the material acts as a lens with a positive focal length gradient, called the Kerr lens, causing the beam to converge in its focus. This phenomenon occurs when the power of the laser beam is greater than or equal to the critical power defined by the relationship [53] :

$$P_{cr} = \frac{\pi(0{,}61\lambda_0)^2}{8 n_0 n_2} \quad \text{(Eq. I.17)}$$

where λ_0 is the wavelength of the laser in vacuum. In the case of our silica sample irradiation experiments, we have: $\lambda_0 = 1030\,nm$; $n_2 = 3.2\times10^{-16}\,\frac{cm^2}{W}\,and$ $n_0 = 1.45\ at\ 1030nm$. The critical power deduced is 3.3 MW.

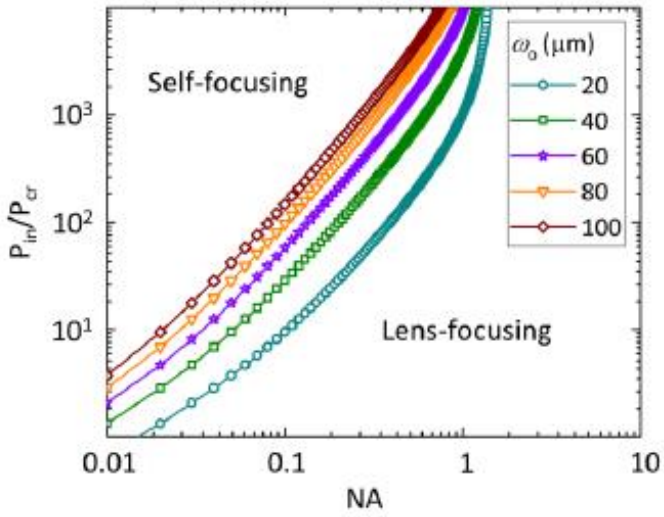

Fig. I - 4 Self-focusing versus lens-focusing in a ratio of radiation by critical power -numerical aperture of the focusing lens graph. Close to the boundary obtained for a given spot size (ϖ_0) of the beam at the plane of lens, both self-focusing and lens-focusing play a role. The calculations performed for fused silica at λ= 1030 nm. Typically, the critical power in silica is around 3,3 MW. Figure extracted from PhD thesis of Ausra Cerkauskeité [59].

Self-focusing of a collimated Gaussian beam is observed if the radiation power is greater than the critical power. In such a situation the Kerr nonlinearity continuously dominates over the transverse diffraction. The situation may be different if the lens is used in the direct writing system as it is our case for laser writing. For tight focusing the lens-focusing is dominating and the Kerr nonlinearity could be neglected, and for loose focusing the self-focusing is dominating. The boundary between these two regimes can be determined by [54, 60]:

$$\sqrt{\frac{P_{in}}{P_{cr}}} = 0.852 + \sqrt{0.0219 + 0.1347 \times \left(\frac{\left(\frac{k\varpi_0}{2}\right)^2 - \left(\frac{n}{NA}\right)^2 + 1}{\left(\frac{n}{NA}\right)^2 - 1} \right)} \quad \text{(Eq. I.18)}$$

when near the boundary obtained for a given spot size ω_0 of the collimated beam before the lens both self-focusing and lens-focusing play a role. For example, if numerical aperture of the focusing lens is less than 0.01, self-focusing is likely to occur at input powers close to critical (Fig. I - 4). If the numerical aperture is higher than 0.1, in order to get self-focusing the input power has to be much higher than critical ($P_{in} > 10P_{cr}$). However, the calculations do not account for plasma generation, and also loses its validity when the incident power is much larger than the critical power ($P_{in} > 100P_{cr}$).

I.3.3 Filamentation

When there is a balance between the effect of self-focusing by Kerr effect, that of defocusing due to the formation of free electrons plasma excited the laser and the diffraction effect present during the entire propagation of the impulse even stronger that the size of the beam is small. The laser beam then propagates with a constant diameter: this is called filamentation (Fig. I - 5).

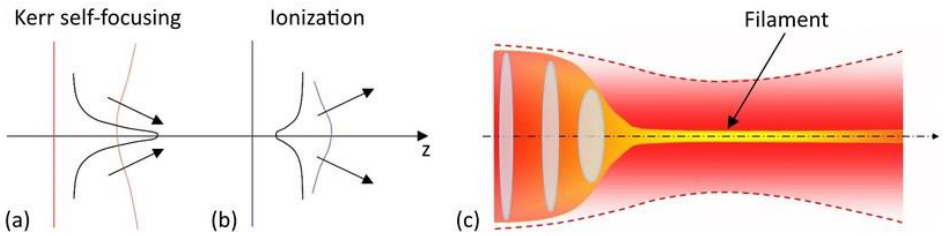

Fig. I - 5 Representation of focusing cycles (due to the Kerr effect) / defocusing (due to plasma formation) giving rise to the phenomenon of Filamentation (c).

I.4 FEMTOSECOND LASER-GLASS INTERACTION

I.4.1 Ionization and relaxation in intense field

In order to introduce the interest of femtosecond lasers in the realm of studying laser-matter interaction, this section briefly presents the mechanisms of interaction in glasses under the influence of an intense and ultrashort laser pulses. Numerous fundamental studies on the physical processes involved have been conducted, allowing significant progress in understanding these mechanisms and leading to a fairly clear vision of the interaction processes shown in Fig. I - 6.

Fig. I - 6 shows the time scale of the interaction mechanisms that can be summarized in three steps: the electronic excitation [61], the thermalization, the different relaxation mechanisms and the permanent modifications. Part of the laser energy absorbed by the electrons is transferred to the network (i.e. to the phonons) over a period of about ten picoseconds in the silica. After a few nanoseconds, a shock wave is emitted. On the time scale from nanosecond to microsecond, heat propagates around the focal zone. For rates that are low enough to prevent heat accumulation build-up [62, 63], the material returns to ambient temperature within a few microseconds in SiO_2. At sufficiently high energy, these processes can also cause non-thermal ionic motion and leave permanent structural changes such as inelastic deformation (densification or expansion depending on the irradiation conditions and the composition of the material), the appearance of an elastic response (stress) [64-68] in and around the irradiated area and the formation of point defects [69] that absorb in UV and VUV, etc ... These mechanisms are developed in the following references [70-74].

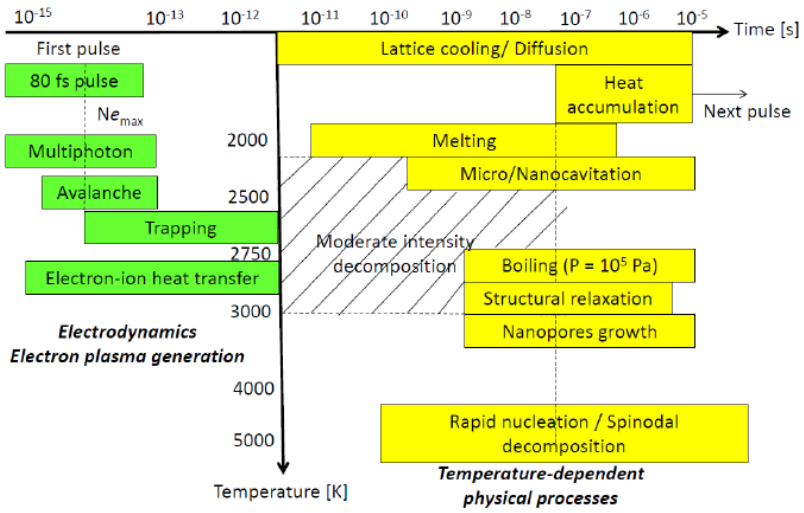

Fig. I - 6 Schematics of main physical processes involved in the ultrashort laser processing of silica glass including temperature-dependent processes. Extracted from A. Rudenko et al. [75].

The solids we have studied in this thesis are dielectric materials with a wide bandgap, and with silica rich compositions. In these materials, the conduction band is empty and the highest populated electronic states are those at the top of the valence band. Between the two, the forbidden band is of the order of 9 eV, and is therefore much higher than the energy of the incident photons (Eq. 1.5 eV for the Ti-Sa laser emitting radiation at the wavelength 800 nm and 1.2 eV for 1030 nm laser). Electronic excitation from the valence band to the conduction band can only occur by a non-linear process such as the simultaneous absorption of several photons. This multi-photon ionization process can only be observed for high laser field amplitude. It has been shown that at these high intensities, there is also a phenomenon of "electron heating" within the conduction band, which continues to absorb a large number of photons after having crossed the forbidden band. Thus, by means of photoemission experiments, the measurement of the kinetic energy of the photoelectrons has made it possible to obtain the energy distribution of the electrons in the conduction band, which ranges between 10 and 40eV in the case of silica [76] and for irradiation conditions similar to the experiments we will performed within this PhD thesis.

Some results obtained by our group and published in collaboration with Stéphane Guizard (LSI, CEA Saclay) on this point shows that in our experimental conditions (NA = 0.5 and I = 1-30T W/cm^2), the main mechanism of ionization happens to be multiphoton ionization: 6 photons in silica and 5 photons in Germanium doped silica. It should be noted that under our experimental conditions, neither tunnel ionization nor the presence of avalanche ionization are detected for pulse durations below 200fs [61, 77]. More recently, it has been shown that in SiO_2, it is possible, under specific conditions, to observe an increase in carrier ionization impact [78]. All these results demonstrate that the avalanche process, which is often invoked in the laser breakdown literature, does not play a dominant role in optical breakdown induced by short pulses. The relative importance of this phenomenon is always subject to intense discussion. It

is now widely accepted that this relative importance depends largely on the experimental parameters [73, 79-82]. In particular, it seems to depend on the pulse duration as well as its illumination or the width of the bandgap of the material.

I.4.2 Relaxation mechanisms

After this phase of electronic excitation, which takes place during the excitatory pulse, the photo-excited charge carriers are "out of equilibrium" and will thermalize with the solid by different mechanisms according to their kinetic energy. If the energy of the electrons is greater than the forbidden band, the inelastic collisions between electrons of the conduction band and the valence band, or the impact ionization, can occur at the attosecond scale (Fig. I - 7 step1). In this case, the electron loses a significant energy, at least equal to the forbidden band and we end up with two electrons of lower energy at the bottom of the conduction band. For time scales from femtosecond to picosecond (Fig. I - 7 step 2), lower energy electrons transfer their energy mainly via collisions with the lattice, by acoustic or optical phonon emission leading to heat effects leading permanents change like phase transition, photochemistry... In some materials, the electron-hole or exciton pairs induces local polarization and lattice deformation (Fig. I - 7 step 3). At this deformation or atomic displacement, defined in the following part, corresponds to the appearance of electronic levels in the forbidden band, on which the charge carriers will be able to locate (Fig. I - 7 step 4). We talk about trapped excitons (or self-trapped excitons noted STE) but also STH (self-trapped holes). This mechanism has a very short lifetime and occurs for a small percentage of charge carriers. STE has been studied in all alkali halides [83]. It has been demonstrated much more recently in silica and doped silica, and constitutes the intermediate step between electronic excitation and the formation of point defects, also known as "colored centers". Finally, non-trapped electrons will recombine with a hole in the valence band (Fig. I - 7 step 5).

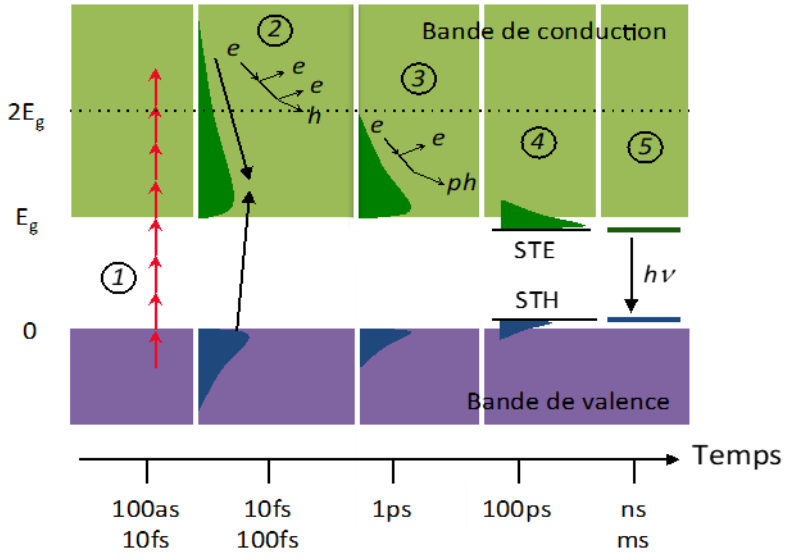

Fig. I - 7 Diagram showing the different elementary mechanisms involved during and after the interaction between a short pulse and a dielectric sample. 1: electronic excitation: either multiphoton (hv < Eg) or one

photon (hv > Eg); 2: electronic relaxation: process of inelastic electron-electron collisions or impact ionization; 3: electronic relaxation, continued: thermalization via collisions with the network; 4: trapping and location of charges (self-trapped excitons); 5: radiative recombination of excitons [extracted from HDR of S. Guizard, CEA/LSI/ Ecole polytechnique].

I.4.3 Material changes induced by femtosecond laser irradiation

The structural modifications of the glass are, of course, dependent on the efficiency of transfer of light energy to the material. As we have said before, in the case of an ultrashort light pulse and sufficiently powerful, interband transitions by multiphoton absorption are possible. They lead to the creation of quasi-free electron plasma, which is followed by electronic relaxations (STE, point defects, network heating). In silica, three structural transformation regimes are observed and correspond to different kind of modifications as shown in Fig. I - 8: an isotropic modification of the refractive index of the medium [84], anisotropic modification of the refractive index mainly due to form birefringence according to the literature [13, 85, 86], and micro-explosions leading to nano/micro-voids formation [87]. These modification regimes depend not only on the laser parameters: energy, pulse duration, laser repetition rate, wavelength, polarization (state and orientation), numerical aperture, depth of focus, writing speed, etc [20] but also properties of the material: band gap, viscosity, density, heat capacity, thermal conductivity and their dependence with temperature [88-91].

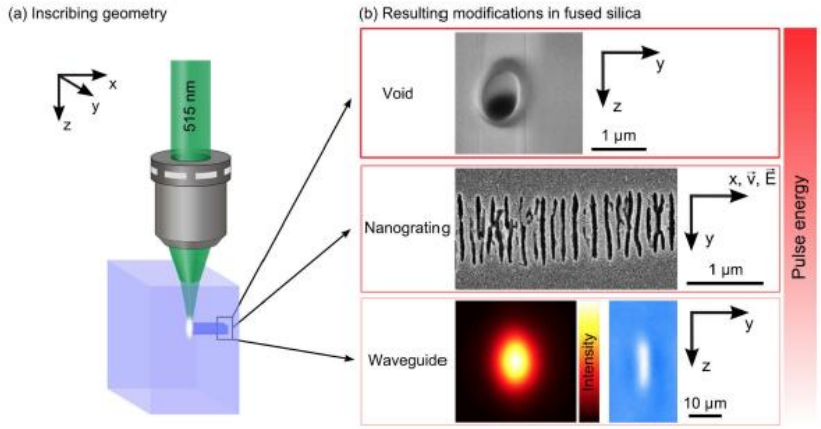

Fig. I - 8 (a) Typical writing geometry for Femtosecond Laser Direct Writing (FLDW) and (b) Description of the three main kind of permanent modifications photo-induced in silica glass as review in Refs [20, 72, 74].

I.4.4 Heat accumulation effects

The time required for the dissipation of the deposited energy out of the focal volume (diffusion time t_D) is given by $\tau_D = \frac{\omega_0}{2D}$, with ω_0 the focal radius and D the diffusivity of the material [92]. The diffusivity is defined as:

$$D = \frac{\kappa}{\rho C_P} \quad \text{(Eq. I.19)}$$

with κ the thermal conductivity, C_p the specific heat and ρ the density of the material. For a focusing with a NA of about 0.5, the width of a single pulse modification in fused

silica is about 1 µm, resulting in a diffusion time of about 1 µs. If the time between two successive pulses is shorter that this heat diffusion time, the temperature inside the focal volume will increase stepwise by each pulse. This process is called heat accumulation [62, 63, 73]. Fig. I - 9 shows the calculated temperature rise for different repetition rates at fixed pulse energy of 200 nJ in fused silica in a distance of 2 µm from the focal center (pulse duration 450 fs, NA of 0.5). The model used to calculate the temperatures is based on Fourier equation with a Gaussian heat source along the radial axis and a Lorentzian distribution along the beam propagation.

In irradiation regime with a large number of pulses at a low repetition rate (for example <200 kHz in silica), the material cools to room temperature between two successive pulses. Indeed the energy deposited by a pulse in the focal volume is "removed" by thermal diffusion in the mass of the material in about a microsecond in SiO_2. No thermal accumulation mechanism is expected a priori, the modification of the material being carried out independently by each pulse. However, it is possible to observe incubation effects due to the large number of pulses. During strong focusing (NA = 1.4), Schäffer et al. [93] do not observe any incubation effects: the size of the modified zone increases with energy but not with the number of pulses whereas the Δn increases with the number of pulses. On the other hand, at low focusing (typ. NA = 0.25), the incubation is responsible for the reduction of the damage threshold, as observed during surface experiments [94, 95]. In the latter case, it has been demonstrated in experiments [96] that the effect of the incubation is twofold: i) it modifies the absorption by accumulation of point defects ii) it introduces new possibilities of energy deposition in the network, in addition to the electron-phonon coupling. These possibilities are based on a coupling of electrons trapped in the network. The increase in the concentration of the defects is proportional to the initial concentration of defects, to the increment of the number of pulses, and also depends on the number of atomic sites likely to be affected during the accumulation process. Still in this low repetition rate regime (<200 kHz), Streltsov and Borelli [97] have shown in silica that the refractive index increase as a function of the laser energy seems to follow the temperature increase caused by a single pulse. On the other hand, since a high temperature (2500 °C) limits the refractive index increase, the effect of the temperature is not clearly established.

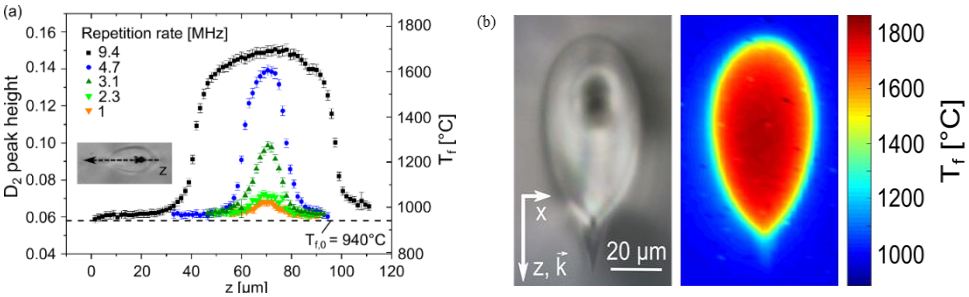

Fig. I - 9 Results of the Raman measurements from our group's previous work [98]. (a) D_2 peak height (left axis) and corresponding fictive temperature (right axis) as function of the longitudinal cross section (inset shows an optical micrograph with indication of the measurement trace). (b) Microscopic optical image and

corresponding map of the fictive temperature for a laser-induced modification inscribed with 9.4 MHz, 150 nJ and 1000 pulses per laser spot. The arrow indicates the propagation direction of the laser pulses.

Recently Yoshino et al. have [99] measured the temperature inside glass during femtosecond laser microprocessing by time-resolved micro-Raman microscopy. They successfully obtained the time evolution of heat and its dependence on pulse energy, which were found be different for fused silica and Borofloat33. The maximum temperature was found to be as high as 5000 K in silica for 2 μJ whereas the temperature remains limited below 1500 K in Borofloat33, whereas their thermal properties are of the same magnitude. However the melting temperature and the viscosities are quite different since the viscosity of Borofloat33 is several orders of magnitude lower than SiO_2. This indicates that the maximum temperature is relaxation time dependent and it seems limited by phase transformation like in Borofloat33.

In the high repetition rate regime (> 0.5 MHz in SiO_2), the period between two consecutive pulses is shorter than the thermal diffusion time out of the focal volume. The pulse train then gradually heats the material, this thermal accumulation leads to the permanent modification of a volume that is much greater than the focal volume [62]. In addition, the thermal diffusion is isotropic and the volume of the heated-affected zone increases with the number of pulses. The main mechanism is based on a local melting, in agreement with the corresponding simulations [62]. When the irradiation is stopped, the material resolidifies with possible densification mechanisms for the silica (due to the existence of an "anomaly" between the density and the fictive temperature: the silica becomes denser at high fictive temperature unlike other vitreous materials). A study of the thermal contribution to the increase of the refractive index as a function of the laser rate is proposed by Eaton et al. [63], following the increase of the size of the modified zone with the repetition rate [100]. A thermal accumulation effect was demonstrated from 200 kHz in a borosilicate glass with a weak bandgap of 3.9 eV, in agreement with the experiments of Schäffer et al. [62]. In both cases, the diameter of the modified zone corresponds to the diameter calculated to be melted, when considering the thermal characteristics of the corresponding glass. Osellame et al. [101] show that thermal accumulation effects for the production of high-speed waveguides depend closely on the type of glass used. Recently our group report on the processing of silica-based glasses by ultrashort laser pulses at high repetition rates. Heat accumulation leads to strong local heating of the glass and the subsequent quenching results in a fictive temperature rise those scales with the repetition rate as shown in Fig. I - 9. For all heat affected zones a significant increase of fictive temperature in contrast to the value for pristine glass of $T_{f,0}$= (940 ± 20) °C is measured. Interestingly, T_f scales with the laser repetition rate and reaches values up to 1700 °C at 9.4 MHz for 150 nJ and 1000 pulses per laser spot [98].

I.5 DIFFERENT TYPE OF PERMANENT MODIFICATIONS AND THEIR THRESHOLDS

Refractive index changes induced by femtosecond laser irradiation in silica have been reported in several papers. Authors investigated the magnitude, the kinetics, the

stability, the anisotropy according to the laser pulse energy, pulse duration, numerical aperture and writing velocity etc… From these results, it is possible to identify 4 regimes with 3 "damage" thresholds in SiO_2 glass as we reviewed according maser parameters (NA, pulse duration, ..) in [20] :

- Below the first threshold, T1, (e.g. 0.085±0.015 μJ/pulse in pure silica, 800 nm, 160 fs, 0.5 NA, 100 kHz, 100 μm/s), the increase of the index relaxes following third order kinetics. The writing process is two-photon dependent when an absorption band exists at the relevant final energy. The index changes decays within a few seconds.
- Between the two damage thresholds, the index change is permanent and nearly isotropic, the thermal stability is increased when compared to UV-induced changes but moderate. The maximum index change is $3\text{-}6\times10^{-3}$ in fused silica [102]. This is very large compared to UV laser-induced one which is limited to 3.10^{-4} using 157 nm or 193 nm excimer laser writing [103].
- Above the second damage threshold, T2, (e.g. 0.31±0.05 μJ/pulse in pure silica, 800nm, 160fs, 0.5 NA, 100 kHz), the characteristics are quite different. The index change magnitude can be as large as $\text{-}10^{-2}$ and resists to decay during at least two hours at 1000°C [104, 105]. The index change is highly anisotropic [85, 106, 107] and this is the most striking feature. The principal axes are determined by the laser polarization [106]. This is attributed to the formation of self-organized nanogratings [13] made of nanoporous silica [15] as extensively described in the next section.
- Above the third damage threshold, T3 (e.g. 4 μJ/pulse in pure silica, 800nm, 160fs, 0.5 NA, 100 kHz), we can observe voids [105, 108].

These three regimes can be clearly distinguished employing laser pulses shorter than 200 fs [82, 86, 109] (Fig. I - 10). But at longer pulses, the region II narrows a lot which make it difficult to realize Type I modifications in multipulses regime.

As shown in Fig. I - 10, another important parameter for femtosecond laser direct writing is focusing conditions, which roughly can be arranged into three groups depending on the numerical aperture. The low NA regime is related to lenses with NA < 0.1, this gives a spot size of more than 10 μm. The femtosecond laser beam weakly focused into the bulk of transparent material turns into filament below damage threshold preventing single-shot permanent structural modification [110, 111]. As a result, low NA lenses are typically used for surface modification, where self-focusing is not playing a crucial role. The lenses with numerical aperture from 0.1 to 0.6 can already induce a confined permanent modification inside of transparent material. At these numerical apertures spherical aberration can strongly affect the laser beam propagation. The refractive index of fused silica is higher than air's by roughly 0.45. The light is therefore non-uniformly refracted at the interface between the air and the material. As a result the adjacent part of the beam is focused deeper than the central, the waist is shifted and the focal spot is elongated in the propagation direction whereas

the lateral spot size remains the same [112]. The strength of this effect is increasing with numerical aperture. The refractive index mismatch can be compensated by using objectives with spherical aberration correction, immersion optics or adaptive optics methods [113, 114]. Even larger numerical apertures (NA>0.9) can be achieved with immersion oil lenses. The immersion optics not only tightly focuses the laser beam but also compensates refractive index mismatch at the surface of the sample. As a result, tightly focused femtosecond laser beam can modify material even at nanojoule energy level [115, 116], i.e. ultrashort pulse oscillator energy is sufficient to induce the permanent modifications. The characteristics of these different regimes and modifications are detailed below.

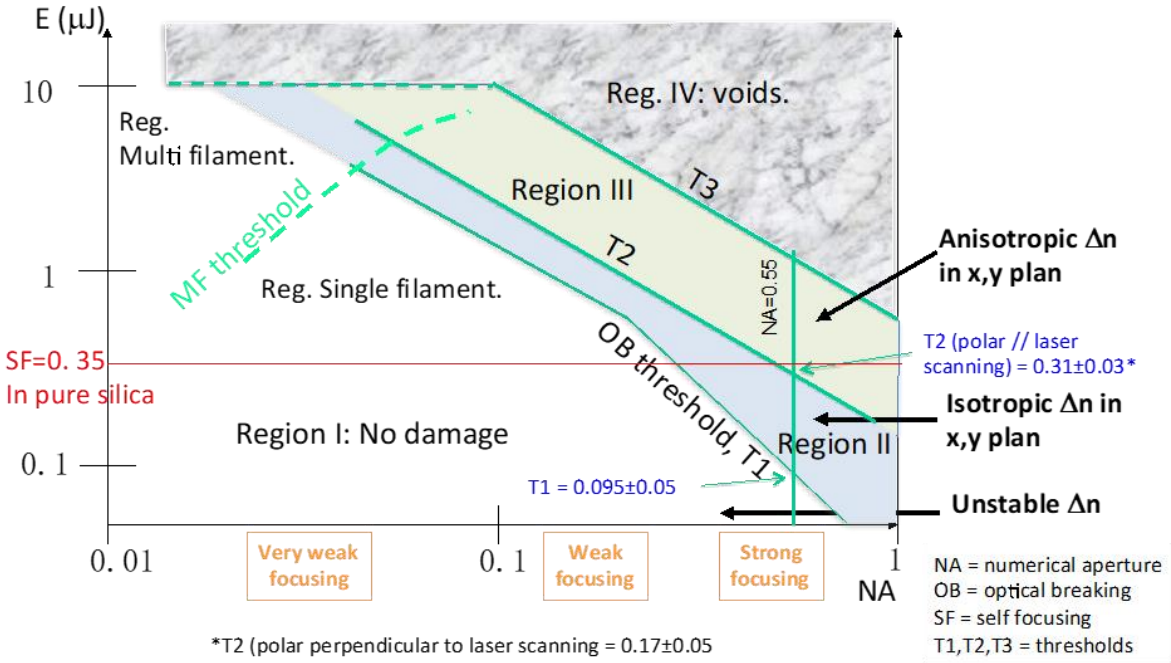

Fig. I - 10 Diagram of the different types of damage according to the energy of the laser pulses and the numerical aperture (NA) of the focusing. MF: multi-filamentation; AF: Self-focusing; T1, T2 and T3: thresholds of the different types of damage; * T2 (polarization perpendicular to the direction of laser writing) = 0.17 ± 0.05µJ. Laser writing parameters: 800nm; 160fs; 100kHz; 100m / s; parallel configuration; SiO_2. Adapted from Ref. [20].

I.5.1 Modifications of isotropic index changes (Type I)

The first observation of a threshold that we can report under a sufficiently intense irradiation is the reduction of the optical transmission. It is observed over a wide range of wavelengths from infrared to blue [58, 117, 118]. This indicates that the glass is modified in its structure. The corresponding threshold energy has been tentatively defined by Schaffer et al. [73] taking into account the beam propagation effect. For diffraction-limited focusing and taking into account the presence of weak self-focusing, the energy required to reach the breakdown intensity is related to the NA by using the relation:

$$E_{th} = \frac{I_{th}\Delta t\lambda^2}{\pi(NA)^2 + I_{th}\frac{\lambda^2}{P_{cr}}}$$ (Eq. I.20)

where I_{th} is the intensity; Δt is the pulse duration; λ is the wavelength; NA is the numerical aperture of the focusing lens and P_{cr} is the critical power defined in the relationship.

At low energy, an increase (from 10^{-4} up to 5.10^{-3}) of the refractive index is observed in the silica which is one order magnitude higher than with UV ns laser (193nm or 157nm) [103]. It is attributed to a permanent densification due to a rapid cooling of the initially very hot focal volume [119, 120]. In addition, the focusing of the femtosecond laser pulses gives rise to a constraint that plays a role in this densification under certain conditions [121]. Defects centers (also called color centers) induced by femtosecond laser irradiation may be responsible for a portion of the refractive index change through the Kramers-Kronig relationship (a change in absorption leads to a refractive index change since these two quantities are conjugate complexes of the dielectric constant) [122]. Although color centers induced in femtosecond laser irradiated glasses have been observed [97, 119], there has been no experimental evidence so far of a strong link between their formation and induced index change. Waveguides formed in silica with an infrared femtosecond laser [123] showed photo-induced absorption peaks at 213nm and 260nm corresponding to the respective center defects E 'and NBOHC. However, the two defects were completely erased after annealing at 400°C, although it retained its guiding properties up to 900°C. As a result, color centers are unlikely to have played a strong role in the refractive index change [123]. Other results lead to the conclusion that the thermal stability of the colored centers produced in borosilicate and silica glasses is not compatible with that of the change in refractive index [97]. It has recently been shown, in pure silica glasses for the realization of waveguides, that colored centers contribute to the refractive index changes for only 20% [102] whereas the major part has been attributed to defects-assisted densification by the authors.

In an extremely simplistic view of the free electron plasma relaxation created by laser irradiation, it can be said that the transfer of energy from free electrons to the glass network leads to very high local temperature. The temperature can reach several thousand degrees [63] at the focal point limited by thermal conduction [124] (and likely high pressures), up to the local melting of the glass, inducing densification (or expansion as a function of the relationship between the density and the cooling rate i.e. glass fictive temperature) after the fast cooling of the glass [125]. This results, for example, in a lower average Si-O-Si angle and thus some changes in some infrared bands (for example, the antisymmetric elongation vibration centered at 1120 cm^{-1}) and a change in the D_1 and D_2 bands observed in Raman spectroscopy [125, 126], D_1 and D_2 being respectively associated with the vibrations of cycles with 4 and 3 tetrahedra. In silica, these structural modifications are correlated with an increase in the refractive index, of the order of a few 10^{-3} in writing conditions close to ours. The hypothesis of

local densification of glass as a contribution to the increase of the refractive index was already advanced during the first publications on this subject [84, 97, 122, 127-131] following atomic force microscopic or phase shift interferometer observation of the depression of the surface (i.e. a valley) by a few tens of nanometers at the level of the irradiated zone.

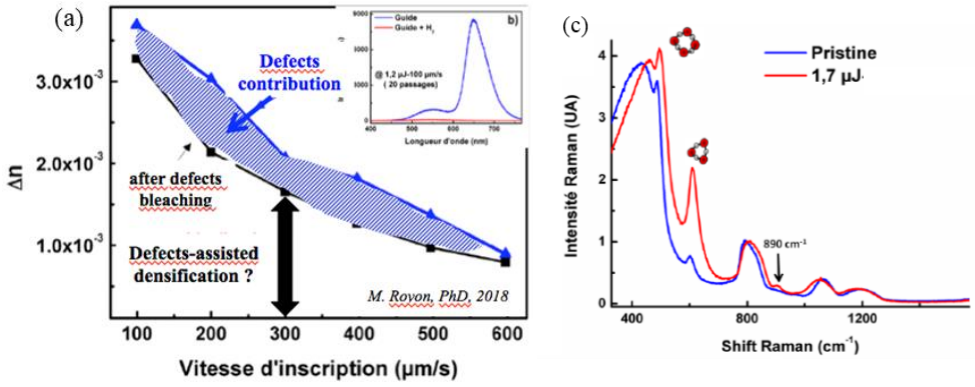

Fig. I - 11 (a) Measurements of Δn waveguides in a Corning 7980 fused silica, adapted from Royon et al. [102]. The blue curve represents the change in index after femtosecond irradiation while the black curve shows the index change following hydrogen loading and complete desorption. (b) NBOHC PL emission that is bleached after H_2-loading. (c) Raman spectra of the pristine sample and of a waveguide ($\Delta n = 3.10^{-3}$, Type I regime) photo-inscribed with the following conditions: 1.7 µJ (slit shaping conditions)- 100 µm/s with 8 passes [132].

Our team recently published a model of an original physico-chemical mechanism to explain these observations for Type I modifications. We proposed that the first threshold, named T1, is based on the modification of the fictive temperature T_f of the glass when the duration of the heat pulse corresponding to the light energy is greater than the glass relaxation time η(T)/G(T). This one depends on the viscosity η and the shear modulus G of the material, the lower the viscosity, the smaller the relaxation time and globally the larger the T, the smaller the relaxation time. If the increase of the temperature is long enough to transform the glass, this defines the first threshold noted T1. For that we have solved the Fourier equation and taken into account the variations of heat capacity, of thermal diffusion, of modulus of shear and viscosity with doping and temperature. The results show that the glass fictive temperature increases (several hundred degrees higher than the original temperature) and then does not change significantly. We have also described the dependence of photosensitivity on the chemical composition of glass in the germanium, phosphorus, F-doped silica family [124].

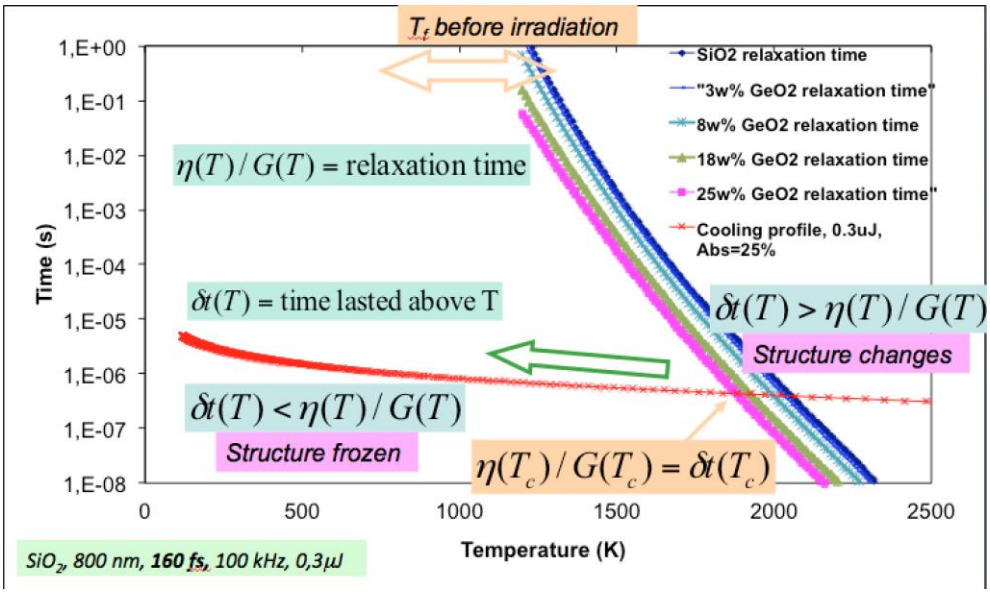

Fig. I - 12 This graph compares the glass relaxation time and the cooling profile after single pulse femtosecond laser irradiation for pure and GeO_2-doped silicaThe heat cooling profile is for pure silica only. Graph adapted from our group work in Ref. [124].

I.5.2 Modifications of anisotropic refractive index changes (Type II)

For higher energy pulses, a second threshold is observed which is based on the appearance of nanostructures (see Fig. I - 13) caused for example by the interference between the laser field and the electron plasma wave (a bulk plasmon) according to the first model that was proposed in 2003 [13].

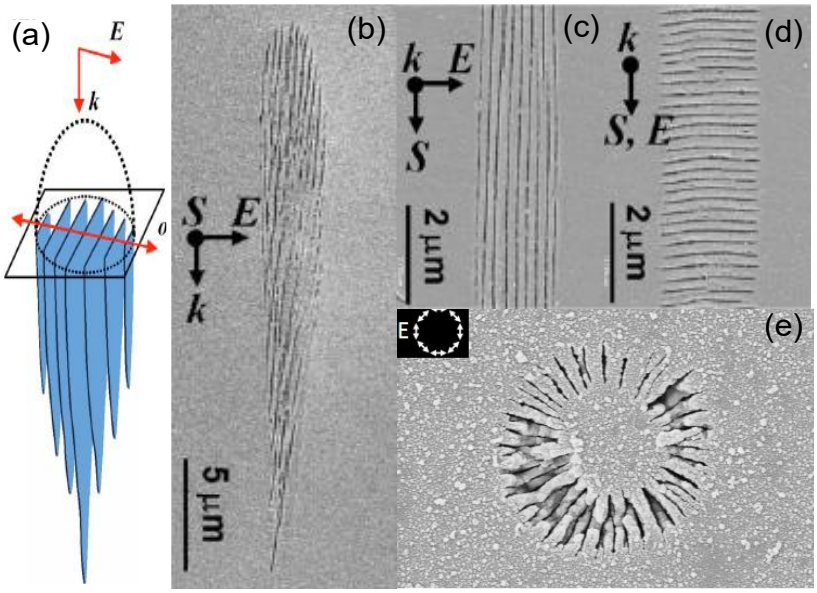

Fig. I - 13 Nanogratings scheme within a laser track cross-section (a). Scanning electron microscopy (SEM) image of the nanogratings inscribed at 65µm from the surface with a linear polarization perpendicular (b, c) and parallel (d) to the writing direction and azimuthal polarization (e). Laser parameters: 125fs, 0,65 NA, 0,3µJ, 100kHz, 30µm/s. Images extracted from Ref. [133].

Y. Shimotsuma and P. Kazansky made this discovery in 2003. It remained to determine

the nature of these nanoplanes. Some saw fractures, others oxygen depletions [13]. In 2011 we finally revealed that nanogratings are formed by a decomposition of silica (nanoporous silica formation [134]) as confirmed in 2013 [15] and shortly described in Fig. I - 14. This decomposition of silica into nanoporous layers can be done, contrary to the fictive temperature modification, only by a pulse-to-pulse accumulation. As the material cooled down completely between pulses, we initially proposed an accumulation of point defects. We then explain the variations with doping by production of defects that vary greatly. This production is favored by the addition of germanium or conversely, it can be inhibited to observe only isotropic index change by adding fluorine in silica, which provide interesting results depending on the type of application envisaged [124].

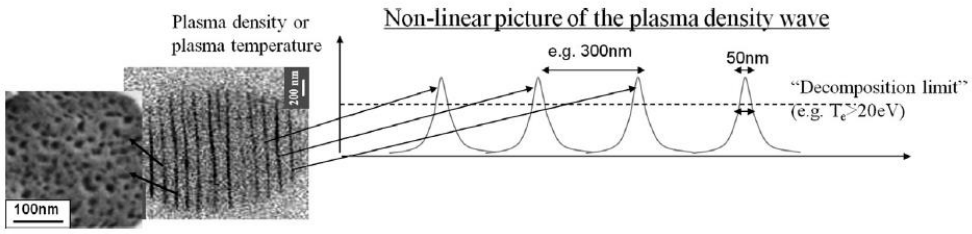

Fig. I - 14 Nonlinear picture of the plasma density wave. At the nanoscale the free-electron density (or electronic temperature) modulation is imprinted in the matter by decomposition of SiO_2, revealing a high plasma temperature Te (or density) that is higher than a "decomposition" limit. Graph extracted from Lancry et al. [15].

I.5.3 Voids (Type III)

For even higher energy pulses giving rise to peak intensities greater than 10^{14} W/cm^2, holes in volume (so-called voids) are achievable by femtosecond laser irradiation. They are at the origin of a mechanism called the micro-explosion. A first model was proposed by Fleischer's team [135] and also reported later by Schaffer [136]. The mechanism at the base of void formation was initially suggested to be a Coulombian explosion i.e. when the density of excitations at a point in the material is very large, the Coulombian force between ions can overcome their binding energy. In this case, ions are also moved to interstitial positions around the starting point. However this is unlikely to happen in the mentioned irradiation conditions so the mechanism was then revisited as follows: the energy is absorbed in a small volume producing a pressure which subsequently drives a shock wave and stress exceeding the Young modulus of the material. The strong spherical shock wave starts to propagate outside the centre of symmetry of the absorbed energy region compressing the material [87, 137-140]. At the same time, a rarefaction wave propagates to the centre of symmetry decreasing the density in the area of the energy deposition. The shock wave stops when the pressure behind the shock front becomes comparable with the Young modulus. The corresponding threshold is noted T3 in our threshold diagram in Fig. I - 10. Such voids can be exploited for 3D storage of information [108].

I.6 FOCUS ON TYPE II MODIFICATIONS AND NANOGRATINGS FORMATION

I.6.1 From LIPSS to self-organized nanogratings in silica

Laser induced periodic surface structures (LIPSS) are a universal phenomenon and can be generated on virtually any type of media including metals, semiconductors and dielectrics upon irradiation with linearly polarized light [141-144]. The ripples can be formed with wavelengths ranging from the mid-infrared to the blue end of the visible spectrum and at pulse durations from continuous wave operation to femtosecond laser systems [145, 146]. For normal incidence, the period of surface structures was known to be close to the wavelength of the light and oriented perpendicular to the laser beam polarization [147]. For oblique incidence and *TM* polarization (electric field is oriented parallel to the plane of incidence) the ripples occur with one of two possible periods [143]:

$$\Lambda = \frac{\lambda}{1 \pm \sin\theta'} \quad \text{(Eq. I.21)}$$

where θ is the angle of the incident of laser beam, and the negative or positive signs correspond to the forward and backward scattering, respectively. One interesting prospect from applications point of view is that when laser beam is moved with respect to the sample, the ripples can coherently extend over the scanned area.

Lately, ultrashort laser pulses were observed to induce two types of periodic surface structures depending on the period of the structure [148]: above single pulse damage threshold – ripples with a period close to the wavelength ($\sim\lambda$), and below single pulse damage threshold – subwavelength ripples with periods down to 30 nm ($\lambda/10$) [142, 149]. Here, the period was found to be dependent on the number of pulses and the subsequent carrier density [142, 150, 151], where the final subwavelength structure is formed only after tens or even thousands of pulses.

In general, the understanding of formation of LIPSS is a challenging task as this involves a complex sequence of inter- and intra-pulse physical processes as review in [152, 153]. It is generally accepted that low-spatial frequency LIPSS (LSFL), are generated by the interference of the incident laser beam with an electromagnetic wave scattered at the rough structure and may involve the excitation of surface plasmon-polaritons (SPPs), particularly important when irradiating with femtosecond laser pulses [146, 151, 154, 155]. The surface wave driven periodic modulation of the electromagnetic field along the laser polarization gives anisotropy in the following modification processes. It is assumed that the further steps are governed by the fast (non-thermal) and slow (thermal) phase transitions [156]. Interestingly, the early stage ripples upon a subsequent pulse irradiation modulates the light-matter interaction and reduces the periodicity of the pattern.

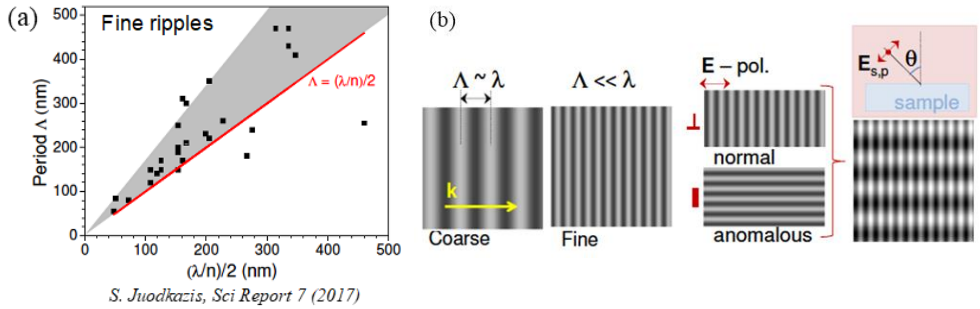

Fig. I - 15 (a) Fine ripple period Λ dependence on the laser wavelength λ and refractive index of materials, n. The gray-shaded region marks an expected (0.5 − 0.85). λ span of Λ values for the absorbing (plasma) surfaces according to the SPP surface plasma wave mechanism. (b) Ripples of period Λ on surfaces irradiated with wavelength λ laser pulses at an incidence angle θ = 0° (normal incidence): coarse, fine, normal (⊥), anomalous and mixture, which occurs at θ > 0°. Graphs extracted from Ref. [153]

In contrast, the high-spatial frequency LIPSS (HSFL) exhibit several features: *(i)* are formed at fluencies very close to the damage threshold of the irradiated material; *(ii)* have spatial periods significantly smaller than the irradiation wavelength; *(iii)* are usually observed for irradiation with ultrashort laser pulses *(iv)* mostly for excitation of transparent materials with a photon energy below the bandgap and *(v)* hundreds to thousands of laser pulses per irradiation spot. Within the interpretations proposed in previous studies, the early stage laser induced unstable nanostructures, during the relaxation of a highly non-equilibrium surface, tend to self-organize into HSFL patterns. However, the origin of the HSFL is still under debate [152, 153].

I.6.2 Physical and optical properties of nanogratings in silica glass

In 2003, a new type of self-organization was observed inside SiO_2 glass after irradiation with an ultrafast laser [13], which was found to be responsible for femtosecond pulse induced anisotropy [85, 106, 107] and the propeller shape of light scattering reported earlier in 1999 [157]. Under certain irradiation conditions, the interaction of femtosecond pulses with silica is known to induce highly ordered sub-wavelength structures with lamellae-like nanoporous regions oriented perpendicular to the incident beam polarization [15], as sketched in Fig. I - 16. At that early time, linear birefringence and related original structures such as self-organized nanogratings and chiral mechanical structures [68, 158] are spectacular but they appear to be only in specific materials (namely fused silica and Ge-doped silica). For instance, in BK7, no such structure is detected, although strong damage occurs [159]. In $84SiO_2$-$16SnO_2$ no birefringence is detected and, in addition, the index change is positive in contrast to pure silica [159].

Among the first discovered properties, Bricchi et al. [106] demonstrated that such nanostructures due to the sub-wavelength periodicity behave as a uniaxial linear birefringent material where the optical axis is parallel to the orientation of the laser polarization and *the slow axis is perpendicular to the writing laser polarization*. The effect of form birefringence, unlike intrinsic birefringence, which is due to the

anisotropy of oriented molecules, manifests itself due to the alignment of submicroscopic rodlets or platelets. The light polarized parallel to the interfaces experiences a larger refractive index and as a result a phase difference for two perpendicular polarizations is acquired. The strength of the form birefringence can be controlled by periodicity and material composition of the microstructure. Under a linear approximation, refractive indices of nanogratings for ordinary n_o and extraordinary n_e waves can be extracted [106, 160, 161]. Let's determine the theoretical linear birefringence. We consider a wave of the form:

$$\vec{E} = \begin{bmatrix} E_{O,x}\cos(\omega t - k_z z - \phi_x) \\ E_{O,y}\cos(\omega t - k_z z - \phi_y) \end{bmatrix} \text{ (Eq. I.22)}$$

where $\phi_{x,y} = \frac{2\pi}{\lambda} n_{x,y} l$ is the phase shift along the axis considered x or y. Bricchi [162] theoretically shows that the refractive indices are of the form:

$$n_x^2 = \frac{n_1^2 n_2^2}{\tau n_2^2 + (1-\tau) n_1^2} = n_e^2 \text{ (Eq. I.23)}$$

$$n_y^2 = \tau n_1^2 + (1-\tau) n_2^2 = n_o^2 \text{ (Eq. I.24)}$$

where $\tau = \frac{t_1}{t_1 + t_2}$ est the fraction of the total volume occupied by the thin sections. We deduce the linear birefringence of the assembly shown in Fig. I - 16:

$$\Delta n = n_x - n_y = n_e - n_o \leq 0 \text{ (Eq. I.25)}$$

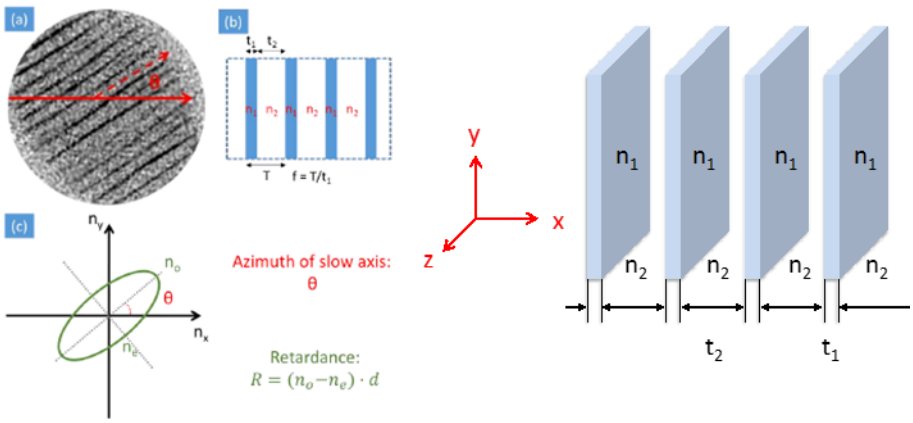

Fig. I - 16 Periodic assembly of parallel thin strips of index n_1 and thickness t_1 spaced by a distance t_2 in a medium of index n_2. Schemes are adapted from Refs. [162, 163].

Here the negative birefringence of $\Delta n \approx -5.10^{-3}$ up to -10^{-2}, and of the order comparable to the natural birefringence of uniaxial crystals such as quartz (uniaxial positive 8×10^{-3}), ruby and sapphire, was reported.

I.6.3 Tentative mechanisms for nanogratings formation

The formation of the periodic nanostructures in transparent dielectrics remains under debate. However, most of the studies agree that the seeding processes governed by

some kind of randomly distributed inhomogeneity are taking place [13, 164-169] but this is still not clear if whether these are point defects, glass free volume, nano-agregates already present or initiate by the first pulse like nanovoids for example in some recent suggestions. For example, the single isolated nanoplane was achieved in porous silica prepared from the phase-separated alkali-borosilicate glass [170-172]; and combining the experimental results with the concept of the surface plasma wave excitation, the significance of the seed structure was proposed. In addition, the constructive interference of scattered light was considered to explain the extreme reduction down to sub-100 nm of the nanogratings period, which breaks the limits of some models like λ/n or $\lambda/2n$. This correlates very well with the formation of surface ripple, when experimentally is proven that the period depends on the number of pulses [142].

One of the first models for nanogratings formation was proposed by P. Kazansky and based on the interference of the bulk electron plasma longitudinal wave propagating in the plane of light polarization with the incident light [13]. The early stage coupling is triggered by inhomogeneities induced along with the motion of free carriers. The periodic structure results due to the interference, enhances the coupling and generates a periodic modulation of the plasma concentration ($N_e > 10^{21}$ cm^{-3}). As a result, this modulation is further frozen into a material structural change. Conversely, the model does not work in the case of subcritical plasma concentrations. Further, this model was adjusted by assuming a two-plasmons decay [173]. The two-plasmons decay is the parametric process in which the incident photon is separated into two plasmons, i.e. two electron plasma waves. The interference between two plasmons of the same frequency propagating in opposite directions produces periodic sub-wavelength modulations (Cherenkov mechanism of momentum conservation). The characteristic generation of the 3/2 harmonic may be observed due to the decay process. Although the model is valid for plasma concentrations ($\sim 10^{20}$ cm^{-3}) lower than the critical density N_{cr}, this was never confirmed experimentally by independent research groups.

The model based on attractive interaction and self-trapping of exciton–polaritons was suggested to explain the periodicity of nanogratings in the direction of light propagation [167]. The two dispersion branches of exciton–polaritons are excited simultaneously by multi-photon absorption. As a result, the interference of propagating exciton–polaritons results in the polarization grating. After the relaxation process (< ps) to indirect states decoupled from light, the excitons can be trapped freezing the grating pattern formed by the exciton-polariton interaction with light [174]. The process is followed by the generation of molecular oxygen [15, 175] and nanoporous structure [15, 176] that originate the formation of nanogratings.

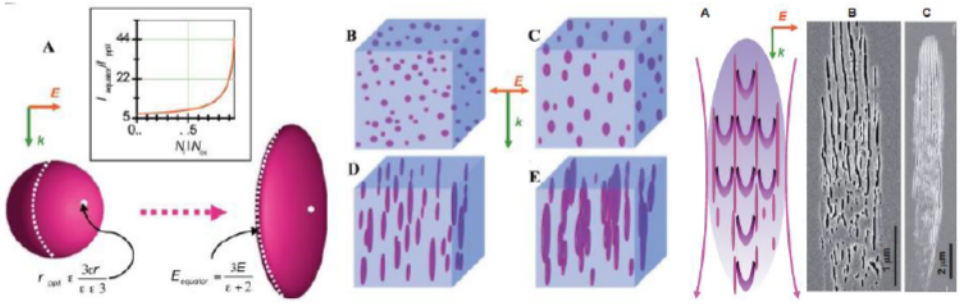

Fig. I - 17 (a) Asymmetric field enhancement at two locations on a nanoplasma under the influence of the laser electric field E [165]. (b to e) Evolution of nanoplasmas into nanoplanes. Randomly distributed under-dense nanoplasma droplets (typ. a few nm- 10'snm) grow asymmetrically in the presence of the laser field over hundreds of laser pulses to become ellipsoidal and finally flatten and merge to become micrometer-sized nanoplanes. (Right side, [177, 178]) Panel A: schematic diagram of periodic λ/2n-spaced planar structures. When irradiated they form plasma planes (Ne > Ncr) that guide light to reinforce the growth of planes in the bottom portion of the carrot structure. Panels B and C: cross-sectional SEM images of plane formation. Panel B: 100 fs, 350 nJ and 1 mm/s scanning speed. Panel C: 150 fs, 300 nJ and scanning speed of 30μm/s.

The most accepted model for nanogratings formation is thus based on a nanoplasmonic process [165, 177, 178] as described in Fig. I - 17. More specifically, the generation of "defects" (still to be identified) inside silica matrix is followed by the formation of inhomogeneous plasma. Under the multipulse regime, the plasma hotspots evolve into spherically shaped nanoplasma. But due to the local field enhancement at the boundaries, the polarization sensitive growth of initially spherical nanoplasma will occur. When the electron concentration is below the critical density, the electric field is enhanced at the equator leading to nanoplanes formation in a multipulses process. The final pattern leads to the period of $\lambda/2n$. However, if the plasma density is too high, the dominant enhancement at poles would be initiated, and nanogratings would not be produced. Recently, the nanoplasmonic model has been improved by introducing randomly distributed inhomogeneities to seed the process in fused silica [168]. When increasing the seed concentration, two types of nanoplanes oriented perpendicular to the polarization were identified. For low concentration of nanospheres, the low spatial frequency nanoplanes with the period of λ/n are formed, and attributed to the interference between the incident wave and the inhomogeneity scattered light waves (see Fig. I - 18 a, b, c). For high concentrations of nanospheres, the mechanism changes as the mutual enhancement induced by the multiple scattering from nanoplasmas becomes dominant. The nanoplasmas develop from random inhomogeneities into the highly ordered high spatial frequency pattern, with the characteristic period around $\lambda/2n$. In fact, as described in Fig. I - 18 b the periodicity may decrease drastically with the further increase of inhomogeneities concentration until the nanoplans merge i.e. generation of uniformly distributed plasma over the irradiated region. Interestingly this model could be adapted explaining both volume

nanogratings and surface ripples.

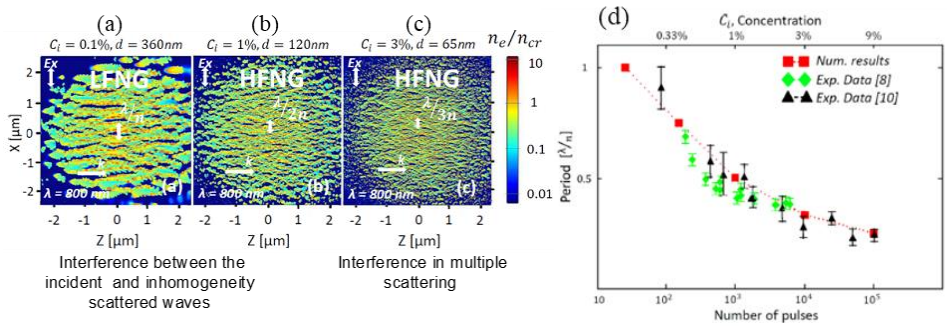

Fig. I - 18 Electron density snapshots are calculated by coupled 2D-FDTD at the end of the pulse duration θ = 240 fs (FWHM) for different initial concentration of randomly distributed (a) Ci = 0.1%, (b) Ci = 1%, and (c) Ci = 3%. The pulse energy is fixed to E = 500 nJ. The irradiation wavelength is 800 nm. (d) Period dependence on the number of pulses from experimental data comparing with the dependence on the concentration of inhomogeneities from numerical modeling. Extracted from Ref. [168].

It remained to determine the nature of these nanoplanes. Some saw fractures, others oxygen depletions [13]. Our recent studies using both SEM and TEM (never published) indicate that nanogratings are formed by the alternation of "uniform" and porous glass layers [15, 134, 176] (see Fig. I - 19 below). The interior of the nanogratings was examined by cleaving the sample after laser irradiation. If the nanograting planes were parallel to the cleavage the interior structure could be observed with field emission electron microscope, which could reveal small features otherwise covered by conductive coating. The areas appearing white are areas that, although having been irradiated, have remained dense, while the parts that are nanoporous are the nanoplanes that have been cleaved in their plane. The formation of nanopores was attributed to SiO_2 decomposition into $SiO_{2(1-x)} + x.O_2$ due to an electronic heating leading to an expulsion of ionized oxygen atoms [15] with a tensile stress mechanism [179] that was recently revisited as a nanocavitation process [75]. The oxygen atoms are thus found in the interstitial position and recombine to form oxygen bubbles as confirmed by Raman spectroscopy. The typical diameter of nanopores ranges from 10 to 30 nm. Small angle X-ray scattering measurements further confirmed nanoporous structure of the nanogratings interior [176, 180, 181].

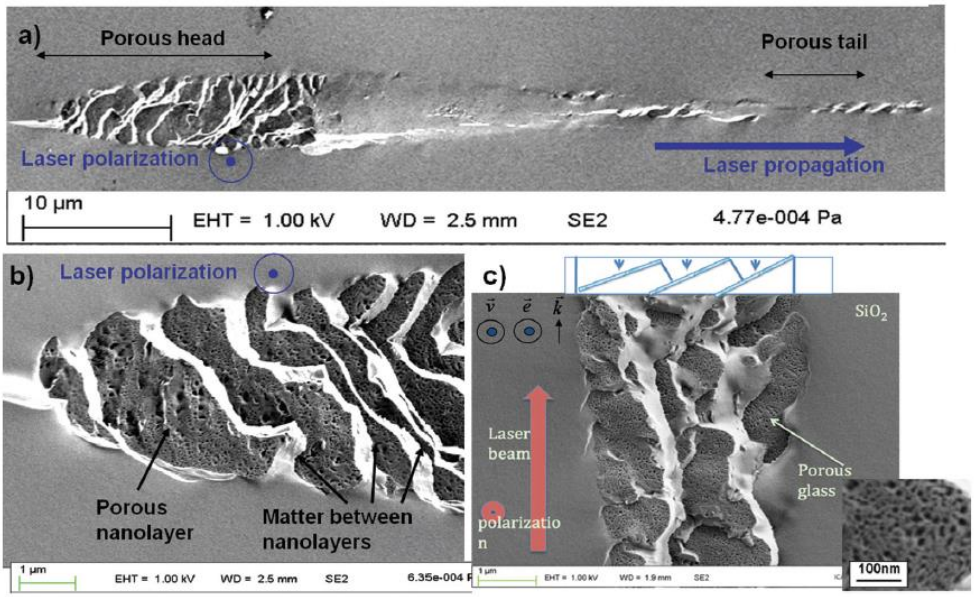

Fig. I - 19 SEM images of laser tracks cross-section. With the laser polarization parallel (a) to the scanning direction. (b) and (c) show close-ups of the nanoporous regions. Images extracted from Lancry et al. [15].

I.7 NANOGRATINGS DEPENDENCY ON LASER PARAMETERS

The ultimate goal is to produce a 3D printable anisotropic material, combining the benefits of durability and polarization sensitivity. In this section, the range of different parameters was discussed in order to gain the basic understanding how to control the ultrafast laser engineered birefringent structure. The main processing parameters are roughly summarized in Fig. I - 20.

I.7.1 Laser parameters (pulse duration, pulse energy, etc.)

Experimental observations suggest that the stationary printing and scanned modification require different parameters to obtain uniform nanostructures towards practical applications. If the target is high retardance, the pulse energy and pulse duration have to be increased, reducing the quality of the structure. If the target is uniform modification in scanning regime, sufficient pulse energy and repetition rate have to be chosen. Therefore, the best trade-off between all the parameters and the nanostructure should be achieved. A summary of the main experimental results and typical trends related to retardance formation within Type II regime in silica glasses is shown in Fig. I - 20. This summary was extracted from the PhD thesis of Ausra Cerkauskeité [59].

Wavelength: Decrease in wavelength leads to lower pulse energy required to obtain the modifications with the same level of retardance and a short period (see Fig. I - 21 a). It has been also demonstrated that shorter wavelength provides lower modification threshold but at the expense of higher losses in the UV-Vis range [182]. This is promising in terms of high density printing for 3D geometric phase optics but also optical data storage (energy reduction). However, the systematic investigation of the

quality of the structure and processing parameters should be done in order to optimize the writing system.

Pulse number: Currently a few pulses are required to induce self-organized nanostructure i.e. to create orientable linear birefringence. Retardance tends to saturate within at least tens of pulses delivered to the same spot. Period is decreasing with increasing pulses (see Fig. I - 21 a).

Pulse duration: As it can be seen in see Fig. I - 22, with the increase of pulse duration and pulse energy, the increase of retardance is observed leading to more rough structure [20, 86, 109, 183]. This suggests working close to the modification threshold, as in general smooth modification produces less scattering and allows recording information with the distance of the modification spot leading to high-density data storage. Strongest retardance is observed in the 500-2000 fs range.

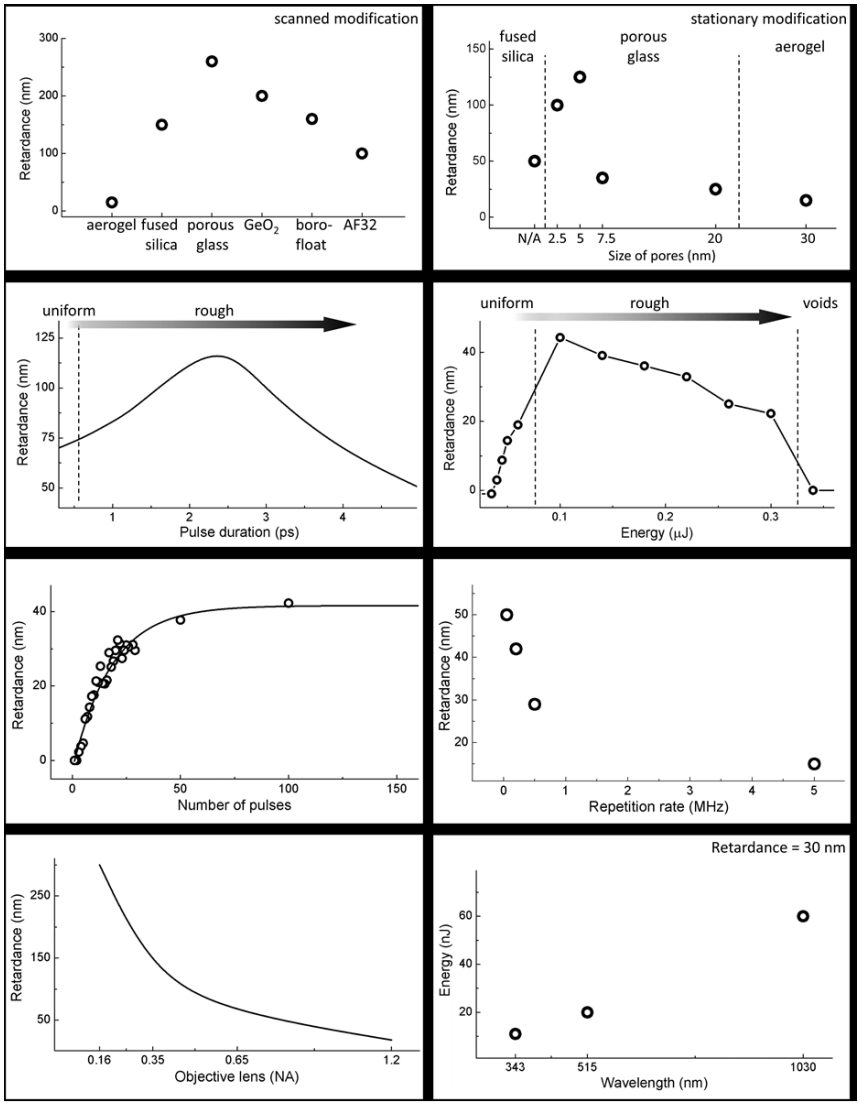

Fig. I - 20 Summary of the main experimental results and typical trends related to retardance formation within Type II regime in silica glasses. Extracted from PhD thesis of Ausra Cerkauskeité [59].

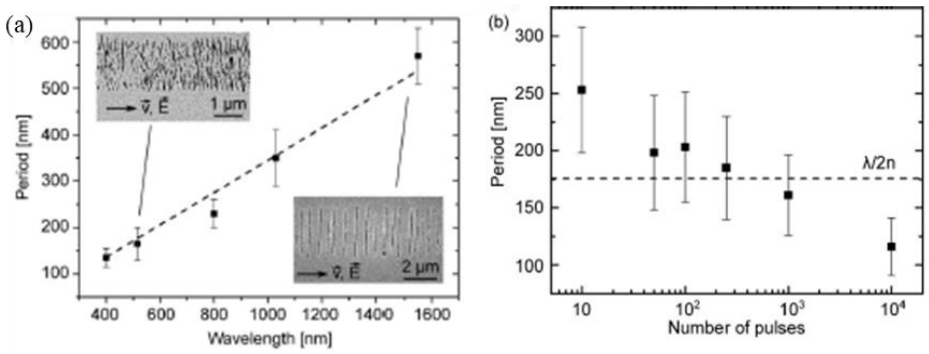

Fig. I - 21(a) Nanogratings period dependence on the laser wavelength. Dash line is for the λ/2n theoretical limit predicted by the nanoplasmonic model and considering material dispersion. (b) Nanogratings period dependence with the number of pulses. Laser parameters: 515 nm, 450 fs, 500 kHz, 190 nJ/pulse. Data extracted from Ref. [184].

Repetition rate: The nanogratings formation is very sensitive to the laser processing conditions and usually is affected by other effects such as heat accumulation and further local temperature increase. Although the periodic structure is formed within hundreds of picosecond after the irradiation, under high local temperatures the self-organized nanostructure can relax to its initial state before the resolidification takes place leading to the erasure of nanogratings [75, 98, 185]. So with the increase of repetition rate up to the tested region of 10 MHz, retardance decreases [184] as shown in Fig. I - 23 a. However, the nanogratings induced with 5 MHz still could be exploited for fast data printing, high-speed writing of space variant birefringent optics, 5D optical data storage [59] or polarization maintaining waveguides.

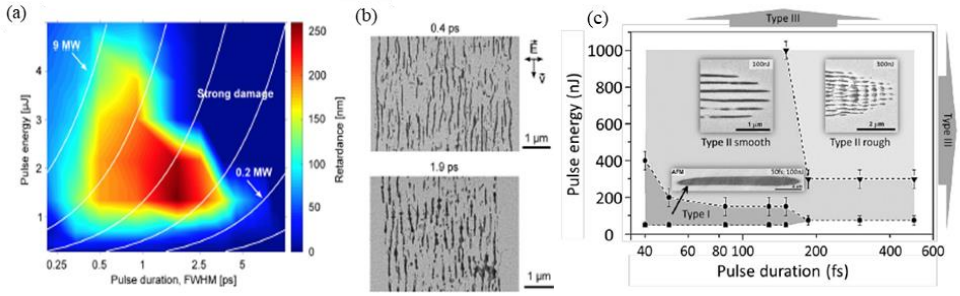

Fig. I - 22 False-color map of the optical retardance within Type II regime (nanogratings) in dependence of pulse energy and pulse duration, extracted from Ref. [175]. (b) Typical SEM images are shown for 0,4 ps and 1,9 ps pulse durations (1030 nm, 0,55 NA, 1,5 µJ/pulse). (c) Threshold pule energies for the different regimes in silica glass according to the laser pulse duration, from Ref. [86].

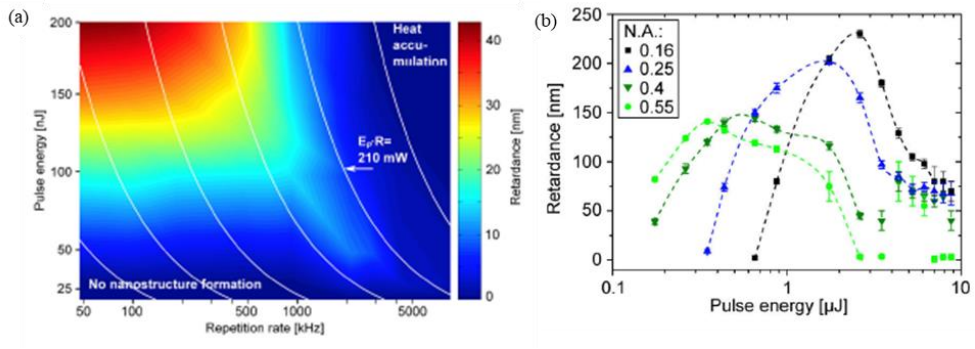

Fig. I - 23(a) Fast color map of the retardance as function of repetition rate and pulse energy. White lines correspond to constant average power in Watts. Laser parameters: 515 nm, 450 fs, 0,55 NA and the pulse number was kept fixed at 10^3 per micron by adjusting the scanning speed. (b) Optical retardance in Type II regime for different objectives NA and according to the laser pulse energy. Dashed lines represent a guide-to-the eye. Laser parameters: 1030 nm, 450 fs, 200 kHz, 10^3 pulses per micron. Graphs are extracted from Ref. [175].

Focusing conditions: Using tight focusing, the shorter structure is induced providing the lower value of retardance [12, 20, 110, 186] as illustrated in Fig. I - 23 b. Nonetheless, the use of nanogratings for multidimensional data storage lies behind relative high and low levels of retardance, and not behind absolute values. Thus, even with high numerical aperture objective the additional dimension can be explored. Apart from that, using tight focusing, it is expected to have smaller structure leading to higher spatial density of "printed data".

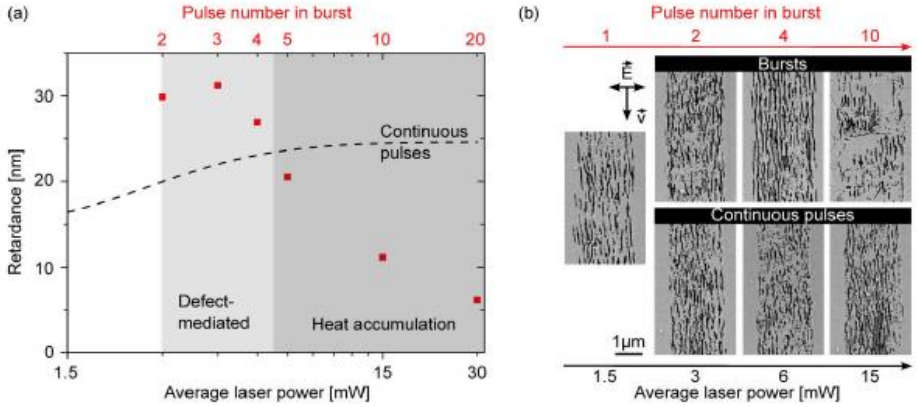

Fig. I - 24(a) Retardance within Type II regime for laser tracks written with bursts of different pulse numbers within each burst and with continuous pulses (dash line). (b) SEM images for nanogratings written with continuous pulses and burst mode. Laser parameters: 515nm, 450 fs, 1 MHz, 0,55 NA and 0,15 µJ/pulse. Extracted from PhD thesis of F. Zimmermann [175].

Formation timescales: The ultrashort pump pulses will be used to seed electrons and defects to facilitate nanogratings formation [184, 187, 188]. The ability to control self-assembly processes by ultrashort laser pulses (seeding and efficient energy deposition) will allow to induce nanostructures with several pulses (burst of pulses) increasing writing speed by multiple orders of magnitude. For example, when the number of pulses within a pulse is between 2 and 4, a much higher retardance is measured (See Fig. I - 24 a). The short time (typ. 100ns) between pulses within a burst promotes a more efficient absorption due to laser-induced transient defects from previous pulse.

In particular the relaxation of excited electrons involves the formation of STE [77, 189], which decays at least several hundred ps into point defects. Thus it seems that transient defects facilitates the formation of nanostructures [167, 187] as shown in Fig. I - 24 b.

Structure quality: Optical scattering is one of the key factors limiting the technology for multiple layer printing. Because of imperfections of induced nanostructures, like stress, cracks, melting, typically as much as 10-50% of the incident light is scattered in visible spectral range [182]. Also, for most optical components the slow-axis and retardance uniformity have to be achieved. As it was shown in[59], the uniformity of nanogratings can be realized working close to modification threshold but also using nanoporous silica materials [190].

Future work: It is technologically attractive to use the ultrafast laser direct writing, which offers manufacturability and rapid prototyping of optical elements at reduced costs. However, the mechanisms, which lead to the induced modification in the bulk material, are still not well understood. It is known that the process is strongly compromised by plasma scattering and self-focusing, which clamps laser intensity. The lack of control over these processes leads to slow writing speed and uneven nanostructures resulting in excessive scattering in the fabricated optical elements. Therefore, the key challenges towards the practical use of the technology have to be considered and explored in the future work including this PhD thesis.

As an intermediate conclusion, the observation of femtosecond laser-induced nanogratings structures in transparent medium has opened an avenue to a new research topic in the field of laser-matter interaction. The self-assembly periodic structures of nanogratings not only imply new mechanisms of the ultrafast laser-matter interaction process under extreme physical conditions but also exhibit favorable properties that are promising in developing micro-optical elements and new micromachining technologies. Therefore, it will continue to be a hot research topic in future time. Through years of study, the details of the nanogratings formation process have been constantly revealed, leading to new theories and improvement in previous models. However, there are still plenty of contradictory results between physical models and experimental results, since none of the existing theories can completely explain all the formation mechanisms of nanogratings induced in different mediums. And even the existence of a universal theory still remains controversial. Much more fundamental research is needed in the future to fully understand the whole process. Concerning practical application, great progress has been gained in recent years and some research groups have demonstrated several impressive integrated optical elements in labs. Despite all these achievements, the regularity of nanogratings prepared by existing process is yet far from commercialization and the available materials for practical nanogratings fabrication are still very limited. This is because that the mechanism of nanogratings formation in many materials is not very clear yet. Namely, the exact relationship between processing conditions and final dimension of nanogratings in difference materials has not been fully established. Besides, due to the

limit of the size of tightly focused light spot, the efficiency of inducing nanogratings is also not high enough for large-scale fabrication. Hence, further investigation is necessary in expanding available materials, refining quality and improving efficiency. In recent years, we witnessed a quick development of various advanced ultrafast laser related techniques such as time-resolved femtosecond laser technique, real-time femtosecond imaging, femtosecond pulse shaping, multi-beam interference and phase control of ultrafast light field, etc. We believe these technological advances will definitely contribute a lot to help researchers to understand the dynamics of ultrafast laser-matter interaction and will lead to a much more precise control of optical properties of the nanogratings.

I.8 CHEMICAL COMPOSITION EFFECT ON THE FORMATION OF NANOGRATINGS

One of the most spectacular effects of the interaction of tightly focused femtosecond (fs) laser pulses inside or at the sur-face of materials is the production of a special nanostructure called nanogratings (NG) or "Type II" modification regime. One example, inscribed in silica (SiO_2) glass, is provided above in Fig. I - 19. Inside the focal volume (here approximately 3 µm and 25 µm in width and length, respectively), the observed contrast takes the shape of dashes or lamellae, which are parallel to each other and perpendicular to the laser polarization orientation. After the discovery of these structures inside silica glass in 2003 [13], the substructure was found to be similar to an assembly of disks being a few µm in diameter [191].

This exemplar of NGs is the conventional view, since most of the work has been carried out in silica glass. But they have also been observed and reported in many other solid compounds. Overall, NGs can be sorted into several categories. The most popular, as mentioned above, is the one primarily revealed in SiO_2 with an arrangement of porous nanoplanes containing spherical nanopores of 10–20 nm diameter in size [13]. It is produced by oxide decomposition due to local temperature increase [192], sensitive to the laser polarization, and giving rise to form birefringence with a large retardance amplitude as a resulting property. This type of NGs induced in volume and by femtosecond (fs) laser were observed in several glasses or crystals, including doped silica with F, P, Ge, Cl, OH [124], GeO_2 glass [193-195], SiO_2-GeO_2 glasses [179, 180], TiO_2-SiO_2 glasses ([185, 196], TeO_2 single crystal [197], sapphire [198], Al_2O_3-Dy_2O_3 binary glass [199], lithium niobium silicate [200], or titanium silicate glasses (ULE, Corning) [196] and even in multicomponent aluminoborosilicate glasses (Borofloat 33, Schott) [196]. In β-Ga_2O_3 [201, 202] and in the Ba_2O_3-GeO_2-Ga_2O_3 glass family (BGG) doped with Na, K, or La, there is no laser irradiation conditions pointing out NG formation, although doping with Ta, Gd, or Zn showed otherwise [21, 203]. This is an example to highlight that a small addition of dopants can significantly impact the dynamics of NGs formation.

To continue the above list, NGs were obtained in alumino-silicate families [21, 204, 205], i.e., alumino-silicate glasses including B_2O_3, Na_2O, and/or CaO that can vary in a large

proportion. NGs are also found in crystals with small forbidden gaps such as Si, GaP, 4H-SiC, GaN, or GaS [206]. In recent work, the possibility to inscribe NGs was shown in sodium borosilicate glass (SBS) with the molar composition of 68% SiO_2, 27% B_2O_3, 4% Na_2O, and 1% Al_2O_3 [207]. This composition lies in the range of metastable liquation, which makes it possible to form a phase-separated structure in it by means of thermal treatment. Microregions with polarization-sensitive birefringence are formed when typ. $\geq 10^5$ fs laser pulses are deposited inside the glass. The laser pulse energy range enabling the formation of nanogratings and the phase shift obtained in the birefringent regions increase with the increasing number of writing pulses, and the formation of nanogratings is accompanied by the migration of sodium cations outside the laser-modified region.

Additionally, nanogratings inscription was demonstrated in nanoporous silica (sol-gel, Vycor) [190] and in binary sodium silicate glasses $xNa_2O—(100—x)SiO_2$ with x = 5 and 15. It revealed the effect of nano-periodical chemical differentiation inside NGs in the x = 15 glass composition, with the Na concentrated near the nanoplanes [208, 209]. Very recently, J. Wang et al. [210] showed the formation of NGs in sodium germanate (SG) glass with a $5Na_2O$-$95GeO_2$ molar composition. Unlike in sodium silicate glasses, an increasing Na_2O content to 10 mol% was reported to prevent NG formation in these compositions.

In Ref. [211], the authors also investigated the formation of NGs in SG glasses, but for Na_2O contents ranging from 3 to 22 mol.%. They revealed aspects of their inscription drastically different from those in fused silica, although their structure is shown to have much in common. This is another exemplar that the glass composition has a critical effect on the NG writing conditions. Moreover, a minimal number of pulses required to induce form birefringence grows exponentially with the Na_2O content. The formation of NGs in $22Na_2O{\cdot}78GeO_2$ glass is accompanied with precipitation of $Na_2Ge_4O_9$ crystals inside and around them. For completeness, it must be pointed out that a form of birefringent nanostructure, appearing at a low pulse energy regime, has been recently observed by Sakakura et al. [2] (labeled Type “X”, as opposed to “Type II” for NGs). It is a homogeneous production of asymmetric nanopores, oblate in the direction parallel to the laser polarization. One possible explanation is the destabilization of the oxide [15] or nanocavitation [16, 212] by multiphoton ionization on lattice irregularities. The effect of nanopores flattening is attributed to near field enhancement with linear polarization [213]. For larger pulse energies (i.e., larger intensities), the induced plasma is observed to reorganize in arrays as predicted for higher energies [167, 214] and drag the nanopores into nanoplanes.

A second type on NGs is found in oxide crystals and semiconductors (TeO_2 [197], Al_2O_3 [198], and Si [206]), where mostly arrangements of cracks, perpendicular to laser polarization, reveal the nanogratings. A third kind of NG is found in quartz crystal by periodic amorphization likely due to local fluctuations of thermal effect induced by the electron plasma structure [215]. Finally, a fourth kind of NG appears to be a partially

crystalline nano-periodic structures. They were observed, for example, in $33Li_2O$-$33Nb_2O_5$-$34SiO_2$ glasses (LNS glass precipitating $LiNbO_3$, [200]), in ($33Li_2O$-$33Nb_2O_3$-34-$xSiO_2$)-xB_2O_3 glasses (LNSB non-congruent glasses) [216], in $65Al_2O_3$-$35Dy_2O_3$ glass (congruent glass composition for $Dy_3Al_5O_{12}$) [199], and in $20Na_2O$-$80GeO_2$ glasses (congruent glass composition for $Na_2Ge_4O_9$ [211]). Obviously, the periodicity arises from an interplay between multiphoton ionization and the glass constituents.

In the case of $20Na_2O$-$80GeO_2$ glasses, the crystallization occurs mainly around the NGs and in the experimental conditions of the study. However, it is not the case for $65Al_2O_3$-$35Dy_2O_3$ glasses, for which crystallization is inside the NG region, but the experimental resolution cannot bring up information on its distribution. As for LNS, the only noncongruent glass studied, the NGs are produced through an allotropic phase separation (SiO_2 lamellas and $LiNbO_3$ in between) [200]. A thorough study of this irradiated glass in Ref. [217] demonstrated that the spatial periodicity of the phase separation is influenced by the induced plasma. Indeed, it is much larger than the spontaneous one, i.e., simply induced by a temperature elevation. However, for NGs composed of nanopores or cracks such as in silica, there is no periodic chemical migration. Moreover, in all models describing the mechanisms on NG formation, there is no feature that can explain a phase separation, because the material is always considered homogeneous; just some defects can play a role in the mechanism by seeding a hot spot of nanoplasma [213] and triggering a local thermal effect. The distribution difference between positive and negative charges is not taken into account and cannot explain the influence of light on the phase separation [39]. For that purpose, in a recent paper from our group, B. Poumellec et al. [218] consider the charge distribution induced upon light irradiation, analyzing more deeply compared to our previous publication and showing semi-quantitatively that the quasi-free electron plasma arrangement may interact with the phase separation, opening a way to its engineering.

I.9 CONCLUSION

This chapter introduces the background of this thesis. The necessary information is summarized in this chapter.

First, the structures and the point defects of the silica and multicomponent oxide glasses are illustrated briefly, and they affect the optical, mechanical, and thermal properties. One important thermal property, the viscosity of the glass and the equations of the viscosity versus temperature is introduced. The viscosity of the glass versus temperature plays an essential role in the formation and erasure of NGs induced by FLDW. There are few reports about the viscosity effect on the formation of NGs.

Second, we briefly introduce the propagation of ultrashort laser pulse in a dielectrics medium, including the related definitions of femtosecond laser pulses, the interaction between laser and glasses, and the related effects in the process. FLDW is a powerful tool to create both local and volumetric modifications in transparent materials, such as optical glasses. The different types of modifications, especially Type Ⅱ (NGs), and their properties and tentative formation mechanisms, are reviewed. NGs are the most exciting modifications imprinted inside most oxide glasses. The orientation of NGs can be controlled by light polarization, and they behave as negative uniaxial birefringent material. NGs have drawn attention to applications/fields, including birefringent optical devices, 3D geometric phase optics, optical data storage, microfluidic, structural health monitoring, and high-temperature sensing. We focus on the Type Ⅱ (NGs) in this thesis. Meanwhile, our objective is to study the mechanism of the equilibrium between the NGs' formation and erasure.

Finally, the chemical compositions of glass significantly influence the nanostructuring, properties, and morphologies of the formation of NGs. The different chemical composition effects on the formation of NGs is introduced in short at the end of this chapter. However, a comprehensive understanding of the reasons behind the various discrepancies observed is still lacking.

So, how do the glass's chemical compositions and viscosity affect the NGs' formation/erasure? The following chapters give some proposals about it.

Chapter II. STUDY OF NANOGRATINGS FORMATION INDUCED BY FLDW IN MULTIPLE OXIDE GLASSES

II.1 INTRODUCTION

Nanogratings (NGs) imprinted by femtosecond laser direct writing (FLDW) inside glasses are extraordinary nanostructures with application fields such as optics, microfluidics, optical data storage, sensors etc. Based on previous chapter, the origin of NGs based on state-of-the-art results, has been discussed. In this chapter, we focus on studying the role of glass composition on their formation, by investigating FLDW in multiple oxide glasses.

In the first part, we investigate the Type II (NGs) window in a pulse energy-repetition rate (E_p-RR) landscape inside five different oxide glasses, SiO_2(SuprasilCG), GeO_2, free/low alkali aluminoborosilicate (Schott glasses AF32 and Borofloat33) and alkali borosilicate (BK7) using the similar laser parameters. Following this, we discuss the impact of glass viscosity on the formation of NGs, which is a key property to consider. The domain of the NGs existence is defined using a viscosity argument under thermal and pressure confinement conditions. The lower limit corresponds to the NGs formation or nanocavitation and is defined as the temperature(T) for which the glass viscosity reaches around $10^{6.6}$ Pa·s. The higher limit relates to the NGs erasure through nanopore collapsing and is defined as the temperature at which the viscosity reaches $10^{3.0}$ Pa·s. The experimental windows agree with the arguments developed through this viscosity approach.

In the second part, the investigated glasses are extended to more glass including commercial ones: aluminoborosilicates (Eagle XG and 7059), Soda-lime, titanium silicate (ULE), in addition to the previously investigated glasses. They all exhibit interests in different applications such as flat glass for display and silicon wafer assembly (Eagle XG, AF32), glass substrate for electronic components (7059), infrared photonic devices (GeO_2), precision optics for medical technologies, photovoltaic or space telescope substrates (Borofloat33), visible and near-infrared prisms and micro-optic elements (BK7). The E_p-RR landscapes or NGs windows inside these 9 commercial glasses are summarized and compared. The retardance (R) of the NGs is measured by polarized microscopy. Scanning electron microscopy (SEM) is used to confirm the porous nature of the nanolayers composing the NGs. Moreover, the quantitative birefringence values of the NGs can be determined with complementary information of the laser track length from SEM analysis. The alkali or alkali earth content effects on the NGs window and the performance were compared and rationalized. The viscosity approach applies well in this extended glass composition range, and theoretical NGs window is well correlated to the experimental one.

In the third part, we investigate the NGs formation in a series of aluminoborosilicate

doped with alkali (Na^+) and alkaline earth (Ca^{2+}) element, named SAN, SAC, and SACN. The NGs possessing window is in the E_p and pulse duration (t_p) landscape and R is measured via polarized optical microscopy. The NGs possessing windows are assessed according to the $(Na_2O + CaO)/Al_2O_3$ and B_2O_3/Al_2O_3 ratios. The effects of the glass chemical composition and its correlation to viscosity is discussed.

In the last part of this chapter, we analyze the internal nanostructure of the NGs and its formation inside silica glass via SEM, scanning transmission electron microscopy (STEM), high-resolution transmission electron microscopy (HRTEM) and atomic force microscopy (AFM) techniques. Through NG observation under different orientations, it is revealed that oblate nanopores compose the nanolayers, being discontinuous and of a wavy shape. The periodicity of the NGs is investigated, along with the effect of deposited pulse density on it. Based on the findings herein and literature, we discuss formation mechanisms of the NGs in a plasma-mediated nanocavitation process.

II.2 APPLICATION AND VALIDATION OF A VISCOSITY APPROACH TO THE EXISTENCE OF NANOGRATINGS IN OXIDE GLASSES

Optical Materials 130 (2022) 112576

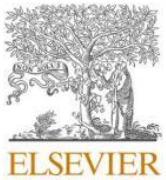

Contents lists available at ScienceDirect

Optical Materials

journal homepage: www.elsevier.com/locate/optmat

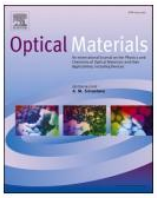

Application and validation of a viscosity approach to the existence of nanogratings in oxide glasses

Qiong Xie [a], Maxime Cavillon [a,*], Bertrand Poumellec [a], Diego Pugliese [b], Davide Janner [b], Matthieu Lancry [a]

[a] Institut de Chimie Moléculaire et des Matériaux d'Orsay (ICMMO), Université Paris-Saclay, CNRS, 91405 Orsay, France
[b] Department of Applied Science and Technology (DISAT) and RU INSTM, Politecnico di Torino, 10129 Torino, Italy

A B S T R A C T

Nanogratings are self-organized and sub-wavelength birefringent structures that are formed upon the action of high intensity ultrashort light pulses in the bulk of a transparent material. They have found interest in optics/photonics, microfluidics, optical data storage or sensing applications. However, the ability to successfully imprint 3-dimensional (3D) nanogratings in silicate glasses is a strong function of the glass composition. In this work, we investigate the role of glass viscosity on the ability to induce these nanogratings. We first study the nanogratings formation window in an energy-repetition rate laser parameter landscape for five common oxide glasses: SiO_2 (Suprasil), GeO_2, and Schott glasses AF32, Borofloat, and BK7. Secondly, and based on previous work, we define a domain of existence of the nanogratings using viscosity-based arguments. The lower limit corresponds to a temperature at which the viscosity is $\sim 10^{6.6}$ Pa·s, where nanocavitation of the glass occurs, forming the nanopores that compose the nanogratings. An upper temperature limit, set for a viscosity value of $\sim 10^{3.0}$ Pa·s, relates to either collapse or growth of the nanopores, resulting in the erasure of the nanopores, hence the nanogratings. The experimental results agree with the predictions made by this viscosity approach and literature data. This work opens the door to future glass viscosity engineering to maximize 3D nanogratings imprinting.

1. Introduction

Nanogratings, also labeled as "Type II" transformations, were first observed in 2003 [1] after femtosecond (fs) laser irradiation inside silica glass. These nanostructures exhibit the remarkable property of being birefringent with a slow/fast axis that can be spatially controlled through light properties such as polarization. Original properties can arise from these nanostructures, such as anisotropic light scattering, linear dichroism, chiral optical properties, and high thermal stability [2,3]. The ability to harvest these properties has therefore driven strong interest for applications including 3D geometric phase optics and micro optical polarization sensitive elements, 5D optical data storage, microfluidics, or temperature/pressure fiber-based sensors etc. [4–9].

In the pioneering work of Ref. [1], the authors proposed that the existence of these sub-wavelength and pseudo-organized structures, yielding to birefringence, originated from the interference between the incident light field and the plasma induced by ultrashort laser pulses. Electronic inhomogeneities were proposed as the triggering cause of this coupling mechanism. In 2008 a transient nanoplasmonics model was introduced [10], describing the appearance of spherical nanoplasma preferentially located at the hot spots induced by localized multiphoton ionization at defects or color center locations. In this view, the nanoplasma would experience an asymmetric growth oriented preferentially in the direction perpendicular to the laser polarization, due to an asymmetric field enhancement. It would then move from a spherical to an ellipsoidal shape, and ultimately to a disk-like shape, as more pulses are deposited inside the focal volume. Moreover, an exciton-polariton model was thus proposed in 2012 [11], through the coupling of light with plasmons. Later results suggested that these nanogratings originated from nanometric or sub-nanometric heterogeneities initially present in the glass, leading to coherently interfering scattering wavelets, hence the formation of a standing wave (2014: [12], and 2016 [13]). It is worth pointing out that this process is reinforced by a pulse-to-pulse effect, and both the dose and the pulse energy are key parameters in the formation of nanogratings including their pseudo-periodicity. Finally, inside the plasma dense region, the formation of porous nanolayers is observed in silica and silica-rich glasses [14]. The nanopores constituting these nanolayers typically show a size of few tens of nm. In 2013 the presence of free molecular O_2 was detected inside these nanopores [15]. In the same work, the birth of these nanopores was associated to a tensile stress-assisted nanocavitation and a "soft" Coulomb force necessary to overcome the oxygen binding energy and to form nanopores by recombination (to form O_2) upon an intense stress field. A cavitation mechanism was also proposed in the formation of

* Corresponding author.
E-mail address: maxime.cavillon@universite-paris-saclay.fr (M. Cavillon).

https://doi.org/10.1016/j.optmat.2022.112576
Received 10 March 2022; Received in revised form 23 May 2022; Accepted 31 May 2022

these nanopores, building on the theory developed by Grady on spall fracture of matter [16–18].

A direct observation from the above introductory discussion is that the electron plasma is self-organized in hot (dense) nanoplanes, and this is *a priori* not composition limited, as it is the case for surface nanogratings (LIPSS, laser-induced periodic surface structures) [19]. While the origin(s) of nanogratings formation has not been fully elucidated yet, these features have been observed in a variety of glasses, and most specifically oxide and silica-based glasses. These include but are not limited to silica [1,9,20], germanosilicates [21,22], sodium silicates [23], germania [20,24], sodium germanates [25], alkali-free aluminoborosilicate (AF32 Schott) [26], alkali-containing borosilicate (BK7 Schott, Borofloat 33 Schott), and titanium silicate (ULE Corning) [20,27]. However, it is worth pointing out that for some glasses such as SiO_2, GeO_2, or Borofloat 33, the laser-processing window to form nanogratings is large. On the opposite, glasses such as AF32 or likely BK7 have shown a narrower window. For BK7, only a weak birefringence response was shown, without laser-polarization dependence of the slow/fast axis orientation nor supported by electron microscope techniques demonstrating the presence of organized porous nanogratings.

In this context, this work provides insights on the relative difficulty to form nanogratings in some of these glasses. The goal is to describe, based on a viscosity approach, the ability for a glass to yield permanent formation of nanogratings. First, five commercial glasses are selected, namely BK7, AF32, Borofloat 33, GeO_2, and SiO_2 (Suprasil). In addition to SiO_2 being the backbone material of many of today's photonic applications, all these glasses present interests for diverse applications. These include, among others, mid-infrared optical devices (GeO_2), silicon wafer assembly in semi-conductor industry and flat glass for display (AF32), precision optics for space telescope substrates, or photovoltaic, medical technologies (Borofloat 33), visible and near-infrared micro-optic elements, prisms (BK7). The selected glasses are then irradiated by a fs-laser and using similar conditions. This systematic work allows a direct comparison between the glass samples and their respective nanogratings processing windows. The observed differences are then tentatively linked to viscosity-driven mechanisms, framing the existence of the aforementioned nanogratings processing window. Consequently, this work is expected to establish guidelines for future glass development when nanogratings 3D structuring is required for a wide range of applications.

2. Experimental details

To investigate the effect of glass composition, hence viscosity, on the ability to form nanogratings, a series of five bulk glasses was selected based on literature results and viscosity profile (more information on this later in the paper): BK7, AF32, Borofloat 33, GeO_2, and SiO_2 (Suprasil). Each glass sample, taking the form of a plate, was irradiated in similar conditions using a femtosecond laser (Satsuma, Amplitude Système, Bordeaux, France) having a central wavelength at 1030 nm and a numerical aperture objective NA = 0.6, at a pulse duration τ_p of 800 fs. In cartesian coordinates, z is the laser beam direction, and the laser scanning irradiation was performed in the plane (x,y) perpendicular to it. This pulse duration was chosen as it corresponds to a large window of nanogratings formation in SiO_2, AF32, and Borofloat 33 [26]. In this work, the investigation of nanogratings existence was probed in a pulse energy (E_p, in μJ) – repetition rate (RR, in kHz) landscape. For all the samples excepted the BK7 glass, a constant pulse density was used (10^3 pulses/μm). Since the repetition rate is varied in this experiment, the scanning speed was varied accordingly (e.g., 10 μm/s for a RR = 10 kHz, 100 μm/s for a RR = 100 kHz, etc.). For BK7, a constant writing speed of 1 μm/s was chosen in order to enable the formation of nanogratings.

There exists a variety of possible laser-induced transformations in oxide glasses, such as formation of defects, densification, nanogratings and/or voids formation, elemental migration, partial crystallization, and appearance of a stress field [28–30]. Therefore, an experimental procedure must be employed to decipher if there is, or not, the presence of nanogratings inside the laser track. First, each glass sample was irradiated using two different laser writing configurations: laser writing polarization parallel (along y) and perpendicular (along x) to the scanning direction (along y). Following this step, polarized optical microscopy (Olympus BX51) was used to quantify the birefringence response, along with its sensitivity (neutral axis orientation, amplitude) with respect to light polarization orientation, characteristic of nanogratings. Additionally, a complementary electron microscopy analysis (FEG–SEM Zeiss Supra 55 VP) was performed on the laser track cross-sections (x,z plane) to ensure the existence of porous nanolayers and nanopores, therefore confirming the polarized optical microscopy results.

The data taken for all commercial glasses investigated were provided by the glass suppliers (technical datasheets). Additionally, the temperature dependence of the glass viscosities ($\eta(T)$) was fitted using the Vogel–Fulcher–Tammann (VFT) equation. The viscosity data for GeO_2 were taken from Refs. [31,32] while its other parameters were taken from Refs. [33,34]. Most of the collected viscosity data points, in log(η, in Pa·s), are comprised between 3 and 13. Outside this interval the value of viscosity is less known.

3. Results and discussion

3.1. Domain of nanogratings existence

The formation of nanogratings in the E_p – RR landscape was investigated for SiO_2 (Suprasil), GeO_2, Borofloat 33, AF32, and BK7 glasses. The domain of nanogratings existence for each glass is shown in Fig. 1(a). As can be observed, the glass material strongly influences the ability to imprint nanogratings from the "self-organized" plasma. For BK7, which presents the smallest nanogratings window, porous nanogratings could be observed nevertheless, as shown in Fig. 1(b), but for very specific conditions (<100 kHz, and for typ. 50,000 pulses/μm). Additionally, and for all glasses, an example of measured retardance values (i.e., birefringence x nanogratings length along z axis) with respect to energy and at a constant RR = 50 kHz is provided in Fig. 1(c). Each measured retardance data point has a ± 5 nm uncertainty. The nanogratings window is the largest for SiO_2, intermediate for GeO_2, Borofloat 33, and AF32, and is extremely reduced for BK7 (an alkali "rich" borosilicate). Correspondingly, much higher values of retardance are found in silica glass compared to AF32 and BK7, which agree with the tendency to form nanogratings more easily in SiO_2 or GeO_2 that are strong network formers.

The principal aim of this paper is to highlight the link between nanogratings window and glass viscosity, being temperature dependent. Therefore, and to better appreciate the discussion in the next Section, below is briefly discussed how the temperature elevation upon fs-laser irradiation is impacted in an E_p – RR landscape, as in Fig. 1(a). There exist two principal situations when considering this landscape:

i) Low RR, increasing E_p. From the heat equation (Fourier's law), the temperature profile distribution in space is unchanged, but the deposited heat inside the material would increase. Consequently, the maximal temperature increase (ΔT) at the center of the irradiated area would also increase, following a general form of $\Delta T \sim aE_p/\rho C_p V$. Here a is the fraction of the pulse energy absorbed by the material and effectively transmitted to the glass phonons, ρ and C_p, respectively, are the glass density and heat capacity, and V the volume within which the pulse energy is absorbed. It is worth pointing out that a is a function of fluence (e.g., in silica glass [35]), and such temperature rise has already been investigated for several glass matrices including silica or Borofloat 33 [36,37]. As E_p is increased (and so ΔT), the spatial volume for which the temperature is beyond a transformation temperature threshold (e.g., formation of nanogratings) would be enlarged.

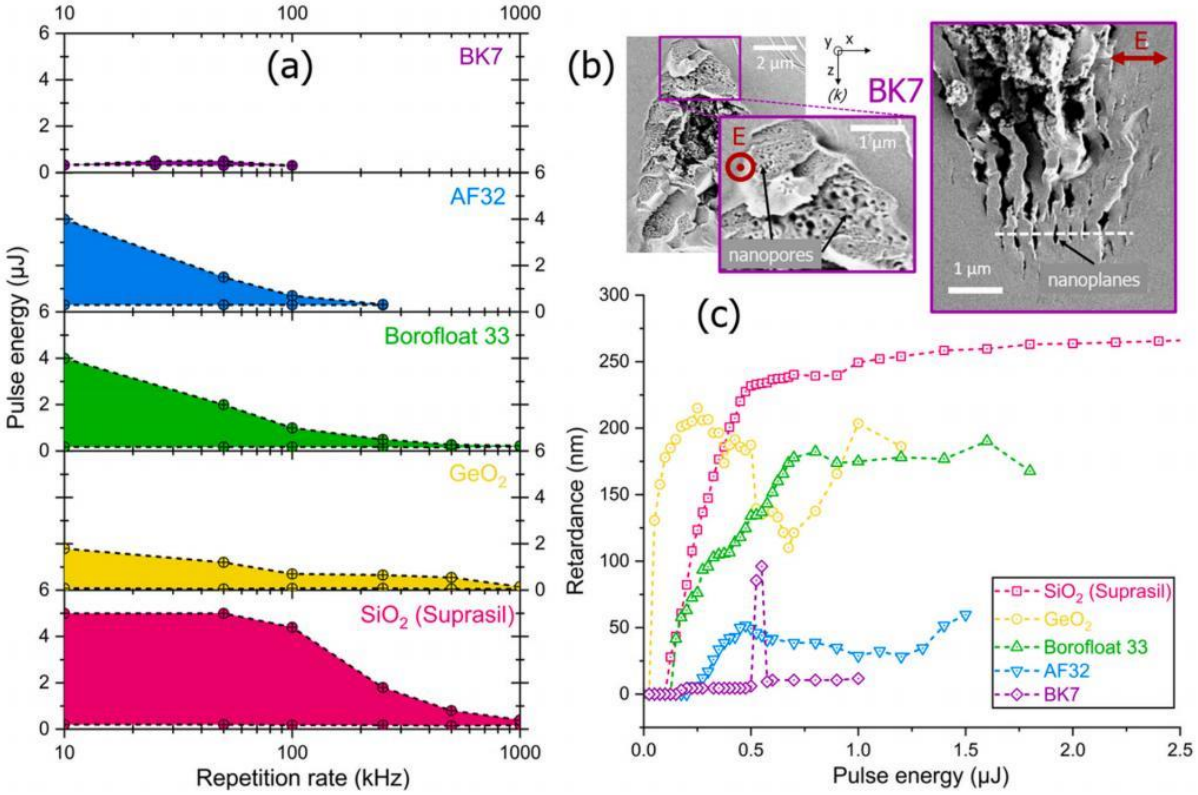

Fig. 1. a) Determination of observed nanogratings in an energy-repetition rate landscape for five glasses: SiO_2 (Suprasil), GeO_2, Borofloat 33, AF32, and BK7. b) Nanogratings observed in BK7 using scanning electron microscopy analysis; conditions are: pulse duration = 800 fs, writing speed = 1 μm/s, RR = 25 kHz, E_p = 0.6 μJ, focal depth = 300 μm. c) Evolution of retardance as a function of pulse energy (800 fs, 50 kHz, NA = 0.6); each data point has a ± 5 nm uncertainty.

ii) High RR, fixed E_p. This condition is also called "heat accumulation regime". In this regime, the heat generated by a pulse in the irradiated area does not have enough time to fully diffuse away before the next pulse is delivered. This effect would typically result into an increase of the average temperature, hence a decrease of the glass viscosity, in the heat affected zone. The characteristic time to evacuate the heat can be estimated as $\tau_{th} \approx \omega_0^2/(D_{th})$, where $D_{th} = \kappa/(\rho C_p)$ is the diffusion coefficient, κ is the thermal conductivity, and ω_0 is the characteristic length corresponding to the beam waist radius at an intensity of $1/e^4$ (typ. 1.5 μm). As an example, this gives D_{th} (SiO_2) ≈ 8.9×10^{-7} m^2/s and D_{th} (BK7) ≈ 5.2×10^{-7} m^2/s, and consequently τ_{th} (SiO_2) ≈ 2.5 μs while τ_{th} (BK7) ≈ 4.3 μs Turning these values into heat accumulation threshold frequencies, this gives f_{th} (SiO_2) ≈ 400 kHz and f_{th} (BK7) ≈ 230 kHz. Consequently, one would expect heat accumulation to be more pronounced in BK7 with respect to SiO_2.

From this short discussion and circling back to Fig. 1(a), one can note that the narrowing of the nanogratings window typically comes from both lower E_p and RR values. Consequently, the "temperature sensitivity" or "temperature interval" to make nanogratings appears reduced in glasses such as BK7 with respect to SiO_2. This reasoning is the starting point of the next Section dedicated to establishing a rational approach related to viscosity.

3.2. Rationale for a viscosity-based approach

Both the mechanisms of cavitation and erasure of the nanogratings take their roots in the material ability to break and reform itself in a time-temperature frame. In the following Section, the upper and lower limits of nanogratings existence are discussed on a temperature dependent viscosity basis.

3.2.1. Minimum viscosity to induce cavitation

When ultrashort laser pulses are deposited inside a large bandgap oxide glass as in our case, the pulse energy is absorbed by the glass material mostly through nonlinear effects (multi-photon absorption and tunnel ionization) and a significant part is subsequently transformed into heat through electron-lattice energy transfer. This takes a maximum of few 10s of picoseconds in most glasses [4,38], while the maximum temperature increases, as already discussed in the previous Section, reaching typical values of few thousands of degrees [36,37]. For small-to-moderate pulse energy values, the generated heat cannot escape the irradiated volume in the time of a pulse duration (typ. 100–1000 fs). This is the condition of so-called "thermal confinement". For such condition to be valid, the pulse duration τ_p must be shorter than the thermal relaxation time τ_{th} [39]. As calculated above, for silica $\tau_{th} \approx$ 2.5 μs and therefore $\tau_p \ll \tau_{th}$ for fs or ps laser pulses. The criterion of thermal confinement is thus satisfied. Additionally, if there are no significant strain or volume changes of the medium during heating, we are in the condition of so-called "stress confinement" [39]. For this second condition to be valid, the required time for the pulse to heat the sample must be shorter than the characteristic acoustic relaxation time $\tau_{ac} \approx 2\omega_0/c_s$, with c_s being the sound speed (≈ 6000 m/s for silica glass). This gives $\tau_{ac} \approx$ 500 ps, whereas the electron-phonon coupling time is on the order of 10 ps for silica and therefore the criterion of stress confinement is also satisfied. Therefore, the experimental conditions are met to yield nanocavitation in the glass samples.

Subsequently to this and following the wave equation from isotropic solids, the maximum tensile stress internally developed can be approximated as $p \approx B\beta\Delta T$. Here B is the bulk modulus (36 GPa for silica), β is the volumetric expansion coefficient ($\beta \approx 3\alpha \approx 3 \times 5.5 \times 10^{-7}$ K^{-1} for silica), and ΔT is the temperature elevation following the pulse energy deposition. Some caveats are worth pointing out: we use solid properties for each material (bulk modulus, thermal expansion coefficient), and

assume them constant with respect to temperature. Although this is questionable, it provides a guideline for reasoning. Interestingly, it must be pointed out that the resulting tensile stress is drastically different depending on the glass material considered. Furthermore, at low pulse densities, nanopores are initially formed but no nanogratings, close to the so-called Type X regime [40,41]. Before the onset of this regime, formed nanopores are dispersed, disordered, and quasi-spherical. The asymmetry of the nanopores is progressively reinforced during the self-organization and the formation of the nanogratings, mostly due to the action of light (and its polarization orientation and state), but not a stress field asymmetry. Additionally, the geometry of the heat affected zone can impact the overall energy deposition volume, and consequently temperature rise and stress distribution. However, here we consider nanopores of the size of few 10s of nm, which is much smaller than the irradiated volume (10s of μm^3). Therefore, it is quite reasonable to consider as a first approximation that at some places inside the irradiated volume, the volume expansion and induced pressure are isotropic, similar to a hydrostatic pressure.

For a moderate temperature increase (e.g., 1000 °C [37]), there is an order of magnitude difference between p values for silica (≈ 60 MPa) and BK7 (≈ 1160 MPa). Once the tensile stress is developed, a positive pressure difference exists between the initiated pore and the surrounding material. Beyond a certain critical tension, the heated glass volume is expected to experience cavitation [16,17]. For silica glass, Rudenko et al. demonstrated that the minimal temperature for cavitation is set when the viscosity is on the order of 10^6 Pa·s [17,18]. Such temperature is very close to the softening point (T_{soft}) of the material, i.e., $10^{7.6}$ P or $10^{6.6}$ Pa·s, 1873 K for Suprasil. This temperature of cavitation is calculated for a viscosity of $\eta_{cav} \approx B\xi\tau_{th}^2 \approx 10^{6.3}$ Pa·s for silica, using a strain rate of $\xi = 10^7$ s^{-1}, so indeed close to the softening temperature as previously stated. In this work we use $\xi \approx p/(B \times \tau_{ac})$ which falls within the magnitude of η_{cav} values provided by Rudenko et al. [17,18]. Written only in terms of glass and laser parameters, this gives $\eta_{cav} \approx p \times \left(\frac{\tau_{th}^2}{\tau_{ac}}\right) = \frac{\omega_0^3 \cdot p \cdot c_s}{2 \cdot D_{th}^2} = \frac{\omega_0^3 \cdot 3\alpha \cdot B \cdot \Delta T \cdot c_s \cdot \rho^2 \cdot C_p^2}{2\kappa^2}$. Some key properties, from the above discussion, are provided in Table 1. It is worth mentioning that for a constant p value (e.g., 100 MPa), η_{cav} is comprised between $10^{6.1}$ and $10^{6.6}$ Pa·s for all glasses considered. The cavitation temperature (T_{cav}) in Table 1 deduced from the VFT fit performed for each glass is found close to T_{soft}.

3.2.2. Maximum viscosity before growth instability or erasure of nanogratings

Following the formation of nanopores beyond the cavitation temperature, the stability of a cavitated pore, i.e., its ability to exist, must be considered. From this view, one must investigate what are the key mechanisms that drive the pore size evolution (either its growth or collapse) once it is formed. This can be achieved through the analysis of the non-dimensional Rayleigh-Plesset (R–P) equation, which takes the following form [42]:

$$(\overline{R})\ddot{\overline{R}} + \frac{3}{2}(\dot{\overline{R}})^2 = -\left(\frac{\tau}{\tau_p}\right)^2 \frac{p_\infty(t) - p_v}{p_{\infty\ ref} - p_v} - \left(\frac{\tau}{\tau_s}\right)^2 \frac{1}{\overline{R}} - \frac{\tau}{\tau_v}\frac{\dot{\overline{R}}}{\overline{R}} \quad (1)$$

where $\overline{R} = R/a$ is a dimensionless radius near unity (a is a characteristic length, typ. the initial pore radius in few or tens of nm), τ is the characteristic time of bubble evolution (typically ns to μs as per the thermal diffusion timescale), $p_{\infty\ ref}$ is the reference pressure taken far away from the pore, p_v the pressure inside the pore ($p_{\infty\ ref} - p_v = p$ as defined above), and $\dot{\overline{R}}$ and $\ddot{\overline{R}}$ are the first and second derivatives of the radius with respect to time. In the above equation three characteristic times are set originating from: pressure $\left(\tau_p = a\sqrt{\frac{\rho}{p}}\right)$, viscosity $\left(\tau_v = \frac{\rho a^2}{4\eta}\right)$, and surface tension $\left(\tau_s = a\sqrt{\frac{\rho a}{2\sigma}}\right)$ with σ being the surface tension, taken constant with respect to temperature [42]. These characteristic times can be plotted as a function of the pore radius, as shown in Fig. 2. At this stage, few aspects on the R–P equation must be specified. First, the R–P equation is employed here as a simple tool to investigate the relationship between viscosity and nanogratings existence. In this work, the effect of temperature is taken into account through the viscosity term. However, during laser irradiation, temperature gradients are present, mostly due to the laser intensity distributed profile, and consequently its associated energy deposition and heat transfer. This can be a function of both laser parameters (e.g., pulse energy and duration, repetition rate etc.) but also material properties, including bandgap energy, photoionization rate, nonlinear absorption coefficient, etc. Consequently, a reliable estimate of temperature distribution within irradiated area remains quite difficult. Nevertheless, the R–P equation still provides interesting aspects of reasoning with respect to temperature effects and enables qualitative understanding of the main driven forces involved in the glasses during nanogratings formation. For instance, this equation was successfully applied to predict the erasure of nanopores during isochronal thermal

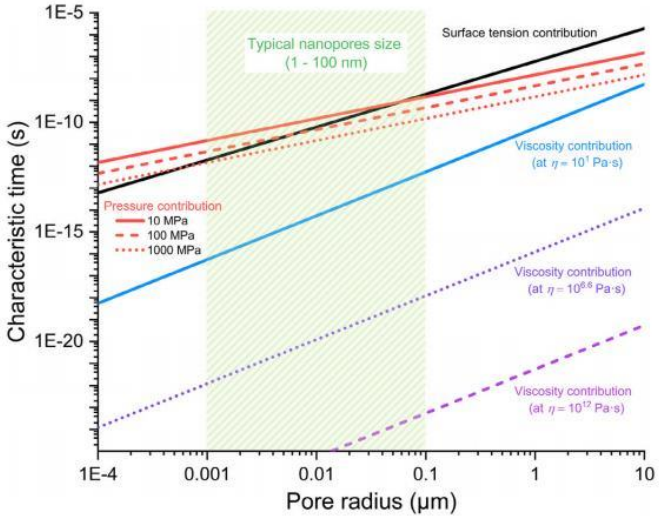

Fig. 2. Evolution of characteristic times as a function of pore radius using the non-dimensional Rayleigh-Plesset equation. The impact of pressure (set at Δp = 10, 100, 1000 MPa), surface tension (with $\sigma = 0.3$ J/m^2), and viscosity can be estimated (the contribution with the smallest characteristic time dominates).

Table 1
Typical values including cavitation and erasure criteria and temperatures for the glasses investigated.

Glass material	$p \approx B \cdot \beta \cdot \Delta T^{a,b}$ (MPa)	$\log(\eta_{cav}, \text{Pa·s}) \approx \log\left(p \cdot \left(\frac{\tau_{th}^2}{\tau_{ac}}\right)\right)$	T_{cav} (T_{soft}) (°C)	$\log(\eta_{max}, \text{Pa·s}) \approx \log(p \cdot \tau_{th})$	T_{max} (°C)	T_{max} - T_{cav} (°C)
SiO_2 (Suprasil)	60	5.9	1688 (1600)	2.2	2298	610
GeO_2	440	7.1	838 (894)	3.3	1332	494
Borofloat 33	350	6.9	797 (821)	3.1	1254	457
AF32	550	7.1	937 (969)	3.2	1277	340
BK7	1160	7.6	675 (720)	3.7	906	231

[a] Given for a ΔT value of 1000 °C, and p is a tensile stress.
[b] Data for B and β (with $\beta = 3\alpha$) can be found in the technical datasheet provided by the glass manufacturers, and in Refs. [33,34] for GeO_2.

annealing for a series of silicate glasses [43]. For completeness, we pinpoint that cavitation could also originate from a nucleation and liquid-vapor phase transformation. While the focus of this work essentially emphasizes the link between viscosity and the existence of nanopores, other cavitation mechanisms than a spall-induced cavitation can be envisioned.

Turning back to the characteristic times provided above and calculated in Fig. 2, the contribution holding the lowest characteristic time (i.e., the slowest process) is the limiting (i.e., driving) factor in the evolution of the nanopores. Typical values for silica at the softening point ($10^{6.6}$ Pa·s) for a 5 nm pore radius would give $\tau_v \approx 10^{-21}$ s, τ_s and $\tau_p \approx 10^{-11}$ s. At the melting temperature (defined as 10^{1} Pa·s) $\tau_v \approx 10^{-15}$ s, which is still 4 orders of magnitude lower than τ_p. It is indicative that the dynamics of nanopore evolution (growth/collapse) is almost exclusively driven by glass viscosity. For completeness, τ_v is proportional to $1/\eta$. Consequently, if the experimental characteristic time is lower than τ_v, the process would not depend on viscosity. In our situation, a realistic nanopores erasure timescale would be in the ns to μs (as per typical thermal diffusion times). Therefore, the viscosity is expected to primarily drive the nanopores size evolution. This is reinforced as the viscosity is increased, yielding to even lower values of τ_v.

Consequently, a criterion must be selected as an indication of pore instability. The use of the dimensionless Peclet number (*Pe*) was proposed to set the limit of "unstable" hydrodynamic growth of the nanopores [44]. The limit is set for $Pe = \frac{p \times \tau_{th}}{\eta_{max}} = 1$, giving the criterion $\eta_{max} \sim p \times \tau_{th}$. For silica glass it gives a value of $\sim 10^{2.2}$ Pa·s, corresponding to a $T \sim 2300$ °C. The calculated η_{max} for the glasses considered in this study are reported in Table 1. The η_{max} value corresponds to the maximal viscosity beyond which a viscous growth would prevent stable nanopores to exist. All the glasses fall within a η_{max} interval of $10^{2.2}$–$10^{3.7}$ Pa·s. Finally, it is worth pointing out that the stress induced upon heating will ultimately relax, yielding to a drop in the initial tensile pressure p. From this perspective and the above equation, one can notice that η_{max} would be lower. Therefore, a potential collapse of the pore is anticipated if the pressure contribution becomes less important than that of the surface tension term [42,45]. This competing effect is exemplified in Fig. 2, where low pressures such as 10 MPa would tend to promote collapse ($\tau_p > \tau_s$), while higher pressures such as 1000 MPa would yield to growth ($\tau_p < \tau_s$). In an intermediate regime, the pore could experience either growth or collapse, and perhaps both within the laser track location. This suggests that there may be a competing effect between pore growth and collapse depending on the temperature/viscosity and conditions considered. However, beyond η_{max} the existence of nanopores is expected to be compromised and this viscosity value is kept as the upper bound of nanogratings existence.

3.3. Prediction of nanogratings imprinting in various glass systems

From the above discussion, it becomes clear that the temperature difference between the T_{max} and T_{cav}, reported in Table 1, must be maximized for a glass in order to present a larger nanogratings window. In Fig. 3(a) the viscosity as a function of temperature for multiple oxide glasses (in addition to the ones discussed in this paper) is reported. An estimated domain of nanogratings existence is provided in Fig. 3(b), by taking the temperature difference between T_{max} (set as $\eta = 10^{3.0}$ Pa·s) and T_{soft} ($\eta = 10^{6.6}$ Pa·s), respectively upper and lower bounds.

The predicted "effectiveness" to imprint "stable" nanogratings in the selected glasses, in a sense that they can be observed after laser irradiation, agrees with the results reported in Fig. 1, where BK7 presents the lowest temperature interval and the narrowest nanogratings window, while it is the opposite for silica. Moreover, these findings concur with literature data. For example, in Ref. [26], for 800 fs pulse duration, the nanogratings window was found larger for SiO_2, the Borofloat 33, and finally AF32, which is what is found and predicted herein (Figs. 1a and 3b). In GeO_2 and GeO_2-doped SiO_2 glasses, it was found relatively easy to induce nanogratings with various sets of laser parameters and writing conditions [20–22,24,25]. Moreover, the birefringence response observed in Ref. [27] for BK7 was likely due to nanogratings. Indeed, from this work we demonstrated the nanogratings imprinting in BK7 through SEM observations (Fig. 1(b)), while both the experimentally and predicted narrow nanogratings windows agree with the difficulty in this cited work to detect the nanopores/nanoplanes using scanning electron microscopy.

Several other aspects are worth discussing. First, BK7 displays a much lower bandgap energy compared to silica (~3.5 eV versus ~9 eV). Consequently, even with a 3-photon nonlinear absorption (in our case λ = 1030 nm, i.e., 1.2 eV), the formation of bulk nanogratings is still possible. Secondly, in some glasses such as alkali-rich glasses (e.g., Na_2O–SiO_2 [23]) a large number of pulses (multi-pulse regime) is required to trigger nanogratings (typ. > 10^5 or 10^6 pulses). Interestingly, network modifiers are found to migrate outward of the irradiated volume [30]. A direct consequence, based on our work, could be a local variation in the glass viscosity enabling not only the formation of nanogratings at short timescale but also their survival to the

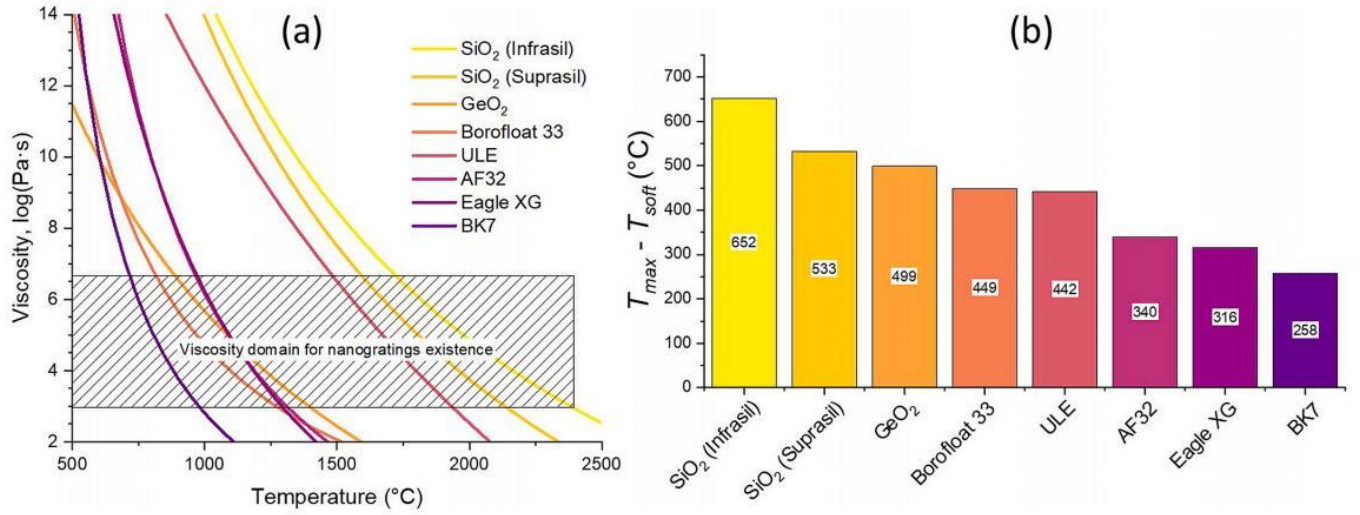

Fig. 3. a) Viscosity as a function of temperature for a variety of commercial and typical glasses, along with an estimated domain of nanogratings existence from T_{soft} ($\eta = 10^{6.6}$ Pa·s) to T_{max} ($\eta = 10^{3.0}$ Pa·s). b) Temperature difference ($T_{max} - T_{soft}$) as a function of glass composition. A larger value suggests a wider processing window (with respect to temperature) to form nanogratings.

heating-cooling processes during pulse deposition. Moreover, contrarily to LIPSS, the formation of nanogratings still requires a multi-pulse regime even for silica [23,28]. As mentioned earlier in this paper, at low pulse energies or pulse densities, a regime (so-called Type X) was identified where nanopores can exist, but the nanogratings are not formed yet. At this stage of the process, the nanopores are not highly elongated yet and self-organized into nanolayers [41,46]. Interestingly, this regime suggests that the cavitation process can already take place after the first few pulses are being deposited. In fact, this work anticipates cavitation after the very first pulses are deposited, and therefore takes the Type X into account. Furthermore, the heat accumulation process, as discussed in section III.1 and triggered by a multi-pulse regime, may play a direct role in the formation and erasure of these pores through an increase of temperature in the heat affected region. We therefore expect that the minimum pulse density to induce nanogratings would be a strong function of glass composition.

For completeness, several studies have highlighted, based on thermo-mechanical arguments, strong evidence of a void-to-nanogratings transitioning upon progressive laser irradiation (e.g., Refs. [47,48]). Although this requires a more in-depth analysis based on the proposed approach, several aspects are anticipated herein. High tensile stress, generated by high energy deposition and absorption, would favor voids formation as the pressure contribution would overcome the surface energy term (Fig. 3), yielding viscous growth of the nanopores. Additionally, the description of higher thermal gradients, associated with the fastest growth of nanobubbles in the laser track head as described in Ref. [48], is in agreement with our findings. While the topic of another study, this approach could also frame the existence domain of voids-like transformations.

Finally, no direct observation of porous bulk nanogratings has been reported for other glass systems. However, recently sub-surface formation of nanopores revealed to be possible under specific conditions in tellurite or chalcogenide glasses [49,50]. This might be because the viscosity of these glasses strongly varies with respect to temperature (short glasses). This would further narrow the nanogratings window and compromise nanogratings formation, in agreement with the presently advocated viscosity approach. For crystalline structures, such as in Al_2O_3 [51] or TeO_2 [52], the laser-induced modifications would depend on the internal structure of the nanogratings (nanopores, nanoscale phase separation, or local amorphization or recrystallization etc.). Additionally, for crystals the viscosity would be abruptly reduced above the melting temperature as the material transits from crystal to liquid phase. This is much different from glasses, which exhibit a slow varying decrease in viscosity as the temperature increases. Hence, at this step our approach is restricted to nanogratings made of nanopores in oxide glasses. Still, we expect that it can be broaden to other types of nanogratings, since chemical migration and crystallization kinetics partly are viscosity-related phenomena.

4. Conclusion

Understanding the formation of nanogratings inside silicate and germanate glasses is an attractive research field, since these sub-wavelength and self-organized structures enable miniaturized functionalization and unique properties. In this context, this work addresses the challenges to imprint, or not, nanogratings through a viscosity approach. It is shown, building from previous work, that the nanogratings domain is bound between two limits: i) a low temperature one, corresponding to a cavitation mechanism, and for which the viscosity is situated at $\sim 10^{6.6}$ Pa·s, and ii) a high temperature one for which the pores experience either growth or collapse, this time for a viscosity value typically around $\sim 10^{3.0}$ Pa·s. These predictions are validated by experimental work performed on five glasses, for which nanogratings domains are either large (SiO_2), intermediate (GeO_2, AF32, Borofloat 33), and narrow (BK7). The results agree with the literature and the proposed viscosity approach. A direct consequence of this work is to demonstrate that nanogratings can be achieved in most, if not any, glasses. However, the processing windows can be drastically different, and a systematic analysis must be undertaken to find the adequate conditions for which nanogratings can survive the laser-irradiation process.

Future work includes simulation of the temperature elevation during the irradiation process for each glass composition. This will help to target and anticipate in which conditions the temperature range, hence viscosity range (see Fig. 3) corresponding to the formation of nanogratings, can be achieved.

Funding

This research was funded by Agence Nationale pour la Recherche, FLAG-IR project, grant number ANR-18-CE08-0004-01 and CNRS Défi Instrumentation aux Limites, UltraBragg project. Qiong Xie acknowledges the China Scholarship Council (CSC) for the funding of her PhD fellowship.

CRediT authorship contribution statement

Qiong Xie: Validation, Investigation, Methodology, Writing – original draft, Writing – review & editing, Visualization. **Maxime Cavillon:** Conceptualization, Methodology, Writing – original draft, Writing – review & editing, Visualization. **Bertrand Poumellec:** Conceptualization, Writing – review & editing. **Diego Pugliese:** Writing – review & editing, Visualization. **Davide Janner:** Writing – review & editing, Supervision, Project administration. **Matthieu Lancry:** Conceptualization, Methodology, Resources, Writing – review & editing, Supervision, Project administration, Funding acquisition.

Declaration of competing interest

The authors declare that they have no known competing financial interests or personal relationships that could have appeared to influence the work reported in this paper.

References

[1] Y. Shimotsuma, P.G. Kazansky, J. Qiu, K. Hirao, Self-organized nanogratings in glass irradiated by ultrashort light pulses, Phys. Rev. Lett. 91 (2003), 247405, https://doi.org/10.1103/PhysRevLett.91.247405.
[2] J. Tian, R. Li, S.H. Yoo, B. Poumellec, E. Garcia-Caurel, R. Ossikovski, M. Stchakovsky, C. Eypert, J. Canning, M. Lancry, Spectral dependence of femtosecond laser induced circular optical properties in silica, OSA Continuum 2 (2019) 1233–1241, https://doi.org/10.1364/osac.2.001233.
[3] J. Tian, M. Lancry, S.H. Yoo, E. Garcia-Caurel, R. Ossikovski, B. Poumellec, Study of femtosecond laser-induced circular optical properties by Mueller matrix spectropolarimetry, Opt. Lett. 42 (2017) 4103–4106, https://doi.org/10.1364/ol.42.004103.
[4] R.R. Gattass, E. Mazur, Femtosecond laser micromachining in transparent materials, Nat. Photonics 2 (2008) 219–225, https://doi.org/10.1038/nphoton.2008.47.
[5] S.J. Mihailov, D. Grobnic, C. Hnatovsky, R.B. Walker, P. Lu, D. Coulas, H. Ding, Extreme environment sensing using femtosecond laser-inscribed fiber Bragg gratings, Sensors 17 (2017), 2909, https://doi.org/10.3390/s17122909.
[6] B. Zhang, X. Liu, J. Qiu, Single femtosecond laser beam induced nanogratings in transparent media - Mechanisms and applications, J. Materiomics 5 (2019) 1–14, https://doi.org/10.1016/j.jmat.2019.01.002.
[7] Y. Shimotsuma, M. Sakakura, P.G. Kazansky, M. Beresna, J. Qiu, K. Miura, K. Hirao, Ultrafast manipulation of self-assembled form birefringence in glass, Adv. Mater. 22 (2010) 4039–4043, https://doi.org/10.1002/adma.201000921.
[8] M. Beresna, M. Gecevičius, P.G. Kazansky, Polarization sensitive elements fabricated by femtosecond laser nanostructuring of glass [Invited], Opt. Mater. Express 1 (2011) 783–795, https://doi.org/10.1364/ome.1.000783.
[9] R. Stoian, Volume photoinscription of glasses: three-dimensional micro- and nanostructuring with ultrashort laser pulses, Appl. Phys. A 126 (2020), 438, https://doi.org/10.1007/s00339-020-03516-3.
[10] R. Taylor, C. Hnatovsky, E. Simova, Applications of femtosecond laser induced self-organized planar nanocracks inside fused silica glass, Laser Photon. Rev. 2 (2008) 26–46, https://doi.org/10.1002/lpor.200710031.
[11] M. Beresna, M. Gecevičius, P.G. Kazansky, T. Taylor, A.V. Kavokin, Exciton mediated self-organization in glass driven by ultrashort light pulses, Appl. Phys. Lett. 101 (2012), 053120, https://doi.org/10.1063/1.4742899.

[12] R. Buschlinger, S. Nolte, U. Peschel, Self-organized pattern formation in laser-induced multiphoton ionization, Phys. Rev. B Condens. Matter 89 (2014), 184306, https://doi.org/10.1103/PhysRevB.89.184306.
[13] A. Rudenko, J.-P. Colombier, T.E. Itina, From random inhomogeneities to periodic nanostructures induced in bulk silica by ultrashort laser, Phys. Rev. B 93 (2016), 075427, https://doi.org/10.1103/PhysRevB.93.075427.
[14] J. Canning, M. Lancry, K. Cook, A. Weickman, F. Brisset, B. Poumellec, Anatomy of a femtosecond laser processed silica waveguide [Invited], Opt. Mater. Express 1 (2011) 998–1008, https://doi.org/10.1364/ome.1.000998.
[15] M. Lancry, B. Poumellec, J. Canning, K. Cook, J.-C. Poulin, F. Brisset, Ultrafast nanoporous silica formation driven by femtosecond laser irradiation, Laser Photon. Rev. 7 (2013) 953–962, https://doi.org/10.1002/lpor.201300043.
[16] D.E. Grady, The spall strength of condensed matter, J. Mech. Phys. Solid. 36 (1988) 353–384, https://doi.org/10.1016/0022-5096(88)90015-4.
[17] A. Rudenko, J.-P. Colombier, T.E. Itina, Nanopore-mediated ultrashort laser-induced formation and erasure of volume nanogratings in glass, Phys. Chem. Chem. Phys. 20 (2018) 5887–5899, https://doi.org/10.1039/c7cp07603g.
[18] A. Rudenko, Numerical study of ultrashort laser-induced periodic nanostructure formation in dielectric materials, Optics/Photonic, Université de Lyon, 2017. English. NNT: 2017LYSES020. tel-02107355.
[19] M. Huang, F. Zhao, Y. Cheng, N. Xu, Z. Xu, Origin of laser-induced near-subwavelength ripples: interference between surface plasmons and incident laser, ACS Nano 3 (2009) 4062–4070, https://doi.org/10.1021/nn900654v.
[20] M. Lancry, F. Zimmerman, R. Desmarchelier, J. Tian, F. Brisset, S. Nolte, B. Poumellec, Nanogratings formation in multicomponent silicate glasses, Appl. Phys. B Laser Opt. 122 (2016), 66, https://doi.org/10.1007/s00340-016-6337-8.
[21] F. Zimmermann, M. Lancry, A. Plech, S. Richter, B. Hari Babu, B. Poumellec, A. Tünnermann, S. Nolte, Femtosecond laser written nanostructures in Ge-doped glasses, Opt. Lett. 41 (2016) 1161–1164, https://doi.org/10.1364/ol.41.001161.
[22] M. Lancry, J. Canning, K. Cook, M. Heili, D.R. Neuville, B. Poumellec, Nanoscale femtosecond laser milling and control of nanoporosity in the normal and anomalous regimes of GeO_2-SiO_2 glasses, Opt. Mater. Express 6 (2016) 321–330, https://doi.org/10.1364/ome.6.000321.
[23] S. Lotarev, S. Fedotov, A. Lipatiev, M. Presnyakov, P. Kazansky, V. Sigaev, Light-driven nanoperiodical modulation of alkaline cation distribution inside sodium silicate glass, J. Non-Cryst. Solids 479 (2018) 49–54, https://doi.org/10.1016/j.jnoncrysol.2017.10.008.
[24] F. Zhang, H. Zhang, G. Dong, J. Qiu, Embedded nanogratings in germanium dioxide glass induced by femtosecond laser direct writing, J. Opt. Soc. Am. B 31 (2014) 860–864, https://doi.org/10.1364/josab.31.000860.
[25] J. Wang, X. Liu, Y. Dai, Z. Wang, J. Qiu, Effect of sodium oxide content on the formation of nanogratings in germanate glass by a femtosecond laser, Opt. Express 26 (2018) 12761–12768, https://doi.org/10.1364/oe.26.012761.
[26] S.S. Fedotov, R. Drevinskas, S.V. Lotarev, A.S. Lipatiev, M. Beresna, A. Čerkauskaitė, V.N. Sigaev, P.G. Kazansky, Direct writing of birefringent elements by ultrafast laser nanostructuring in multicomponent glass, Appl. Phys. Lett. 108 (2016), 071905, https://doi.org/10.1063/1.4941427.
[27] S. Richter, C. Miese, S. Döring, F. Zimmermann, M.J. Withford, A. Tünnermann, S. Nolte, Laser induced nanogratings beyond fused silica - periodic nanostructures in borosilicate glasses and ULE™, Opt. Mater. Express 3 (2013) 1161–1166, https://doi.org/10.1364/ome.3.001161.
[28] S. Richter, M. Heinrich, S. Döring, A. Tünnermann, S. Nolte, U. Peschel, Nanogratings in fused silica: formation, control, and applications, J. Laser Appl. 24 (2012), 042008, https://doi.org/10.2351/1.4718561.
[29] Y. Wang, M. Cavillon, N. Ollier, B. Poumellec, M. Lancry, An overview of the thermal erasure mechanisms of femtosecond laser-induced nanogratings in silica glass, Phys. Status Solidi A 218 (2021) 2100023, https://doi.org/10.1002/pssa.202100023.
[30] T.T. Fernandez, M. Sakakura, S.M. Eaton, B. Sotillo, J. Siegel, J. Solis, Y. Shimotsuma, K. Miura, Bespoke photonic devices using ultrafast laser driven ion migration in glasses, Prog. Mater. Sci. 94 (2018) 68–113, https://doi.org/10.1016/j.pmatsci.2017.12.002.
[31] S.K. Sharma, D. Virgo, I. Kushiro, Relationship between density, viscosity and structure of GeO_2 melts at low and high pressures, J. Non-Cryst. Solids 33 (1979) 235–248, https://doi.org/10.1016/0022-3093(79)90052-8.
[32] E.M. Birtch, J.E. Shelby, J.M. Whalen, Properties of binary GeO_2 – SiO_2 glasses, Phys. Chem. Glasses 47 (2006) 182–185.
[33] M.J. Weber, Handbook of Optical Materials, 1st ed., CRC Press, Boca Raton, 2002.
[34] E.M. Dianov, V.M. Mashinsky, Germania-based core optical fibers, J. Lightwave Technol. 23 (2005) 3500–3508, https://doi.org/10.1109/jlt.2005.855867.
[35] B. Momgaudis, V. Kudriasov, M. Vengris, A. Melninkaitis, Quantitative assessment of nonlinearly absorbed energy in fused silica via time-resolved digital holography, Opt. Express 27 (2019) 7699–7711, https://doi.org/10.1364/oe.27.007699.
[36] M. Shimizu, M. Sakakura, M. Ohnishi, M. Yamaji, Y. Shimotsuma, K. Hirao, K. Miura, Three-dimensional temperature distribution and modification mechanism in glass during ultrafast laser irradiation at high repetition rates, Opt. Express 20 (2012) 934–940, https://doi.org/10.1364/oe.20.000934.
[37] T. Yoshino, Y. Ozeki, M. Matsumoto, K. Itoh, *In situ* micro-Raman investigation of spatio-temporal evolution of heat in ultrafast laser microprocessing of glass, Jpn. J. Appl. Phys. 51 (2012), 102403, https://doi.org/10.1143/jjap.51.102403.
[38] L. Orazi, L. Romoli, M. Schmidt, L. Li, Ultrafast laser manufacturing: from physics to industrial applications, CIRP Ann. 70 (2021) 543–566, https://doi.org/10.1016/j.cirp.2021.05.007.
[39] G. Paltauf, P.E. Dyer, Photomechanical processes and effects in ablation, Chem. Rev. 103 (2003) 487–518, https://doi.org/10.1021/cr010436c.
[40] P. Kazansky, M. Sakakura, L. Wang, Method for Fabricating Nanostructured Optical Elements Using Polarised Light, 2022. US 2022/0009028 A1.
[41] M. Sakakura, Y. Lei, L. Wang, Y.-H. Yu, P.G. Kazansky, Ultralow-loss geometric phase and polarization shaping by ultrafast laser writing in silica glass, Light Sci. Appl. 9 (2020), 15, https://doi.org/10.1038/s41377-020-0250-y.
[42] J.-P. Franc, The Rayleigh-Plesset equation: a simple and powerful tool to understand various aspects of cavitation, in: L. d'Agostino, M.V. Salvetti (Eds.), Fluid Dynamics of Cavitation and Cavitating Turbopumps, CISM International Centre for Mechanical Sciences, Springer, Vienna, 2007, pp. 1–41.
[43] M. Cavillon, Y. Wang, B. Poumellec, F. Brisset, M. Lancry, Erasure of nanopores in silicate glasses induced by femtosecond laser irradiation in the Type II regime, Appl. Phys. A 126 (2020), 876, https://doi.org/10.1007/s00339-020-04062-8.
[44] A. Rudenko, J.-P. Colombier, S. Höhm, A. Rosenfeld, J. Krüger, J. Bonse, T.E. Itina, Spontaneous periodic ordering on the surface and in the bulk of dielectrics irradiated by ultrafast laser: a shared electromagnetic origin, Sci. Rep. 7 (2017), 12306, https://doi.org/10.1038/s41598-017-12502-4.
[45] M.S. Plesset, The dynamics of cavitation bubbles, J. Appl. Mech. 16 (1949) 277–282, https://doi.org/10.1115/1.4009975.
[46] Y. Bellouard, A. Champion, B. McMillen, S. Mukherjee, R.R. Thomson, C. Pépin, P. Gillet, Y. Cheng, Stress-state manipulation in fused silica via femtosecond laser irradiation, Optica 3 (2016) 1285–1293, https://doi.org/10.1364/optica.3.001285.
[47] Y. Dai, A. Patel, J. Song, M. Beresna, P.G. Kazansky, Void-nanograting transition by ultrashort laser pulse irradiation in silica glass, Opt. Express 24 (2016) 19344–19353, https://doi.org/10.1364/oe.24.019344.
[48] E.O. Kissi, Y. Bellouard, Self-organized nanostructures forming under high-repetition rate femtosecond laser bulk-heating of fused silica, Opt. Express 26 (2018) 14024–14037, https://doi.org/10.1364/oe.26.014024.
[49] G. Torun, T. Kishi, Y. Bellouard, Direct-write laser-induced self-organization and metallization beyond the focal volume in tellurite glass, Phys. Rev. Mater. 5 (2021), 055201, https://doi.org/10.1103/PhysRevMaterials.5.055201.
[50] G. Torun, A. Yadav, K.A. Richardson, Y. Bellouard, Ultrafast laser direct-writing of self-organized microstructures in Ge-Sb-S chalcogenide glass, Front. Phys. 10 (2022), 883319, https://doi.org/10.3389/fphy.2022.883319.
[51] D. Wortmann, J. Gottmann, N. Brandt, H. Horn-Solle, Micro-and nanostructures inside sapphire by fs-laser irradiation and selective etching, Opt. Express 16 (2008) 1517–1522, https://doi.org/10.1364/oe.16.001517.
[52] Y. Shimotsuma, K. Hirao, J. Qiu, P.G. Kazansky, Nano-modification inside transparent materials by femtosecond laser single beam, Mod. Phys. Lett. B 19 (2005) 225–238, https://doi.org/10.1142/S0217984905008281.

II.3 On the formation of nanogratings in commercial oxide glasses by femtosecond laser direct writing

nanomaterials

MDPI

Article

On the Formation of Nanogratings in Commercial Oxide Glasses by Femtosecond Laser Direct Writing

Qiong Xie [1], Maxime Cavillon [1], Diego Pugliese [2,3], Davide Janner [3], Bertrand Poumellec [1] and Matthieu Lancry [1,*]

[1] Institut de Chimie Moléculaire et des Matériaux d'Orsay (ICMMO), Université Paris-Saclay, CNRS, 91405 Orsay, France
[2] Department of Electronics and Telecommunications, Politecnico di Torino, 10129 Torino, Italy
[3] Department of Applied Science and Technology (DISAT) and RU INSTM, Politecnico di Torino, 10129 Torino, Italy
* Correspondence: matthieu.lancry@universite-paris-saclay.fr

Abstract: Nanogratings (NGs) are self-assembled subwavelength and birefringent nanostructures created by femtosecond laser direct writing (FLDW) in glass, which are of high interest for photonics, sensing, five-dimensional (5D) optical data storage, or microfluidics applications. In this work, NG formation windows were investigated in nine commercial glasses and as a function of glass viscosity and chemical composition. The NG windows were studied in an energy—frequency laser parameter landscape and characterized by polarizing optical microscopy and scanning electron microscopy (SEM). Pure silica glass (Suprasil) exhibits the largest NG window, whereas alkali borosilicate glasses (7059 and BK7) present the smallest one. Moreover, the NG formation windows progressively reduced in the following order: ULE, GeO_2, B33, AF32, and Eagle XG. The NG formation window in glasses was found to decrease with the increase of alkali and alkaline earth content and was correlated to the temperature dependence of the viscosity in these glasses. This work provides guidelines to the formation of NGs in commercial oxide glasses by FLDW.

Keywords: nanogratings; birefringence; femtosecond laser direct writing; alkali; viscosity

Citation: Xie, Q.; Cavillon, M.; Pugliese, D.; Janner, D.; Poumellec, B.; Lancry, M. On the Formation of Nanogratings in Commercial Oxide Glasses by Femtosecond Laser Direct Writing. *Nanomaterials* **2022**, *12*, 2986. https://doi.org/10.3390/nano12172986

Academic Editor: Jun Liu

Received: 22 July 2022
Accepted: 20 August 2022
Published: 29 August 2022

1. Introduction

Type II modifications, generally characterized by the formation of self-assembled periodical nanostructures known as nanogratings (NGs), were first shown and studied in silica glass [1]. Such NGs, photo-induced in bulk glasses irradiated by femtosecond (fs) laser, have attracted high interest in the past few years due to their peculiar properties such as linear/circular birefringence and dichroism, extraordinary thermal stability, selective chemical etching, etc. These features have enabled applications such as 5D optical data storage, 2D and 3D space-variant birefringent devices, sensors in the harsh environment, microfluidic channels, etc. [2–7]. Femtosecond laser direct writing (FLDW) can create permanent modifications strongly localized in 3D while focusing inside transparent materials, arising from nonlinear absorption phenomena at the root of the laser-matter interaction process.

These nanostructures are made of porous nanolayers mostly observed in silica and silica-rich glasses [8,9]. In our early work, the formation of these nanopores was associated with a tensile stress-assisted oxide decomposition [10] that was recently revisited as a nanocavitation mechanism [11,12]. However, until now, the influence of the glass physical properties (melting temperature, thermal diffusivity, absorption) on the NG formation process has been significantly investigated, but without rationalization yet. Such analysis would enable the tailoring of the chemical composition and structure of glasses including nanoporous silica to define the best laser conditions for a targeted application (e.g., reducing the required number of pulses for optical data storage or increasing the writing speed for writing birefringent optics). As part of the task, different dopants of silica glass

have been analyzed in the context of NG formation, namely, germanium, phosphorus, fluorine, or chlorine [10,13–15]. During the last two decades, nanostructures have been found inside a handful of materials: fused silica, GeO_2 [16–18], sapphire [19], tellurium oxide [20], quartz [21], ULE glass [9,22], and even in some types of alumino-borosilicate glasses [9,22,23]. The influence of alkali cations in a silicate matrix was also proven to be detrimental on the formation of NGs [24,25]. Among this list, fused silica is the most common material to induce NGs. These were also found in porous silica prepared from phase-separated alkali-borosilicate glass by removing the borate phase in a hot acid solution [3]. Even twin or single isolated nanoplanes can be induced by controlling laser pulse energy [26], which could be used to write nanofluidic channels [3,27,28]. Silica provides a relatively large processing window in contrast to other materials. However, the highest retardance was obtained in porous silica glass with a porosity size in the range of 2.5 to 5 nm, also providing Type II modifications with a limited amount of stress [29,30]. The NG formation is also expected to be enhanced in glasses with a high free volume or with compositional fluctuations at the nanoscale, which could act as a precursor for the nanostructure formation.

This work provides insights into the relative difficulty of forming NGs in a wide range of common commercial oxide glasses. The main objective is to identify the so-called Type II windows (i.e., NGs windows) in them, and thus the ability for a glass to imprint NGs but also to provide some indicative performances in terms of energy consumption, writing speed, and birefringence amplitude. The selection of optical glasses investigated covered Suprasil, ULE, B33, AF32, Eagle XG, 7059, BK7, soda-lime, and GeO_2, and for some of them, preliminary results have been published in [12]. They all present interests in diverse applications such as flat glass for display and silicon wafer assembly (Eagle XG, AF32), glass substrate for electronic components (7059), infrared photonic devices (GeO_2), precision optics for medical technologies, photovoltaic or space telescope substrates (Borofloat33), visible and near-infrared prisms and micro-optic elements (BK7). The chosen glasses were then fs-irradiated using similar experimental conditions. This systematic study provides a direct comparison between a wide range of multicomponent glasses and their respective NG existence windows in the energy—repetition rate landscape. In addition to polarized microscopy, complementary scanning electron microscope (SEM) analysis enables the existence of NGs to be proven through the observation of nanopores organized into quasi-periodic planes. Moreover, by determining the laser track length containing the nanopores, the quantitative birefringence value of NGs can be determined. Then, the results in terms of the alkali or alkaline earth cation content on the formation of NGs and related performances were rationalized. Finally, our recent viscosity-based approach [12] was exploited and interestingly revealed that the energy—repetition rate landscape is well-correlated to the predicted NG existence domain.

2. Materials and Methods

All of the glass samples employed in this work were directly acquired from glass makers, except for GeO_2, which was prepared in the laboratory. For this purpose, a powder mixture of 30 g per batch composed of GeO_2 (99.9%, Serlabo technologies, Entraigues-sur-la-Sorgue, France) was placed inside a platinum crucible, dried at 200 °C for 2 h, and finally melted at 1400 °C for 1 h using a heating rate of 10 °C/min. Finally, the molten mixture was quenched between two metal plates preheated at around 350 °C. Glass samples were selected, cut, and polished to an optical grade quality. All of the glass compositions are reported in Table 1.

A commercial Yb-doped fiber amplifier femtosecond laser (Satsuma, Amplitude Systèmes Ltd., Pessac, France) was used to irradiate each sample, with a laser-operating wavelength centered at 1030 nm and a fixed pulse duration of 800 fs. The laser beam was focused using a 0.6 numerical aperture (NA) aspheric lens (estimated beam waist w_0 ~1.5 µm) at a depth of 300 µm (in air). The sample was placed on an XYZ-motorized translation stage, and the direction of the linear polarization was controlled using a $\lambda/2$

waveplate mounted on a rotation stage. The inscription patterns inscribed in the samples were a series of rectangles, which were composed of a series of parallel lines or single lines. For most glasses, a constant pulse density f/v = 1000 pulses/µm was used, with f being the pulse repetition rate (Hz, or pulses/s) and v is the scanning speed (µm/s). f was varied between 10 and 1000 kHz; therefore, the laser v was varied from 10 to 1000 µm/s accordingly. The pulse energy E was varied from 25 nJ to 4 µJ, thus the different modification thresholds were identified [13]. Two different laser polarization orientations were used to write lines: perpendicular (called Xy) and parallel (called Xx) to the laser scanning direction (X-axis). This was then used (1) to highlight the formation of polarization dependent birefringence, which is a key characteristic feature of NG formation [31] and (2) to investigate the nanostructures using SEM.

Table 1. Name, type, and chemical composition of all of the glasses investigated.

Commercial Glass Name	Type	Chemical Composition (mol%)
SuprasilCG	Silica	100 SiO_2
ULE	Titanium silicate	94.25 SiO_2, 5.75 TiO_2
B33	Free/low alkali aluminoborosilicate	81 SiO_2, 2 Al_2O_3, 13 B_2O_3, 4 Na_2O/K_2O
AF32		66.43 SiO_2, 11.28 Al_2O_3, 10.73 B_2O_3, 5.30 CaO, 4.63 MgO, 1.36 BaO, others < 1
Eagle XG		65.71 SiO_2, 11.10 Al_2O_3, 11.65 B_2O_3, 8.64 CaO, 2.28 MgO, others < 1
7059		63 SiO_2, 8.5 Al_2O_3, 16 B_2O_3, 12.5 BaO
BK7	Alkali borosilicate	69.13 SiO_2, 10.75 B_2O_3, 3.07 BaO, 10.40 Na_2O, 6.29 K_2O, others < 1
Soda-lime	Soda-lime silicate	72.6 SiO_2, 13 Na_2O, 8.8 CaO, 4.3 MgO, 0.6 Al_2O_3, 0.3 K_2O, 0.2 SO_3, 0.1 Fe_2O_3
GeO_2	Germania	100 GeO_2

Optical retardance (R) of the laser-induced modifications, defined as the product of linear birefringence (LB) by the thickness (l) of the birefringent object (i.e., $R = LB \times l$) was measured using an Olympus BX51 polarizing optical microscope equipped with a "de Sénarmont" compensator. This compensator coupled a high-precision quarter waveplate with a 180° rotating analyzer to provide retardation measurements in the visible range. Such a setup had an accuracy that approached a few nm when used in our conditions.

In order to investigate the morphology and texturing of Type II modifications, the two different polarization laser modification lines were cleaved perpendicularly to their writing direction, which allowed the laser track cross-sections to be observed by SEM (Field-Emission Gun Scanning Electron Microscope, ZEISS SUPRA 55 VP, 1 kV accelerating voltage). Depending on the laser polarization orientation (i.e., Xx or Xy configurations as described above), the inside of the nanoplanes (Xx) or the periodicity of the nanoplanes (Xy) could be observed.

3. Results and Discussion

3.1. Study of Type II Modifications Windows in the Different Glasses

Different types of modifications induced by fs-laser in glass, reported in the literature as IR-fs Type I, Type II and Type III, were observed in the irradiation landscape (energy—repetition rate). Figure 1a,b shows these modifications in Borofloat33 (B33) glass as an example, along with the corresponding laser parameters and optical microscopy characterization. At very low energies (≤0.10 µJ), no permanent modifications were detected in the glass. As the energy progressively increased (moving vertically up in Figure 1a), the appearance of the Type I modification was identified. Type I corresponds to a permanent isotropic refractive index change (either positive or negative depending on composition) and is typically found at low fluence values. The corresponding optical microscope image is shown in Figure 1b using a transmitted light observation configuration. As the energy is increased, the Type II regime is established. The corresponding optical microscope image,

taken under a first-order full waveplate placed at 45° of a crossed analyzer/polarizer, allowed us to reveal the formation of polarization dependent linear birefringence (i.e., the slow axis orientation rotates almost linearly with the laser polarization), a characteristic feature of NGs. It is worth pointing out that the Type II window becomes smaller at higher repetition rates (f).

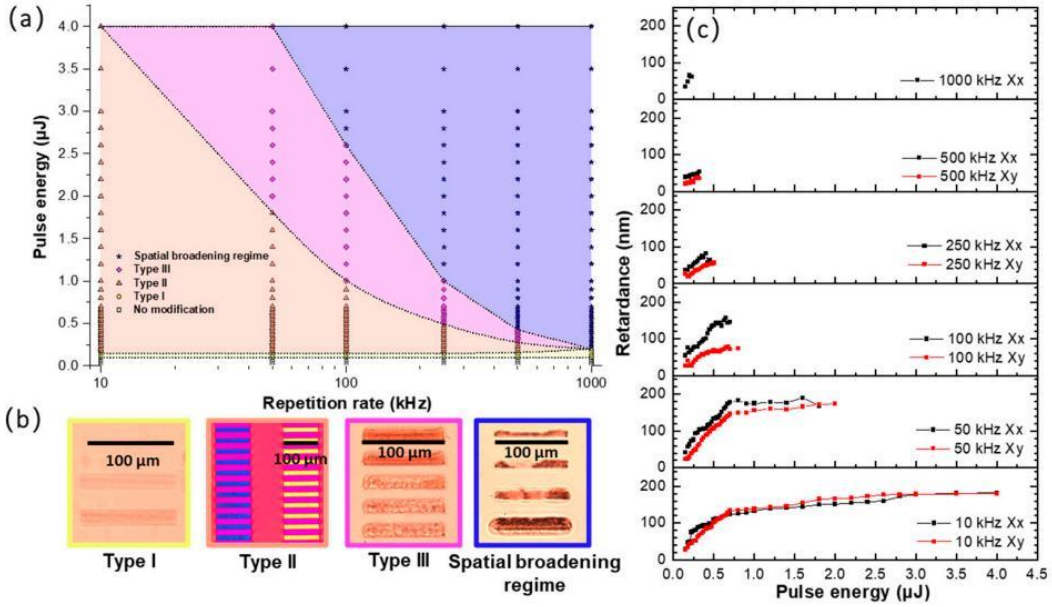

Figure 1. (**a**) Processing windows for the different types of fs-laser modifications in Borofloat33 (B33) glass. (**b**) Optical microscope images of the different types of modifications. (**c**) Retardance measured within the Type II regime by the Sénarmont technique. Experimental conditions: 1030 nm, 800 fs, 0.6 NA, from 0.025 to 4 µJ, pulse density $f/v = 10^3$ pulse/µm, Xx and Xy writing configurations.

By further looking at Figure 1a, the Type III regime appeared at higher energies, the laser tracks looked inhomogeneous, and voids issued from the micro-explosions were erratically induced inside the irradiated affected volume. As the repetition rate increased, the Type III threshold and its processing window decreased. Finally, heat effects occurred at a high repetition rate and energy, whose optical signature was mostly related to the strong spatial extension of the laser tracks (beyond the light beam size itself) accompanied by black areas, as reported in Figure 1b. This spatial broadening is related to the thermal effects (i.e., thermal diffusion coefficient and related thermal diffusion time τ_{th}), but one could find two different origins [32].

In the following, it was assumed that a temperature effect was at the origin of the spatial broadening. At low repetition rates (typ. $1/f >> 7\tau_{th}$ with $\tau_{th} \approx {\omega_0}^2/(4D_{th})$, where w_0 is the diameter of the energy source at $1/e$), the temperature elevation increases with the deposited energy. Thus if one considers that line broadening is related to the overcoming of a local temperature (let us say a "transformation temperature"), the increase in the temperature with the deposited energy indeed progressively enlarges the spatial volume of the transformation, corresponding here to a permanent refractive index change. On the other hand, at high repetition rates and high energy, a well-known heat accumulation progressively occurs [33], meeting the condition where the time between two consecutive pulses is of the order of the thermal diffusion time, typ. $1/f < 7\tau_{th}$ (corresponding here to a 10% increase in the average temperature [32]). In these conditions, the imprinted width for a given temperature can overcome the light energy source size (w_r and w_z) and usually scales up with the increasing repetition rate.

Figure 1c shows the optical retardance (R) writing energy dependence, measured within the Type II regime by the Sénarmont compensator technique for two writing polar-

ization configurations. In B33, a larger R was found at 10 and 50 kHz. Usually, R increases monotonously with the energy before 0.75 µJ and then exhibits a trend to saturation at higher energies. The maximum R values at "saturation" decreased with an RR increase except for 10 kHz. Finally, at higher energies, another regime was established and the retardance dropped down. Note that the retardance of Xx was a little bit larger than for the Xy writing configuration, a feature commonly observed in the literature.

Figure 2 shows a comparison of the Type II modification windows for different commercial oxide glasses for quite similar writing conditions. Here, the ratio between the writing speed and repetition rate was kept fixed at $f/v = 10^3$ pulse/µm for most glasses, especially with the high silica content and GeO_2 glass. However, more pulses were needed to imprint NGs in the alkali silicate glasses, namely 10^4 pulse/µm for soda-lime glass and 10^5 pulse/µm for 7059 and BK7. This is the first report of the effective imprinting of NGs in alkali-rich glasses such as BK7, Corning 7059, or soda-lime glasses.

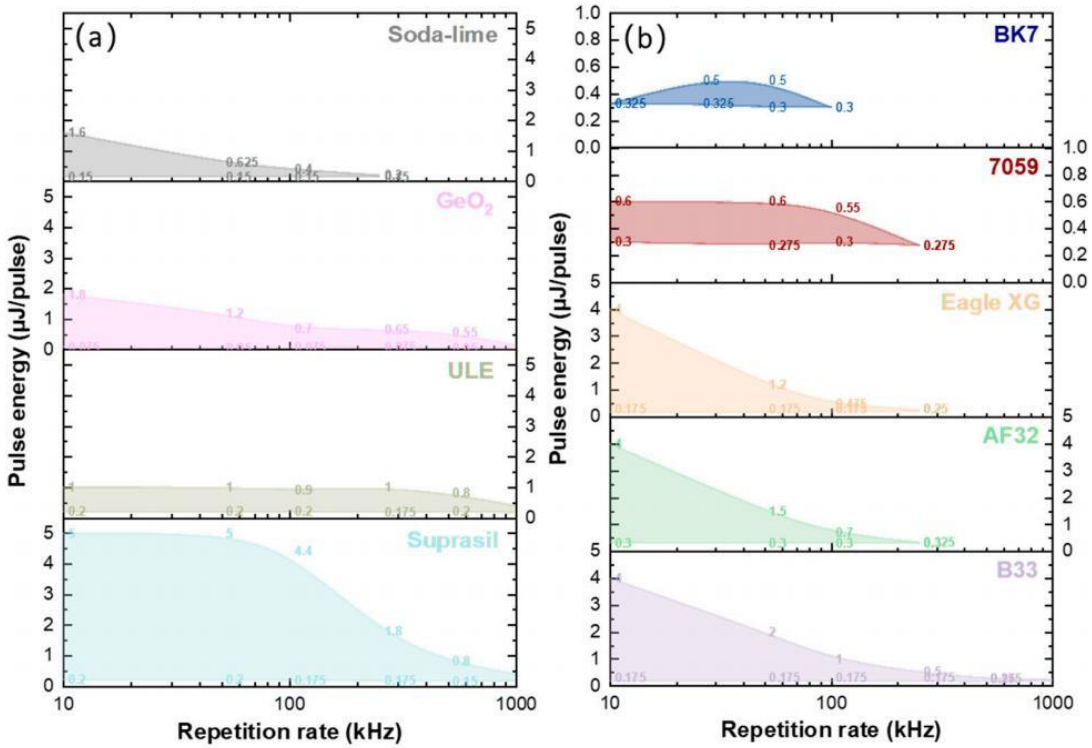

Figure 2. (**a**) Type II modification windows in the Suprasil, ULE, GeO_2, and soda-lime glasses. (**b**) Type II modifications windows in B33, AF32, Eagle XG, 7059, and BK7 alumino-borosilicate glass. (Zoom × 5 in the figure of 7059 and BK7 samples). Experimental conditions: 1030 nm, 800 fs, 0.6 NA, pulses densities $f/v = 10^3$ pulse/µm (Suprasil, GeO_2, AF32, B33, Eagle XG), $f/v = 10^4$ pulse/µm (soda-lime), $f/v = 10^5$ pulse/µm (7059 and BK7), Xx writing configuration.

From Figure 2a, it can be noticed that the pure silica glass (Suprasil) had the largest window related to the existence of NGs, whereas it was the opposite for the borosilicate (BK7) glass; this is likely to be due to its high alkali content but also its high B_2O_3 content. Additionally, only the high silica content glasses (Suprasil, ULE, B33) and GeO_2 glasses showed the NG formation above 250 kHz. Then, by comparing the alkali free or low alkali content alumino-borosilicate (AF32, B33 and Eagle XG) glasses with the alkali borosilicate (7059 and BK7) or soda-lime glasses, larger Type II windows were found for the former. In contrast, it was very difficult to imprint NGs in the 7059 and BK7 glasses; a large number of pulses, typ. > 10^5 pulse/µm, needs to be cumulated, in agreement with previous reports in the literature concerning Na_2O-SiO_2 [25] or Na_2O-GeO_2 [10] glasses.

3.2. Study of Type II Modifications Origin in the Different Glasses

In this section, the presence of Type II nanostructures was investigated by SEM imaging. A micrograph with both parallel and perpendicular writing polarization conditions is provided for each sample in Figure 3, showing the NG structures present in each investigated commercial glass. Our observation technique, based on cleaving the sample, is likely to not be the best way to preserve NGs, but it allows one to easily see the nanopores (in the Xx configuration). First, the nanolayers were found to be quasi-periodic and oriented along the laser polarization direction in agreement with the overall literature. Second, all of them appeared to be nanoporous, thus revealing that a glass oxide decomposition process occurred in all of these compositions, highlighting in such a way that this is a general mechanism. It is worth noting that the nanolayers appeared quite "disrupted" in our conditions. However, based on the literature, a high pulse number or large pulse density [34] will increase the uniformity of the NGs. This needs a low writing speed rather than a high repetition rate to avoid a too high temperature. It is also known that high pulse energy will lead to disrupted NG formation [9], whereas long pulse duration (typ. around 800 fs) [35] makes the NGs more uniform. Key applications where homogenous NGs are needed are micro-optics and optics such as 3D geometric phase optics and 3D space variant birefringent devices, whereas sensing applications and optical data storage do not necessarily require homogeneous NGs. In addition, recent work has indicated that using a Type X regime (individual elongated nanopores) [36] in a multilayer strategy looks to be a promising approach to develop optics and optical storage with much lower optical losses.

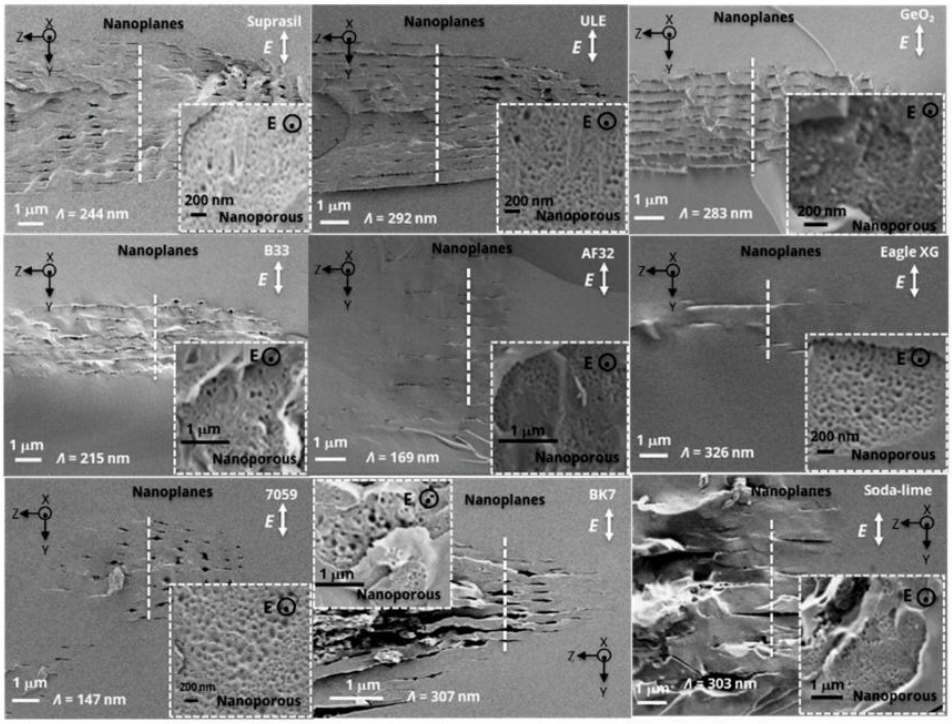

Figure 3. The SEM secondary electron micrographs of laser track cross-sections written in different oxide glasses (Suprasil, ULE, GeO_2, B33, AF32, Eagle XG, 7059, BK7, and soda-lime). The polarization direction (E) was perpendicular or parallel (insert) to the writing direction. Experimental conditions: 1030 nm, 800 fs, 0.6 NA, pulses densities $f/v = 10^3$ pulse/µm (ULE, GeO_2, AF32, B33), $f/v = 10^4$ pulse/µm (soda-lime, Eagle XG), $f/v = 10^5$ pulse/µm (50 kHz for 7059 and 25 kHz for BK7), 250 fs, $f/v = 500$ pulse/µm (Suprasil), Xx writing configuration. The pulse energy was chosen to fall within the Type II regime.

From the SEM micrographs, the thickness $L_{total\ trace}$ of each laser track was measured for both writing configurations. More specifically, the length over which porous NGs were observed along the laser propagation direction, $L_{nanogratings}$, was determined. From these values, the birefringence LB was calculated using the retardance values using the following expression $R = LB \times L_{nanogratings}$. This is exemplified in the inset of Figure 4a. The modified NG structure is clearly visible, and the period (Λ) is much smaller than the laser wavelength (see the insets in Figures 3 and 4b).

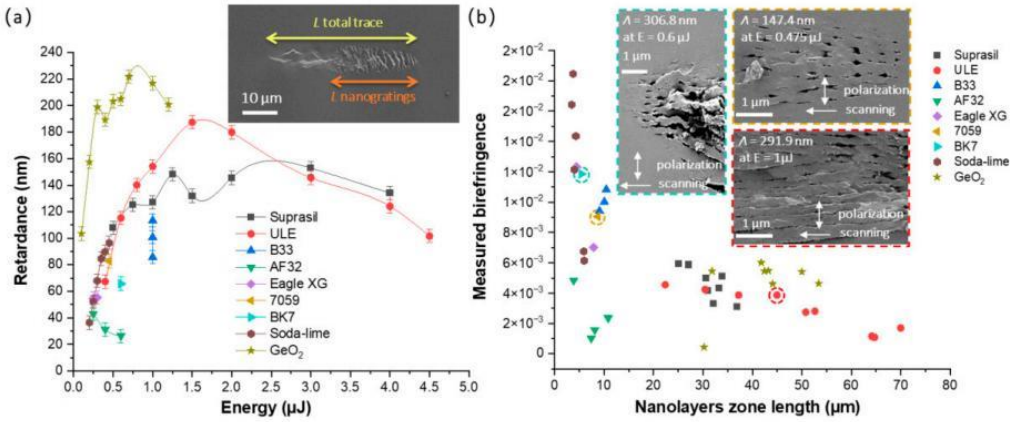

Figure 4. (**a**) The measured optical retardance R and (**b**) corresponding birefringence ($B = R/L_{nanogratings}$) of different glasses (insets are the SEM images of BK7, 7059, and ULE). Experimental conditions: 1030 nm, 800 fs, 0.6 NA, pulses densities $f/v = 10^3$ pulse/µm (ULE, GeO_2, AF32, B33), $f/v = 10^4$ pulse/µm (soda-lime, Eagle XG), $f/v = 10^5$ pulse/µm (50 kHz for 7059 and 25 kHz for BK7), 250 fs, $f/v = 500$ pulse/µm (Suprasil), Xx writing configuration.

In this view, the retardance writing kinetics of all these samples were thus measured according to the pulse energy and in similar writing conditions (1030 nm, 800 fs, 0.6 NA, 50 kHz). From Figure 4, it can be assessed that the glasses with a strong 3D network (e.g., tectosilicates), namely, ULE, Suprasil, and GeO_2, displayed a larger retardance. However, the corresponding birefringence was smaller since they had a quite long nanolayer zone, typ. up to 70 µm at high energy. In contrast, the alumino-borosilicate glasses (B33, AF32, Eagle XG, BK7, and 7059) showed smaller retardance at low energy and a shorter nanolayer zone length, but the related birefringence was relatively larger. This indicates that the NGs had a strong refractive index in contrast to these glasses, which might reveal not only the nanopore formation, but also the nanoscale phase separation. Among all of the commercial glasses, soda-lime possessed similar retardance values at low energy compared to silica (Suprasil), but exhibited the largest birefringence.

3.3. Influence of Alkali Content on NG Windows in Different Glasses

The presence of alkali and alkaline earth cations can affect the NG formation [24,25,37,38]. From Figure 5a, it can be clearly seen that NG window at 50 kHz of the alkali silicate samples consistently decreased as the [alkali and alkaline earth]/[Si] cationic ratio progressively increased, with the exception of the soda-lime glass. One can note that the onset of the NG formation remained quite similar for all of the investigated glasses, whereas the upper boundary in terms of energy decreased when increasing the [alkali and alkaline earth]/[Si] cationic ratio.

Then, in order to tentatively summarize the relative performances of all of these glasses and understand who was the "best performer", three parameters, as a function of the [alkali and alkaline earth]/[Si] cationic ratio, were reported within a single graph (see Figure 5b): (i) the writing speed, which represents the potential for writing a high amount of optical components; (ii) the maximum retardance (a key parameter for birefringent applications); and (iii) the energy consumption in µJ/nm (laser energy µJ used to write

one unit of retardance expressed in nm). In this graph, Suprasil was found to reach the highest *R* value (252 nm) with the highest speed (1 mm/s) and the lowest energy consumption (0.6 µJ/nm). In the Suprasil, ULE, and GeO_2 glasses, the formation of NGs was more likely to occur with higher *R* and speeds (ULE: 232 nm, 0.1 mm/s; GeO_2: 292 nm, 0.05 mm/s) and lower energy consumption (ULE: 6.9 µJ/nm; GeO_2: 1.79 µJ/nm). BK7 and 7059 possessed the lowest *R* values (BK7: 96.16 nm; 7059: 94.34 nm) and required low writing speeds (0.001 mm/s), along with a high energy consumption (BK7: 285.98 µJ/nm; 7059: 251.75 µJ/nm). Finally, B33, AF32, and Eagle XG exhibited relatively high *R*-values at moderate speeds and energy consumption (B33: 190 nm, 0.05 mm/s, 8.41 µJ/nm; AF32: 99 nm, 0.01 mm/s, 16.08 µJ/nm; Eagle XG: 135 nm, 0.01 mm/s, 25.93 µJ/nm). This trend is in agreement with the NG formation window. Other samples reported in the literature have been added in Figure 5b. The $15Na_2O$-$85SiO_2$ [25], $30Dy_2O_3$-$70Al_2O_3$ [39], and $6Na_2O$-$94GeO_2$ [40] samples exhibited a quite useful *R*, but had the highest energy consumption and low writing speeds. Then, even if the speed was quite high for $80SiO_2$-$20Al_2O_3$ and $40SiO_2$-$60Al_2O_3$ [41], they exhibited low *R* with a quite high energy consumption while there were no alkali and alkaline earth cations. Although $80SiO_2$-$20Al_2O_3$, $40SiO_2$-$60Al_2O_3$, $30Dy_2O_3$-$70Al_2O_3$ and $6Na_2O$-$94GeO_2$ possessed lower alkali and alkaline earth cation contents, more energy consumption was required. This is again a clue that viscosity should be the key factor here. The BaO-Ga_2O_3-GeO_2 (BGG) glass [42,43] exhibited a higher *R* and speed, but lower energy consumption. When the content of the alkali and alkaline earth cations increases, much more energy consumption is required for the formation of NGs.

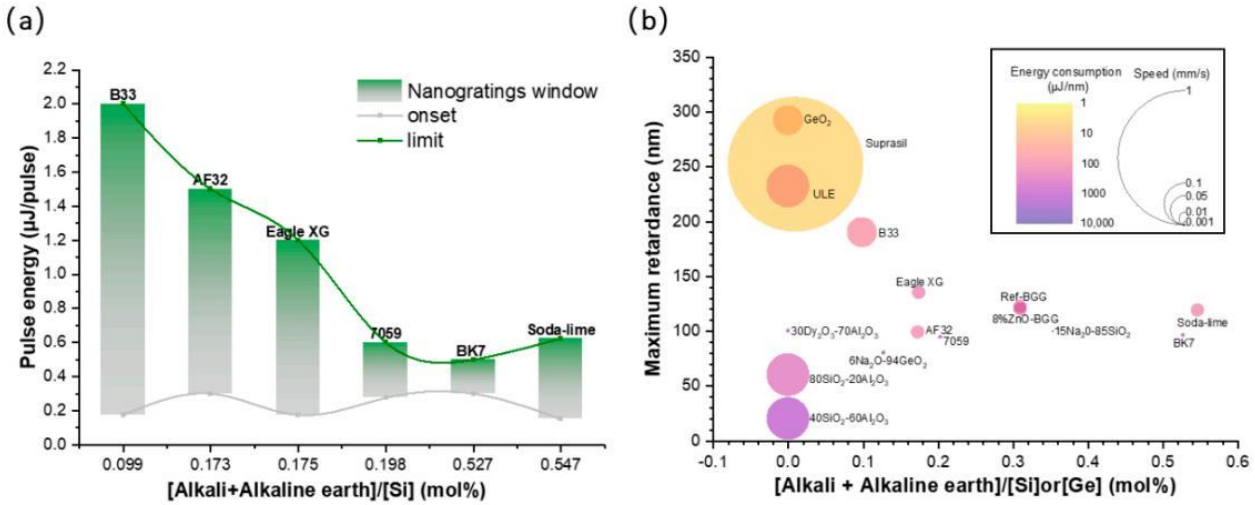

Figure 5. (**a**) NG processing windows at 50 kHz of alkali silicate glass samples and (**b**) bubble graph of the maximum retardance with increasing [alkali + alkaline earth]/[Si] or [Ge] cationic mol%. The Na_2O-SiO_2 and Na_2O-GeO_2 samples were extracted from [25] and [10], respectively.

4. Discussion on Nanopores Formation and Erasure

While this paper mostly focused on Type II, and an extensive discussion of all types of transformation was out of the scope of this work, some explanations on the mechanism that drives the NG formation are emphasized below.

At first, some fluctuations of the dielectric constant at the nm scale were proposed to trigger the process. In this transient nanoplasmonic model [7], this led to the formation of spherical nanoplasma hot spots induced by localized multiphoton ionization initiated by some seeds. The latter can either be defect centers, or glass free volume and voids initiated by the first pulse(s). In this model, these nanoplasma hot spots would experience an asymmetric growth oriented preferentially in the direction perpendicular to the laser polarization, provided that the sub-critical plasma density is reached.

Then, there is a sub-wavelength structuration of the plasma, creating an interference-like pattern or self-organized mechanism with a pseudo-regular array of high-density plasma nanolayers. The latest modeling works suggested that this "self-organization" originated from the above-mentioned heterogeneities of the dielectric constant initially present in the glass (or initiated by the first pulse), leading to multiple scattered wave interference, and hence the formation of a standing wave [44]. In this model, subsequently refined by Rudenko et al. [45], the grating formation process is reinforced by a pulse-to-pulse effect, resulting in a decrease in the NG pseudo-periodicity much lower than $\lambda/2n$, which scales with the increase in the concentration of the heterogeneities.

Finally, inside the plasma dense nanolayers, the formation of nanopores was observed in most oxide glasses, as widely described in this work. In our early work [10], the birth of these nanopores was associated with a tensile stress-assisted decomposition and a "soft" Coulomb force necessary to overcome the oxygen binding energy and to form nanopores upon an intense stress field. This was recently revisited as a tensile stress assisted nanocavitation process [11,12]. However, this is a plasma-mediated nanocavitation occurring within both thermal and stress "confinement conditions", which can thus imprint nanopores at the "image" of the plasma spatial nanostructuration. This explains the formation of polarization dependent nanopores (i.e., spherical when using circular polarization but ellipsoidal when using linearly polarized light) [36].

The above results provide additional clues that the formation of NGs is also highly impacted by glass viscosity, as suggested in a previous work [11,46]. According to the aforementioned cited references, the domain of existence of the nanopores (and thus NGs) was predicted using a simple approach following viscosity-based arguments [12]. The viscosity profile as a function of temperature for all of the oxide glasses investigated in this work, together with the estimated domain of NG existence, are reported in Figure 6a. The domain of NG existence was predicted by taking into account two boundaries in terms of viscosity, which can be then translated in terms of two limiting temperatures. The lower limit corresponds to the temperature, T_{soft}, at which nanocavitation in the glass can occur and for which the viscosity value (η) is situated at around ~$10^{6.6}$ Pa·s, forming nanopores that compose the NGs. The upper temperature limit, T_{max}, relates to either the collapse or unstable hydrodynamic growth of the nanopores, resulting in the disappearance of the nanopores, hence the NGs. This corresponds to a viscosity value typically around ~$10^{3.0}$ Pa·s, and was determined using the Peclet number (ratio between the viscous deformation and diffusion rates) as a local indicator for nanopore erasure [12].

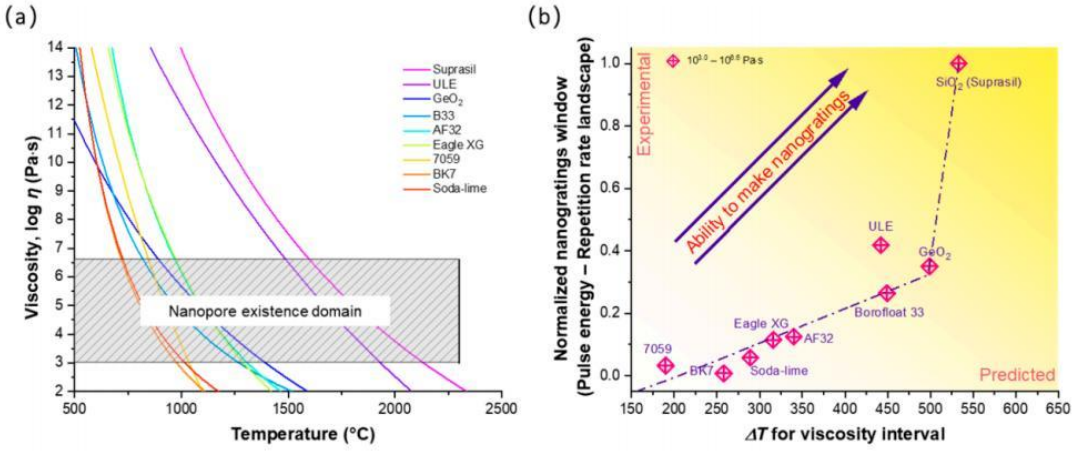

Figure 6. (**a**) Viscosity as a function of temperature for a variety of commercial and typical glasses, along with an estimated domain of NG existence from T_{soft} (η = $10^{6.6}$ Pa·s) to T_{max} (η = $10^{3.0}$ Pa·s). (**b**) Normalized NG window as a function of the temperature interval (ΔT) corresponding to the previously mentioned viscosity interval.

The domain of the NG existence was thus predicted by taking into account the temperature difference between the T_{max} and T_{soft}, respectively, the upper and lower limits, and then compared to the experimental data in the energy—repetition rate landscape. In this view, the "normalized NGs experimental window" was used, that is defined as the integrated area of the Type II domain in Figure 3 divided by the one of SiO_2 taken as the reference. Figure 6b shows a marked reduction in the normalized NG experimental window (normalized window area from Figure 2) as a function of the predicted temperature interval ($\Delta T = T_{max} - T_{soft}$) between the two above-mentioned viscosity values. A strong link was found here and supports the previously reported work and the above-reported results.

5. Conclusions

In this work, the NG formation windows in a wide range of commercial oxide glasses were addressed in an energy—repetition rate laser parameter landscape and thoroughly characterized by polarizing optical microscopy and SEM analysis. The pure silica glass (Suprasil) and the alkali-rich borosilicate glasses (7059 and BK7) showed the largest and the smallest NG formation windows, respectively. The NG formation windows of the ULE, GeO_2, B33, AF32, and Eagle XG lay between these two limits and progressively exhibited decreasing values. In agreement with the literature, the alkali and alkaline earth contents, closely connected to the glass viscosity, were proven to play a key role in the formation of NGs. The NG formation window decreased with the increase in the alkali and alkaline earth contents, which appeared to be correlated to the reduction in the predicted temperature difference determined from the "allowed viscosity interval". The results agree with the literature and the proposed viscosity approach based on a nanocavitation process [12]. Although the soda-lime, BK7, and B33 glasses exhibited higher birefringence, the pure silica glass remained the "best performer" (high writing speed, low energy consumption, high retardance) compared to other oxide glasses. Future work includes the simulation of the temperature elevation during the irradiation process for each glass composition in order to predict the processing windows and exploitation of the Rayleigh–Plesset model to predict the lifetime of the NGs.

Author Contributions: Conceptualization, M.C. and M.L.; Funding acquisition, B.P. and M.L.; Investigation, Q.X.; Methodology, Q.X., M.C. and M.L.; Project administration, D.J. and M.L.; Resources, M.L.; Supervision, D.J. and M.L.; Validation, Q.X.; Visualization, Q.X., M.C. and D.P.; Writing—original draft, Q.X.; Writing—review & editing, Q.X., M.C., D.P., D.J., B.P. and M.L. All authors have read and agreed to the published version of the manuscript.

Funding: This research was funded by the Agence Nationale pour la Recherche, FLAG-IR project, grant number ANR-18-CE08-0004-01 and CNRS Défi Instrumentation aux Limites, UltraBragg project. Qiong Xie acknowledges the China Scholarship Council (CSC) for the funding of her PhD fellowship.

Institutional Review Board Statement: Not applicable.

Informed Consent Statement: Not applicable.

Data Availability Statement: Not applicable.

Conflicts of Interest: The authors declare no conflict of interest.

References

1. Shimotsuma, Y.; Kazansky, P.G.; Qiu, J.; Hirao, K. Self-organized nanogratings in glass irradiated by ultrashort light pulses. *Phys. Rev. Lett.* **2003**, *91*, 247405. [CrossRef] [PubMed]
2. Yu, X.; Liao, Y.; He, F.; Zeng, B.; Cheng, Y.; Xu, Z.; Sugioka, K.; Midorikawa, K. Tuning etch selectivity of fused silica irradiated by femtosecond laser pulses by controlling polarization of the writing pulses. *J. Appl. Phys.* **2011**, *109*, 053114. [CrossRef]
3. Liao, Y.; Shen, Y.; Qiao, L.; Chen, D.; Cheng, Y.; Sugioka, K.; Midorikawa, K. Femtosecond laser nanostructuring in porous glass with sub-50 nm feature sizes. *Opt. Lett.* **2013**, *38*, 187–189. [CrossRef] [PubMed]
4. Hnatovsky, C.; Taylor, R.S.; Simova, E.; Rajeev, P.P.; Rayner, D.M.; Bhardwaj, V.R.; Corkum, P.B. Fabrication of microchannels in glass using focused femtosecond laser radiation and selective chemical etching. *Appl. Phys. A* **2006**, *84*, 47–61. [CrossRef]
5. Beresna, M.; Gecevičius, M.; Kazansky, P.G.; Taylor, T.; Kavokin, A.V. Exciton mediated self-organization in glass driven by ultrashort light pulses. *Appl. Phys. Lett.* **2012**, *101*, 053120. [CrossRef]

6. Liao, Y.; Cheng, Y.; Liu, C.; Song, J.; He, F.; Shen, Y.; Chen, D.; Xu, Z.; Fan, Z.; Wei, X.; et al. Direct laser writing of sub-50 nm nanofluidic channels buried in glass for three-dimensional micro-nanofluidic integration. *Lab Chip* **2013**, *13*, 1626–1631. [CrossRef]
7. Taylor, R.; Hnatovsky, C.; Simova, E. Applications of femtosecond laser induced self-organized planar nanocracks inside fused silica glass. *Laser Photon. Rev.* **2008**, *2*, 26–46. [CrossRef]
8. Lancry, M.; Poumellec, B.; Canning, J.; Cook, K.; Poulin, J.-C.; Brisset, F. Ultrafast nanoporous silica formation driven by femtosecond laser irradiation. *Laser Photon. Rev.* **2013**, *7*, 953–962. [CrossRef]
9. Lancry, M.; Zimmerman, F.; Desmarchelier, R.; Tian, J.; Brisset, F.; Nolte, S.; Poumellec, B. Nanogratings formation in multicomponent silicate glasses. *Appl. Phys. B* **2016**, *122*, 66. [CrossRef]
10. Lancry, M.; Canning, J.; Cook, K.; Heili, M.; Neuville, D.R.; Poumellec, B. Nanoscale femtosecond laser milling and control of nanoporosity in the normal and anomalous regimes of GeO_2-SiO_2 glasses. *Opt. Mater. Express* **2016**, *6*, 321–330. [CrossRef]
11. Rudenko, A.; Colombier, J.P.; Itina, T.E. Nanopore-mediated ultrashort laser-induced formation and erasure of volume nanogratings in glass. *Phys. Chem. Chem. Phys.* **2018**, *20*, 5887–5899. [CrossRef] [PubMed]
12. Xie, Q.; Cavillon, M.; Poumellec, B.; Pugliese, D.; Janner, D.; Lancry, M. Application and validation of a viscosity approach to the existence of nanogratings in oxide glasses. *Opt. Mater.* **2022**, *130*, 112576. [CrossRef]
13. Poumellec, B.; Lancry, M.; Chahid-Erraji, A.; Kazansky, P.G. Modification thresholds in femtosecond laser processing of pure silica: Review of dependencies on laser parameters. *Opt. Mater. Express* **2011**, *1*, 766–782. [CrossRef]
14. Shimotsuma, Y.; Kubota, S.; Murata, A.; Kurita, T.; Sakakura, M.; Miura, K.; Lancry, M.; Poumellec, B. Tunability of form birefringence induced by femtosecond laser irradiation in anion-doped silica glass. *J. Am. Ceram. Soc.* **2017**, *100*, 3912–3919. [CrossRef]
15. Zimmermann, F.; Lancry, M.; Plech, A.; Richter, S.; Babu, B.H.; Poumellec, B.; Tünnermann, A.; Nolte, S. Femtosecond laser written nanostructures in Ge-doped glasses. *Opt. Lett.* **2016**, *41*, 1161–1164. [CrossRef]
16. Asai, T.; Shimotsuma, Y.; Kurita, T.; Murata, A.; Kubota, S.; Sakakura, M.; Miura, K.; Brisset, F.; Poumellec, B.; Lancry, M. Systematic control of structural changes in GeO_2 glass induced by femtosecond laser direct writing. *J. Am. Ceram. Soc.* **2015**, *98*, 1471–1477. [CrossRef]
17. Zhang, F.; Cerkauskaite, A.; Drevinskas, R.; Kazansky, P.G.; Qiu, J. Microengineering of optical properties of GeO_2 glass by ultrafast laser nanostructuring. *Adv. Opt. Mater.* **2017**, *5*, 1700342. [CrossRef]
18. Zhang, F.; Zhang, H.; Dong, G.; Qiu, J. Embedded nanogratings in germanium dioxide glass induced by femtosecond laser direct writing. *J. Opt. Soc. Am. B* **2014**, *31*, 860–864. [CrossRef]
19. Wortmann, D.; Gottmann, J.; Brandt, N.; Horn-Solle, H. Micro- and nanostructures inside sapphire by fs-laser irradiation and selective etching. *Opt. Express* **2008**, *16*, 1517–1522. [CrossRef]
20. Shimotsuma, Y.; Hirao, K.; Qiu, J.R.; Miura, K. Nanofabrication in transparent materials with a femtosecond pulse laser. *J. Non-Cryst. Solids* **2006**, *352*, 646–656. [CrossRef]
21. Zhang, F.; Nie, Z.; Huang, H.; Ma, L.; Tang, H.; Hao, M.; Qiu, J. Self-assembled three-dimensional periodic micro-nano structures in bulk quartz crystal induced by femtosecond laser pulses. *Opt. Express* **2019**, *27*, 6442–6450. [CrossRef] [PubMed]
22. Richter, S.; Miese, C.; Döring, S.; Zimmermann, F.; Withford, M.J.; Tünnermann, A.; Nolte, S. Laser induced nanogratings beyond fused silica—periodic nanostructures in borosilicate glasses and ULE™. *Opt. Mater. Express* **2013**, *3*, 1161–1166.
23. Zimmermann, F.; Plech, A.; Richter, S.; Tünnermann, A.; Nolte, S. Ultrashort laser pulse induced nanogratings in borosilicate glass. *Appl. Phys. Lett.* **2014**, *104*, 211107. [CrossRef]
24. Fedotov, S.S.; Lipat'ev, A.S.; Lotarev, S.V.; Sigaev, V.N. Local formation of birefringent structures in alkali-silicate glass by femtosecond laser beam. *Glass Ceram.* **2017**, *74*, 227–229. [CrossRef]
25. Lotarev, S.; Fedotov, S.; Lipatiev, A.; Presnyakov, M.; Kazansky, P.; Sigaev, V. Light-driven nanoperiodical modulation of alkaline cation distribution inside sodium silicate glass. *J. Non-Cryst. Solids* **2018**, *479*, 49–54. [CrossRef]
26. Desmarchelier, R.; Poumellec, B.; Brisset, F.; Mazerat, S.; Lancry, M. In the heart of femtosecond laser induced nanogratings: From porous nanoplanes to form birefringence. *World J. Nano Sci. Eng.* **2015**, *5*, 115–125. [CrossRef]
27. Liao, Y.; Ni, J.; Qiao, L.; Huang, M.; Bellouard, Y.; Sugioka, K.; Cheng, Y. High-fidelity visualization of formation of volume nanogratings in porous glass by femtosecond laser irradiation. *Optica* **2015**, *2*, 329–334. [CrossRef]
28. Liao, Y.; Pan, W.J.; Cui, Y.; Qiao, L.L.; Bellouard, Y.; Sugioka, K.; Cheng, Y. Formation of in-volume nanogratings with sub-100-nm periods in glass by femtosecond laser irradiation. *Opt. Lett.* **2015**, *40*, 3623–3626. [CrossRef]
29. Čerkauskaite, A. Ultrafast Laser Nanostructuring for Photonics and Information Technology. Ph.D. Thesis, University of Southampton, Southampton, UK, 2018.
30. Cerkauskaite, A.; Drevinskas, R.; Rybaltovskii, A.O.; Kazansky, P.G. Ultrafast laser-induced birefringence in various porosity silica glasses: From fused silica to aerogel. *Opt. Express* **2017**, *25*, 8011–8021. [CrossRef]
31. Bricchi, E.; Klappauf, B.G.; Kazansky, P.G. Form birefringence and negative index change created by femtosecond direct writing in transparent materials. *Opt. Lett.* **2004**, *29*, 119–121. [CrossRef]
32. Muzi, E.; Cavillon, M.; Lancry, M.; Brisset, F.; Que, R.; Pugliese, D.; Janner, D.; Poumellec, B. Towards a rationalization of ultrafast laser-induced crystallization in lithium niobium borosilicate glasses: The key role of the scanning speed. *Crystals* **2021**, *11*, 290. [CrossRef]

33. Eaton, S.M.; Zhang, H.; Ng, M.L.; Li, J.; Chen, W.-J.; Ho, S.; Herman, P.R. Transition from thermal diffusion to heat accumulation in high repetition rate femtosecond laser writing of buried optical waveguides. *Opt. Express* **2008**, *16*, 9443–9458. [CrossRef] [PubMed]
34. Richter, S.; Heinrich, M.; Döring, S.; Tünnermann, A.; Nolte, S.; Peschel, U. Nanogratings in fused silica: Formation, control, and applications. *J. Laser Appl.* **2012**, *24*, 042008. [CrossRef]
35. Mauclair, C.; Zamfirescu, M.; Colombier, J.P.; Cheng, G.; Mishchik, K.; Audouard, E.; Stoian, R. Control of ultrafast laser-induced bulk nanogratings in fused silica via pulse time envelopes. *Opt. Express* **2012**, *20*, 12997–13005. [CrossRef] [PubMed]
36. Sakakura, M.; Lei, Y.; Wang, L.; Yu, Y.H.; Kazansky, P.G. Ultralow-loss geometric phase and polarization shaping by ultrafast laser writing in silica glass. *Light Sci. Appl.* **2020**, *9*, 15. [CrossRef]
37. Zhang, F.; Tu, Z.; Du, X.; Zhang, H.; Qiu, J. Femtosecond laser induced migration of alkali ions in calcium silicate glasses. *Mater. Lett.* **2014**, *137*, 92–95. [CrossRef]
38. Fernandez, T.T.; Sakakura, M.; Eaton, S.M.; Sotillo, B.; Siegel, J.; Solis, J.; Shimotsuma, Y.; Miura, K. Bespoke photonic devices using ultrafast laser driven ion migration in glasses. *Prog. Mater Sci.* **2018**, *94*, 68–113. [CrossRef]
39. Mori, S.; Kurita, T.; Shimotsuma, Y.; Sakakura, M.; Miura, K. Nanogratings embedded in Al_2O_3-Dy_2O_3 glass by femtosecond laser irradiation. *J. Laser Micro Nanoeng.* **2016**, *11*, 87–90. [CrossRef]
40. Lotarev, S.V.; Fedotov, S.S.; Kurina, A.I.; Lipatiev, A.S.; Sigaev, V.N. Ultrafast laser-induced nanogratings in sodium germanate glasses. *Opt. Lett.* **2019**, *44*, 1564–1567. [CrossRef]
41. Wang, Y.; Wei, S.; Cicconi, M.R.; Tsuji, Y.; Shimizu, M.; Shimotsuma, Y.; Miura, K.; Peng, G.D.; Neuville, D.R.; Poumellec, B.; et al. Femtosecond laser direct writing in SiO_2-Al_2O_3 binary glasses and thermal stability of *Type II* permanent modifications. *J. Am. Ceram. Soc.* **2020**, *103*, 4286–4294. [CrossRef]
42. Yao, H.; Zaiter, R.; Cavillon, M.; Sapaly, B.; Calzavara, F.; Delullier, P.; Cardinal, T.; Dai, Y.; Poumellec, B.; Lancry, M. Photosensitivity of barium germano-gallate glasses under femtosecond laser direct writing for Mid-IR applications. *Ceram. Int.* **2021**, *47*, 34235–34241.
43. Yao, H.; Zaiter, R.; Cavillon, M.; Delullier, P.; Lu, B.; Cardinal, T.; Dai, Y.; Poumellec, B.; Lancry, M. Formation of nanogratings driven by ultrafast laser irradiation in mid-IR heavy oxide glasses. *Ceram. Int.* 2022, in press.
44. Buschlinger, R.; Nolte, S.; Peschel, U. Self-organized pattern formation in laser-induced multiphoton ionization. *Phys. Rev. B* **2014**, *89*, 184306.
45. Rudenko, A.; Colombier, J.-P.; Itina, T.E. From random inhomogeneities to periodic nanostructures induced in bulk silica by ultrashort laser. *Phys. Rev. B* **2016**, *93*, 075427.
46. Cavillon, M.; Wang, Y.; Poumellec, B.; Brisset, F.; Lancry, M. Erasure of nanopores in silicate glasses induced by femtosecond laser irradiation in the Type II regime. *Appl. Phys. A* **2020**, *126*, 876.

II.4 VOLUME NANOGRATINGS INSCRIBED BY ULTRAFAST IR LASER IN ALUMINO-BOROSILICATE GLASSES

Research Article Vol. 31, No. 10 / 8 May 2023 / Optics Express 15449
Optics EXPRESS

Volume nanogratings inscribed by ultrafast IR laser in alumino-borosilicate glasses

HENG YAO,[1,2] QIONG XIE,[2,5] MAXIME CAVILLON,[2] DANIEL R. NEUVILLE,[3] DIEGO PUGLIESE,[4] DAVIDE JANNER,[4] YE DAI,[1,6] BERTRAND POUMELLEC,[2] AND MATTHIEU LANCRY[2]

[1]*Department of Physics, Shanghai University, 200444 Shanghai, China*
[2]*Institut de Chimie Moléculaire et des Matériaux d'Orsay, CNRS, Université Paris-Saclay, 91400 Orsay, France*
[3]*Géomatériaux, IPGP-CNRS, Université de Paris, 75005 Paris, France*
[4]*Department of Applied Science and Technology (DISAT) and RU INSTM, Politecnico di Torino, 10129 Torino, Italy*
[5]*qiong.xie@universite-paris-saclay.fr*
[6]*yedai@shu.edu.cn*

Abstract: Self-assembled nanogratings, inscribed by femtosecond laser writing in volume, are demonstrated in multicomponent alkali and alkaline earth containing alumino-borosilicate glasses. The laser beam pulse duration, pulse energy, and polarization, were varied to probe the nanogratings existence as a function of laser parameters. Moreover, laser-polarization dependent form birefringence, characteristic of nanogratings, was monitored through retardance measurements using polarized light microscopy. Glass composition was found to drastically impact the formation of nanogratings. For a sodium alumino-borosilicate glass, a maximum retardance of 168 nm (at 800 fs and 1000 nJ) could be measured. The effect of composition is discussed based on SiO_2 content, B_2O_3/Al_2O_3 ratio, and the Type II processing window is found to decrease as both $(Na_2O + CaO)/Al_2O_3$ and B_2O_3/Al_2O_3 ratios increase. Finally, an interpretation in the ability to form nanogratings from a glass viscosity viewpoint, and its dependency with respect to the temperature, is demonstrated. This work is brought into comparison with previously published data on commercial glasses, which further indicates the strong link between nanogratings formation, glass chemistry, and viscosity.

1. Introduction

In recent years, femtosecond (fs) laser direct writing (FLDW) has been a tool of choice to inscribe photo-induced transformations inside or at the surface of transparent media, including glass [1–3]. By enabling light intensities of several TW/cm^2 at the laser focal point, permanent and localized modifications within a few μm^3 of the material are possible. They are a function of both glass composition and laser parameters and have commonly been observed in silicate glasses. These include refractive index changes, micro-voids, or laser polarization dependent birefringence [4–6]. This birefringence originates from the formation of nanogratings (NGs) [7], which are made of self-aligned porous nanolayers.

Several mechanisms of the NGs formation have been proposed [7–10]. Most recently, the formation of the nanopores composing the NGs has been suggested to come from a tensile stress-assisted nano-cavitation, building on the theory developed by Grady on spall fracture of matter [11,12]. While investigating the underlying mechanisms is still an active research field, several intriguing properties arising from these structures have already been demonstrated, including, but not limited to, anisotropic light scattering [13], highly selective chemical etching [3], and form birefringence with extraordinary thermal stability [14]. In terms of applications, fabrication of polarization sensitive optical elements has been demonstrated [6], along with

#488249 https://doi.org/10.1364/OE.488249
Journal © 2023 Received 20 Feb 2023; revised 6 Apr 2023; accepted 10 Apr 2023; published 24 Apr 2023

Optics EXPRESS

ultra-stable 5-dimensional (5D) optical memory [15,16], micro/nanofluidics [3] or 3D space variant birefringent optical devices. Until now, these NGs, induced by fs-laser in volume, have been observed in various glasses and crystals including SiO_2 (by far the most studied), GeO_2 glass, TeO_2 single crystal, sapphire, Al_2O_3-Dy_2O_3 binary glass, lithium niobium silicate glass [17–23], titanium silicate glasses (ULE, Corning) [24], and even in multicomponent alumino-borosilicate glasses (Borofloat 33, Schott) [24], or barium gallo-germanate (BGG) glasses [6]. It must be pointed out that there exist multiple types of NGs, including porous NGs, crystal/glass phase separated NGs, or crack-like nanostructures. While in this work we focus on the porous NGs typically encountered in silicate or silica-rich glasses, an interested reader can find more details on the various NG types, and associated references, in [25].

Within the above list, the alumino-borosilicate glass family is particularly attractive for its excellent chemical durability, high thermal shock resistance, and low coefficient of thermal expansion. Those properties are of interest in multiple industrial applications such as liquid crystal display substrates [26] and glass fiber-reinforced polymer matrix composites [27]. Complementarily, and with respect to the present work, calcium aluminosilicate (CAS) glasses with large transmission in infrared (IR) are also of interest for a wide variety of applications, ranging from IR domes to laser windows or optical glasses [28–30]. From the discussion above, the ability to master photo-induced transformations in these glass families would therefore be a key asset in developing photonic-based devices.

In this paper, the NGs formation in a series of alumino-borosilicate doped with alkali (Na^+) and alkaline earth (Ca^{2+}) elements, respectively SAN and SAC families, is investigated. More specifically, the study focuses on the effect of composition and glass properties, such as viscosity, which can affect the overall formation of NGs. In order to tackle the latter aspects, NGs were inscribed in alumino-borosilicate glasses by varying a set of laser parameters (pulse duration and energy). Measurements of retardance (R) (see Section 2.2) and polarization dependent birefringence were performed using polarized optical microscopy, as these features indicate the presence of NGs in the glasses. The NGs processing window, defined as the ability to form NGs in a pulse energy - duration landscape, was studied according to the $(Na_2O + CaO)/Al_2O_3$ and B_2O_3/Al_2O_3 ratios. The results are then discussed on the basis of previous work revealing the key role of viscosity (η) in the formation of NGs inside several commercial glasses [11,12].

2. Experimental section

2.1. Glass synthesis and characterization

All glasses were fabricated by melting the appropriate quantities of batch precursor powders, i.e., Al_2O_3, $CaCO_3$, B_2O_3, Na_2CO_3 and SiO_2. For example, a mixture of $CaCO_3$-Al_2O_3-B_2O_3-$NaCO_3$-SiO_2 was crushed and homogenized for 1 h in alcohol using an agate mortar. Following this, the mixture was heated up slowly and progressively to decompose the carbonates, and up to the melting point. This heating process was repeated 3 times to ensure a good glass homogeneity. The studied glass compositions are presented in Table 1. Glasses are labeled according to their chemical compositions, and as follows: SAN x-y-z, with $x = SiO_2$, $y = Al_2O_3$, $z = Na_2O$ and $B_2O_3 = 100 - (x + y + z)$; SAC x-y-z with $x = SiO_2$, $y = Al_2O_3$, $z = CaO$ and $B_2O_3 = 100 - (x + y + z)$; SACN x-y-z-w with $x = SiO_2$, $y = Al_2O_3$, $z = CaO$, $w = Na_2O$ and $B_2O_3 = 100 - (x + y + z + w)$. It is worthwhile highlighting that x, y, z and w refer only to the integer part of the compositions in mol%. Additional typical values of the fabricated glasses, including glass annealing temperature (T_a), density, refractive index, and oxide/element ratios, are also provided in Table 1. The density values were obtained from the average of more than 20 measurements per sample using Archimedes' method by immerging a glass chunk in diethyl phthalate at room temperature on a Precisa XT220A weighing scale. The refractive index (n_d, at 532 nm) values were determined by the Brewster angle method.

Optics EXPRESS

Table 1. Label and batch composition of the alumino-borosilicate glasses employed in this study, along with typical physical characteristics and composition ratios.

Sample	Composition (in mol%)	Density (g/cm^3)	T_a (°C)	n_{532} (±0.005)	$\frac{Na_2O+CaO}{Al_2O_3}$	$\frac{B_2O_3}{Al_2O_3}$
SAN 75-0-12	$75SiO_2$ - $12.5B_2O_3$ - $12.5Na_2O$	2.313	570.6	1.487	No Al	No Al
SAN 75-3-12	$75SiO_2$ - $3.125Al_2O_3$ - $9.375B_2O_3$ - $12.5Na_2O$	2.354	591.7	1.493	4	3
SAN 75-6-12	$75SiO_2$ - $6.25Al_2O_3$ - $6.25B_2O_3$ - $12.5Na_2O$	2.370	618.4	1.492	2	1
SAN 75-9-12	$75SiO_2$ - $9.375Al_2O_3$ - $3.125B_2O_3$ - $12.5Na_2O$	2.386	658.2	1.491	1.33	0.33
SAN 75-12-12	$75SiO_2$ - $12.5Al_2O_3$ - $12.5Na_2O$	2.391	849.8	1.487	1	0
SAC 50-25-25	$50SiO_2$ - $25Al_2O_3$ - $25CaO$	2.624	774.7	1.566	1	0
SAC 50-12-25	$50SiO_2$ - $12.5Al_2O_3$ - $12.5B_2O_3$ - $25CaO$	2.575	700.8	1.570	2	1
SAC 50-18-25	$50SiO_2$ - $18.75Al_2O_3$ - $6.25B_2O_3$ - $25CaO$	2.566	651.9	1.559	1.33	0.33
SACN 50-6-25-5	$50SiO_2$ - $6Al_2O_3$ - $14B_2O_3$ - $25CaO$ - $5Na_2O$	2.610	667.8	1.581	5	2.33
SACN 50-12-25-5	$50SiO_2$ - $12Al_2O_3$ - $8B_2O_3$ - $25CaO$ - $5Na_2O$	2.600	689.7	1.569	2.5	0.67

2.2. Fs-laser irradiation and characterization of laser-induced modified regions

Each sample was double side polished to an optical grade prior to being irradiated by fs laser (Satsuma, Amplitude Systèmes Ltd. Pessac, France). The latter delivers pulses centered at a wavelength of 1030 nm, with a repetition rate set at 100 kHz and with varied pulse durations τ from 250 to 1500 fs. The beam was focused 500 µm below the surface (in air) using a 0.6 numerical aperture (NA) aspheric lens. The beam waist radius was estimated to be around ω_0 ~1.5 µm. The selected irradiation patterns in all samples were rectangular shapes of 10 × 100 µm^2 dimensions. In fact, each rectangle is composed of a set of 10 lines spaced out by $\Delta y = 1$ µm, to get a homogenous irradiated area and avoid any diffraction effect. To favor NGs formation a writing speed of 10 µm/s was used, therefore translating into a pulse density of 10,000 pulses/µm (at 100 kHz), which is a typical value to induce NGs [31]. Moreover, the pulse energy E_p was varied from 0.025 to 3 µJ and two laser polarization configurations were tested, namely "Xx" and "Xy" (X being the laser writing orientation and x, y the laser polarization orientation at 0 and 90° relative to X, respectively) [32]. After fs laser irradiation, the inscribed samples were observed using a polarizing optical microscope (Olympus BX60, Tokyo, Japan) equipped with a high precision quarter waveplate coupled to a rotating analyzer providing a quantitative measurement of R [32]. The R is defined by $R = B \times l$, where B is linear birefringence and l the thickness of the birefringent layer. Such R measurements coupled to slow axis measurements enable one to elucidate the formation of NGs since these structures are both birefringent and oriented by the writing laser polarization.

3. Results

3.1. Optical modifications in the pulse energy - pulse duration landscape

It has been reported that the R detection threshold (characteristic of NGs formation) strongly depends on the laser light intensity for all alkali-free alumino-borosilicate (AF32), multicomponent borosilicate (Borofloat33) and silica glasses [33]. Such threshold is thus a function of the ratio of pulse energy to the pulse duration. The threshold was found to be slightly above 1 TW/cm^2 for AF32 and silica glasses [33,34]. Therefore, the pulse energy - duration landscape is a key point to evaluate the formation of NGs, and therefore was chosen herein. On other hand, the dependence of colouration and scattering to "Type II-like" on the pulse duration has been reported in [13,35]. While probing this landscape, several types of transformations, typically found in most oxide glasses, are revealed. The observed permanent modifications are classified as Type I, Type II, and what we have called "spatial broadening regime". Type I corresponds to an isotropic refractive index change leading to a permanent contrast in non-polarized optical microscopy

Optics EXPRESS

which can be further quantified in optical phase microscopy. Type II corresponds to the NGs regime and is identified as the observation of a birefringence response from the irradiated area whose orientation depends on the writing laser polarization. This is usually identified as form birefringence due to NGs formation [6] and can be observed with polarized light microscopy equipped with a full retardation waveplate. A last type of modification appearing at high laser intensities can be finally defined. Often imprecisely called "heat accumulation regime" in the literature, this modification corresponds to a smooth and homogeneous variation of the refractive index with a tendency of laser tracks to become much larger than the laser beam size. This spatially broadened "Type I-like" modification will therefore be referred to as "spatial broadening regime", which describes more accurately this phenomenon [4].

In the following we will study 3 glass families, namely SAN, SAC and SACN, which exhibit different chemical composition and stoichiometry. At first SAC 50-25-25 glass was selected since its composition contains both no boron and the highest amount of Al_2O_3, which is equal to the amount of CaO, and with the minimum ratio of $(Na_2O + CaO)/Al_2O_3$. Figure 1 summarizes the three different fs laser-induced transformations for such SAC 50-25-25 glass at a fixed repetition

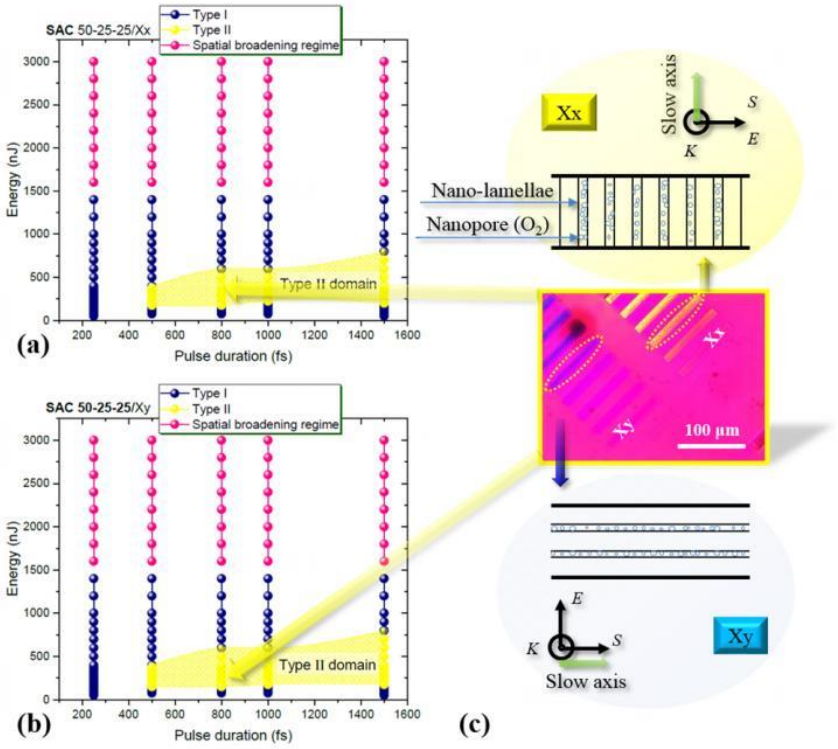

Fig. 1. Laser-induced modifications in pulse energy - duration landscape. Transformation regimes encountered in the experimental conditions: Type I, Type II and spatial broadening regime. The selected sample is SAC 50-25-25 with Xx (a) and Xy (b) writing polarization configurations, respectively. (c) Sketch of two configurations of fs laser induced NGs with the corresponding orientations of slow axis indicated in bulk glass. Inset shows the polarized optical microscope image (bottom light illumination) with crossed polarizers and a full waveplate inserted at 45°. *E*: laser polarization direction, *K*: laser beam propagation direction and *S*: laser scanning direction. Laser parameters: 1030 nm, 0.6 NA, 100 kHz, 10 µm/s.

rate of 100 kHz and is intended to illustrate the observed features, which are common to all investigated glasses, although in varying proportions.

As shown in Fig. 1(a) and (b), our results indicate that SAC 50-25-25 glass irradiated with both Xx and Xy configurations [32] possesses broad energy windows both for Type I (from 25 to 1400 nJ) and spatial broadening regime (from 1600 up to 3000 nJ). Furthermore, there are no NGs detected at 250 fs inside SAC 50-25-25 glass, confirming that shorter pulse durations are disadvantageous for the NGs formation in agreement with the literature [33,34,36,37], which may be related to a limitation in terms of plasma density that is not high enough to initiate the nanopores formation. Then for pulse durations above 500 fs, a Type II processing window appears as revealed by comparing Xx and Xy writing configurations. The typical sketch of these two configurations including nanolayers and the formed O_2-contaning nanopores (usually seen by Raman spectroscopy), is illustrated in Fig. 1(c), in which a polarized optical microscope image with a first order full waveplate inserted is provided. This enables the identification of the slow axis (indicated in Fig. 1(c)) of the laser tracks and its 90° rotation when switching the polarization from x to y in the reference frame, indicative of the existence of Type II modifications. Finally, a slight increase of Type II window width for longer pulse durations was observed, in agreement with Ref. [6]. This is likely related to a lower peak power leading to a less efficient overall absorption by the free electron plasma in relatively long pulse duration, in agreement with recent results reported for silica glass [38], e.g. the absorbed energy was 95 nJ for 300 fs at pulse energy of 690 nJ, while the absorbed energy was 17 nJ for 500 fs at the equivalent pulse energy.

Interestingly, the Type I regime, as previously described, is found to reappear as the energy is progressively increased and while the Type II window collapses. This feature suggests that there is likely a combination / overlap of Type I and Type II domains, which can imply several hypotheses such as i) the material in-between the porous nanolayers is likely a kind of Type I modification and ii) at high energies the nanopores are likely erased after the energy deposition and during the resulting heating-cooling process [31].

3.2. *Effect of the chemical composition on the optical retardance and Type II energy window*

It has previously been established that the deposited energy, pulse duration, and writing configurations are key parameters that impact on the formation of NGs in oxide glasses [6,38]. To study such effects, the dependence of the optical retardance, R, on these factors has been quantitatively investigated. Firstly, quantitative R results obtained in the SAC 50-25-25 glass at different pulse durations are highlighted in Fig. 2(a), as it serves, as before, as an exemplar throughout this work. Above a threshold of around 100-150 nJ, the overall R increases up to a maximum, and then strongly decreases as the energy is continuously increased. The latter part corresponds to the formation of inhomogeneous and disrupted NGs that can be assigned to a significant temperature increase at higher pulse energies [39,40]. Finally, no polarization dependent birefringence, required to confirm the presence of NGs, could be observed above a certain energy value.

Secondly, it was also found that for a given glass the maximum R tends to saturate for all investigated pulse durations (and for both Xx and Xy configurations). It is then followed by a decrease for longer pulse durations (e.g., 1500 fs in Xx configuration). This quantitative increase of R can be simply explained by an elongated focal spot yielding to longer laser tracks. In contrast, the decrease for longer pulse duration might be related to some thermal effects in the picosecond regime that affect the nanopores size and filling factor [41], due to the lower melting point of alumino-borosilicate glasses.

Finally, higher R values are measured in Xx configuration compared to the Xy one, as shown in Fig. 2(a) and (b), due to the combined effect of stress-induced birefringence around nano-lamellae, as previously reported [42]. This is particularly visible in the SAC 50-25-25 glass case at 800

Optics EXPRESS

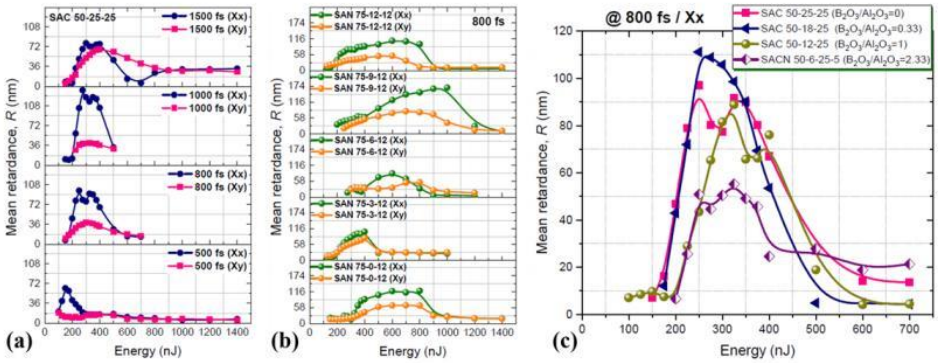

Fig. 2. Mean retardance, *R*, of laser-written structures as a function of pulse energy for (a) SAC 50-25-25 glass with pulse durations of 500, 800, 1000 and 1500 fs, using Xx and Xy configurations, (b) a series of SAN glasses at 800 fs using Xx and Xy configurations, (c) SAC 50-25-25, SAC 50-18-25, SAC 50-12-25 and SACN 50-6-25-5 glasses at 800 fs using Xx configuration.

and 1000 fs, for which the maximum *R* (i.e., 97 nm at 800 fs and 136 nm at 1000 fs) of Xx configuration was 2.5 and 3.4 times higher than that of Xy configuration at 800 fs (i.e., 39 nm) and 1000 fs (i.e., 40 nm), respectively.

To continue investigating the NGs processing windows and the effect of boron/aluminum oxides in the presence of alkali, the results of the SAN glass series were investigated. The *R* values, for a fixed 800 fs laser pulse duration, and for varying pulse energy values, are shown in Fig. 2(b). These alkali-containing glasses showed a wide range of *R* values, strongly dependent on glass composition, pulse energy, and polarization (Xx and Xy configuration). In the SAN family glasses, the maximum *R* (168 nm) was measured in the SAN 75-9-12 glass sample having an Xx writing configuration and at 1000 nJ, where the ratio B_2O_3/Al_2O_3 is equal to 0.33 (see Table 1).

As previously investigated and stated, both Xx configuration and 800 fs pulse duration were found to be optimized parameters, within the context of this study, to imprint high *R* NGs (Fig. 2(a) and (b)). Therefore, the calcium-containing glass series was investigated by keeping these two parameters fixed, and the results of *R* as a function of pulse energy are reported in Fig. 2(c). SAC 50-25-25 glass (i.e., B_2O_3-free glass) is first compared to the two SAC glasses, where B_2O_3 is added. Then, the three aforementioned glasses are compared to the SACN 50-6-25-5 glass, which contains both alkali (Na^+) and alkaline earth (Ca^{2+}) cations (as opposed to only Ca^{2+} cations). It is found that the minimum pulse energy required to induce detectable *R* was in the range of 100-150 nJ and it increased slightly when increasing the B_2O_3/Al_2O_3 ratio. Overall, SAC 50-18-25 glass, which owns the lowest B_2O_3/Al_2O_3 ratio of 0.33, showed a maximum *R* value of 110 nm at 250 nJ. It can be explained that the viscosity (impacted by chemical composition) and created free plasma density are in optimized state to obtain the maximum optical retardance. This needs further investigations. Interestingly, higher *R* values were measured in SAN 75-9-12 and SAN 75-12-12 glasses compared to the calcium containing glasses, as shown in (b). In addition, the *R* decreased as the alkali metal (Na^+) content increased, e.g., SACN 50-6-25-5 glass (see Fig. 2(c)). In short, the effect of sodium seems drastic probably due to Na^+ chemical migration, and the results obtained on the B/Al mixture in SACs are in the same direction as the results for SANs. While this effect requires further investigations to be clarified, this agrees with the literature, which reported on the detrimental effect of Na_2O for NGs formation in SiO_2-Na_2O [43] and GeO_2-Na_2O [44] glasses.

Optics EXPRESS

4. Discussion and rationalization

4.1. Key role played by the viscosity on Type II energy window

The domain of existence of the nanopores (and thus NGs) can be anticipated by using a simple approach following viscosity-based arguments [11,12]. In order to investigate this aspect, the viscosity profiles as a function of temperature and the estimated domain of NGs existence are reported in Fig. 3(a) for all the oxide glasses investigated in this work. Here the investigated glass viscosities were modeled using SciGlass software and the obtained data as a function of temperature were subsequently fitted using the Vogel–Fulcher–Tammann (VFT) equation [45].

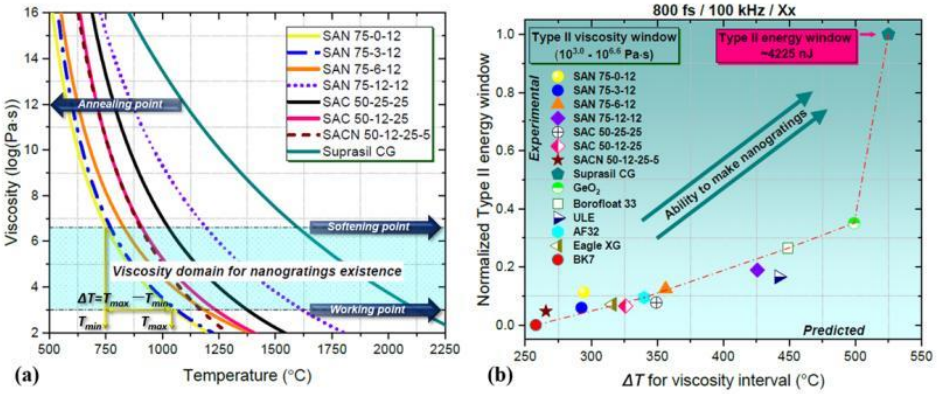

Fig. 3. (a) Viscosity as a function of temperature for a variety of alumino-borosilicate and SiO_2 (Suprasil CG, taken as a reference) glasses, along with an estimated domain of NGs existence from T_{min} ($\eta = 10^{6.6}$ Pa·s, i.e., softening temperature) to T_{max} ($\eta = 10^{3.0}$ Pa·s, working temperature). (b) Normalized Type II energy window vs. temperature interval ($\Delta T = T_{max} - T_{min}$) for a variety of alumino-borosilicate and commercial glasses. The x axis presents the predicted results of temperature interval from (a) and the y axis presents the experimental results.

The domain of NGs existence was predicted by considering two boundaries [11] in terms of viscosity, which can then be translated into two limiting temperatures. The lower limit corresponds to the temperature, $T_{min} = T_{soft}$, i.e., softening temperature, at which nanocavitation in the glass can occur and for which the viscosity value (η) is situated at around $\sim 10^{6.6}$ Pa·s, forming nanopores that compose the NGs. The upper temperature limit, $T_{max} = T_{working}$, i.e., working temperature, relates to either the collapse or unstable hydrodynamic growth of the nanopores, resulting in the disappearance of the nanopores, hence the NGs structuring. This corresponds to a viscosity value typically around $\sim 10^{3.0}$ Pa·s, i.e., the so-called working temperature of glass, and was determined using the Peclet number (ratio between the viscous deformation and thermal diffusion rate) as a local indicator for nanopores erasure [46]. The broadness of NGs existence window (i.e. its extent in terms of pulse energy), was then estimated by considering the temperature interval (ΔT) between T_{max} and T_{min} as previously defined. The upper and lower boundaries of the viscosity corresponding to the T_{min} / T_{max} interval, are provided in Fig. 3(a). Note that $\eta = 10^{12.0}$ Pa·s, also reported in the figure, corresponds to the annealing temperature and is given for completeness. The temperature interval (ΔT) was calculated for each glass and reported on the x-axis of Fig. 3(b). On the y-axis is reported the Type II energy window, calculated by taking the extent of the Type II window in the pulse energy - duration landscape, and subsequently normalized relatively to SiO_2 (set as 1), i.e. $(E_{max(glass)} - E_{min(glass)})/(E_{max} - E_{min})$ where $E_{max(glass)}$ and $E_{min(glass)}$ present the energies to NGs collapsed and formed for the corresponding glass studied, respectively. The E_{max} and E_{min} are respectively energies of SiO_2 glass. ΔT is progressively enlarging for glasses

Optics EXPRESS

in the following order: SAN 75-12-12 > SAN 75-6-12 > SAC 50-25-25 > SAC 50-12-25 > SAN 75-0-12 ≈ SAN 75-3-12 > SACN 50-12-25-5. On average, the normalized Type II window extent (normalized with respect to silica) monotonously increased with ΔT at a slope of 0.0015 $°C^{-1}$ for the alumino-borosilicate glasses and the commercial glasses apart from SiO_2 (Suprasil CG), which exhibited the broadest Type II window and a higher slope of 0.025 $°C^{-1}$ (the slope from GeO_2 to SiO_2). The viscosity modeling results were basically in agreement with experimental data, further supporting and confirming the viscosity (η) role on the NGs formation, recently suggested [11]. As a general view, glasses with low Si and high (alkali + alkaline earth) content possess low network connectivity and relatively abundant non-bridging oxygens (NBOs) [47,48]. This will further lead to lower viscosity of the glass, e.g., the viscosity of SAN 75-12-12 is higher than that of SAC 50-12-25 (low Si and high (alkali + alkaline earth) content).

4.2. Influence of the chemical composition on the Type II energy window

Type II energy window can also be studied with respect to glass composition, and more specifically relative to ratios such as $(Na_2O + CaO)/Al_2O_3$ or B_2O_3/Al_2O_3. The results are displayed in Fig. 4(a) and (b). The first, i.e., $(Na_2O + CaO)$ to Al_2O_3 ratio, distinguishes the glass compositions between peralkaline [$(Na_2O + CaO) > Al_2O_3$] (like SAC, SACN family samples), metaluminous (like most SAN samples) and peraluminous [$Al_2O_3 > (Na_2O + CaO)$], and is a prime factor controlling the formation of NGs. The addition of alkali and alkaline earth elements in glasses can provide strong structural changes due to the role of network modifiers, such as bond breaking and even forming some "channels" as reported for Na_2O glasses [49]. In a simple view, alkali and alkaline earth atoms play the role of depolymerizing cations (i.e., behaving as a modifying cation, breaking T-O-T linkages (T = Si, Al) and forming nonbridging ≡Si-O- bonds [50], lowering the degree of polymerization of the main structural groups and consequently decreasing the viscosity of glass (a key factor in NGs formation/erasure mechanisms [11]. Indeed, Liu *et al.* [51] reported that flow could involve the relative motion of large molecular units (e.g., chains or sheets) due to depolymerized networks. Therefore, with the decrease of the $(Na_2O + CaO)/Al_2O_3$ ratio, the network structure of glass is more rigid and connected, which might favor the formation of NGs [11]. From Fig. 4(a), the increase in $(Na_2O + CaO)/Al_2O_3$ ratio is indeed accompanied with a decrease of the Type II window (materialized by the green area and bounded by lower and upper energy limits yielding to the observation of NGs). Fernandez *et al.* [47] also reported that (alkali + alkaline earth)/Al_2O_3 ratio directly affected the viscosity, and the viscosity was at its maximum when the (alkali + alkaline earth)/Al_2O_3 ratio was 1, where in other words there was a kind of balance between Al and charge compensating modifiers. This is the case for SAN 75-12-12 glass, which correspondingly owns the largest processing window. Since Na is always more mobile than Ca, one could imagine that Ca compensates and Na makes non-bridging oxygen which could explain the behavior of Na-containing glasses (e.g. SACN).

Interestingly, although exhibiting the same $(Na_2O + CaO)/Al_2O_3$ ratio equal to 2, the two peralkaline glasses SAC 50-12-25 and SAN 75-6-12 revealed significantly different Type II windows. Na-containing alumino-borosilicate glass (SAN 75-6-12) showed a roughly 2 times broader Type II window with respect to the Ca-containing one (SAC 50-12-25). At a first sight, one could think that the higher SiO_2 content should rather lead to the opposite observation since $(Na_2O + CaO)/SiO_2$ ratio is much lower for SAN 75-6-12 glass (i.e., 12.5/75) compared to SAC 50-12-25 glass (i.e., 25/50). However, it appears clearly from the glass annealing temperatures, T_a, and the viscosity curves (see Fig. 3(a) and Table 1) that SAC 50-12-25 glass owns a higher viscosity revealing in a more rigid network structure or increased network connectivity compared to SAN 75-6-12 glass. It appears again here that the main driver for NGs formation is not simply the viscosity, but it is rather the temperature dependence of viscosity and especially its slope in the range between $\eta = 10^{6.6}$ Pa·s (softening point) and $\eta = 10^{3.0}$ Pa·s (working point) [11]. However, it is worthwhile noting that the chemical composition is one of the causes which indirectly decides

Optics EXPRESS

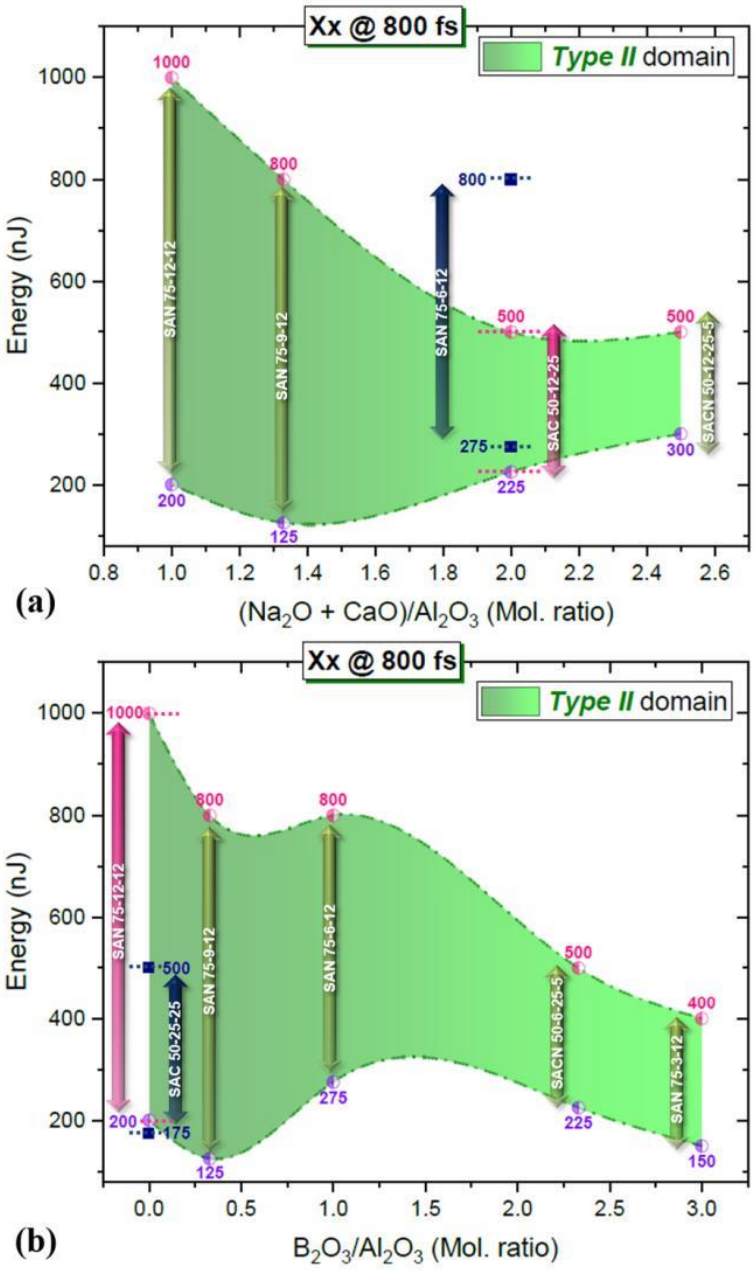

Fig. 4. Type II processing window for the different glass groups under study illustrated in a pulse energy vs. (a) $(Na_2O + CaO)/Al_2O_3$ and (b) B_2O_3/Al_2O_3 ratio landscape. The ratios are given by using glass composition in mol.%. Fixed laser parameters are: 800 fs and Xx writing configuration. The length of double head arrow indicates roughly the width of type II energy window.

Optics EXPRESS

the amplitude of viscosity of the glass. The viscosity is impacted by the network structure and, in parallel, network structure is determined by the chemical composition.

Finally, the width of the type II windows has been reported in Fig. 4(b) as a function of B_2O_3/Al_2O_3 ratio (in mol. ratio). As a general trend, the Type II window decreased while increasing the B_2O_3/Al_2O_3 ratio or along B/Al mixture. Here, the substitution of Al_2O_3 by B_2O_3 leads to a strong viscosity declining as a function of temperature, as visible from Fig. 3(a) when considering the SAN glass series. More specifically, the viscosity curves become steeper, in the $10^{6.6}$ - $10^{3.0}$ Pa·s viscosity range of interest, when increasing B_2O_3/Al_2O_3 ratio, which turns out to be detrimental for NGs formation in the framework of our model. In addition, by comparing the two glasses SAN 75-12-12 and SAC 50-25-25, which both have no Boron oxide and the same $(Na_2O + CaO)/Al_2O_3$ ratio, it is worthwhile noting that SAN 75-12-12 owns a much wider Type II processing window. This has been attributed to the different $(Na_2O + CaO)/SiO_2$ ratio, namely 12.5/75 for SAN 75-12-12 glass against the much higher value of 25/50 exhibited by the SAC 50-25-25 glass. Again, one can clearly see in Fig. 3(a) that the SAN 75-12-12 appears to be a "long glass" [11] compared to SAC 50-25-25, for which the viscosity drastically reduces at high temperature. The corresponding temperature intervals $\Delta T = T_{max} - T_{min}$ are thus estimated to be 425 °C for SAN 75-12-12 and 350 °C for SAC 50-25-25 glasses.

5. Conclusion

In summary, (alkali, alkaline earth)-doped alumino-borosilicate glasses revealed the formation of NGs by irradiation through fs laser. The upper limit of existence of NGs occurred at relatively high pulse energies (i.e., 600 nJ for SAC 50-25-25 glass), while Type I modification was observed again surpassing this energy. The maximum retardance of 168 nm was exhibited by SAN 75-9-12 glass at 800 fs and 1000 nJ, revealing that the B_2O_3/Al_2O_3 molar ratio and relatively high SiO_2 content are of primary importance in the formation of NGs. Moreover, an interpretation from the viscosity point of view is demonstrated and the normalized Type II processing windows of a series of alumino-borosilicate glasses along with the current commercial glasses vs. temperature interval are exhibited, in turn basically confirming the consistence between viscosity modeling results and experimental data. Furthermore, Type II window was found to be gradually narrower while increasing (alkali + alkaline earth)/Al_2O_3 and B_2O_3/Al_2O_3 molar ratios due to the depolymerizing network of alkali plus alkaline earth metal elements, the increased connectivity of SiO_2 network and the glass "fragility" induced by B_2O_3 doping further indicate the dependence of Type II processing window on the chemical composition.

Funding. National Natural Science Foundation of China (12274280, 11774220); Science and Technology Innovation Plan of Shanghai Science and Technology Commission (20JC1415700); China Scholarship Council; Agence Nationale de la Recherche (ANR-18-CE08-0004-01, FLAG-IR Project).

Disclosures. The authors declare no conflicts of interest.

Data availability. Data underlying the results presented in this paper are not publicly available at this time but may be obtained from the authors upon reasonable request.

References

1. L. Orazi, L. Romoli, M. Schmidt, and L. Li, "Ultrafast laser manufacturing: from physics to industrial applications," CIRP Ann. **70**(2), 543–566 (2021).
2. R. Stoian, "Volume photoinscription of glasses: three-dimensional micro- and nanostructuring with ultrashort laser pulses," Appl. Phys. A **126**(6), 438 (2020).
3. Y. Bellouard, A. Said, M. Dugan, and P. Bado, "Fabrication of high-aspect ratio, micro-fluidic channels and tunnels using femtosecond laser pulses and chemical etching," Opt. Express **12**(10), 2120–2129 (2004).
4. H. Yao, R. Zaiter, M. Cavillon, B. Sapaly, F. Calzavara, P. Delullier, T. Cardinal, Y. Dai, B. Poumellec, and M. Lancry, "Photosensitivity of barium germano-gallate glasses under femtosecond laser direct writing for Mid-IR applications," Ceram. Int. **47**(24), 34235–34241 (2021).
5. E. N. Glezer and E. Mazur, "Ultrafast-laser driven micro-explosions in transparent materials," Appl. Phys. Lett. **71**(7), 882–884 (1997).

Optics EXPRESS

6. H. Yao, R. Zaiter, M. Cavillon, P. Delullier, B. Lu, T. Cardinal, Y. Dai, B. Poumellec, and M. Lancry, "Formation of nanogratings driven by ultrafast laser irradiation in mid-IR heavy oxide glasses," Ceram. Int. **48**(21), 31363–31369 (2022).
7. Y. Shimotsuma, P. G. Kazansky, J. Qiu, and K. Hirao, "Self-organized nanogratings in glass irradiated by ultrashort light pulses," Phys. Rev. Lett. **91**(24), 247405 (2003).
8. R. Taylor, C. Hnatovsky, and E. Simova, "Applications of femtosecond laser induced self-organized planar nanocracks inside fused silica glass," Laser Photonics Rev. **2**(1-2), 26–46 (2008).
9. V. R. Bhardwaj, E. Simova, P. P. Rajeev, C. Hnatovsky, R. S. Taylor, D. M. Rayner, and P. B. Corkum, "Optically produced arrays of planar nanostructures inside fused silica," Phys. Rev. Lett. **96**(5), 057404 (2006).
10. M. Beresna, M. Gecevičius, P. G. Kazansky, T. Taylor, and A.V. Kavokin, "Exciton mediated self-organization in glass driven by ultrashort light pulses," Appl. Phys. Lett. **101**(5), 053120 (2012).
11. Q. Xie, M. Cavillon, B. Poumellec, D. Pugliese, D. Janner, and M. Lancry, "Application and validation of a viscosity approach to the existence of nanogratings in oxide glasses," Opt. Mater. **130**, 112576 (2022).
12. A. Rudenko, J. -P. Colombier, and T. E. Itina, "Nanopore-mediated ultrashort laser-induced formation and erasure of volume nanogratings in glass," Phys. Chem. Chem. Phys. **20**(8), 5887–5899 (2018).
13. M. Sakakura, Y. Lei, L. Wang, Y. -H. Yu, and P. G. Kazansky, "Ultralow-loss geometric phase and polarization shaping by ultrafast laser writing in silica glass," Light: Sci. Appl. **9**(1), 15 (2020).
14. E. Bricchi and P. G. Kazansky, "Extraordinary stability of anisotropic femtosecond direct-written structures embedded in silica glass," Appl. Phys. Lett. **88**(11), 111119 (2006).
15. Y. Shimotsuma, M. Sakakura, P. G. Kazansky, M. Beresna, J. Qiu, K. Miura, and K. Hirao, "Ultrafast manipulation of self-assembled form birefringence in glass," Adv. Mater. **22**(36), 4039–4043 (2010).
16. J. Zhang, M. Gecevičius, M. Beresna, and P. G. Kazansky, "Seemingly unlimited lifetime data storage in nanostructured glass," Phys. Rev. Lett. **112**(3), 033901 (2014).
17. Y. Shimotsuma, T. Asai, M. Sakakura, and K. Miura, "Femtosecond-laser nanostructuring in glass," J. Laser Micro/Nanoeng. **9**(1), 31–36 (2014).
18. F. Zhang, H. Zhang, G. Dong, and J. Qiu, "Embedded nanogratings in germanium dioxide glass induced by femtosecond laser direct writing," J. Opt. Soc. Am. B **31**(4), 860–864 (2014).
19. T. Asai, Y. Shimotsuma, T. Kurita, A. Murata, S. Kubota, M. Sakakura, K. Miura, F. Brisset, B. Poumellec, and M. Lancry, "Systematical control of structural changes in GeO_2 glass induced by femtosecond laser direct writing," J. Am. Ceram. Soc. **98**(5), 1471–1477 (2015).
20. Y. Shimotsuma, K. Hirao, J. Qiu, and P. G. Kazansky, "Nano-modification inside transparent materials by femtosecond laser single beam," Mod. Phys. Lett. B **19**(05), 225–238 (2005).
21. Q. Zhai, H. Ma, X. Lin, Y. Li, W. Yin, X. Tang, X. Zeng, and Y. Dai, "Evolution of self-organized nanograting from the pre-induced nanocrack-assisted plasma–laser coupling in sapphire," Appl. Phys. B **127**(5), 74 (2021).
22. Y. Shimotsuma, S. Mori, Y. Nakanishii, E. Kim, M. Sakakura, and K. Miura, "Self-assembled glass/crystal periodic nanostructure in Al_2O_3-Dy_2O_3 binary glass," Appl. Phys. A **124**(1), 82 (2018).
23. J. Cao, L. Mazerolles, M. Lancry, F. Brisset, and B. Poumellec, "Modifications in lithium niobium silicate glass by femtosecond laser direct writing: morphology, crystallization, and nanostructure," J. Opt. Soc. Am. B **34**(1), 160–168 (2017).
24. S. Richer, C. Miese, S. Döring, F. Zimmermann, M. J. Withford, A. Tünnermann, and S. Notle, "Laser induced nanogratings beyond fused silica - periodic nanostructures in borosilicate glasses and ULE^{TM}," Opt. Mater. Express **3**(8), 1161–1166 (2013).
25. B. Poumellec, M. Cavillon, and M. Lancry, "Electrostatic interpretation of phase separation induced by femtosecond laser light in glass," Crystals **13**(3), 393 (2023).
26. A. Ellison and I. A. Cornejo, "Glass substrates for liquid crystal displays," Int. J. Appl. Glass Sci. **1**(1), 87–103 (2010).
27. F. T. Wallenberger, "The effects of lithia and alumina on the viscosity and strength of commercial fibreglass and other glass compositions," Glass Technol.: Eur. J. Glass Sci. Technol., Part A **52**(4), 117–126 (2011).
28. M. E. Lines, J. B. MacChesney, K. B. Lyons, A. J. Bruce, A. E. Miller, and K. Nassau, "Calcium aluminate glasses as potential ultralow-loss optical materials at 1.5–1.9 μm," J. Non-Cryst. Solids **107**(2-3), 251–260 (1989).
29. L. -G. Hwa, S. -L. Hwang, and L. -C. Liu, "Infrared and Raman spectra of calcium alumino-silicate glasses," J. Non-Cryst. Solids **238**(3), 193–197 (1998).
30. F. T. Wallenberger, R. J. Hicks, and A. T. Bierhals, "Design of environmentally friendly fiberglass compositions: ternary eutectic SiO_2–Al_2O_3–CaO compositions, structures and properties," J. Non-Cryst. Solids **349**, 377–387 (2004).
31. Q. Xie, M. Cavillon, D. Pugliese, D. Janner, B. Poumellec, and M. Lancry, "On the formation of nanogratings in commercial oxide glasses by femtosecond laser direct writing," Nanomaterials **12**(17), 2986 (2022).
32. J. Tian, H. Yao, M. Cavillon, E. Garcia-Caurel, R. Ossikovski, M. Stchakovsky, C. Eypert, B. Poumellec, and M. Lancry, "A comparison between nanogratings-based and stress-engineered waveplates written by femtosecond laser in silica," Micromachines **11**(2), 131 (2020).
33. S. S. Fedotov, R. Drevinskas, S. V. Lotarev, A. S. Lipatiev, M. Beresna, A. Čerkauskaitė, V. N. Sigaev, and P. G. Kazansky, "Direct writing of birefringent elements by ultrafast laser nanostructuring in multicomponent glass," Appl. Phys. Lett. **108**(7), 071905 (2016).

Optics EXPRESS

34. Y. Liao, B. Zeng, L. Qiao, L. Liu, K. Sugioka, and Y. Cheng, "Threshold effect in femtosecond laser induced nanograting formation in glass: influence of the pulse duration," Appl. Phys. A **114**(1), 223–230 (2014).
35. T. Ohfuchi, Y. Yamada, M. Sakakura, N. Fukuda, T. Takiya, Y. Shimotsuma, and K. Miura, "The Characteristic of Birefringence and Optical Loss in Femtosecond-Laser-Induced Region in terms of Nanogratings Distribution," J. Laser Micro Nanoen. **12**(3), 217–221 (2017).
36. F. Zimmermann, A. Plech, S. Richter, S. Döring, A. Tünnermann, and S. Nolte, "Structural evolution of nanopores and cracks as fundamental constituents of ultrashort pulse-induced nanogratings," Appl. Phys. A **114**(1), 75–79 (2014).
37. C. Mauclair, M. Zamfirescu, J. P. Colombier, G. Cheng, K. Mishchik, E. Audouard, and R. Stoian, "Control of ultrafast laser-induced bulk nanogratings in fused silica via pulse time envelopes," Opt. Express **20**(12), 12997–13005 (2012).
38. H. Wang, Y. Lei, L. Wang, M. Sakakura, Y. Yu, G. Shayeganrad, and P. G. Kazansky, "100-layer error-free 5D optical data storage by ultrafast laser nanostructuring in glass," Laser Photonics Rev. **16**(4), 2100563 (2022).
39. F. Zhang, A. Cerkauskaite, R. Drevinskas, P. G. Kazansky, and J. Qiu, "Microengineering of optical properties of GeO_2 glass by ultrafast laser nanostructuring," Adv. Opt. Mater. **5**(23), 1700342 (2017).
40. F. Zhang, Z. Nie, H. Huang, L. Ma, H. Tang, M. Hao, and J. Qiu, "Self-assembled three-dimensional periodic micro-nano structures in bulk quartz crystal induced by femtosecond laser pulses," Opt. Express **27**(5), 6442–6450 (2019).
41. M. Gecevičius, "Polarization sensitive optical elements by ultrafast laser nanostructuring of glass," University of Southampton, Physical Sciences and Engineering, Doctoral Thesis (2015), 197 pp.
42. M. Gecevičius, M. Beresna, J. Zhang, W. Yang, H. Takebe, and P. G. Kazansky, "Extraordinary anisotropy of ultrafast laser writing in glass," Opt. Express **21**(4), 3959–3968 (2013).
43. J. Wang, X. Liu, Y. Dai, Z. Wang, and J. Qiu, "Effect of sodium oxide content on the formation of nanogratings in germanate glass by a femtosecond laser," Opt. Express **26**(10), 12761–12768 (2018).
44. S. V. Lotarev, S. S. Fedotov, A. I. Kurina, A. S. Lipatiev, and V. N. Sigaev, "Ultrafast laser-induced nanogratings in sodium germanate glasses," Opt. Lett. **44**(7), 1564–1567 (2019).
45. D. R. Neuville, "Viscosity, structure and mixing in (Ca, Na) silicate melts," Chem. Geol. **229**(1-3), 28–41 (2006).
46. A. Rudenko, J. -P. Colombier, S. Höhm, A. Rosenfeld, J. Krüger, J. Bonse, and T. E. Itina, "Spontaneous periodic ordering on the surface and in the bulk of dielectrics irradiated by ultrafast laser: a shared electromagnetic origin," Sci. Rep. **7**(1), 12306 (2017).
47. T. T. Fernandez, S. Gross, K. Privat, B. Johnston, and M. Withford, "Designer glasses—future of photonic device platforms," Adv. Funct. Mater. **32**(3), 2103103 (2022).
48. T. T. Fernandez, M. Sakakura, S. M. Eaton, B. Sotillo, J. Siegel, J. Solis, Y. Shimotsuma, and K. Miura, "Bespoke photonic devices using ultrafast laser driven ion migration in glasses," Prog. Mater. Sci. **94**, 68–113 (2018).
49. G. S. Henderson and J. F. Stebbins, "The short-range order (SRO) and structure," Rev. Mineral. Geochem. **87**(1), 1–53 (2022).
50. D. R. Neuville, L. Cormier, and D. Massiot, "Al coordination and speciation in calcium aluminosilicate glasses: Effects of composition determined by ^{27}Al MQ-MAS NMR and Raman spectroscopy," Chem. Geol. **229**(1-3), 173–185 (2006).
51. S. -B. Liu, J. F. Stebbins, E. Schneider, and A. Pines, "Diffusive motion in alkali silicate melts: An NMR study at high temperature," Geochim. Cosmochim. Acta **52**(2), 527–538 (1988).

II.5 NANOSCALE INVESTIGATIONS OF FEMTOSECOND LASER INDUCED NANOGRATINGS IN OPTICAL GLASSES

Nanoscale Advances

ROYAL SOCIETY OF CHEMISTRY

PAPER

View Article Online
View Journal

Cite this: DOI: 10.1039/d3na00748k

Nanoscale investigations of femtosecond laser induced nanogratings in optical glasses

Qiong Xie, Nadezhda Shchedrina, Maxime Cavillon, Bertrand Poumellec and Matthieu Lancry*

Received 6th September 2023
Accepted 18th November 2023

DOI: 10.1039/d3na00748k

rsc.li/nanoscale-advances

Femtosecond (fs) laser irradiation inside transparent materials has drawn considerable interest over the past two decades. More specifically, self-assembled nanogratings, induced by fs laser direct writing (FLDW) inside glass, enable a broad range of potential applications in optics, photonics, or microfluidics. In this work, a comprehensive study of nanogratings formed inside fused silica by FLDW is presented based on high-resolution electron microscopy imaging techniques. These nanoscale investigations reveal that the intrinsic structure of nanogratings is composed of oblate nanopores, shaped into nanoplanes, regularly spaced and oriented perpendicularly to the laser polarization. These nanoporous layers are forced-organized by light, resulting in a pseudo-organized spacing at the sub-wavelength scale, and observed in a wide range of optical glasses. In light of the current state of the art, we discuss the imprinting of nanoporous layers under thermomechanical effects induced by a plasma-mediated nanocavitation process.

Introduction

When a femtosecond (fs) laser beam is focused inside a glass material such as silica, the light is nonlinearly absorbed through multiphoton, tunneling and avalanche ionization mechanisms. These complex light/matter interactions lead to the formation of permanent modifications inside, and sometimes around, the irradiated volume. The transformations, while being a function of both glass composition and laser parameters, yield typical transformations classified into regimes, including (i) positive or negative refractive index modifications (commonly called type I),[1] (ii) formation of volume nanogratings (NGs) (at the root of form birefringence and labeled type II),[2,3] and (iii) nanovoid-like structures.[4] The NGs are believed to be the smallest self-organized structures ever created by light in the volume of a transparent material.

The focus of this work is on NGs, which have found use in various fields and applications such as health,[5] optical data storage,[6–8] optofluidics,[9,10] sensors in harsh environments[11,12] and a wide range of optical components like 3D optical waveguides, 3D geometric phase optics,[13] and polarizing optical devices.[14,15] Porous NGs and related strong birefringence are a spectacular manifestation of a light controlled glass decomposition, and have been primarily reported in pure silica[16] and slightly doped silica glasses.[17,18] Unlike surface ripples,[19] NGs were initially found only in a handful of materials: fused silica, sapphire, tellurium oxide, ULE glass and alkali-free aluminoborosilicate glasses.[20–23] From this list, silica is the material of choice to induce NGs. It brings a wide range of optical functionalities, coupled with high thermal and chemical stability, ease of nanoplasma initiation,[13,24] and its ability to form nanopores (high viscosity values over a wide temperature range *i.e.* a so-called "long glass"), as opposed to other optical glasses,[25] thereby offering significant industrial potential as the backbone of many today's photonics applications. Several studies on NG formation were conducted on multicomponent silicate glasses doped with germanium, phosphorus or titanium.[26] NGs were also found in porous silica prepared from phase-separated alkali-borosilicate glass by removing the borate phase in a hot acid solution.[27]

The importance of understanding NG formation mechanisms lies in the ability to reliably reproduce and potentially scale up the production of NGs, as well as to gain a deeper fundamental understanding of the complex light–matter interactions involved. Numerous research groups have investigated mechanisms behind the formation of self-organized nanogratings, providing valuable frameworks for advancing related scientific inquiries. At the nanoscale, Shimotsuma *et al.*[28] showed contrast NGs (around 20 nm width and periodicity from 140 to 320 nm) in back-scattered electron imaging corresponding to atomic density contrast. Chemical analysis by Auger spectroscopy revealed that these variations could correspond to oxygen depletion and related density modulation.[29] Hnatovsky *et al.*[30,31] reported the presence of nano-cracks and raised questions about whether these NGs can best be described as highly modified regions of differing materials (*e.g.* through bond breaking accumulation) or

Institut de Chimie Moléculaire et des Matériaux d'Orsay, CNRS-Université Paris Sud, Université Paris Saclay, Bât. 410, 91405 Orsay, France. E-mail: matthieu.lancry@universite-paris-saclay.fr

as some nanovoids. Regardless of the precise mechanistic explanation of nanoplanes (nanoplasma,[32] photon–plasmons interference,[33] plasmon–polaritons[34] or complex self-organization similar to a Turing structure), Lancry *et al.* observed that nanoplanes undergo a glass decomposition coupled with oxygen release.[35] Asai *et al.* observed a similar feature in GeO_2 glass[36] reinforcing the theory of the suggested decomposition process in these oxide glasses. This nanoporosity has been confirmed recently by Richter *et al.* using small angle X-ray scattering,[37] revealing the formation of elongated nanopores. In 2014 [38] and 2018,[19,39,40] the self-organization process was suggested to be seeded by nanoscale inhomogeneities such as voids and a nanocavitation mechanism was proposed. In 2013, the formation of SiO_{2-x} nanocrystals within nanoplanes was reported,[41] which could be in agreement with oxide decomposition.[42] In a second publication, the same group did not report nanocrystals but instead revealed that damaged nanoplanes contain randomly dispersed nanopores with a bimodal size distribution.[43] However, it appears that the use of HF etching degrades the quality of the observations and there are still no reliable nanoscale observations of NGs.

In this paper, we analyze NGs and related nanopore formation inside silica glass using transmission electron microscopy imaging and atomic force microscopy (AFM) techniques. We explored various geometries to probe not only the assembly of nanolayers but also their internal nanostructures. Through high-resolution imaging, we observed a nanoscale assembly of oblate nanopores constituting the nanolayers. Their long axis is found perpendicular to the light polarization while the average periodicity is decreased with the pulse number. These results are then discussed within the framework of a plasma-mediated nanocavitation process and generalized to a wide range of optical glasses.

Experimental details

The imprinting of NGs in the bulk of fused silica (Suprasil type-I) was performed using a 1030 nm mode locked Yb^{3+} doped fiber laser system (Satsuma, Amplitude Systemes Ltd.). The emitting laser delivered pulses of 250 fs at 100 kHz. Additionally, an aspheric lens (numerical aperture NA = 0.6) was used to focus the laser beam below the sample surface. Due to the minimization of spherical aberration, a laser track was inscribed at a depth of 200 μm. When the laser is translating along *X* and the linear polarization lying along *x*, we define it as "*Xx* writing" (or "*Xy* writing" for a polarization along the *y* axis). Then by moving the sample along the +*X*-axis with a scanning speed of 100 μm s^{-1}, a series of adjacent lines being 5 mm long were inscribed. The pulse energy was fixed to either 0.5 μJ or 1 μJ, that is, above the NG formation threshold.[44] Under these conditions, a strong form birefringence appears due to the presence of porous NGs. For completeness, the optical retardance was measured using a quarter waveplate technique and found to be on the order of 200 nm.[45]

To observe the NG nanostructure, each irradiated sample was cleaved using a diamond pen as shown in Fig. 1. Following this, the laser track cross-sections were analyzed by field emission gun scanning electron microscopy (FEG-SEM ZEISS SUPRA 55 VP) for studying the surface morphology. Furthermore, thin samples were prepared using a focus ion beam (FIB) instrument (Zeiss Neon 60, current 50 pA, accelerating voltage 30 kV) to extract slices of NG regions embedded in fused silica glass with a thickness under 50 nm. Here, we used a commercial TOPCON 002B electron microscope (200 kV with a resolution of 0.18 nm). Note that various geometries were employed as sketched in Fig. 1 *i.e.*, through transversal (*XY* plane) and longitudinal (*XZ* plane) views.

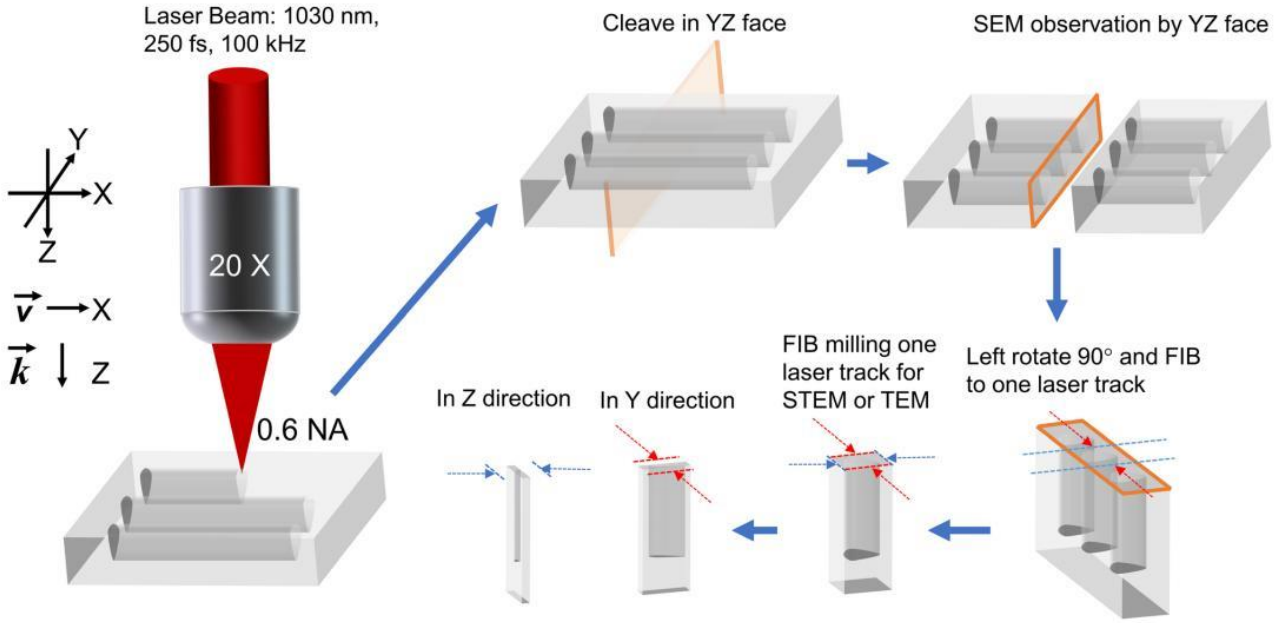

Fig. 1 Scheme of FLDW and sample cleaving orientation for subsequent electronic microscopy (SEM, STEM, and TEM) analyses.

Finally, scanning transmission electron microscopy (STEM) and high-resolution transmission electron microscopy (HR-TEM) were employed to analyze the internal nanostructures of NGs.

Results

After the FLDW step and before being sliced using the FIB technique, the cleaved samples were observed under a SEM. The resulting cross-sections are shown in Fig. 2 for both *Xx* and *Xy* writing configurations. The darker regions correspond to the nanopores (see Fig. 2(a)) and nanoplanes (see Fig. 2(b)). The gray and white parts correspond to the materials between nanoplanes and nanopores.[46] Fig. 2(a) corresponds to the inside of the nanoplanes that reveal a nanoporous material due to ultrafast oxide decomposition.[46] In addition, Fig. 2(b) exhibits the sub-wavelength periodicity of the nanoplanes (around $\lambda/2n$ with λ and n being the laser wavelength and the glass refractive index, respectively) along the laser track cross-section and oriented perpendicularly to the laser polarization orientation *Y*. The non-uniformity of the nanoplanes visible from Fig. 2(b) is detailed and discussed in the later analysis of TEM and STEM imaging.

To observe the NGs in the transverse view (*i.e.*, in the *XY* plane as indicated by the blue rectangles from Fig. 2), the samples were prepared using a FIB milling process as already described. The resulting morphology of the nanoplanes within the *XY* plane is shown in Fig. 3, with Fig. 3(a) serving as a guide for the reader. In these TEM micrographs, the bright regions are attributed to the fluctuations of the effective electronic thickness of laser-irradiated SiO_2. The bright lines are thinner regions and likely correspond to the nanoplanes and nanopores. The dark regions correspond to the material situated between nanoplanes. From **E** or **v** (*X*) direction, the nanoplanes exhibit an average period, labeled Λ, of 297 ± 14 nm (Fig. 3(c) and (d)). We observe that the nanoplanes are not perfectly aligned perpendicular to **v** or **E** and can present some tilt or wavy appearance. The white porous parts of the nanolayers appear to be several hundred nm long, discontinuous but connected by lamellas of weaker density along *Y* (perpendicularly to the polarization direction). In Fig. 3(e)–(g), the nanostructures are displayed with higher magnification. Nanopores clearly appear as the brightest part of the nanoplanes. They are aligned along each other but quite distributed in size and merging into some whiter matter lamellae like in Fig. 3(e). Based on TEM micrographs of Fig. 3(e)–(g), the nanoporous layer thickness exhibits variable values, averaged to 18 ± 12 nm. The size variation of the nanopores along the *Y* direction ranges from 36 to 56 nm. These observations are consistent with SEM observations in Fig. 2(a), and in agreement with the literature.[46]

In the aforementioned representation where **E** is parallel to **v**, the nanoplanes are thus aligned along **k**(*Z*) and *Y* directions in SEM or TEM observations. Now by selecting an additional slice by FIB milling identified by the red selection in Fig. 2(a), observations in the longitudinal view (*i.e.*, *XZ* plane) become possible. Corresponding micrographs are provided in Fig. 4(b)–(d). Fig. 4(a) serves as a guide for the reader. Along the *X* direction, which corresponds to either the **E** or **v** direction, the measured period Λ and thickness of the observed nanoplanes are around 296 ± 20 nm and 14 ± 2 nm, respectively. The observed nanoplanes showed discontinuities such as partially formed in the **k**(*Z*) direction and it appears pseudo-periodic as first observed in Fig. 2(b). Additionally, from Fig. 4(d) one can observe that both the shape and contrast of the nanoplanes are not homogeneous. The brighter parts correspond to more nanopores superimposed, or larger nanopores, and this is schematically visualized in Fig. 4(a). These overall nanoscale observations align with SEM images in Fig. 2(b), which contain nanopores and with a periodicity along *Z*. This process was attributed to an exciton–polariton-mediated light-organization

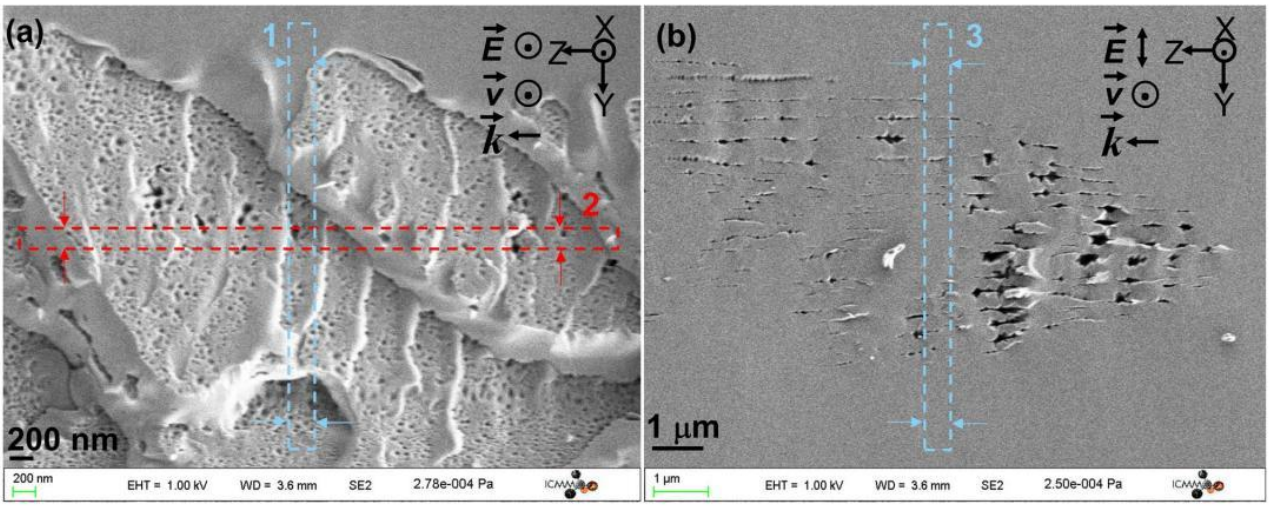

Fig. 2 SEM micrographs of (a) nanopores (*Xx* writing) and (b) nanoplanes (*Xy* writing). The red arrows in the *Y* direction and blue ones in the *Z* direction are the directions of FIB milling for TEM sample preparation (typical slice thicknesses are smaller than 50 nm). The numbers 1–3 correspond to the 3 slices extracted by FIB and subsequently observed.

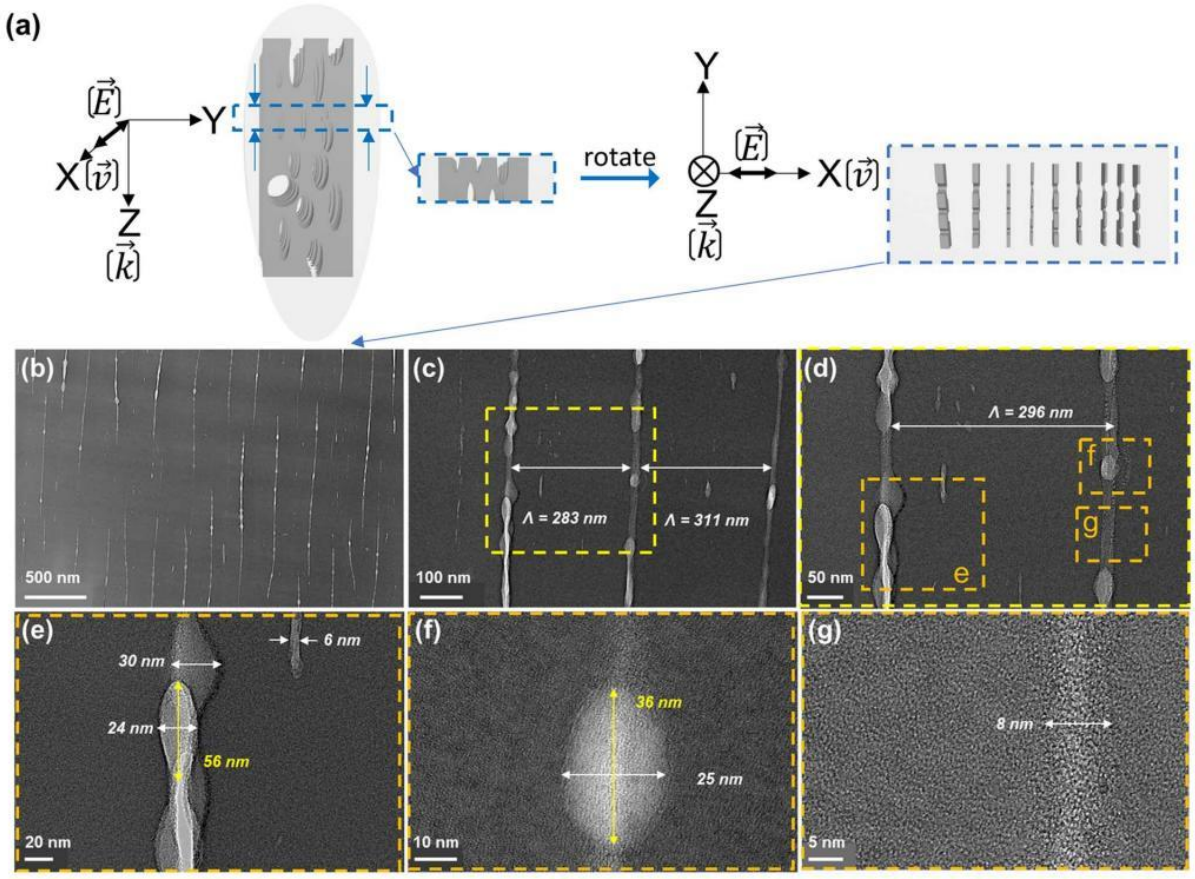

Fig. 3 (a) Geometry of the *XY* slice extracted by the FIB milling process. (b–g) TEM micrographs from Fig. 2(a) in blue arrows and *XY* plane observation with different size magnifications. The writing configuration is *Xx*.

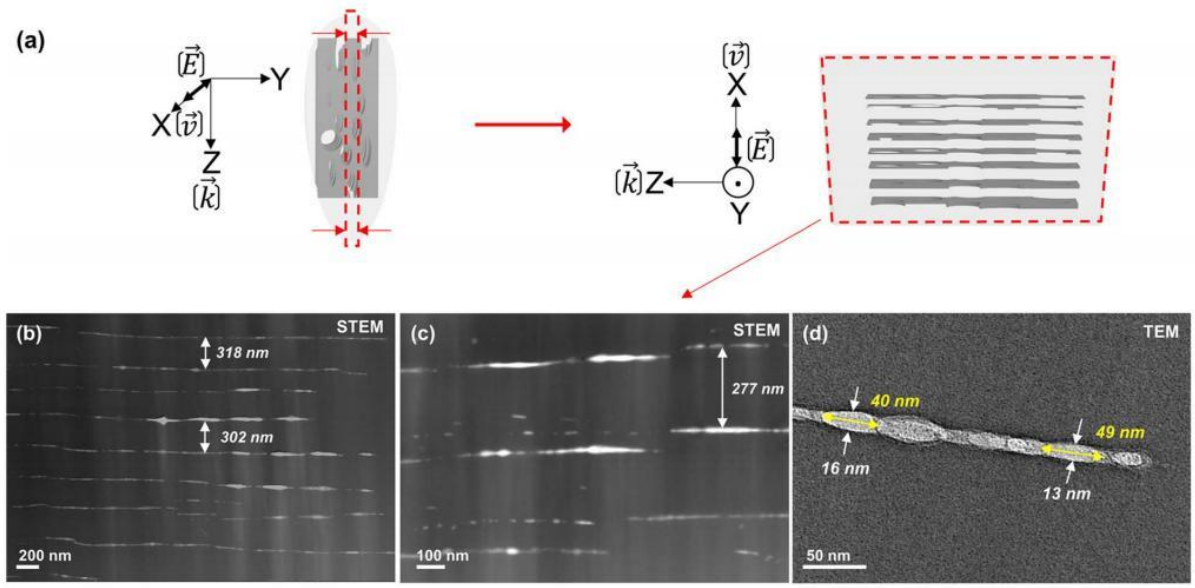

Fig. 4 (a) Schematic of the FIB milling process for extracting the *XZ* slice (see red arrows in Fig. 2(a)). (b and c) STEM and (d) TEM micrographs. The writing configuration is *Xx*.

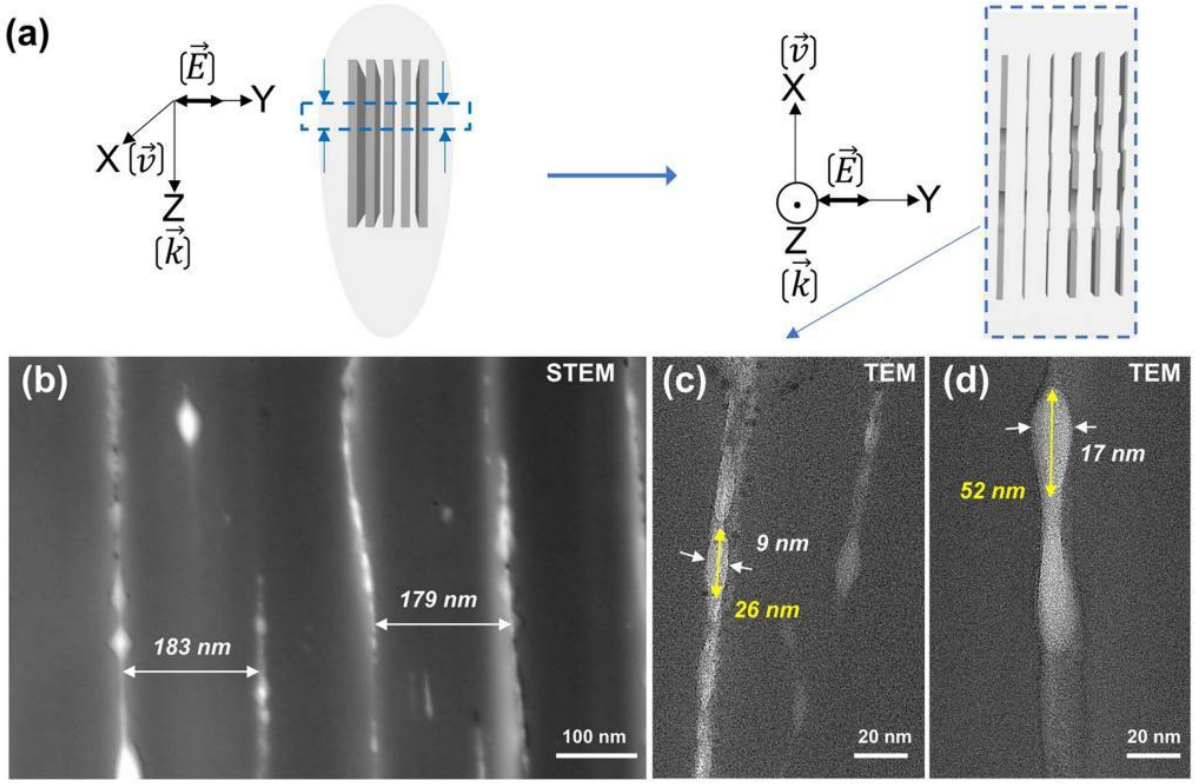

Fig. 5 (a) The schematic of the FIB milling process. (b) STEM and (c and d) TEM micrographs from Fig. 2(b) (nanoplanes) in blue arrows in *XY* plane observation. The writing configuration is *Xy*.

effect in glass similar to the exciton pattern formation effect observed in cold exciton gases.[34]

Now, changing again our point of view, the results in Fig. 5 represent the *XY* face by taking a sample slice along the blue arrows as sketched in Fig. 2(b). In this configuration, the nanoplanes are aligned along **k**(*Z*) and **v**(*X*) directions. In the **E**(*Y*) direction, the period and thickness of the nanoplanes are respectively 181 ± 4 nm and 13 ± 4 nm. The assembly of sub-wavelength nanolayers has a shorter period than for *Xx* configuration in agreement with the literature.[47] However, the dimensions of the nanopores are similar to the one observed for the *Xx* configuration. The nanoplanes exhibit a wavy shape along the **v**(*X*) direction as observed in Fig. 3 and 4.

To investigate NG formation in a multipulse regime, we investigated by SEM the step-by-step nanoscale modifications when pulse density is progressively varied from 1 to 2 × 10^5 pulses per μm. The resulting SEM micrographs are provided in Fig. 6 and highlight the transformation morphology occurring for a perpendicular writing configuration (*i.e.*, *Xy*). The pulse energy was fixed to 0.5 μJ. At a pulse density of 1 pulse per μm, only isotropic index changes are detected by optical microscopy and SEM reveals no specific nanostructure other than a slight contrast related to volume change. At lower pulse densities, between 2 and 10 pulses per μm, we detect a topographic contrast and interestingly some kind of nanopores that evolve into elongated ones (1–2 μm in length and 180–220 nm wide) as pulse density increases. The upper part of Fig. 6 shows atomic force microscopy (AFM) images obtained using intermittent contact mode. Besides the conventional surface topography image (left inset), the cantilever is driven close to a system resonance, to give reasonable amplitude for the oscillation and also to provide phase information, as shown in the right inset of Fig. 6. In particular the phase signal is sensitive to properties of the tip–sample interaction, and may reveal "mechanical information" about the surface such as elasticity, viscosity or adhesion. The observations reveal that the single elongated nanolayer seen below on the SEM micrograph is effectively made of an assembly of nanopores.

At higher pulse densities, these nanopores merge, thus creating some apparently long and thin (typ. 20–30 nm) nanolayers in agreement with the above HR-TEM results. Finally, as the number of nanolayers increases, their average spacing Λ decreases for pulse densities higher than 100 pulses per μm and reaching up to 2 × 10^5 pulses per μm in agreement with the literature.[48] Such quantitative evolution measured in SiO_2 is shown in the inset of Fig. 7.

Discussion

From the above HR-TEM and STEM imaging analysis, we can probe the 3D nanostructure of fs-imprinted NGs in silica. We can observe an array of oblate nanopores, which have a long axis oriented both along **k** and perpendicularly to **E**. The thickness of the nanolayers ranges from 6 to 30 nm and their extension perpendicularly to the laser polarization could reach a few μm or more. As shown in Fig. 6, under a multipulse regime, these

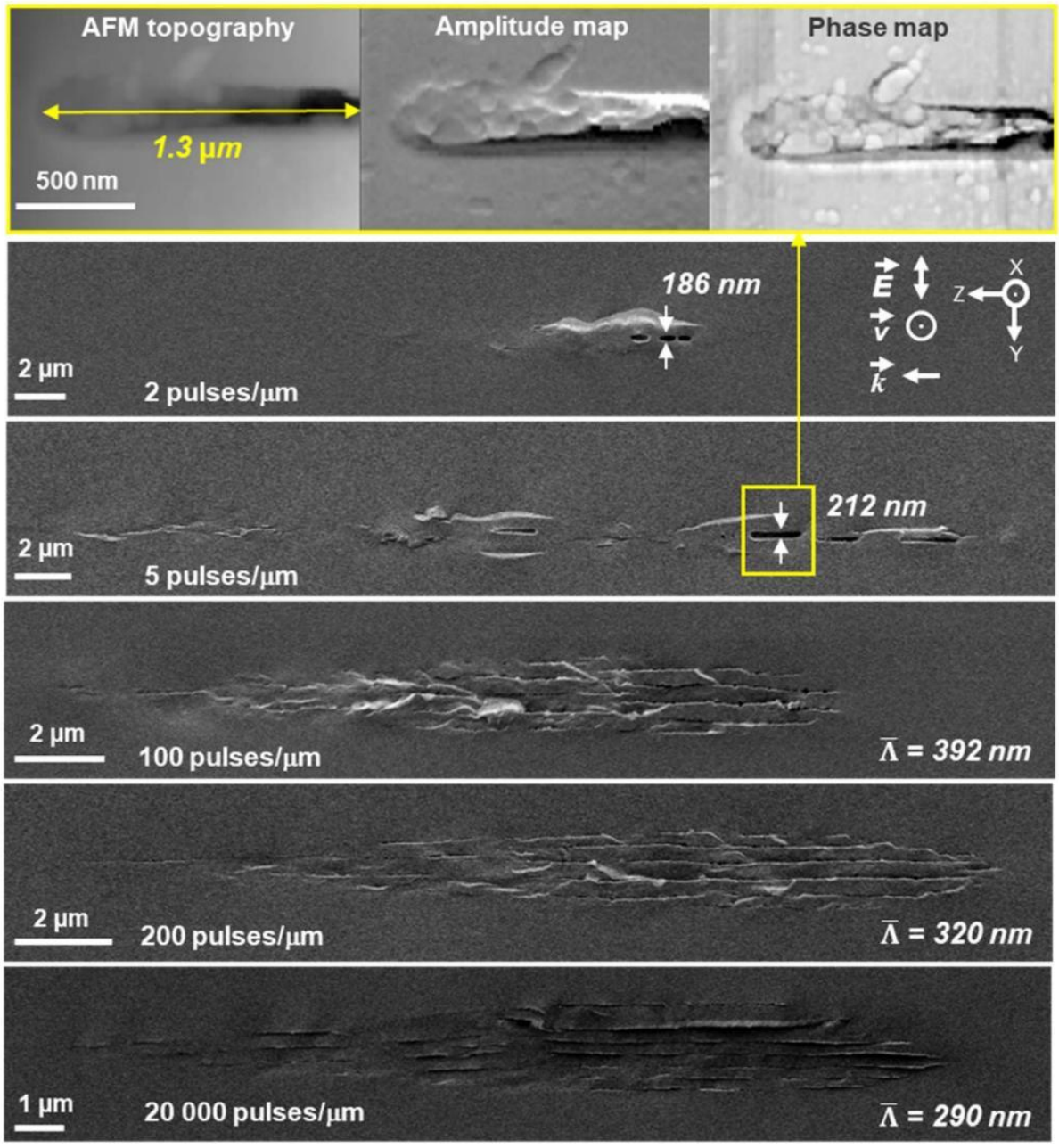

Fig. 6 AFM intermittent contact mode and SEM secondary electron images of laser track cross-section according to pulse density expressed in pulses per µm. The laser parameters were: 0.5 µJ per pulse, 1030 nm, 300 fs, 0.6 NA, 100 kHz and *Xy* configuration.

nanolayers are made of oblate nanopores that obviously "self-align" along each other to create these nanoplanes over quite long distances, as observed in the literature over the last two decades.[28] We can also observe a subwavelength ordering resulting in an average periodicity, perpendicular to **E**, on the order of 290–390 nm depending on the writing configuration.

Based on these results and on the reported mechanisms of the NG formation in the overall literature, we suggest that NGs are imprinted through a plasma-mediated nanocavitation process with a spatial ordering due to scattered wave interference,[38,49] which is described below.

The first step would be that some inhomogeneities of dielectric constant seed the process. These inhomogeneities (or seeds) could either be already present in the pristine glass or be photo-induced by the first pulse(s). Following these first instants, a spherical nanoplasma forms, stimulated by plasma density or temperature and evolves into an oblate-shaped nanoplasma over several pulses. This plasma-mediated process has been suggested in the literature. For example, Taylor R. *et al.*[50] suggested in 2008 that the presence of defects or color centers might seed the plasma, creating locally and easily ionized "nanospots" creating high plasma density. In the

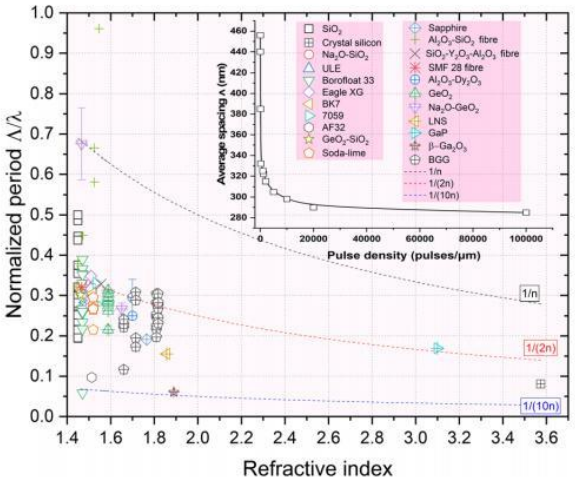

Fig. 7 Normalized period Λ/λ of the overall investigated glasses in the literature including commercial glasses *vs.* refractive index, *n*, measured at 550 nm. The laser wavelength λ used in the various experiments was typically between 515 and 1030 nm. Data were extracted from the following ref. 17, 20, 23–26, 45, 48 and 54–67.

model developed by Bhardwaj *et al.*,[51] the period Λ of nanogratings was assumed to remain between λ/n and $\lambda/2n$ and a period initially to be independent of pulse energy. However, the period was shown to decrease continuously with the number of laser pulses[52,53] but also when playing with the chemical composition such as doped SiO_2 (ref. 26) or in multicomponent glasses.[23,24] This is clearly illustrated in Fig. 7 where we summarized the normalized period Λ/λ *vs.* refractive index reported in the overall literature including a wide range of commercial glasses.

In 2014 Buschlinger R. *et al.*[38] conducted finite-difference time-domain (FDTD) modeling of plasma spatial structuration to investigate the periodicity of the NGs. These originated from the randomly distributed nanometer-size inhomogeneity that seeded the plasma structure. Due to the interference between scattered and incident light, the plasma owns a spatial structuration and grows against the direction of the light polarization. In 2016 A. Rudenko *et al.*[68] developed a numerical model to explain the formation of periodic volume NGs from random inhomogeneities with varying concentration and laser parameters. The contribution of an interplay of the physical processes (*e.g.*, the interference between the incident and the scattered waves, multiple scatterings, local field enhancement, and accumulation processes driven by multiphoton ionization) reinforced in the formation of NGs. Importantly, the period of NGs was found to scale down with growing pulse number, which in turn relies on scattering originating from nanoscale inhomogeneities. Following the above views, we suggest that nanogratings are not self-organized or self-assembled through diffusion-reaction mechanisms like Turing structures but rather "forced aligned" by the light pattern itself. In addition, the authors suggested the presence of some kinds of nanovoids, 0.6 nm average diameter, that are initiating the process. However, what seeds the process is not yet fully elucidated. It could be point defects (like self-trapped excitons (STEs) or self-trapped holes (STHs)), where the valence band possesses high energy and can easily be excited, some voids generated by the first pulse or even some glass-free volume that is already "available" in the pristine glass. Moreover, it exhibits a quite regular structure in the short range, with some *n*-membered rings creating well-known porosity at the sub-nm scale.[69] This is even reinforced in nanoporous sol–gel silica where the pulse number needed to imprint NGs was observed to be smaller,[70] when increasing the glass free volume.

From Fig. 3(c) and 4(c), we can observe some short (typ. <50 nm) but always oblate nanopores (with a long axis along **k** and perpendicular to **E**) with a thickness much smaller than 5 nm. They appear to be dispersedly distributed, but sometimes start to align along each other. When increasing the number of pulses, we can expect having more seeds (*e.g.*, some first nanopores or some STH) generated by the first pulses. This, in turn, leads to additional scattering centers resulting in a smaller periodicity based on the scattered wave interference model suggested by A. Rudenko *et al.*[68] and in agreement with F. Zimmermann *et al.*[48] who reported a decrease in NG period. It's worth mentioning that there are many "small size nanopores" between the long and well-arranged ones revealing the emergence, and growth, of new nanolayers like in Fig. 3(c) and 4(c). These are some kinds of "seeds" that will grow and merge (see Fig. 6) with neighboring nanopores to become a new porous nanolayer when increasing the number of pulses. According to the suggested "memory effects" involved in the mechanism of nonlinear ionization, new inhomogeneities are generated from pulse to pulse resulting in additional multiple scattering thus organizing the plasma distribution. It assumes that the pulse density is proportional to the concentration of the inhomogeneity.[68] As the pulse density increases, new plasma nanoplanes are generated "here and there" between the pre-existing ones following the light pattern. The imprinted nanolayers are initially made of elongated nanopores that grow from pulse-to-pulse and merge resulting in new nanolayers. Finally, from pulse to pulse, this will lead to a reduction of the average spacing $\bar{\Lambda}$ of the nanogratings as observed in the inset of Fig. 7.

The second step would be plasma formation and the local field enhancement resulting in ellipsoid (oblate) nanoplasma hot spot (high electron plasma density or energy) formation. Indeed, and even for a single pulse, the disordered spherical nanoplasma would evolve into an ellipsoidal shape and become oblate perpendicularly to the laser linear polarization. This occurs because the laser electric field triggers an asymmetric growth of the nanoplasma.[50] In contrast, for a circular polarization the nanoplasma hot spots should remain symmetric, resulting in spherical nanopores as has been observed in the type X regime.[13] Then in a multipulse view, there is an evolution of the oblate nanoplasmas into nanoplanes as shown in "post-mortem" experiments in Fig. 6.[53] The lengths of the oblate voids, whose direction is perpendicular to **E**, increase as the pulse number increases in agreement also with observations made in the type X regime.[13] From Fig. 4 one can also notice that such step by step nanopore growth also creates a longitudinal

component since nanopores are also "elongated" along the laser beam direction (**k**) and self-aligned to form nanoplanes.

The third step would be the energy transfer between electrons and phonons resulting in localized heat distribution at the nanoscale. Indeed, the modification of transparent glasses with wide bandgap dielectrics is induced rapidly by fs laser pulses through a multiphoton ionization (MPI) within a few femtoseconds. The electron plasma produced by MPI heats the media by electron–lattice coupling. Here we first assume no heat accumulation either considering a single pulse or multiple pulses in this process. The low heat capacity of electrons allows them to be easily heated to extremely high temperatures, but the glass matrix (the lattice) initially remains "cold" due to the relatively long electron–phonon relaxation time, typically 10 ps in SiO_2. After this time, the lattice will finally heat up, by a few 1000s of °C but this is a local effect. Indeed, after the free electron plasma energy is transferred to the lattice, the spatial distribution of the temperature is quite the same as the one of the plasmas because the timescale (<1 nanosecond) is too short to have some significant heat diffusion (on the order of the μs). In that sense, this is a plasma-mediated process, and the temperature distribution is the image of plasma 3D nanostructuration or the plasma "map".[46]

The fourth step would be the strain creation due to the temperature difference, between the nanoplasma hot spot and the background, resulting in a local thermal expansion. While the heat diffuses inside the material, the silicon–oxygen bonds would elongate and the glass specific volume expand within a time scale shorter than the characteristic acoustic relaxation time (typ. 500 ps in silica glass)[25] thus creating a moderate shock wave. So at a short time scale, there exists a localized nanostrain, which distributes ellipsoidally as a mirror image of the temperature map. This in turn will initiate the nanocavitation process at these specific locations. Indeed, a decrease of the local pressure would be created due to the formation of a rarefaction zone behind the "shock wave". Once this "negative pressure" difference develops between the "pore nuclei" and surrounding materials,[46] nanopores are imprinted at the image of the plasma ellipsoidal nanostructuration where the nanocavitation process starts. Finally, the formation of nanopores was observed in most oxide glasses[20,24,25,63,66,71–73] thus revealing that the glass oxide decomposition process occurred in all these compositions, highlighting in such a way that this is a general mechanism.

In this process it seems that nanopores may not have the chance to grow from a spherical shape but rather ellipsoid like the nanoplasma distribution itself for a linear polarization whereas a circular polarization would induce substantially spherical nanopores and thus no/low birefringence.[74] Following this view, type X is in fact the early birth of nanograting formation mostly observed for a low number of pulses and low energy. These type X modifications refer to oblate (for linear or elliptical polarization) nanopores with low birefringence and ultralow optical losses.[13] In this mechanism, the small nanopore diameters that are quite randomly arranged result in a decrease of the Rayleigh scattering and thus low optical losses offering exciting prospects for applications. For example, these type X modifications were exploited for achieving a 5D optical storage with high data capacity and long lifetime in fused silica[75] or to imprint ultralow loss 3D geometric phase optics.[13]

Conclusions

We investigated some nanoscale aspects of the formation of self-assembled porous nanogratings in oxide glasses. Oblate nanopores populate some array of non-continuous nanoplanes, which grow perpendicularly to the laser polarization direction and along the laser propagation direction. Some tiny elongated nanopores were also found between the long and fully-grown nanoplanes. These nanopores will grow and merge in a multipulse regime, resulting in a pulse-to-pulse decrease of the average periodicity much below $\lambda/2n$ as reviewed in this paper. The plasma-mediated nanocavitation model discussed the formation of these "light forced-organized" (rather than self-organized) sub-wavelength NGs in a multipulse view. Our tentative interpretation supported by HR-TEM and STEM investigations proposes an overall framework for NG formation. This mechanism is useful to guide future experiments to explore the interaction between laser and optical materials, along with enabling one to better control NG formation and its generalization in any kind of optical glasses.

Author contributions

Conceptualization, M. C. and M. L.; funding acquisition, B. P., M. C. and M. L.; investigation, Q. X., N. S.; methodology, Q. X., M. C. and M. L.; project administration, M. L.; resources, M. L.; supervision, M. L.; validation, Q. X.; visualization, Q. X. and M. C.; writing—original draft, Q. X.; writing—review & editing, Q. X., N. S., M. C., B. P. and M. L. All authors have read and agreed to the published version of the manuscript.

Conflicts of interest

There are no conflicts to declare.

Acknowledgements

This research was funded by Agence Nationale de la Recherche (ANR), FLAG-IR project, award number ANR-18-CE08-0004-01; and REFRACTEMP project, award number ANR-22-CE08-0001-01. Qiong Xie acknowledges the China Scholarship Council (CSC) for the funding of her PhD fellowship, no. 202007040018. We acknowledge the support of the SMIS beamline from synchrotron SOLEIL.

References

1 K. Davis, K. Miura, N. Sugimoto and K. Hirao, *Opt. Lett.*, 1996, **21**, 1729–1731.
2 Y. Shimotsuma, P. G. Kazansky, J. R. Qiu and K. Hirao, *Phys. Rev. Lett.*, 2003, **91**, 247405.

3 J. Lu, Y. Dai, Q. Li, Y. Zhang, C. Wang, F. Pang, T. Wang and X. Zeng, *Nanoscale*, 2019, **11**, 908–914.
4 C. Schaffer, A. Brodeur, N. Nishimura and E. Mazur, *Proc. SPIE*, 1999, **3616**, 143.
5 L. He, K. Sheehy and W. Culbertson, *Curr. Opin. Ophthalmol.*, 2011, **22**, 43–52.
6 E. N. Glezer, M. Milosavljevic, L. Huang, R. J. Finlay, T. H. Her, J. P. Callan and E. Mazur, *Opt. Lett.*, 1996, **21**, 2023–2025.
7 A. Podlipensky, A. Abdolvand, G. Seifert and H. Graener, *Appl. Phys. A: Mater. Sci. Process.*, 2005, **80**, 1647–1652.
8 M. Watanabe, H. Sun, S. Juodkazis, T. Takahashi, S. Matsuo, Y. Suzuki, J. Nishii and H. Misawa, *Jpn. J. Appl. Phys.*, 1998, **37**, L1527–L1530.
9 C. Monat, P. Domachuk and B. Eggleton, *Nat. Photonics*, 2007, **1**, 106–114.
10 Y. Bellouard, A. Said, M. Dugan and P. Bado, *Opt. Express*, 2004, **12**, 2120–2129.
11 Y. Wang, M. Cavillon, J. Ballato, T. Hawkins, T. Elsmann, M. Rothhardt, R. Desmarchelier, G. Laffont, B. Poumellec and M. Lancry, *Adv. Opt. Mater.*, 2022, **10**, 2200379.
12 S. J. Mihailov, *Sensors*, 2012, **12**, 1898–1918.
13 M. Sakakura, Y. Lei, L. Wang, Y. H. Yu and P. G. Kazansky, *Light Sci. Appl.*, 2020, **9**, 15.
14 K. M. Davis, K. Miura, N. Sugimoto and K. Hirao, *Opt. Lett.*, 1996, **21**, 1729–1731.
15 R. Nielsen, A. Boltasseva, A. Kristensen, S. Bozhevolnyi, V. Volkov, I. Fernandez Cuesta and A. Klukowska, presented in part at *Advanced Fabrication Technologies for Micro/Nano Optics and Photonics*, San Jose, California, USA, 2008.
16 S. Richter, M. Heinrich, S. Döring, A. Tünnermann, S. Nolte and U. Peschel, *J. Laser Appl.*, 2012, **24**, 042008.
17 M. Lancry, J. Canning, K. Cook, M. Heili, D. R. Neuville and B. Poumellec, *Opt. Mater. Express*, 2016, **6**, 321–330.
18 Y. Shimotsuma, S. Kubota, A. Murata, T. Kurita, M. Sakakura, K. Miura, M. Lancry and B. Poumellec, *J. Am. Ceram. Soc.*, 2017, **100**, 3912–3919.
19 A. Rudenko, J.-P. Colombier, S. Höhm, A. Rosenfeld, J. Krüger, J. Bonse and T. E. Itina, *Sci. Rep.*, 2017, **7**, 12306.
20 Y. Wang, S. Wei, M. R. Cicconi, Y. Tsuji, M. Shimizu, Y. Shimotsuma, K. Miura, G. D. Peng, D. R. Neuville, B. Poumellec and M. Lancry, *J. Am. Ceram. Soc.*, 2020, **103**, 4286–4294.
21 Y. Shimotsuma, K. Hirao, J. R. Qiu and K. Miura, *J. Non-Cryst. Solids*, 2006, **352**, 646–656.
22 S. Richter, D. Möncke, F. Zimmermann, E. I. Kamitsos, L. Wondraczek, A. Tünnermann and S. Nolte, *Opt. Mater. Express*, 2015, **5**, 1834–1850.
23 S. S. Fedotov, R. Drevinskas, S. V. Lotarev, A. S. Lipatiev, M. Beresna, A. Čerkauskaitė, V. N. Sigaev and P. G. Kazansky, *Appl. Phys. Lett.*, 2016, **108**, 071905.
24 Q. Xie, M. Cavillon, D. Pugliese, D. Janner, B. Poumellec and M. Lancry, *Nanomaterials*, 2022, **12**, 2986.
25 Q. Xie, M. Cavillon, B. Poumellec, D. Pugliese, D. Janner and M. Lancry, *Opt. Mater.*, 2022, **130**, 112576.
26 S. Richter, C. Miese, S. Döring, F. Zimmermann, M. J. Withford, A. Tünnermann and S. Nolte, *Opt. Mater. Express*, 2013, **3**, 1161–1166.
27 Y. Liao, Y. Shen, L. Qiao, D. Chen, Y. Cheng, K. Sugioka and K. Midorikawa, *Opt. Lett.*, 2013, **38**, 187–189.
28 Y. Shimotsuma, P. G. Kazansky, J. Qiu and K. Hirao, *Phys. Rev. Lett.*, 2003, **91**, 247405.
29 Y. Shimotsuma, P. Kazansky, J. Qiu and K. Hirao, *Phys. Rev. Lett.*, 2003, **91**, 247405.
30 C. Hnatovsky, R. Taylor, P. Rajeev, E. Simova, V. Bhardwaj, D. Rayner and P. Corkum, *Appl. Phys. Lett.*, 2005, **87**, 014104.
31 C. Hnatovsky, R. Taylor, E. Simova, V. Bhardwaj, D. Rayner and P. Corkum, *Opt. Lett.*, 2005, **30**, 1867–1869.
32 P. Rajeev, M. Gertsvolf, C. Hnatovsky, E. Simova, R. Taylor, P. Corkum, D. Rayner and V. Bhardwaj, *J. Phys. B: At., Mol. Opt. Phys.*, 2007, **40**, S273.
33 P. G. Kazansky, E. Bricchi, Y. Shimotsuma and K. Hirao, presented in part at *Conference on Lasers and Electro-Optics/ Quantum Electronics and Laser Science Conference and Photonic Applications Systems Technologies*, Baltimore, Maryland, 2007.
34 M. Beresna, M. Gecevičius, P. G. Kazansky, T. Taylor and A. V. Kavokin, *Appl. Phys. Lett.*, 2012, **101**, 053120.
35 M. Lancry, B. Poumellec, J. Canning, K. Cook, J. Ä. Poulin and F. Brisset, *Laser Photon. Rev.*, 2013, **7**, 953–962.
36 T. Asai, Y. Shimotsuma, T. Kurita, A. Murata, S. Kubota, M. Sakakura, K. Miura, F. Brisset, B. Poumellec and M. Lancry, *J. Am. Ceram. Soc.*, 2015, **98**, 1471–1477.
37 S. Richter, A. Plech, M. Steinert, M. Heinrich, S. Döring, F. Zimmermann, U. Peschel, E. B. Kley, A. Tünnermann and S. Nolte, *Laser Photon. Rev.*, 2012, **6**, 787–792.
38 R. Buschlinger, S. Nolte and U. Peschel, *Phys. Rev. B: Condens. Matter Mater. Phys.*, 2014, **89**, 184306.
39 A. Rudenko, H. Ma, V. P. Veiko, J.-P. Colombier and T. E. Itina, *Appl. Phys. A: Mater. Sci. Process.*, 2017, **124**, 63.
40 A. Rudenko, J. P. Colombier and T. E. Itina, *Phys. Chem. Chem. Phys.*, 2018, **20**, 5887–5899.
41 V. Oliveira, S. P. Sharma, P. Herrero and R. Vilar, *Opt. Lett.*, 2013, **38**, 4950–4953.
42 C. M. Pépin, E. Block, R. Gaal, J. Nillon, C. Hoenninger, P. Gillet and Y. Bellouard, *arXiv*, 2018, preprint, arXiv:1806.10802, DOI: **10.48550/arXiv.1806.10802**.
43 S. P. Sharma, V. Oliveira, P. Herrero and R. Vilar, *J. Appl. Phys.*, 2014, **116**, 053106.
44 B. Poumellec, M. Lancry, A. Chahid-Erraji and P. G. Kazansky, *Opt. Mater. Express*, 2011, **1**, 766–782.
45 Y. Wang, S. Wei, M. Cavillon, B. Sapaly, B. Poumellec, G.-D. Peng, J. Canning and M. Lancry, *Appl. Sci.*, 2021, **11**, 600.
46 M. Lancry, B. Poumellec, J. Canning, K. Cook, J.-C. Poulin and F. Brisset, *Laser Photon. Rev.*, 2013, **7**, 953–962.
47 R. Buividas, M. Mikutis and S. Juodkazis, *Prog. Quant. Electron.*, 2014, **38**, 119–156.
48 F. Zimmermann, A. Plech, S. Richter, A. Tünnermann and S. Nolte, *Appl. Phys. Lett.*, 2014, **104**, 211107.
49 A. Rudenko, J. P. Colombier, T. E. Itina and R. Stoian, *Adv. Opt. Mater.*, 2021, **9**, 2100973.

50 R. Taylor, C. Hnatovsky and E. Simova, *Laser Photon. Rev.*, 2008, **2**, 26–46.
51 V. R. Bhardwaj, E. Simova, P. P. Rajeev, C. Hnatovsky, R. S. Taylor, D. M. Rayner and P. B. Corkum, *Phys. Rev. Lett.*, 2006, **96**, 057404.
52 F. Zimmermann, A. Plech, S. Richter, A. Tünnermann and S. Nolte, *Laser Photon. Rev.*, 2016, **10**, 327–334.
53 R. Desmarchelier, B. Poumellec, F. Brisset, S. Mazerat and M. Lancry, *World J. Nano Sci. Eng.*, 2015, **5**, 115–125.
54 S. E. Wei, Y. Wang, H. Yao, M. Cavillon, B. Poumellec, G. D. Peng and M. Lancry, *Sensors*, 2020, **20**, 762.
55 S. V. Lotarev, S. S. Fedotov, A. I. Kurina, A. S. Lipatiev and V. N. Sigaev, *Opt. Lett.*, 2019, **44**, 1564–1567.
56 M. Cavillon, M. Lancry, B. Poumellec, Y. Wang, J. Canning, K. Cook, T. Hawkins, P. Dragic and J. Ballato, *J. Phys.: Photonics*, 2019, **1**, 042001.
57 J. Wang, X. Liu, Y. Dai, Z. Wang and J. Qiu, *Opt. Express*, 2018, **26**, 12761–12768.
58 S. Lotarev, S. Fedotov, A. Lipatiev, M. Presnyakov, P. Kazansky and V. Sigaev, *J. Non-Cryst. Solids*, 2018, **479**, 49–54.
59 Y. Nakanishi, Y. Shimotsuma, M. Sakakura, M. Shimizu and K. Miura, presented in part at the *Laser-Based Micro- and Nanoprocessing XII*, San Francisco, California, United States, 2018.
60 P. Dragic, M. Cavillon and J. Ballato, *Int. J. Appl. Glass Sci.*, 2017, **9**, 421–427.
61 J. Cao, B. Poumellec, L. Mazerolles, F. Brisset, A.-L. Helbert, S. Surble, X. He and M. Lancry, *J. Am. Ceram. Soc.*, 2017, **100**, 115–124.
62 Y. Shimotsuma, T. Sei, M. Mori, M. Sakakura and K. Miura, *Appl. Phys. A: Mater. Sci. Process.*, 2016, **122**, 122.
63 S. Mori, K. Torataro, S. Yasuhiko, S. Masaaki and M. Kiyotaka, *J. Laser Micro/Nanoeng.*, 2016, **11**, 87–90.
64 M. Lancry, F. Zimmerman, R. Desmarchelier, J. Tian, F. Brisset, S. Nolte and B. Poumellec, *Appl. Phys. B: Lasers Opt.*, 2016, **122**, 66.
65 M. Mori, Y. Shimotsuma, T. Sei, M. Sakakura, K. Miura and H. Udono, *Phys. Status Solidi A*, 2015, **212**, 715–721.
66 T. Asai, Y. Shimotsuma, T. Kurita, A. Murata, S. Kubota, M. Sakakura, K. Miura, F. Brisset, B. Poumellec, M. Lancry and J. Ballato, *J. Am. Ceram. Soc.*, 2015, **98**, 1471–1477.
67 W. Dirk, G. Jens, B. Nelli and H.-S. Herbert, *Opt. Express*, 2008, **16**, 1517–1522.
68 A. Rudenko, J.-P. Colombier and T. E. Itina, *Phys. Rev. B*, 2016, **93**, 075427.
69 R. H. Doremus, *Glass Science*, Wiley, 1973.
70 A. Cerkauskaite, R. Drevinskas, A. O. Rybaltovskii and P. G. Kazansky, *Opt. Express*, 2017, **25**, 8011–8021.
71 H. Yao, Q. Xie, M. Cavillon, D. R. Neuville, D. Pugliese, D. Janner, Y. Dai, B. Poumellec and M. Lancry, *Opt. Express*, 2023, **31**, 15449–15460.
72 H. Yao, R. Zaiter, M. Cavillon, B. Sapaly, F. Calzavara, P. Delullier, T. Cardinal, Y. Dai, B. Poumellec and M. Lancry, *Ceram. Int.*, 2021, **47**, 34235–34241.
73 F. Zhang, H. Zhang, G. Dong and J. Qiu, *J. Opt. Soc. Am. B*, 2014, **31**, 860–864.
74 Y. Lei, G. Shayeganrad, H. Wang, M. Sakakura, Y. Yu, L. Wang, D. Kliukin, L. Skuja, Y. Svirko and P. G. Kazansky, *Light: Sci. Appl.*, 2023, **12**, 74.
75 H. Wang, Y. Lei, L. Wang, M. Sakakura, Y. Yu, G. Shayeganrad and P. G. Kazansky, *Laser Photon. Rev.*, 2022, **16**, 2100563.

II.6 CONCLUSION

This chapter provides insights on the effect of viscosity on the existence of NGs during FLDW, supported by experimental evidences and theoretical ones (Rayleigh-plesset (R-P) equation), applied to predict the NGs possessing window. The pressure and thermal confinement conditions are considered in this approach. The NGs domain is bound between two limits: i) a low temperature one, the viscosity at ~$10^{6.6}$ Pa·s, corresponding to a cavitation mechanism, ii) a high temperature one the viscosity value typically around ~$10^{3.0}$ Pa·s, for which the pores experience either growth or collapse, leading to a disappearance of the NG structure. There is a high correlation between the temperature interval from the viscosity curve and the NGs processing window landscape in different commercial glasses and a series of alumino-borosilicate glasses. The viscosity plays a key role in the formation of NGs window.

Secondly, the NGs window in the E_p-RR landscapes among 9 different oxide commercial glasses and in the pulse energy and pulse duration landscapes among a series of alumino-borosilicate glasses, shows narrow when the alkali and alkali earth elements / glass network formers (Si, Al or Ge element) ratio increase. And the B / Al ratio has effects on the NGs window in negative correlation. The doping of alkali and alkali earth elements in silicate glasses decrease the NGs window because the fast mobility during the laser processing, and is closely related to the glass viscosity.

Finally, the formation of the ''self-organized'' pores NGs in oxide glasses was investigated by SEM, HR-TEM and STEM to the intrinsic nanostructure. From the images, the oblate nanopores populate some array of non-continuous nanoplanes, which grow perpendicularly to the laser polarization direction and along the laser propagation direction. Some tiny elongated nanopores were also found between the long and fully-grown nanoplanes. These nanopores will grow and merge in a multipulse regime, resulting in a pulse-to-pulse decrease of the averaged periodicity much below λ/2n as reviewed. The plasma-mediated nanocavitation model discussed the formation of these "light forced-organized" (rather than self-organized) sub-wavelength NGs in a multipulse view.

Chapter III. STUDY OF THE ERASURE OF THE NANOGRATINGS BY THERMAL PROCESS

III.1 INTRODUCTION

The investigation of thermal stability for self-organized porous NGs imprinted by FLDW in transparent materials is useful for high temperature optical devices application, especially for the designers to predict their working conditions (upper temperature and time). Upon thermal annealing, the retardance (R) or linear birefringence is progressively erased, characteristic of NGs erasure.

In the first part of the chapter, we study the thermal stability of NGs in 8 commercial oxide glasses (Schott BK7, Borofloat 33 and AF32, Corning ULE, Eagle XG and 7059, Heraeus Suprasil CG and Marienfield Superior soda lime, as listed in the second chapter) by monitoring R induced by the NGs and upon isochronal thermal annealing experiments (time step = 30 min). The upper temperature of NGs erasure can be recorded during the evolution of the R as the temperature increase. From the observations gained by annealing experiments, we demonstrate that the collapse of nanopores created during the laser irradiation is also strongly related to the temperature dependence of the glass viscosity. An upper temperature limit to the NGs survival can be deduced based on the thermal process considered (annealing, laser irradiation process etc.). The time and temperature couple must be considered in the erasure of NGs since it is a kinetics problem, and a relationship between the two in a NGs erasure context is established.

In the second part, we exploit and adapt the VAREPA (variable reaction pathways) framework to predict the lifespan of NGs inscribed by FLDW inside 8 commercial oxide glasses. First, a model of NGs aging taking into account the evolution of nanopores as a function of temperature is considered using the Rayleigh-Plesset (R-P) equation. Second, we exploited the modeled thermal ageing data using the master curve approach. Finally, we rationalize the predictions in different commercial glasses, extending our work much beyond silica, and obtained theoretical results are then compared to experimental ones.

In the last part of this chapter, we develop a heat diffusion model combined with Rayleigh-Plesset equation to simulate the time-temperature evolution of nanopores along the laser heat cooling profile. And we define a criterion to determine the energy threshold that results in the collapse of the NGs processing window in the E_p-RR landscapes. Then we consider a multiple pulses approach to analyze the heat accumulation at steady state for various repetition rates. we simulate the maximum deposited energy that leads to the erasure of NGs along the laser cooling profile for a wide range of commercial optical glasses compared to available experimental data.

III.2 UPPER TEMPERATURE LIMIT FOR NANOGRATING SURVIVAL IN OXIDE GLASSES

Upper temperature limit to nanogratings survival in oxide glasses

QIONG XIE,[1] MAXIME CAVILLON,[1,*] BERTRAND POUMELLEC[1], AND MATTHIEU LANCRY[1]

[1]*Institut de Chimie Moléculaire et des Matériaux d'Orsay (ICMMO), Université Paris-Saclay, CNRS, Orsay 91405, France*
**maxime.cavillon@universite-paris-saclay.fr*

Abstract: The thermal stability of self-assembled porous nanogratings inscribed by infrared femtosecond (fs) laser in 5 commercial glasses (BK7, Sodalime, 7059, AF32, and Eagle XG) is monitored using step isochronal annealing experiments. Their erasure, ascertained by retardance measurements and attributed to the collapse of nanopores, is well predicted from the Rayleigh-Plesset equation. This finding is thus employed to theoretically predict the erasure of nanogratings in a context of any time-temperature process (e.g., thermal annealing, laser irradiation process). For example, in silica glass (Suprasil CG) and using a simplified form of the Rayleigh-Plesset equation, nanogratings with pores being 50 nm in size will erase within ~ 30 mins, ~ 1 µs, and ~ 30 ns at temperatures of ~ 1250 °C, 2675°C, and 3100 °C respectively. Such conclusions are expected to provide guidelines for imprinting nanogratings in oxide glasses, for instance in the choice of laser parameters, or to design appropriate thermal annealing protocols for temperature sensing.

1. Introduction

Self-assembled nanogratings (NGs), fabricated inside transparent materials such as glasses, have found interest in many fields of optics, including optical data storage, harsh environment temperature and pressure sensing, structural health monitoring, 3D space variant birefringent devices, optofluidics, optomechanics, or integrated optics [1–5]. These NGs, also labeled Type II regime in the literature, are typically made of pseudo-periodic porous nanolayers containing nanopores, or nanocavities. The latter can also be formed at low fluence and under few pulses, and are labeled Type X [6]. While other types of nanogratings exist, including crystal/glass phase-separated gratings [7–9], we focus our attention on porous NGs, and their use for high temperature (HT) applications.

A key asset for designers of HT NGs-based optical devices would be to anticipate the working conditions (maximum time and temperature) at which the devices can operate. This allows one to set an upper limit for the user, and to design protocols to erase the unstable parts of an evolving quantity (e.g., yielding to drift in optical sensors [10]). From this view, a convenient way to study the NGs evolution as a function of time / temperature is to monitor the retardance (R) amplitude, which is a characteristic signature of the NGs, due to their birefringent nature [11,12]. R corresponds to an optical phase shift between two polarization direction. Typically, as the temperature is progressively increased, R usually decreases, and the laser-written tracks fully erase (no contrast can be detected by optical microscopy). Following work from Ref. [13,14], we have recently outlined the relationship between the thermal stability of the NGs and the glass viscosity (η), using the Rayleigh-Plesset (R-P) equation [15].

In this work, we first provide compelling evidence to the aforementioned work, through the monitoring of femtosecond (fs) laser induced NGs erasure in 5 commercial glasses (Schott BK7 and AF32, Corning Eagle XG and 7059, and Marienfeld Superior Sodalime) upon isochronal thermal annealing experiments (time step = 30 mins), setting an upper temperature of NGs erasure in such conditions. This is completed by 3 commercial glasses from previous work (Corning ULE, Heraeus Suprasil CG, and Schott Borofloat 33). All 8

glasses are chosen since i) they are commercially available, spanning a large range of applications including optics, micro-optics, and substrate / display applications in visible or near-IR wavelength windows, ii) their compositions, and thermal / mechanical properties are provided, iii) they exhibit different proportion of network modifiers and formers, strongly affecting their temperature - viscosity curve, and iii) adequate conditions to form NGs have already been found in such glasses [16–18].

Secondly, we observe that, for some glasses, bubbles can be formed after NGs are erased. From the observations gained by annealing experiments, we demonstrate that the collapse of nanopores created during the laser irradiation is also strongly related to the temperature dependence of the glass viscosity. Since the thermal diffusion timescale of the irradiation process is much shorter than the annealing experiments (µs or less), a different upper temperature limit to the NG survival can be found. In fact, the erasure of NG is a kinetics problem, for which both time and temperature must be considered. This link is clearly established at the end of the article, providing a useful framework for Engineers to the design of high temperature operating devices involving NGs in oxide glasses.

2. Experimental details

The investigated glasses, along with their molar composition and laser parameters used to imprint NGs, are provided in Table 1. The additional three glass compositions already investigated in previous work (ULE, Suprasil CG, and Borofloat 33) are provided for sake of comparison with respect to the investigated glass. In all these glasses, NGs, inscribed by femtosecond laser (Satsuma, Amplitude, France) have been identified through both optical and electron microscopy techniques, and adequate references to these works are provided in caption of Table 1. Note that the laser parameter conditions to make NGs can significantly vary from one glass to another, this being a prerequisite to obtain NGs in all the investigated glasses. For completeness, the nanopore morphologies for all the glass samples investigated can be found in Figure 3 of Ref. [17]. From electron microscope imaging, the initial averaged pore size can be estimated. Additionally, in the same reference, the NGs formation window in an Energy – Repetition Rate (RR) landscape was investigated.

Table 1. Glass samples and irradiated conditions used in the study, along with viscosity parameters (fit)

Glass samples	Molar composition	Laser parameters [a,b]	Viscosity parameters (A; B; T_0)
BK7	69.13 SiO_2, 10.75 B_2O_3, 3.07 BaO, 10.40 Na_2O, 6.29 K_2O, 0.36 As_2O_3 others < 1	800 fs, 0.6 µJ, 1 µm/s, 25 kHz, 300 µm, 5x4000 µm²	(-2.475 ; 4677 ; 527.8)
Sodalime	72.6 SiO_2, 13 Na_2O, 8.8 CaO, 4.3 MgO, 0.6 Al_2O_3, 0.3 K_2O, 0.2 SO_3, 0.1 Fe_2O_3	800 fs, 0.2 to 0.45 µJ, 10 µm/s, 100 kHz, 500 µm, 10x4500 µm²	(-1.741 ; 4309 ; 537.7)
Borofloat 33	81 SiO_2, 2 Al_2O_3, 13 B_2O_3, 4 Na_2O/K_2O	250 fs, 2 µJ, 100 µm/s, 100 kHz, 200 µm, 100x100 µm²	(-1.681 ; 6578; 384.8)
7059	63 SiO_2, 8.5 Al_2O_3, 16 B_2O_3, 12.5 BaO	800 fs, 0.45 µJ, 1 µm/s, 50 kHz, 300 µm, 5×3500 µm²	(-19.81 ; 34510 ; -140)
AF32	66.43 SiO_2, 11.28 Al_2O_3, 10.73 B_2O_3, 5.30 CaO, 4.63 MgO, 1.36 BaO, others < 1	800 fs, 0.25 to 3 µJ, 50 µm/s, 50 kHz, 300 µm, 10x4500 µm²	(-4.062 ; 8876 ; 480.8)
Eagle XG	65.71 SiO_2, 11.10 Al_2O_3, 11.65 B_2O_3, 8.64 CaO, 2.28 MgO, others < 1	800 fs, 0.9 µJ, 10 µm/s, 100 kHz, 500 µm, 700x700 µm²	(-6.584 ; 13170 ; 319.4)
ULE	94.25 SiO_2, 5.75 TiO_2	250 fs, 2 µJ, 100 µm/s, 100 kHz, 200	(-21.47 ; 90920 ; -1365)

		µm, 100x100 µm²	
Suprasil CG	100 SiO_2	250 fs, 2 µJ, 100 µm/s, 100 kHz, 200 µm, 100x100 µm²	(-9.5 ; 34200 ; -127)

[a]Common laser parameters: wavelength (λ) = 1030 nm, numerical aperture (NA) = 0.6; other parameters provided are pulse duration (fs), pulse energy (E_p, µJ), writing speed (µm/s), repetition rate (RR, kHz), focusing depth (in air, µm), and size/shape of the irradiated regions (µm²).

[b]More information on each glass can be found in Refs. [16,17], and for Borofloat 33, ULE and Suprasil in Refs. [18].

Subsequently to the laser inscription, the NGs were annealed through isochronal annealing with a Δt = 30 min time step and the evolution of R was monitored, similarly as in Refs [12,19]. Typical temperature steps of 50 °C were chosen and reduced down to 25°C or 12°C when requested to accurately monitor the R decay over the temperature increase. For completeness, we note that in order for each data point to be independent to the other, the criterion from Ref. [20] as $(\Delta t \cdot k_0)^{-(\frac{\Delta T}{T_{max}})} \ll 1$must be fulfilled. In this criterion, k_0 is estimated to be comprised typically between between 5.10^5 to $5{\cdot}10^7$ s^{-1} for NGs erasure in silica [21], ΔT is the temperature step and T_{max} the maximum temperature achieved during the isochronal annealing. In our case, the criterion value is not fully met at high temperature i.e., the datapoint are not fully independent so we slightly underestimate the effective thermal stability at high temperatures. Nevertheless, the above annealing parameters were chosen since they enable to capture to progressive monitoring of R over temperature and time, as shown in previous works cited above, and this while considering all glasses investigated.

The global evolution of the R (t,T) can take various forms, discussed elsewhere [19], arising from contributions of stress relaxation, densification, bleaching of defects, and nanopore erasure. However, herein we concentrate our attention on the last portion of the R decay, corresponding to the erasure of the nanopores composing the NGs [15,22]. The decrease of the nanopore diameter as a function of annealing temperature has been investigated in both Suprasil CG and Infrasil glasses [15,23]. It shows that both the average pore diameter and the filling factor progressively decrease as a function of heat treatment. It must be specified here that the full erasure of nanopore is attributed to the decrease of the initial value of R towards zero, corresponding to a nanopore diameter decrease of 99%. This will be the criterion to consider NG full erasure. Additionally, the R values measured during annealing are normalized with respect to the as irradiated R value. One must bear in mind that R is not linearly dependent on the pore diameter, and a slight variation of the latter can drastically impact R. For instance, a decrease of a pore diameter from 30 nm to 20 nm leads to a decrease of 92% of R (estimated using expressions from Ref. [15]).

The R-P equation is then used to simulate the evolution of the nanopore diameter following the same time-temperature annealing conditions used experimentally. To compare the simulated data with the experimental ones, the R-P results are converted into a normalized retardance as well. The set of equations are clearly described in Ref. [15] for an interested reader. In short, the pore diameter directly impacts the refractive index of the porous nanolayers composing the NGs structure. This index modification induces a variation of the NG birefringence (B) value, which translates into a change in the retardance, through the relationship R = B·L, with L being the length of the birefringence object (e.g., the laser track). Finally, since the viscosity plays a key role here, we added in Table 1 the values of the coefficients used to calculate the glass viscosity (η) as a function of temperature from Vogel–Fulcher–Tammann (VFT) equation taking the form $\log(\eta) = A + B/(T-T_0)$, where A, B, T_0 are constants. The latter are given for each glass in Table 1. Note that these coefficients are given for a viscosity in Poise. Additionally, it must be stressed that these fits are performed based on data provided by the glass manufacturers, typically in the 10^3 to 10^{12} Pa.s range.

Consequently, significant deviation from experimental data can arise when expending these fits outside the aforementioned viscosity interval.

3. Results and discussion

3.1 Comparison between experimental and simulated erasure of nanogratings upon annealing

The experimental evolution of retardance as a function of isochronal annealing (time step Δt = 30 min.), are provided in Fig. 1a using the solid lines, for BK7, AF32, and Suprasil CG (from Ref. [18]) glass samples. They serve as examples of the typical trends observed. We compared the experimental values with simulated ones using the Rayleigh-Plesset (R-P) equation, replicating the experimental thermal treatment (time – temperature couple). Details on the simulation conditions, similar to the ones employed here, can be found in Ref. [15]. The simulated results are reported in Fig. 1a using the dashed lines. Furthermore, an initial pore diameter of must be chosen. Previous analysis performed by electron microscopy, in Ref. [17], enabled the calculation of an averaged pore size for the irradiated glass under same or nearly similar investigation conditions (see Table 1): BK7 (57 ± 14 nm); Sodalime (44 ± 2 nm and 59 ± 6 nm at 0.2 and 0.45 µJ, respectively); 7059 (54 ± 7 nm), AF32 (50 ± 2 nm at 0.25 µJ); Eagle XG (47 ± 4 nm at 0.3 µJ), SuprasilCG (30 ± 1 nm at 0.5 µJ and 2 µJ), ULE (48 ± 1 nm and 36 ± 2 nm at 0.4 and 2 µJ), Borofloat 33 (55 nm ± 0.5 nm at 1 µJ). These diameters were employed as initial pore diameters to perform the simulation (for Sodalime a value of 44 nm was selected). However, the effect of pore diameter remains rather limited. For example, in Suprasil CG and as shown in Ref. [15], going from 30 nm to 50 nm as initial pore size only shifts the erasure temperature by few tens of °C.

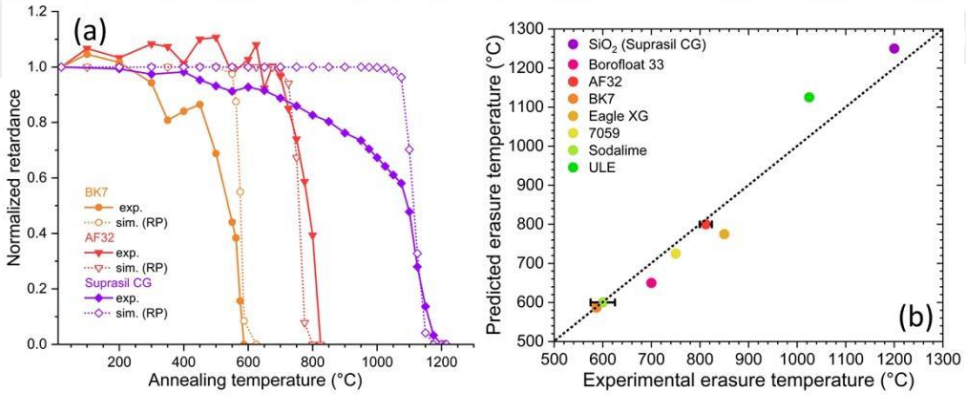

Fig. 1. a) Experimental (exp.) and simulated (sim.) evolution of retardance as a function of annealing temperature for BK7, AF32, and silica (Suprasil CG) glasses. b) Predicted erasure temperature of irradiated glasses using the Rayleigh-Plesset equation versus experimental values, for 8 glasses under isochronal annealing heat treatment (Δt = 30 min). Laser parameters, along with appropriate references, are provided in Table 1. The error bars for AF32 and Sodalime glasses correspond to varying erasure temperature due to multiple pulse energies investigated (Table 1).

Since in this work we are principally interested in the temperature limit at which the nanogratings fully erase, we compare the predicted (simulated) versus experimental results for all glass samples listed in Table 1. For this, the full erasure from the predicted results using the R-P equation set the vertical axis of Fig. 1b, while the experimental erasure temperature, for which the measured R value first drops to zero, sets the horizontal axis of Fig. 1b.

As one can observe, there is an excellent agreement between experimental and predicted erasure temperatures, as they do not differ by more than 50 °C for all glasses investigated. However, discrepancies can arise from several combined effects including i) temperature dependence viscosity fit uncertainties, ii) averaged initial pore size chosen (and not taking a real size distribution instead), iii) glass composition assumed constant while chemical migration can occur during irradiation process, hence significantly impacting the viscosity [24], iv) constant surface tension (σ) of the bubble used in the R-P equation (0.3 J/m^2), and v) assuming spherical pore shapes although they are ellipsoidal or oblate. Future improvements require, among others, high temperature viscosity measurements of the pristine glass samples, probing the chemical composition as a function of annealing conditions to take into account glass composition variation.

Nevertheless, this analysis validates the approach proposed in Ref. [15] to predict the erasure of the NGs in silicate glasses from the R-P equation. We must pinpoint that annealing experiments including two polarization conditions (parallel and perpendicular to the writing speed) were performed, and the erasure temperature was essentially the same for both configurations.

3.2 Formation of bubbles during annealing

During the annealing and in some glasses including BK7, Sodalime, and Eagle XG, we observe the formation of bubbles . They form once the temperature is above the NGs erasure temperature (defined from Fig. 1) These bubbles must be distinguished from the nanopores composing the NGs that yield to smooth birefringent lines as displayed in Fig. 2a with using polarized optical microscope illumination. The blue and yellow colors arise from the birefringent nature of the NGs when a full retardation waveplate is inserted at 45° from the crossed polarizers. Not shown here but the bubbles are preferentially formed for the highest energies investigated. For example, in Sodalime, the 0.2 µJ lines (with E ∥ to v), fully erased during annealing and as in agreement with the R-P simulation, but the 0.45 µJ (E ∥ and ⊥to v) revealed formation of many micrometer size bubbles at 725 °C, i.e., above the erasure temperature of ~600 °C (see Fig. 2b for an example, and caption of Fig. 2 for definition of E and v).

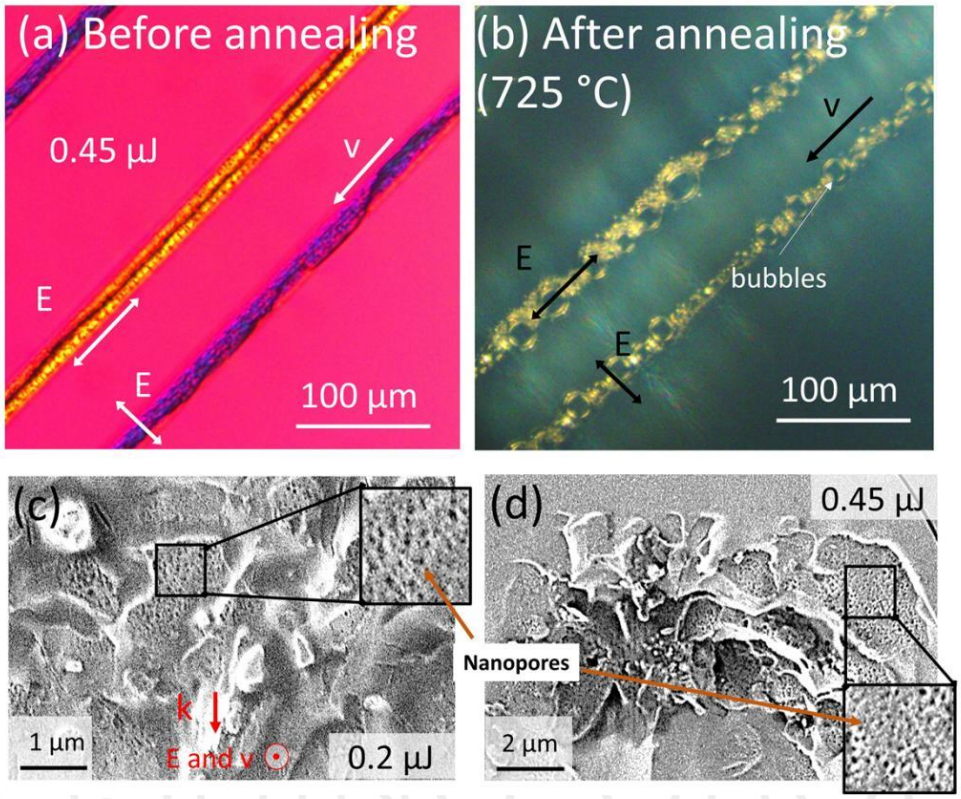

Fig. 2. a) Optical image under polarized light and using a full waveplate revealing oriented NGs before annealing, and b) formation of bubbles at high temperatures above the nanogratings erasure temperature in Sodalime glass. c and d) Electron microscope micrographs of the glass for 2 energies (0.2 and 0.45 µJ), revealing the presence of nanopores inside the nanogratings. E, v, and k are respectively the laser polarization orientation, the scanning direction, and the beam propagation direction.

Scanning electron microscopy (SEM) performed on the as irradiated regions (E ∥ to v configuration) revealed the presence of nanopores for both 0.2 and 0.45 µJ, as shown in Fig. 2b and 2c. An averaged pore diameter of ~45 nm and ~60 nm was measured from the SEM micrographs for 0.2 and 0.45 µJ, respectively. Additionally, the irradiated region of the 0.45 µJ presents a greater number of cracks, holes, and irregularities compared to the 0.2 µJ irradiation. We expect this "chaotic" structure to favor nucleating sites and promote formation of bubbles during the heat treatments. Finally, the presence of volatile species such as alkali, B_2O_3, SO_3 or As_2O_3 (from glass formulations, Table 1) might be responsible of bubble nucleation and growth in these few glasses, although this aspect requires complementary investigation and is outside the scope of this work. It must be specified that a nucleation process necessitates some incubation time, similarly to crystal nucleation observed in lithium niobium silicate glasses [25], which may explain why they are not observed post irradiation but only post heat treatment.. Finally, the observed bubbles are exclusively located in the laser irradiated area, and not in the bulk (pristine glass), clearly suggesting a heterogeneous nucleation mechanism. This aspect of bubble nucleation can be proved detrimental over long-term use of devices in a high temperature environment and must therefore be anticipated through adequate glass formulation.

3.3 Erasure of nanopores during the irradiation process: An upper limit

Nanopores composing NGs and micrometer scale bubbles are therefore distinct modifications, and in our experimental conditions only nanopores are observed post-irradiation. As shown earlier, they typically erase within 30 min at ~1.1T_a where T_a stands for the glass annealing temperature, for which the viscosity is log(η, Pa.s) = 12. Therefore, one may wonder how these nanopores can survive an ultrafast laser induced process when temperatures can easily exceed 1000 °C in glass [26–28]. For this purpose, let us consider the situation of fs-laser inscription from which porous NGs are produced. Once the nanopores are created (or re-created) just after the end of a pulse (at the maximum temperature), they erase until the next pulse through which they can be regenerated. As the gaussian beam is moving away and the maximum temperature is decreasing, the nanopores will remain if the conditions are suitable. This last cooling curve is driven by thermal diffusion and the nanopores must survive it. For this purpose, we take the situation of a 50 nm cavity (the pore) surrounded by a molten glass at atmospheric pressure. This view is reasonable since the stress relaxation will be achieved in only few 100s of ps after a laser pulse is absorbed [16]. With this in mind, and using the full R-P equation again, we can compute the time required to erase such a nanopore at a given temperature. The results are summarized in Fig. 3a for both Sodalime and silica (Suprasil CG). As previously mentioned, here we keep σ term constant, which is a reasonable assumption for this work [29].

The intuitive trend that the pore will collapse faster when brought to higher temperature is verified. Additionally, the glass viscosity, η(T), is found to perfectly correlate with the erasure time (right vertical axis of Fig. 3), demonstrating that the latter is proportional to viscosity within our experimental conditions.

Now, let us consider the thermal cooling of a pulse in silica glass. Laser processing conditions, and temperature-dependent glass properties such as thermal diffusion coefficient (D_{th}) can play a role, but this is out of the scope of this work. Here we simply take initial temperature values of the cooling profile and solve the classical heat equation while taking materials properties constant. Typical equations can be found for instance in Refs. [24,28,30]. The cooling profiles for silica are reported in Fig. 3b. For all glasses investigated, although the value of D_{th} can be slightly different, the reasoning remains the same. From Fig. 3b, we can define a characteristic erasure time by setting the time at which the cooling curve touches the erasure one. In fact, the thermal cooling curves are just shifted to high temperatures while preserving their shape. The characteristic time interval is materialized by the blue band in the figure, and corresponds to typ. ~ 30 ns, hence a viscosity "limit" of log(η, Pa.s) ~ -0.75. In fact, this time is much smaller than a typical diffusion time (~ 1 µs). The difference arises from the cooling temperature profile where the temperature drastically decreases within the first instant of the cooling, and the viscosity varies in a log scale with respect to temperature. With such a characteristic time, it is shown that temperatures around 2450 °C and 3100°C are required to collapse the pore for Sodalime and Suprasil CG, respectively. If another characteristic timescale is considered, the upper temperature of nanopore erasure will be shifted accordingly. For example, 1 µs characteristic time yields to an erasure temperature of 2675 °C in silica. Consequently, provided the characteristic time-temperature couple in the irradiation process is known and the assumptions implied by the proposed model hold true, an upper limit temperature can be anticipated. It must be stressed that such calculations imply low viscosity values (i.e., high temperatures), which are determined using viscosity fits, and therefore one must bear in mind that uncertainties can be quite large (typ. Δlog(η, Pa.s) ± 1.5).

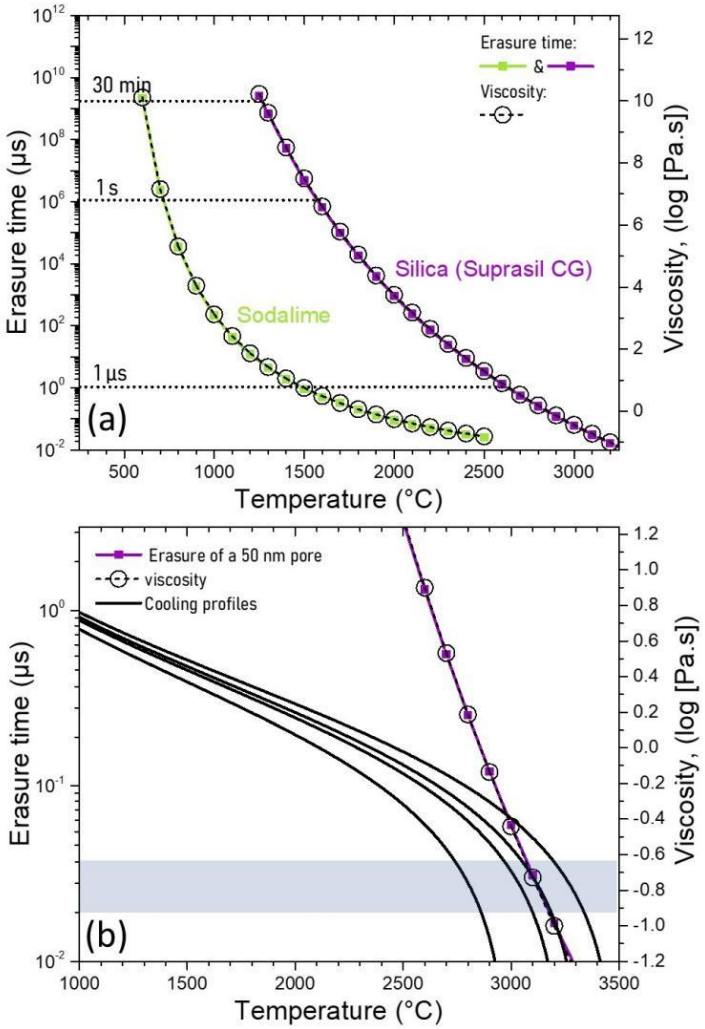

Fig. 3. a) Erasure time for a nanocavity in glass (left axis), and glass viscosity (right axis) as a function of temperature, modeled using the R-P equation for a 50 nm pore diameter in both Sodalime and Suprasil CG. b) Simulated thermal cooling profiles for a pulse in silica glass, showing that the characteristic time of erasure is situated in the 10s of nm range.

Therefore, when viscosity for any glass reaches log (η, Pa.s) ~ -0.75, a 50 nm nanopore cannot survive the laser process if we consider 30 ns as a relevant characteristic time. This value is several orders of magnitude lower to what was found in Ref. [16] based on viscous flow arguments using the Peclet number, and one can set this value as the upper temperature limit for nanopore survival during laser irradiation process. Again, this viscosity value can be varied if another characteristic time is chosen. For completeness, Fig. 3a also illustrates that nanopores, hence NGs, do erase within 30 minutes once the glass viscosity reaches log(η, Pa.s) ~ 10.1, as expected and in agreement from Fig. 1.

From the above findings, we compare the temperature of NGs erasure for the series of glasses listed in Table 1, as a function of NGs processing window. The latter, normalized with respect to silica, can be found in Ref. [17], and corresponds to observation of NGs in a E_p-RR landscape. The results are displayed in Fig. 4. However, in this case, we chose log(η,

Pa.s) ~ 1 as a viscosity criterion, corresponding to a erasure time of 1 µs, since for all glasses the viscosity fits do not allow reasonable estimations beyond this viscosity value. The survival of NGs appears to be strongly correlated a defined upper temperature limit of NGs erasure which increases with both Ep and RR. When considering glasses with low erasure temperature, such as BK7 or 7059, a careful choice of laser parameters must then be employed in order to form stable NGs (i.e., that can withstand the irradiation process). Typically, strategies can consist of increasing the pulse density (pulses / µm) to locally change the glass viscosity through ionic migration, or remain in a low deposited power regime, through reduction of Ep and RR. Note that the laser processing window can be very small for some glasses (Fig. 4). Moreover, the nanograting will survive if a single nanopore does. Hence, this approach can potentially be generalized and inspire other works related to the field, for e.g., when dealing with a single pore like voids (Type III) and microvoid-based Fiber Bragg Gratings (FBG), holes and 3D assembly of them as seeds, or nanopores (Type X) [6,31–33].

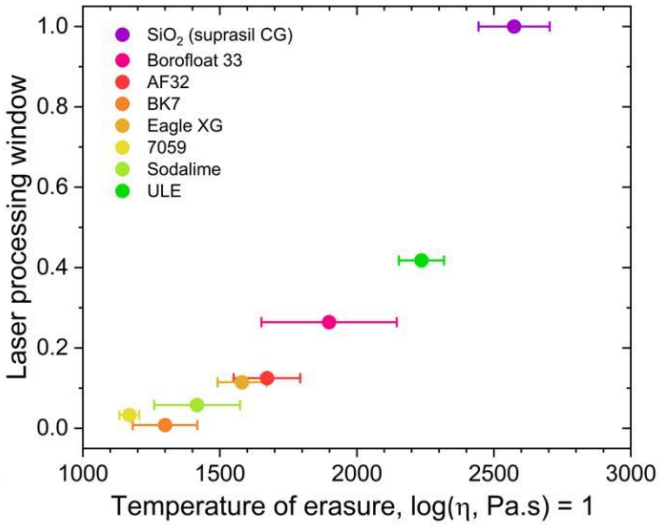

Fig. 4. Erasure temperature defined as log(η, Pa.s) = 1 as an example, versus laser processing window (in a E_p-RR landscape) related to NGs (from Ref. [17]) and normalized with respect to silica (Suprasil CG). Error bars arise from uncertainties in the viscosity fits using Vogel–Fulcher–Tammann (VFT) equation.

Although a scenario of pore collapsing is envisioned, along with the corresponding decrease in optical properties such as R or effective refractive index for optical components, several contributions can modify the so defined NGs upper temperature limit. For this purpose, we can discuss the contribution to the R-P equation but neglecting the inertia contribution since we are interested in the long-time limit of the pore evolution. This view is particularly important in sensing applications. This gives:

$$\frac{dR}{dt} = \frac{R(p_x - p_\infty)}{4\eta} - \frac{\sigma}{2\eta} \qquad (1)$$

With $\left(\frac{dR}{dt}\right)$ being the rate of pore radius variation, R the pore radius, p_x and p_∞ the pressures inside the pore and in the surrounding medium, σ the surface tension and η the viscosity. The pore will grow or collapse when the first or second term of the right-hand side of Eq. 1 dominates, respectively. In our situation, only collapse is expected since the second term is several orders of magnitude higher than the first one. Additionally, this collapse is

reinforced when the pore size becomes smaller (small pores erase faster than large ones). From Eq. 1 we can express the minimum time (τ_e) requested to erase the pore as:

$$\boldsymbol{\tau_e = \frac{2 \cdot \eta \cdot R_{ini}}{\sigma} = \frac{2 \cdot 10^{[A+B/(T-T_0)]} \cdot R_{ini}}{\sigma}} \quad (2)$$

Here R_{ini} is the initial pore radius, and glass viscosity can be substituted using a law (e.g., VFT) and taking the form $\log(\eta) = A + B/(T-T_0)$ as described in the experimental section. From this expression, we therefore link the erasure time and the viscosity in a context of pore erasure. This opens the door to thermal stabilization of optical components for instance using the VAREPA formalism based on activation energy distribution [20]. For completeness, a different mechanism yielding to growth rather than collapse can be anticipated when i) large pressure difference $(\boldsymbol{p_x - p_\infty})$ is achieved either through high pressure (gas) inside the pore (formation of a bubble), pressure decrease in the medium, or a combination thereof ii) the surface tension is decreased, and iii) to pore radius increases. Considering large bubbles as in Ref. [34], some conditions can be met where growth over collapse can exist. Overall, $\left(\frac{dR}{dt}\right)$ scales with $1/\eta$, and either growth / collapse of a pore / bubble would ultimately be a function of the glass viscosity.

Although this work sets an upper temperature limit for NGs modifications survival during laser irradiation process, the temperature distribution in the laser track cross section, and its evolution over time, can be challenging to estimate or measure. Additionally, the laser parameter – temperature profile relationships are far from trivial, as many combined effects come into play (e.g., spatio-temporal electron excitation and clamping, plasma absorption and reflection, heat accumulation, temperature dependent glass properties, etc.). Each individual laser parameter (e.g., pulse duration, pulse energy, NA, repetition rate) or a combination thereof must be considered, and ongoing work is underway to tackle these aspects.

From a technological standpoint, we clearly demonstrate that porous NGs are intimately related to viscosity. To overcome this limitation, especially for HT sensing applications, specific types of laser-induced structures can be used, including i) voids like structures (so called Type III), as we shown that larger pores are more stable than small ones, or ii) thermally stable crystalline phases, as it may be the case in highly some Al_2O_3-SiO_2 glasses with formation of Mullite [5,35].

Finally, an "erasure temperature" relates to a kinetics problem (time-temperature couple) [22]. We can thus define different "high temperature limits" depending on the operating conditions: i) short times (minutes, seconds) in fire alarms and some kind of structural health monitoring, ii) long times (years timescale) for sodium cooled nuclear reactors, metal recycling, airplanes or process monitoring, and iii) laser writing timescale in either repetitive or cumulative regimes, for which either average temperature and cooling profiles are dissimilar. This is exemplified if Fig. 5 using Eq. 2 for all glasses investigated herein. It is worth pointing out that the results previously found in Fig. 3 are retrieved with this simplified version of the Rayleigh-Plesset equation and can therefore be a useful tool to predict the survival of NGs with respect to a given thermal process.

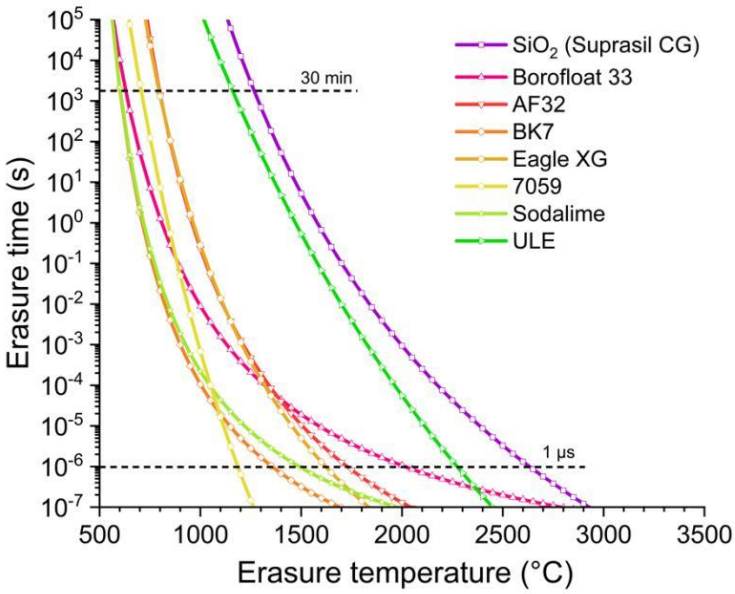

Fig. 5. Erasure time versus temperature for all glasses investigated in this work calculated from Eq. 2, for an initial pore diameter of 50 nm. The fit parameters for the viscosity curves are provided in Table 1.

4. Conclusion

This paper provides compelling evidence that the erasure of nanogratings in glass is intimately related to viscosity, and these 8 glasses with erasure temperature spanning from 600 °C to 1200 °C under isochronal annealing experiments (30 min time step). The results provide useful information of optical component designers to select an adequate glass (and its viscosity profile) when considering high temperature operations, or simply thermal ageing considerations. Moreover, the approach is then used to consider the erasure of nanopores during the irradiation process, i.e., what is the maximum temperature a nanopore can survive upon laser cooling timescale? We found that the upper limit in the irradiation conditions corresponds to a temperature for which the glass viscosity value is log (η, Pa.s) ~ -0.75 in the hypothesis where we consider a characteristic time of 30 ns, or log (η, Pa.s) ~ 1 for a timescale of 1 µs, corresponding to a typical diffusion time. However, this temperature limit is lowered for much longer processes like isothermal / isochronal annealing where log(η, Pa.s) ~ 10.1. The relationship between the process time (irradiation, annealing, "any thermal treatment") and the temperature (or viscosity) is established in Eq. 2. Therefore, an adequate knowledge of the time-temperature couple of a given thermal process, either through thermal annealing of laser irradiation, will inevitably impact the thermal stability of the NGs.

5. Back matter

5.1 Funding

Agence Nationale de la Recherche (ANR), Project REFRACTEMP. Qiong Xie acknowledges the China Scholarship Council (CSC) for the funding of her PhD fellowship.

5.3 Disclosures

The authors declare no conflicts of interest.

5.4 Data availability statement

Data underlying the results presented in this paper are not publicly available at this time but may be obtained from the authors upon reasonable request.

6. References

1. R. Drevinskas and P. G. Kazansky, "High-performance geometric phase elements in silica glass," APL Photonics **2**, 066104(1)-066104(9) (2017).
2. J. Zhang, M. Gecevičius, M. Beresna, and P. G. Kazansky, "Seemingly unlimited lifetime data storage in nanostructured glass," Phys. Rev. Lett. **112**, 033901(1)-033901(5) (2014).
3. R. Osellame, H. J. W. M. Hoekstra, G. Cerullo, and M. Pollnau, "Femtosecond laser microstructuring: An enabling tool for optofluidic lab-on-chips," Laser Photonics Rev. **5**, 442–463 (2011).
4. S. J. Mihailov, D. Grobnic, C. Hnatovsky, R. B. Walker, P. Lu, D. Coulas, and H. Ding, "Extreme Environment Sensing Using Femtosecond Laser-Inscribed Fiber Bragg Gratings," Sensors **17**, (2017).
5. Y. Wang, M. Cavillon, J. Ballato, T. Hawkins, T. Elsmann, M. Rothhardt, R. Desmarchelier, G. Laffont, B. Poumellec, and M. Lancry, "3D Laser Engineering of Molten Core Optical Fibers: Toward a New Generation of Harsh Environment Sensing Devices," Adv. Opt. Mater. **10**, 2200379(1)-2200379(9) (2022).
6. M. Sakakura, Y. Lei, L. Wang, Y. H. Yu, and P. G. Kazansky, "Ultralow-loss geometric phase and polarization shaping by ultrafast laser writing in silica glass," Light Sci. Appl. **9**, 1–10 (2020).
7. Y. Shimotsuma, S. Mori, Y. Nakanishii, E. Kim, M. Sakakura, and K. Miura, "Self-assembled glass/crystal periodic nanostructure in Al_2O_3-Dy_2O_3 binary glass," Appl. Phys. A Mater. Sci. Process. **124**, 1–8 (2018).
8. S. Lotarev, S. Fedotov, A. Lipatiev, M. Presnyakov, P. Kazansky, and V. Sigaev, "Light-driven nanoperiodical modulation of alkaline cation distribution inside sodium silicate glass," J. Non. Cryst. Solids **479**, 49–54 (2018).
9. J. Cao, B. Poumellec, L. Mazerolles, F. Brisset, A. L. Helbert, S. Surble, X. He, M. Lancry, and L. Pinckney, "Nanoscale Phase Separation in Lithium Niobium Silicate Glass by Femtosecond Laser Irradiation," J. Am. Ceram. Soc. **100**, 115–124 (2017).
10. D. Grobnic, C. Hnatovsky, S. Dedyulin, R. B. Walker, H. Ding, and S. J. Mihailov, "Fiber Bragg Grating Wavelength Drift in Long-Term High Temperature Annealing," Sensors **21**, 1–29 (2021).
11. E. Bricchi, B. G. Klappauf, and P. G. Kazansky, "Form birefringence and negative index change created by femtosecond direct writing in transparent materials," Opt. Lett. **29**, 119–121 (2004).
12. Y. Wang, S. Wei, M. Cavillon, B. Sapaly, B. Poumellec, G. D. Peng, J. Canning, and M. Lancry, "Thermal stability of type II modifications inscribed by femtosecond laser in a fiber drawn from a 3D printed preform," Appl. Sci. **11**, 1–11 (2021).
13. A. Rudenko, J. P. Colombier, S. Höhm, A. Rosenfeld, J. Krüger, J. Bonse, and T. E. Itina, "Spontaneous periodic ordering on the surface and in the bulk of dielectrics irradiated by ultrafast laser: A shared electromagnetic origin," Sci. Rep. **7**, 1–14 (2017).
14. A. Rudenko, J. P. Colombier, and T. E. Itina, "Nanopore-mediated ultrashort laser-induced formation and erasure of volume nanogratings in glass," Phys. Chem. Chem. Phys. **20**, 5887–5899 (2018).

15. M. Cavillon, Y. Wang, B. Poumellec, F. Brisset, and M. Lancry, "Erasure of nanopores in silicate glasses induced by femtosecond laser irradiation in the Type II regime," Appl. Phys. A **126**, 876(1)-876(9) (2020).
16. Q. Xie, M. Cavillon, B. Poumellec, D. Pugliese, D. Janner, and M. Lancry, "Application and validation of a viscosity approach to the existence of nanogratings in oxide glasses," Opt. Mater. (Amst). **130**, 112576(1)-112576(7) (2022).
17. Q. Xie, M. Cavillon, D. Pugliese, D. Janner, B. Poumellec, and M. Lancry, "On the Formation of Nanogratings in Commercial Oxide Glasses by Femtosecond Laser Direct Writing," Nanomaterials **12**, 2986(1)-2986(12) (2022).
18. S.-E. Wei, Y. Wang, H. Yao, M. Cavillon, B. Poumellec, G. D. G.-D. Peng, and M. Lancry, "Thermal stability of type II modifications by IR femtosecond laser in silica-based glasses," Sensors **20**, 1–14 (2020).
19. Y. Wang, M. Cavillon, N. Ollier, B. Poumellec, and M. Lancry, "An Overview of the Thermal Erasure Mechanisms of Femtosecond Laser-Induced Nanogratings in Silica Glass," Phys. Status Solidi Appl. Mater. Sci. **218**, 2100023(1)-2100023(15) (2021).
20. B. Poumellec and M. Lancry, "Kinetics of Thermally Activated Physical Processes in Disordered Media," Fibers **3**, 206–252 (2015).
21. M. Gecevičius, "Polarization Sensitive Optical Elements By Ultrafast Laser Nanostructuring of Glass," University of Southampton (2015).
22. Y. Wang, M. Lancry, M. Cavillon, and B. Poumellec, "Lifetime prediction of nanogratings inscribed by a femtosecond laser in silica glass," Opt. Lett. **47**, 1242–1245 (2022).
23. Y. Wang, "A contribution to high temperature applications using femtosecond laser direct writing in silica-based glasses and optical fibers To cite this version : Thèse de doctorat," Université Paris-Saclay (2022).
24. T. T. Fernandez, M. Sakakura, S. M. Eaton, B. Sotillo, J. Siegel, J. Solis, Y. Shimotsuma, and K. Miura, "Bespoke photonic devices using ultrafast laser driven ion migration in glasses," Prog. Mater. Sci. **94**, 68–113 (2018).
25. E. Muzi, M. Cavillon, M. Lancry, F. Brisset, R. Que, D. Pugliese, D. Janner, and B. Poumellec, "Towards a Rationalization of Ultrafast Laser-Induced Crystallization in Lithium Niobium Borosilicate Glasses : The Key Role of The Scanning Speed," Cryst. MDPI **11**, 1–26 (2021).
26. T. Yoshino, Y. Ozeki, M. Matsumoto, and K. Itoh, "In situ micro-raman investigation of spatio-temporal evolution of heat in ultrafast laser microprocessing of glass," Jpn. J. Appl. Phys. **51**, (2012).
27. M. Sakakura, M. Shimizu, Y. Shimotsuma, K. Miura, and K. Hirao, "Temperature distribution and modification mechanism inside glass with heat accumulation during 250 kHz irradiation of femtosecond laser pulses," Appl. Phys. Lett. **93**, (2008).
28. M. Shimizu, M. Sakakura, M. Ohnishi, M. Yamaji, Y. Shimotsuma, K. Hirao, and K. Miura, "Three-dimensional temperature distribution and modification mechanism in glass during ultrafast laser irradiation at high repetition rates," Opt. Express **20**, 934–940 (2012).
29. K. Boyd, H. Ebendorff-Heidepriem, T. M. Monro, and J. Munch, "Surface tension and viscosity measurement of optical glasses using a scanning CO2 laser," Opt. Mater. Express **2**, 1101–1010 (2012).
30. R. Que, "Demonstration of anisotropy control of optical properties induced by IR fs laser irradiation in organic materials : birefringence, di-attenuation, SHG, photoluminescence," Université Paris-Saclay (2022).
31. Y.-S. Xu, Z.-Z. Li, H. Fan, Y.-F. Liu, H. Xia, S. Juodkazis, Q.-D. Chen, and L. Wang, "Optical near fields for ablation of periodic structures," Opt. Lett. **48**, 2841–2844 (2023).
32. Z.-Z. Li, L. Wang, H. Fan, Y.-H. Yu, Q.-D. Chen, S. Juodkazis, and H.-B. Sun, "O-

FIB: far-field-induced near-field breakdown for direct nanowriting in an atmospheric environment," Light Sci. Appl. **9**, 1–7 (2020).
33. G. Laffont, R. Cotillard, N. Roussel, R. Desmarchelier, and S. Rougeault, "Temperature resistant fiber bragg gratings for on-line and structural health monitoring of the next-generation of nuclear reactors," Sensors **18**, 1–20 (2018).
34. E. O. Kissi and Y. Bellouard, "Self-organized nanostructures forming under high-repetition rate femtosecond laser bulk-heating of fused silica," Opt. Express **26**, 14024 (2018).
35. Y. Wang, S. Wei, M. R. Cicconi, Y. Tsuji, M. Shimizu, Y. Shimotsuma, K. Miura, G. Peng, D. R. Neuville, B. Poumellec, and M. Lancry, "Femtosecond laser direct writing in SiO2-Al2O3 binary glasses and thermal stability of Type II permanent modifications," J. Am. Ceram. Soc. **103**, 4286–4294 (2020).

7. Article thumbnail upload

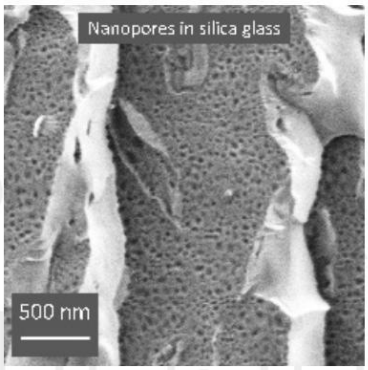

III.3 LIFESPAN PREDICTION PROCEDURE OF VOLUME NANOGRATINGS IMPRINTED BY FEMTOSECOND LASER IN OPTICAL GLASSES

Ceramics International 50 (2024) 20303–20312

Contents lists available at ScienceDirect

Ceramics International

journal homepage: www.elsevier.com/locate/ceramint

Lifespan prediction procedure of volume nanogratings imprinted by femtosecond laser in optical glasses

Qiong Xie [a], Maxime Cavillon [a], Bertrand Poumellec [a], Matthieu Lancry [a,*]

[a] Institut de Chimie Moléculaire et des Matériaux D'Orsay (ICMMO), Université Paris-Saclay, CNRS, Orsay, 91405, France

ARTICLE INFO

Handling Editor: Dr P. Vincenzini

Keywords:
Nanogratings
Nanopores
Oxide glasses
Thermal aging
Master curve
Viscosity

ABSTRACT

Volume nanogratings imprinted by infrared femtosecond laser in oxide glasses exhibit a characteristic birefringent signature, which translates into measurable retardance. Upon thermal annealing, such signature is progressively erased, typical of nanograting erasure. In this work, we propose a procedure to predict the lifespan of nanogratings by two main approaches: 1/ numerical modeling of optical retardance ageing using the Rayleigh-Plesset equation, and 2/exploiting VAREPA (VAriable REaction PAthways) framework fed by simulated ageing data. By considering experimental time – temperature annealing conditions, the modeled retardance is gathered as a function of demarcation energy to build a so-called Master Curve and then compared to accelerated ageing experiments. The erasure constant rate k_0 can be determined for 8 commercial optical glasses. Based on a distributed Rayleigh-Plesset model, k_0 and activation energy distribution are linked to glass viscosity and its temperature dependency. Finally, we discussed the restrictions on VAREPA application for an accurate lifetime prediction. This work provides guidelines for the future development of nanogratings based devices and applications, including optical data storage, birefringent devices, and optical sensors, through a judicious choice of glass composition and associated properties.

1. Introduction

Femtosecond laser direct writing (FLDW) enables both local and volumetric transformations of transparent materials, such as optical glasses [1]. Among the possible modifications to be imprinted inside glass, volume nanogratings (NGs), also labelled Type II in the literature, are of prime interest [2,3]. These structures are composed of self-organized pseudo-periodic nanolayers, and their orientation can be controlled by light polarization [2]. In oxide glasses, they generally take the form of porous nanolayers [4] composed of nanopores (typ. few tens of nm in size), but other NGs can be composed of alternate layers of crystalline and amorphous phases [5]. Porous NGs lamellar structuring induces a strong birefringence optical response from negative index variation [6], and can even lead to optical chirality [7]. Consequently, they have drawn attention for applications/fields including birefringent optical devices [8], 3D geometric phase optics [9], optical data storage [10,11], microfluidic [12], structural health monitoring and high-temperature sensing [13–15].

From a practical standpoint, the lifespan of a given device composed of NGs must be anticipated, principally considering a time - temperature couple. Expected lifespans can be very different depending on the application, for example i) 25 years at 50 °C for telecommunication [16,17] ii), few years at 400 °C–600 °C for the oil or gas drilling industry [18], or 600 °C–800 °C in new nuclear reactors generation cooled with liquid sodium [19] and Tokamak [20], iii) higher temperatures for aeronautics instruments of aircraft engines (typ. 800–1600 °C) [21–24], and iv) 600 °C–1100 °C for the recycling of precious metals or metal-based manufacturing processes [13,25–28]. In all these applications, it is mandatory to have temperature and/or strain sensors that ideally must be stabilized (i.e., without unpredicted drifts of their monitored response) [14]. This requires the predictions of the correct stabilization conditions for related components. However, when considering glass as the device material, difficulties arise from its intrinsic disordered and amorphous nature. Therefore, to model the relaxation process(es) in disordered media, several approaches have been proposed, where an extended report can be found in Ref. [29]. This disorder impacts the various steps of a given physicochemical reaction leading to a progressive relaxation of the observed quantity (e.g., laser induced refractive index modification [30,31]). For instance, if atomic hopping is involved in a reaction where a given modification is erased to

* Corresponding author.
E-mail address: matthieu.lancry@universite-paris-saclay.fr (M. Lancry).

https://doi.org/10.1016/j.ceramint.2024.03.153
Received 12 December 2023; Received in revised form 27 February 2024; Accepted 12 March 2024
Available online 16 March 2024

return to an "initial state", the disorder will factor into the hopping distance or frequency. Hence, the resulting activation energy of the given reaction will be distributed due to the multiplicity of transition state configurations. While the approach is based on several previous works in glasses, e.g., Kohlrausch in 1847 for the residual electric discharge in Leyde bottle [32], W.A. Yager in 1936 for the relaxation function in dielectrics [33], V. Vand (1943) [34] or W. Primak (1955) [35], the aforementioned aspects were first introduced in optical fibers by Lemaire et al., in 1984 [36] to predict hydrogen-induced loss. Then Erdogan et al. developed in 1994 a comprehensive formalism on thermal decay of UV-induced fiber Bragg gratings [30]. Later in 1997, Kannan et al. [37] refined this framework to improve the reliability of fiber gratings lifetime predictions. In 1998 and based on these previous works, Poumellec generalized the approach by introducing the VAREPA (VAriable REaction PAthways) framework, [38,39]. Under conditions that must be validated beforehand, it becomes possible to predict the lifespan of optical components which are based on a property variation, including the ubiquitous refractive index changes [16,39], or retardance (proportional to birefringence), characteristic of nanogratings imprinted in silica, or silicate glasses [40].

In this paper, we investigate the applicability of VAREPA to predict the lifespan of nanogratings inscribed by femtosecond laser inside a wide variety of oxide glasses. First, we remind the key hypotheses of VAREPA and its experimental applicably for the prediction of nanograting erasure at high temperature in silica. Second, a model of nanogratings aging considering the evolution of nanopores as a function of temperature is considered using the Rayleigh-Plesset equation [41,42]. Third, based on a distributed Rayleigh-Plesset model, we rationalize the applicability of VAREPA using modeled thermal ageing data. Then, we compare experimental data to the simulated Master Curves (MC) and related activation energies in 8 commercial glasses, extending our work much beyond silica. Finally, we exploited these results by comparing lifetime predictions at high temperature using both approaches namely VAREPA and based on the Rayleigh-Plesset equation.

2. Preliminary hypotheses and experimental details

Preliminary hypothesis on the investigation of nanograting thermal stability: In most applications, the exploited property of NGs is their form birefringence, resulting to an optical retardance that can be optically measured. Form birefringence is the dominating factor to the overall birefringence response [7,43], and in this work, we solely focus on this contribution. It is worth mentioning that other contributions can arise from point defects, stress fields, interlayers densification, or any kind of birefringent contribution [43], but this aspect goes beyond the framework of this study that is focused on the "ultimate" thermal stability of nanogratings [43]. Especially, we work on "burnt-in" samples from which defects [43], silicon [44] and residual stress have been erased. Our previous work done in a multitude of glass compositions [45] reveals that it is experimentally relevant to assume that linear birefringence *LB* (t, T) is solely related to the kinetics of nanopores erasure at high temperatures ($T > 0.9\ T_a$, T_a being the glass annealing temperature). In addition, we assume also that retardance erasure is mainly due to nanopores erasure and not to any laser track length variation, nanoplane distortion, dispersion of the nanopores, or any other change. Alternatively, the presence of refractory oxide nanocrystals will be instead something that could likely leads to some deviation from this model like quartz formation in silica [40]. However, for all the chosen compositions in this paper, we did not find any nanocrystals formation (including post laser irradiation and thermal treatments) and such behavior has neither been reported as well in the literature contrarily to what could happen in SiO_2–Na_2O [46], GeO_2-Na_2O [47], Dy_2O_3–Al_2O_3 [48], SiO_2–Al_2O_3 [49]or LNS glasses [50] in specific laser conditions.

Accelerated ageing data: To investigate the lifespan of NGs in oxide glasses, optical retardance (R) is monitored both experimentally and theoretically/numerically. In both cases, R is defined as the product of the linear birefringence (*LB*) with the thickness (l) of the birefringent object. From an experimental point of view, R is monitored by optical microscopy using the Sénarmont method after isochronal thermal annealing for NGs with a time step $\Delta t = 30$ min [45].

Relationship between nanogratings and the modeled optical properties: To numerically compute the optical retardance R from the NGs structure (i.e., arising from its form birefringence), a series of expressions, given in Ref. [51], and also provided in the Appendix, are employed. In short, NGs in the investigated glasses are all composed of a subwavelength assembly of porous nanolayers with a significant refractive index contrast [4]. The *LB* can be calculated from knowing this opto-geometric morphology, along with the refractive indices of the porous nanolayers and in between those layers (e.g., considering pristine glass) [6,52].

3. Analysis of the experimental retardance data with VAREPA framework

From both modeled or experimental accelerated ageing data (e.g., using isothermal or isochronal annealing experiments), the VAREPA framework can be applied to predict the lifetime of an optical property [38] as it was extensively done in the literature for UV written fiber Bragg gratings [31,53,54], providing that several assumptions are fulfilled. This allows to find the distribution function of the activation energy by providing only one constant: the erasure rate k_0 of the main erasure reaction, that is assumed to be the nanopores erasure. In simple cases, this is determined by a simple variable change from (t, T) to an activation energy, noted E_d. Then one can use this distribution function to predict the lifetime at any temperature and it is also possible determine some suitable annealing conditions for extending a lifetime [38]. In this work, we focus on the evolution of R_{norm} (t, T). There are two groups of assumptions that should be validated in order to use this framework.

3.1. First group of assumptions (on the reaction)

a) Only one elementary reaction is involved in the process. The reaction pathway is symbolically written as B → A, and B and A are respectively attached to some configurations in the nanostructured and rejuvenated glass. In our case, we will assume that the measured or simulated R_{norm} is originated from a single type of contribution through the form birefringence, e.g., the change of nanopores radius in the porous nanolayers. We will thus neglect others processes such as Si formation or point defects as mentioned above if a suitable annealing (burnt-in) erased them.

b) The process is an Arrhenius based process with a reaction constant k (E, T) that is thermally activated. $k(E,T) = k_0 e^{-\frac{E_a}{k_B T}}$ where k_B is Boltzman constant (eV/K), k_0 is a pre-exponential factor (s^{-1}), E_a the activation energy (eV), and T the temperature (K).

c) E_a is distributed here (not a single value) in the case of nanopores erasure, arising from the disordered nature of glass as it is the case for radiation-induced loss, recovery of photo- or radio-darkening [55], stress relaxation [56,57], viscosity [58] or UV-induced refractive index changes [38].

3.2. Second group of assumptions (on the process)

We assume that R_{norm} is formed by the superposition of elementary retardance contributions that we call R_{elem}. We consider that the erasure mechanism of the elementary reaction with activation energy E_a follows a first order reaction kinetics, and this in all investigated oxide glasses. As a result, $\frac{dR_{elem}}{dt} = -k(E,T)R_{elem}$ and so we assume that R_{elem} (t, T) can be written as follow: $R_{elem}(E_a, t, T) = e^{-k_0.t.e^{-\frac{E_a}{k_B T}}}$. Then, with the assumption of additivity of the elementary contributions, we get $R_{norm}(t,T) = \int_0^\infty R_{elem}(E_a,t,T)g(E_a)dE_a$ where $g(E_a)$ is the distribution

of the activation energy ($\int_0^{\infty} g(E_a)dE_a = 1$). This integral is solvable assuming that $R_{elem}(E_a, t, T)$ can be assimilated to a rapid varying function at a specific energy called demarcation energy, $E_d = k_B T \ln(k_0 t)$, associated to any given T and t couple (a Vand cutting energy [34,59]), and corresponds to the boundary between an achieved and a non-achieved reaction. The consequence of this last assumption is that $R_{norm}(t, T)$ becomes $R_{norm}(E_d) = \int_0^{E_d} g(E_a)dE_a$ only dependent on E_d whatever T or t [40,57] provided the distribution is independent on temperature or time. With a proper choice of k_0, isotherms or isochrons can be collapsed into a unique curve, the so-called Master Curve (MC), here describing $R_{norm}(E_d)$. Note that the shape of the distribution function $g(E)$ can be obtained from the differentiation of the MC against E_d. It is important to note that several reasons may lead to the impossibility to find a MC, e.g., if there are multiple reactions with additional rate constants or distributions associated. Finally, on the premise of meeting a single function gathering all isotherms, the master curve plot (i.e., the lifetime function) can be used to predict the NGs lifetime at various temperatures.

To summarize, in the following we suppose that the measured optical retardance $R_{norm}(t,T)$ of nanogratings during an annealing treatment is mostly proportional to one "chemical species" B included in the nanogratings namely the population of nanopores. In this Arrhenius first order erasure reaction (e.g., nanopores erasure in ta viscous fluid), the activation energy will be distributed, as it is the case for viscoelastic relaxation or stress relaxation mechanisms in glasses. This overall approach was succesfully applied in silica to a many isochronal data made by Wang et al. [40] proving that VAREPA can be exploited for porous nanogratings. In the next sections after introducing Rayleigh-Plesset equation and developping a new distributed Rayleigh-Plesset model, we will investigate if VAREPA can be reliably applied on a set of data obtained using Rayleigh-Plesset and which are the restrictions on its application for an accurate lifetime prediction.

4. Rayleigh-Plesset modelling of nanopores erasure kinetics

In the following calculations of the optical retardance as a function of annealing conditions in a context of thermal ageing, the Rayleigh-Plesset (R–P) equation is employed as initially suggested by Rudenko [60]. The Rayleigh-Plesset (R–P) equation was used to accurately simulate the evolution of nanopores erasure $R_{pore}(t,T)$ over time (t) and temperature (T), and then compared to isochronal annealing experiments. This equation describes the evolution of a spherical bubble inside an incompressible Newtonian fluid, and it can be expressed as follows:

$$\frac{\Delta P}{\rho} = R_{pore}\frac{d^2R_{pore}}{dt^2} + \frac{3}{2}\left(\frac{dR_{pore}}{dt}\right)^2 + \frac{4\eta(T)}{\rho R_{pore}}\frac{dR_{pore}}{dt} + \frac{2\sigma}{\rho R_{pore}}$$

Here, ΔP is the pressure difference (in Pa) between the inside of the nanopore (supposed spherical) and far away from it; ρ is the glass density (in kg m^{-3}); R_{pore} the radius (in m) of the spherical nanopore; t is the time (in s); $\eta(T)$ is the glass viscosity (in Pa•s), and σ is the surface energy (around 0.3 J m^{-2} for silica [61], whose temperature dependence remains within <5% and does not change lifetime prediction significantly). Note that the non-sphericity of the nanopores, which are oblate [62], does not change the physical observation and thus that nanopores are considered spherical. Initial conditions are R_{pore} (at $t = 0$) $= R_{ini}$ i.e. the initial nanopore size and $\frac{dR_{pore}}{dt} = 0$ at $t = 0$.

In the R–P equation, the second derivative and the square of the first derivative have very small contributions numerically in our conditions and are therefore neglected, i.e., slow dynamics so no inertial pressure. ΔP is small enough and thus set to be null in the erasure case. As the glass viscosity $\eta(T)$ is the main driven force in this process, this gives a simplified R–P equation: $\frac{dR_{pore}}{dt} = \frac{d(R_{pore}-R_{ini})}{dt} = -\frac{\sigma}{2\eta}$. It leads to $\frac{R_{pore}(t,T)}{R_{ini}(0,20°C)} = 1 - \frac{\sigma \bullet t}{2\eta(T)R_{ini}}$ which can be also deduced from Ref. [45].

Then, and as described in Appendix, by using the effective medium theory using the Maxwell-Garnet equation [63], an average refractive index of the porous nanolayer can be calculated based on nanopore radius $R_{pore}(t,T)$ introduced in a volumic filling factor (FF), i.e., the volume fraction occupied by the nanopores inside the nanolayers. We assume also that non-sphericity contribution to the birefringence is negligible. Finally, LB can be calculated using the so-called form birefringence model [51,52]. In these calculations, $R_{norm}(t,T)$ or $LB_{norm}(t,T)$ are normalized by the initial value before annealing $R_{norm}(0,T)$ and $LB_{norm}(0,T)$ respectively. In other words, $R_{norm}\left(t,T\right) = f\left(1 - \frac{\sigma \bullet t}{2\eta(T)R_{ini}}\right)$ with $f(t=0, \forall T) = 1$ and $f\left(t > \frac{2\eta(T)R_{ini}}{\sigma}\right), T\Big) = 0$. Recently, the thermal stability of form birefringence was quantitatively correlated to the one of nanograting's porosity-filling factor, which has been demonstrated recently in various oxide glasses including the ones of this study [45,51]. Their erasure kinetic, ascertained by isochronal retardance measurements and attributed to the collapse of nanopores, was well predicted from the Rayleigh–Plesset equation.

5. A distributed Rayleigh-Plesset model and its impact in the erasure process

In the following we will now develop a "distributed Rayleigh-Plesset" model by considering elasticity that is usually not negligible in the solids. At the beginning of the discussion, the variation of the apparent activation energy of the dynamical viscosity (macroscopic) with the temperature arises from a distribution of activation energy (E_i) at the microscopic level. The relevant elementary process is the change of distance (l) between two groups of atoms under a stress φ that is partly considered in the R–P model, it is the deformation: $\varepsilon = \ln\left(\frac{l}{l_0}\right)$, l_0 is the distance at rest. Due to the large number of structural configurations in the glass, the way to respond to the stress solicitation leads to consider a distribution of the activation energy according to a distribution function $g(E_i)$ normalized on all possible values (ca. 0 to ∞). Usually, one can simply use Maxwell viscoelastic model that works well for soft solids (e.g., in the vicinity of softening temperature) but here we used Kelvin-Voigt visco-elastic model allowing for example to model creep and deformation behavior at low loading. So, the relation between the stress and the deformation takes the following form:

$\varphi = G.\,\varepsilon_i(E_i,t,T) + \eta(E_i,T)\frac{d\varepsilon_i(E_i,t,T)}{dt}$ and $\eta(E_i,T) = \eta_0.\exp\left(\frac{E_i}{k_BT}\right)$, where G is the shear modulus. This gives:

$$\frac{d\varepsilon_i(E_i,t,T)}{dt} = -\frac{G}{\eta(E_i,T)}.\,\varepsilon_i(E_i,t,T) + \frac{\varphi}{\eta(E_i,T)}$$

As t is independent of T and E_i, the differential equation can be solved when considering a constant stress φ suddenly applied and we obtain:

$$\varepsilon_i(E_i,t,T) = \frac{\varphi}{G} + \left(\varepsilon_i^0 - \frac{\varphi}{G}\right)\exp\left(-\frac{G}{\eta(E_i,T)}t\right)$$

We note that when G is small in front of $\frac{\eta(E_i,T)}{t}$, $\varepsilon_i(E_i,t,T) = \varepsilon_i^0 + \frac{\varphi}{\eta(E_i,T)}t$. Also note that for a solid, G is never null. For obtaining the macroscopic value considering the glass disorder, we must make the sum over all configurations, on all values of E_i. We get:

$$\varepsilon(t,T) = \int_0^{\infty}\left(\varepsilon_i^0 - \frac{\varphi}{G}\right)\exp\left[-\frac{Gt}{\eta_0}\exp\left(-\frac{E_i}{k_BT}\right)\right]g(E_i)dE_i + \frac{\varphi}{G}$$

The first term of this solution can be treated as in the frame of VAREPA as the double exponential function can be assimilated to a Heaviside function of E_i. The cutting energy defines a demarcation energy. $E_d = k_BT\ln(k_0t)$ with $k_0 = \frac{G}{\eta_0}$. Note this is also the constant rate, k_0, we obtained using a simple Maxwell model when considering that G is small enough (e.g., in the vicinity of melting temperature). This part will be just a function of E_d after expressing t into E. Note that $\frac{1}{\eta(T)} = \int_0^{\infty}\frac{1}{\eta_0}\exp\left(-\frac{E_i}{k_BT}\right)g(E_i)dE_i$. This defines the "average viscosity".

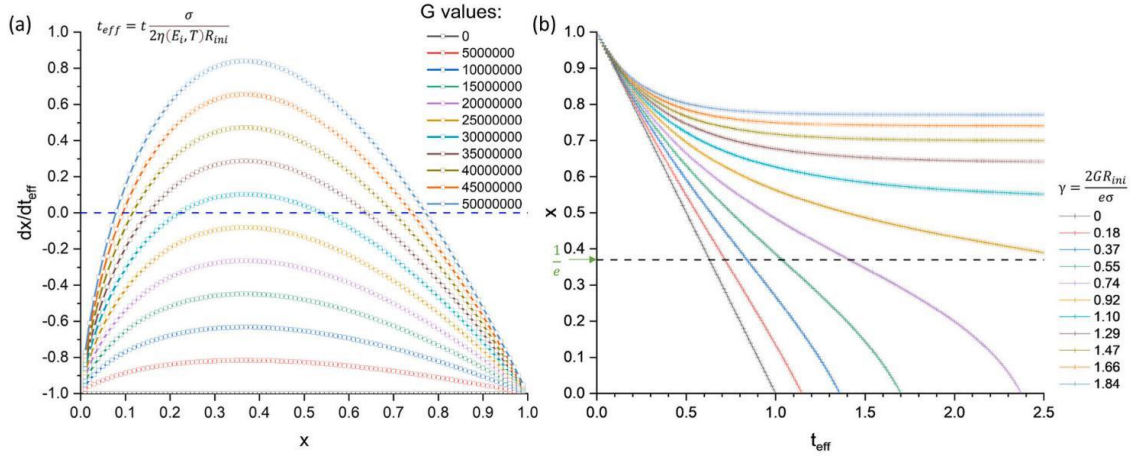

Fig. 1. (a) Plotting of dx/dt_{eff} versus x, (b) plotting of x versus effective time, t_{eff}, for various values of the shear stress G ($G = 0$ is for a liquid); for $G<e\sigma/2R_{ini}$ we have a monotonous behavior. The situation described here corresponds to high temperatures much beyond T_g when G decreases strongly.

Let us now make the remark that the nanopore radius and their eventual deformation (non-sphericity mentioned above) are quantities of the same nature and thus similar law can be applied. Now, we consider thus just one nanopore and let us apply what we showed above. Following the R–P equation and its simplification, the elementary reaction including now a visco-elastic term by taking into account that $\varepsilon_i(E_i,t,T) = \ln\left(\frac{R_i(E_i,t,T)}{R_{ini}}\right)$ and $\varphi_i = -\frac{\sigma}{2R_i(E_i,t,T)}$, the interfacial term (with the orientation convention at the interface) and σ the surface tension, we get:

$$\frac{dR_i(E_i,t,T)}{dt} = -\frac{G.}{\eta(E_i,T)}R_i(E_i,t,T)\ln\left(\frac{R_i(E_i,t,T)}{R_0}\right) + \frac{\varphi R_i(E_i,t,T)}{\eta(E_i,T)} = -\frac{G.}{\eta(E_i,T)}R_i(E_i,t,T)\ln\left(\frac{R_i(E_i,t,T)}{R_{ini}}\right) - \frac{\sigma}{2\eta(E_i,T)}$$

Without φ, the differential equation is solvable but not with it. What we must know is if the solution is a rapid varying function with E_i or not. We can rewrite the equation as the following posing $x_i(E_i,t,T) = \frac{R_i(E_i,t,T)}{R_{ini}}$.

$$\frac{dx_i(E_i,t,T)}{dt} = -\frac{G.}{\eta(E_i,T)}x_i(E_i,t,T)\ln x_i(E_i,t,T) - \frac{\sigma}{2\eta(E_i,T)R_{ini}}$$

A plot of dx/dt versus x reveals a monotonous behavior according to time and the ratio as shown in Fig. 1. When $2GR_{ini}/e\sigma < 1$ there is a monotonous behavior (as for $G = 0$, for a liquid). However, when $2GR_{ini}/e\sigma > 1$, the nanopores do not disappear and can even grow before to be erased. This gives an aspect of the nanopore resistance, i.e., it is necessary to heat above the glass-transition temperature T_g and then the viscosity determines the temporal behavior. Note the interfacial energy is not obviously increasing on heating. At high temperatures, there is no simple solution for x, but assuming G small enough in front of $e\sigma/2R_{ini}$, we can write:

$$x_i(E_i,t,T) = 1 - \frac{\sigma t}{2\eta(E_i,T)R_{ini}} - \frac{G}{\eta(E_i,T)}\int_{x(0)}^{x(t)}\frac{x\ln(x)}{dx/dt}dx$$

The numerical analysis shows that this expression leads to a rapid varying function of $x_i(E_i,t,T)$ with the energy E_i when G is large enough in front of $\frac{\sigma}{2R_{ini}}$ although smaller than $e\sigma/2R_{ini}$. In that case, the average variation of normalized nanopore radius that is obtained by summation on activation energy is $x(t,T) = \int_0^\infty x_i(E_i,t,T)g(E_i)dE_i = \int_{E_d}^\infty g(E_i)dE_i$ with a demarcation energy conventionally taken for $x_i = 0.5$, this a good approximation and the resulting distribution is not dependent of t or T. Note that when G decreases strongly much beyond T_g, the approximation is worse. So, the pseudo demarcation energy obtained in the frame of the conventional definition is $E_d(t,T) = k_BTln\left[\frac{\sigma t}{2\eta_0 R_{ini}}\right]$. Here we can state $\frac{\sigma}{2\eta_0 R_{ini}} = k_0$, that is also the reaction rate constant we can obtain using Maxwell model if G is large enough in front of $\frac{\sigma}{2R_{ini}}$ (e.g. in the vicinity of T_g). As the normalized retardance is obtained by $x(t,T)$[6], the same conclusion applied and the expressions of the pseudo-distributions are:

$$For\ isochrones, \frac{\partial R_{norm}(E_d,t)}{\partial E_d} = \begin{cases} 0, k_0te^{-\frac{Bln10}{E_d/k_B\,ln(k_0t)-T_0}} > 1 \\ \frac{6Bln10}{k_B\,ln(k_0t)}\left[1-e^{-\frac{Bln10}{E_d/k_B\,ln(k_0t)-T_0}}\right]^5 k_0te^{-\frac{Bln10}{E_d/k_B\,ln(k_0t)-T_0}}\frac{}{(E_d/k_B\,ln(k_0t)-T_0)^2}, otherwise \end{cases}$$

$$For\ Isotherms, \frac{\partial R_{norm}(E_d,T)}{\partial E_d} = \begin{cases} 0, e^{\frac{E_d}{k_BT}-\frac{Bln10}{T-T_0}} > 1 \\ \frac{6}{k_BT}\left(1-e^{\frac{E_d}{k_BT}-\frac{Bln10}{T-T_0}}\right)^5 e^{\frac{E_d}{k_BT}-\frac{Bln10}{T-T_0}}, otherwise \end{cases}$$

A priori, we have thus to make the difference between $k_{0\_isotherms}$ and $k_{0\_isochrones}$. The plot of these T dependent distribution functions in the case of SuprasilCG is shown in Fig. 2. We note that the energy range is similar and some variation with either the isochronal time or the isothermal temperature but if the variations are moderate and thus are weakly detectable on the experimental data. This dispersion arises from the dispersion of activation energy on the viscosity in the model. The relations between the position of the maximum and the viscosity at the same T can be obtained. Through derivation of the viscosity law as a function of T, the activation energy in the viscosity is $E_{visco} = \frac{k_BT^2Bln10}{(T-T_0)^2}$. For isotherms: $E_{isoT} = \frac{k_BTBln10}{T-T_0} - 1.8k_BT$. As seen in Fig. 2b, the shift remains quite small, 0.1–0.2 eV with respect to the 6 eV. So, the position of the pseudo master curve at $R_{norm} = 0.5$ is almost coincident with the activation energy of the viscosity at the operating T. *So, from that point, the VAREPA framework can now be tentatively applied to data obtained through Rayleigh-Plesset data* thus we can make the link not only between the matter and k_0 but also between the distribution and the temperature dependence of viscosity.

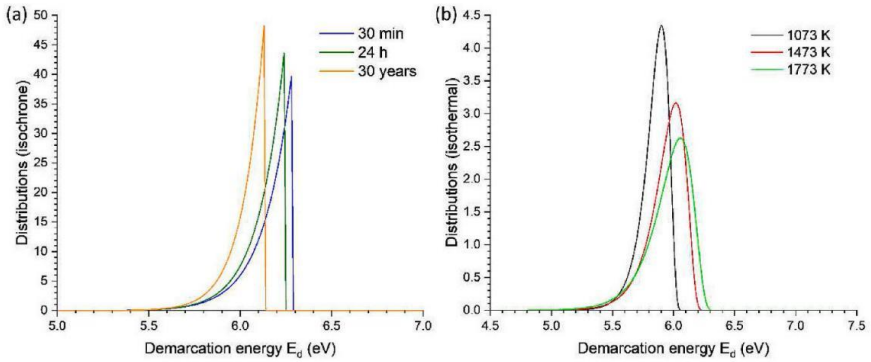

Fig. 2. Plotting of the T dependent distribution functions for SuprasilCG silica. (a) is for isochronal experiments, while (b) is for isothermal ones.

6. Applying VAREPA approach to data provided by Rayleigh-Plesset model

6.1. Building the master curve from Rayleigh-Plesset simulated R_{norm} values

Normalized retardance values, $R_{norm}(t,T)$, were calculated based on the Rayleigh-Plesset equation (see Section 4), for a serie of isothermal annealing conditions. Fig. 3 shows such predicted R_{norm} values in the case of SuprasilCG silica for several temperatures ranging from 1100 °C to 1350 °C for a total time duration of 24 h (plotted according to log time in Fig. 3a), and according to an activation energy defined as $k_BTln(t)$ in Fig. 3b. It is worth pointing out that during the numerical simulation, the effect of temperature was introduced by varying the viscosity $\eta(T)$. The viscosity was calculated using Vogel-Fulcher-Tammann (VFT) law taking the form $\log(\eta, Pa \bullet s) = A - 1 + \frac{B}{T-T_0}$, and all parameters (A, B and T_0) are available in Ref. [45]. Here, the initial pore size was set to 30 nm for SuprasilCG, which is a typical value that was obtained from electron microscopy imaging analysis from Ref. [45]. As expected, $R_{norm}(t,T)$ decreases faster for the highest temperatures, for which the viscosity is lower. Indeed, a lower viscosity facilitates the collapse of the nanopores, hence the decrease of R_{pore} and FF, and ultimately R_{norm}. If all the curves follow the same trend, they appear shifted when plotted as a function of $k_BTln(t)$ as seen in Fig. 3b. The shift is $k_BTln(k_0)$ and one can tentatively try to gather the isotherms into a single curve by identifying the k_0 value. To do this, the k_0 value is progressively varied using least squares optimization until the χ^2 value reaches a minimum. Here, the optimal/best curves overlapping is found for $k_0 = 7.45 \times 10^{16}$ s^{-1} ($ln\ k_0 = 38.85$ where χ^2 is minimized). The results are provided in Fig. 4, with the merged curve identified as a Master Curve, and the optimization shown in the inset. From the inset, the uncertainty on k_0 can be calculated in the range of $ln\ k_0 = 38.8 \pm 0.8$ with a 90% confidence interval. *So, from that point, it appears that VAREPA framework may be applied on Rayleigh-Plesset data but one must keep in mind the restrictions mentioned above, in particular the T dependence of the distribution.*

6.2. Comparing the modeled master curve to experimental ageing data

VAREPA framework was now applied for 8 oxide glasses namely Schott Borofloat 33, BK7 and AF32, Corning ULE, EagleXG and 7059, Sodalime, and Heraeus Suprasil CG whose viscosity laws and compositions can be found in Ref. [45]. Here we have fixed the nanopores radius (R_{ini} = 30–50 nm) [2,3] and the surface tension (σ = 0.3 J m^{-2}) for all glasses and we have simply adjusted $\eta(T)$. Following this procedure, it was possible to simulate thermal aging data using Rayleigh-Plesset model to feed coherently VAREPA, so we obtain a Master Curve and the corresponding k_0 for all investigated glasses. A set of specific examples is shown in Fig. 3a with Borofloat 33, ULE and SurprasilCG. Following this work, and to validate these predicted lifetime curves, step isochronal annealing experiments were performed to verify if the datapoint would align on Master Curve. Since the experimental data were obtained from step isochronal annealing, one must first evaluate if the isochronal datapoints are independent. The achieved condition for independency of the datapoints is $(\Delta t \bullet k_0)^{-\left(\frac{\Delta T}{T_{max}}\right)} \ll 1$ [54], where Δt is the time step (30 min) of the isochronal annealing experiment; ΔT is the temperature step separating two datapoints; T_{max} is the maximum temperature during the isochronal experiment. In this work, this criterion is mostly satisfied for all data.

In Fig. 5a, the experimental R_{norm} (Δt = 30 min, T) resulting from step-isochronal annealing as a function of E_d are drawn and compared to

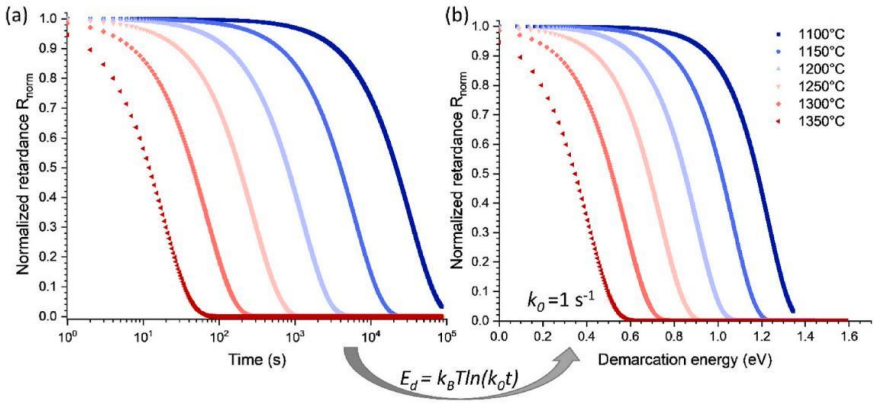

Fig. 3. (a) Calculated $\boldsymbol{R_{norm}}$ as a function of **time** for a series of isotherms. (b) Identical $\boldsymbol{R_{norm}}$ data but plotted as a function of $\boldsymbol{k_BTln(t)}$. Data were calculated for SuprasilCG silica glass with an initial pore diameter R_{ini} of 30 nm and σ = 0.3 J m^{-2}.

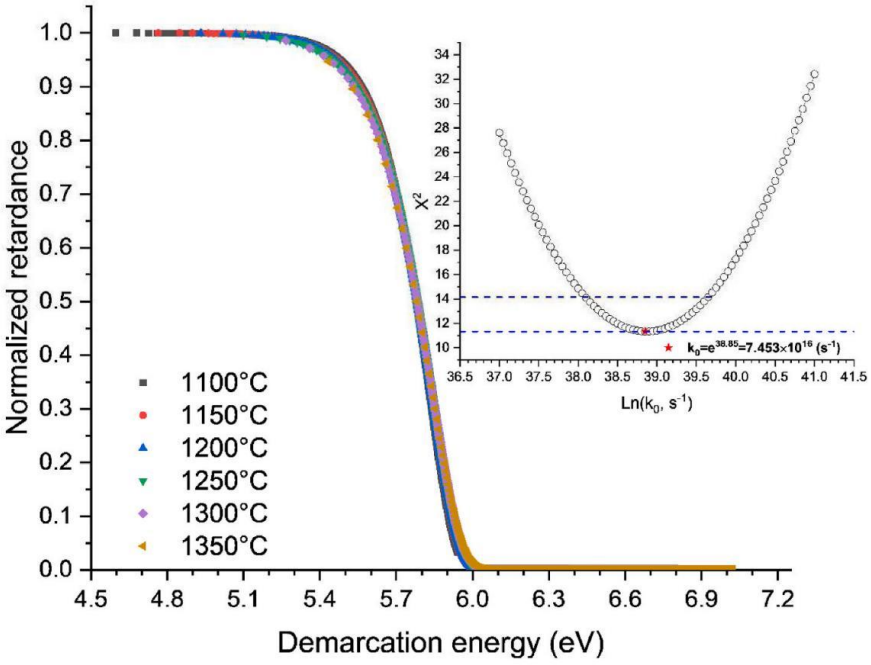

Fig. 4. Master curve of simulated data in Fig. 1(b) with an optimized k_0 value. Note that E_d for $R_{norm} = 0.5$ is around 5.8 eV for SiO_2. The inset shows the least squares method to obtain **the best** k_0. All data are for SuprasilCG silica.

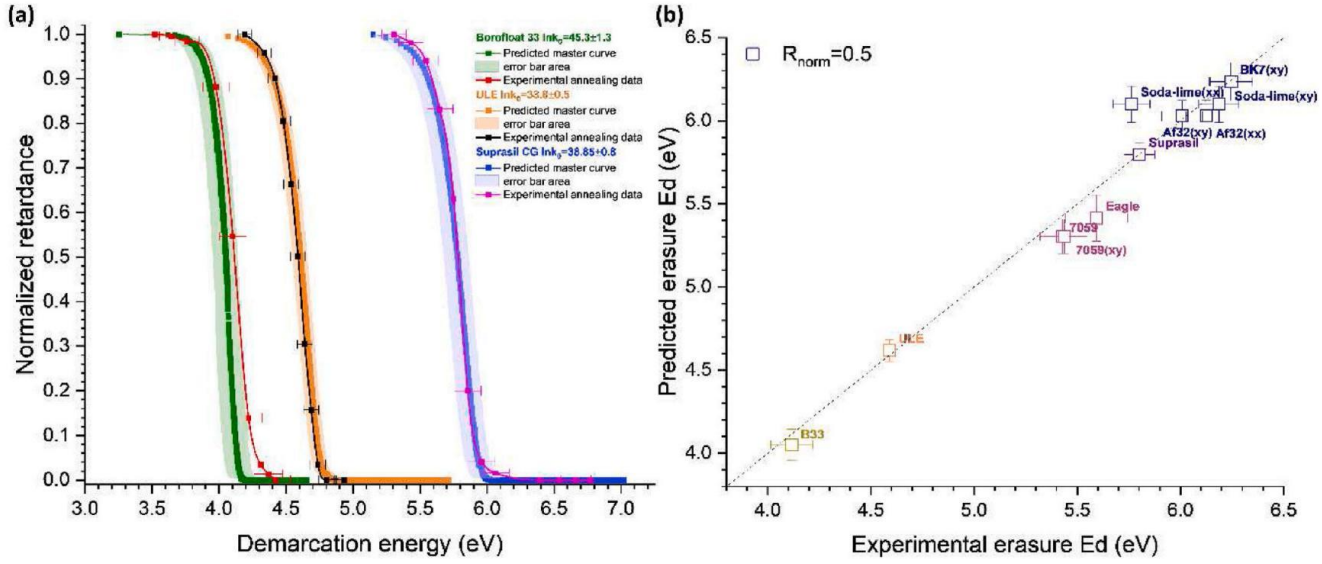

Fig. 5. (a) The MC curves of Borofloat 33, ULE, and Suprasil CG glasses, along with experimental data obtained from step isochronal thermal annealing. (b) The predicted erasure E_d values of different oxide glasses as a function of experimental one taken at $R_{norm} = 0.5$. The error bar is from the confidence interval of k_0.

the theoretical master curves within the whole E_d interval for those three glasses. It appears there that experimental results are matching the predicted master curves deduced from the Rayleigh-Plesset modeling within the error bar from the confidence interval of k_0. To generalize the comparison between predicted and the experimental master curve for all glasses, we tentatively compared the E_d values (predicted and experimental ones) for multiple degrees of erasure. As an example, in Fig. 5b the predicted versus experimental E_d values for 8 oxide glasses are displayed, taking $R_{norm} = 0.5$ (corresponding to 50% erasure). As can be shown in the figure, experimental and simulated results are in excellent agreement. Note that this degree of erasure was validated from 20% up to 99% (not presented here), strengthening our approach. The quite good agreement between model and experimental data may suggest that the glass viscosity η(T) has not been impacted significantly by the laser writing process and the formation of nanogratings while Frenkel defects and eventually Si formation happen at the nanopores interface due to the SiO_2 reduction as discussed in section 5.

7. Lifetime prediction

Using VAREPA framework, we show above that $R_{norm}(t, T)$ can be expressed as a function of the unique variable called demarcation energy

E_d. The curve $R_{norm}(E_d)$ is called Master Curve. In simple cases, it is unique whatever the (t, T) couple may be but here we show that the distribution is T or t dependent. So, we can note that T is not equivalent to ln(t) in E_d expression and thus isochronal ageing data are not equivalent to isothermal ageing data for establishing MC. Anyway, for specific using conditions (t_{use}, T_{use}), we can determine k_0 values for any glasses and thus the corresponding E_d limit. Then the MC plot allows the user to predict the optical component lifetime, providing that the anticipated conditions of use $E_d = f(t_{use}, T_{use})$ correspond to a point on the MC that has been actually sampled during the annealing experiments. Let us go on further to exemplify such prediction in all investigated optical glasses. There are two solutions: one is to fit the Master Curve with a polynomial function and the second one is to fit a known expression. Since the life function is now available, it is possible to calculate the lifetime for either isothermal or isochronal working conditions, e.g. $T =$ 600 °C and 30 years, by using the optimized k_0 value (determined following the above procedure) As a results, for predictions shown in Fig. 6, R_{norm} will decrease to 0.95 at 600 °C for AF32 glass and 30 years' duration or 42% erasure in Eagle XG glass while there is no significant erasure for silica in these conditions. Among the investigated glasses, Suprasil silica glass (above hundred million years) has the longest lifetime, whereas BK7 (around 10 min) holds the shortest one. In addition, it is also possible to increase the lifetime of these components eventually. The principle is based on the distribution of activation energies and thus nanopores stability at various sites. A burning step during the process suppresses the less stable sites, which cannot be achieved with a simple exponential kinetic. This widespread method has been proven to be effective for enhancing the stability of index changes in UV written Fiber Bragg Gratings [39] but also in fs-laser induced FBG [40]. Of interest, our approach based on nanopores erasure kinetics is quite general and one can predict others optical properties related to nanopores by linking the adequate optical model to the nanopores population. For example, one can predict not only nanopores birefringence or nanogratings form birefringence but also light scattering or anisotropic light scattering dependence on time and temperature. Another possibility would be to predict refractive index changes using effective medium theory or eventually more complex objects such as the spectral properties of FBG for various sensing applications.

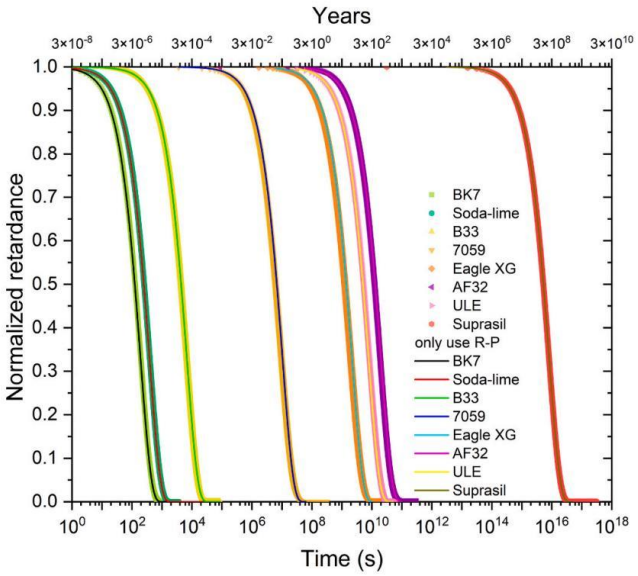

Fig. 6. The predicted lifetime of normalized retardance for isothermal annealing at 600 °C in all investigated glasses. Dots are for predictions made with VAREPA approach whereas full lines are for predictions made using the Rayleigh-Plesset equation.

8. Discussion

Within this work, a distributed Rayleigh-Plesset model was developed to make the link with VAREPA framework and then to obtain master curves using a database made on simulated R–P data. The validity of the approach was further confirmed using step isochronal annealing experiments. From that point we performed some examples of lifetime prediction according to (t_{use}, T_{use}) based on a rationale extrapolation made within VAREPA that was successfully compared to Rayleigh-Plesset predictions.

The main driving force is the interfacial force, but the viscosity is the limiting process. It is commonly assumed that shear viscosity is a thermally activated process. Viscous flow follows an Arrhenius law in the high and low (typ. below the strain point) temperature limit regimes with constant activation energy in a Frenkel-Andrade model [64]. However, between high and low temperature regimes, the activation energy of flow changes and the viscosity cannot be described simply using the Arrhenius-type behavior. For example, the activation energy of viscosity varies with temperature [65–68] and there is a need to introduce a distribution of activation energy [58,69–71]. More specifically, in the intermediate T range between strain and melting points, the VFT model [72,73] is commonly used especially in the industry, which is derivate from free volume theory, and can be written as $\log(\eta, Pa \bullet s) = A - 1 + \frac{B}{T - T_0}$, where A and B are temperature independent and T_0 is the extrapolated temperature where viscosity tends to infinity. This empirical equation of viscosity converts to $\eta(T) = \eta_0 e^{\frac{B \ln 10}{T - T_0}}$ where $\eta_0 = 10^{A-1}$. Developing the distributed Rayleigh-Plesset model, we have identified above that k_0 takes the following form $k_0 = \frac{\sigma}{2\eta_0 R_{ini}}$ and we have extracted the expression of the master curve and its differentiation (i.e., the distribution) that is not solely proportional to E_d but also to the working temperature (for isotherms). The origin of this T dependence is simply related to the chosen expression of the glass viscosity $\eta(T)$ and inherent to its non-Arrhenius behavior. In addition, in the literature, the apparent activation energy that can be derived from $\ln \eta$ vs $1/T$ can be found around 4.0 eV for $T > 2000$ °C (up to 2400 °C for Ref. [68]) and around 8.1 eV for $T = 1400$ °C [67,74–76] for silica. This agrees with recent results from Shao et al. in the 1000–1200 °C temperature range [65]. For sodalime silicate, the apparent activation energy lied around 4–6 eV for temperatures within T_g - 1.4T_g [77]. These values agree with activation energies deduced within our framework, which originated from the viscosity. Note that the irradiated glass structure is slightly different with Frenkel defects, silicon formation [78] at the interfaces due to the SiO_2 reduction and a larger fictive temperature after a first pulse resulting in a smaller viscosity with different η_0 and activation energy. However, within the logic of the prediction procedure, there is no importance excepted that the proof of the model is more difficult.

In the intermediate temperature range (between strain and meting temperatures), Adam-Gibbs (AG) [79] and Avramov and Milchev (AM) [70] developed viscosity models based on a different theory which fits well viscosity measurements like the VFT model (relative to an Arrhenius law). Of interest here, AM viscosity model assumes that the magnitude of activation energy varies due to the disordered nature of glass. Consequently, the distribution function of the activation energy is determined by its configurational entropy $S_{conf}(T)$ [58]. The viscosity can be written as $ln\,\eta(T) = A_{AM} + 2,3(12,5 - A_{AM})\left(\frac{T_g}{T}\right)^{\alpha}$ where the glass-transition temperature (T_g) is defined as $ln\,\eta(T), Pa \bullet s = 12.5$ and α is the Avramov fragility parameter, that is related to the distribution width. In this model the resulting activation energy distribution is thus a T dependent function as we discussed above. However, if the working conditions (t_{use}, T_{use}) fall down within a reasonable temperature range, e.g., below or around the strain point, the viscosity can thus be approximated by an Arrhenius law (i.e. the Frenkel-Andrade model [64]). As a result, the Master Curve and the underlying distribution g(E_d) will be independent of the temperature within this restricted range of

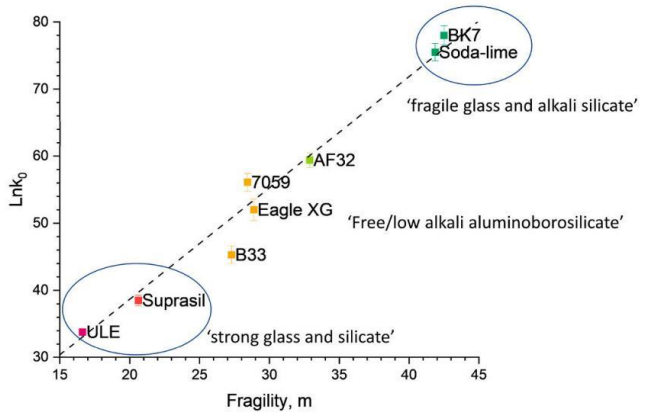

Fig. 7. Relationship between lnk_0 and Angell glass fragility m in the investigated glasses. k_0 values were determined by feeding VAREEPA framework using simulated RP data and confirmed through step isochronal annealing experiments.

temperatures.

Trying to bring some roadmap for engineers, one can compare k_0 values (obtained using VAREPA being fed by Rayleigh-Plesset data) to the Angell fragility, m, deduces from the slope of the glass viscosity-temperature curve when T approach T_g, thus defined as $m = \frac{\partial \log \eta(T)}{\partial \frac{T_g}{T}}|_{T=T_g}$ [80]. It reflects the strong or fragile behavior of the glass material. From the AM expression we obtain $m = \alpha(12.5 - A_{AM}), where\ A_{AM} = \ln(\eta_0)$ which is thus link with the above-suggested expression of $k_0 = \frac{\sigma}{2\eta_0 R_{ini}}$. Illustrating this purpose, Fig. 7 shows $\ln(k_0)$ as a function of the fragility m revealing a linear correlation for all investigated oxide glasses. Note that here we assume surface tension σ remains similar (around 0.3 J m^{-2} for all glasses) and the same initial pore size (around 30 nm) in all investigated oxide glasses. As a guideline, the erasure constant rate k_0 is much smaller for "strong glasses" like SuprasilCG and ULE whereas k_0 own higher values (faster nanopores erasure) for "fragile glasses" such as BK7 and Soda-lime glass while alumino-borosilicate remain in the intermediate range.

9. Conclusion

In conclusion, the VAREPA framework was applied to determine the lifetime of IR-fs Type II modifications (i.e., nanogratings) written in 8 commercial optical glasses. Providing several assumptions are fulfilled, this Master Curve could effectively be obtained in all investigated oxide glasses and was shown to originate from the distribution of the glass viscosity thanks to a distributed Rayleigh-Plesset model. The approach was further strengthened by comparing the Master Curves to accelerated aging experiments through the monitoring of nanogratings birefringence signature. In addition, the log of the erasure constant rate, $\ln(k_0)$, was shown to linearly scale up together with the Angell's glass fragility. These conclusions are expected to provide guidelines for the future exploitation of nanogratings [2,3] and related devices such optical data storage, birefringent devices or sensors written in wide range of oxide glasses.

Funding

This research is funded by Agence Nationale de la Recherche (ANR), FLAG-IR Project, award number ANR-18-CE08-0004-01; and REFRACTEMP project, award number ANR-22-CE08-0001-01. Qiong Xie acknowledges the China Scholarship Council (CSC) for the funding of her PhD fellowship, NO.202007040018.

Disclosures

The authors declare no conflicts of interest.

Author contributions

Conceptualization, M.C. and M.L.; Funding acquisition, M.L.; Investigation, Q.X.; Methodology, Q.X., M.C., B.P. and M.L.; Project administration, M.L.; Resources, M.L.; Supervision, M.L. and M.C.; Validation, Q.X.; Visualization, Q.X. and M.C.; Writing—original draft, Q.X.; Writing—review & editing, Q.X., M.C., B.P. and M.L. All authors have read and agreed to the published version of the manuscript.

Declaration of competing interest

The authors declare that they have no known competing financial interests or personal relationships that could have appeared to influence the work reported in this paper.

Acknowledgments

Qiong Xie is grateful to Jiafeng Lu for the help of Matlab coding.

Appendix

The form birefringence related to the so-called nanogratings is quantitatively correlated to the porosity-filling factor of these nanostructures has been demonstrated by our group recently [51]. The nanopore size diameter from the R–P equation needs to be converted into a normalized retardance (R) value. In the first step, the Maxwell-Garnet equation is first used to calculate the average refractive index of the porous nanolayer (n_{pl}):

$$n_{pl} = \sqrt{n_G^2 \frac{n_G^2 + \frac{(1+2FF)}{3}\left(n_{pore}^2 - n_G^2\right)}{n_G^2 + \frac{(1-FF)}{3}\left(n_{pore}^2 - n_G^2\right)}}. \quad \text{(A1)}$$

n_G is the glass refractive index (taken as $n_G = 1.4599$, index of silica at 551 nm), n_{pore} is the nanopore refractive index (taken equal to 1). Another important factor is the filling factor (FF) which is defined as the proportion of the nanopores' volume taken in a unit volume of porous nanolayer (V), so it is obviously related to the number of nanopores (N) with an averaged nanopore radius (R_{pore}) and can be calculated using:

$$FF = N\frac{4\pi R_{pore}^3}{3V}. \quad \text{(A2)}$$

The birefringence LB can be determined by the difference between the refractive indices of the ordinary axis (n_o) and the extraordinary axis (n_e). The following equation illustrates the detail:

$$LB = n_o - n_e = \sqrt{\left[1-\frac{\delta}{\Lambda}\right]n_G^2 + \frac{\delta}{\Lambda}n_{pl}^2} - \left[\sqrt{\frac{\left[1-\frac{\delta}{\Lambda}\right]}{n_G^2} + \frac{\frac{\delta}{\Lambda}}{n_{pl}^2}}\right]^{-1} . \quad \text{(A3)}$$

n_G represents the refractive index between the porous nanolayers, Λ is the average spacing between nanolayers, δ is the porous nanolayer thickness, and $(\Lambda - \delta)$ is the interlayer thickness. With the birefringence LB calculated, the retardance R can be worked out by the expression $R = LB \times l$, where LB is the birefringence and l is the length of the birefringent object being measured. We assume the $R_{norm}(t,T)$ and $LB_{norm}(t,T)$ are normalized by the initial value $R_{norm}(0,T)$ and $LB_{norm}(0,T)$ respectively. They change square of FF and the sixth power of R_{pore}.

References

[1] K. Itoh, S. Nolte, C.B. Schaffer, W. Watanabe, Ultrafast processes for bulk modification of transparent materials, MRS Bull. 31 (2006) 620–625, https://doi.org/10.1557/mrs2006.159.

[2] Y. Shimotsuma, P.G. Kazansky, J. Qiu, K. Hirao, Self-organized nanogratings in glass irradiated by ultrashort light pulses, Phys. Rev. Lett. 91 (2003) 247405, https://doi.org/10.1103/PhysRevLett.91.247405.

[3] H. Yao, Q. Xie, M. Cavillon, Y. Dai, M. Lancry, Materials roadmap for inscription of nanogratings inside transparent dielectrics using ultrafast lasers, Prog. Mater. Sci. 142 (2024) 101226, https://doi.org/10.1016/j.pmatsci.2023.101226.

[4] M. Lancry, B. Poumellec, J. Canning, K. Cook, J.-C. Poulin, F. Brisset, Ultrafast nanoporous silica formation driven by femtosecond laser irradiation, Laser Photon. Rev. 7 (2013) 953–962, https://doi.org/10.1002/lpor.201300043.

[5] M. Cavillon, J. Cao, M. Vallet, F. Brisset, L. Mazerolles, B. Dkhil, M. Lancry, B. Poumellec, Thermal and electron plasma effects on phase separation dynamics induced by ultrashort laser pulses, Crystals 12 (2022) 496, https://doi.org/10.3390/cryst12040496.

[6] E. Bricchi, B.G. Klappauf, P.G. Kazansky, Form birefringence and negative index change created by femtosecond direct writing in transparent materials, Opt Lett. 29 (2004) 119–121, https://doi.org/10.1364/OL.29.000119.

[7] J. Lu, J. Tian, B. Poumellec, E. Garcia-Caurel, R. Ossikovski, X. Zeng, M. Lancry, Tailoring chiral optical properties by femtosecond laser direct writing in silica, Light Sci. Appl. 12 (2023), https://doi.org/10.1038/s41377-023-01080-y.

[8] M. Beresna, M. Gecevičius, P.G. Kazansky, Ultrafast laser direct writing and nanostructuring in transparent materials, Adv. Opt Photon 6 (2014) 293–339, https://doi.org/10.1364/AOP.6.000293.

[9] R. Drevinskas, P.G. Kazansky, High-performance geometric phase elements in silica glass, APL Photonics 2 (2017), https://doi.org/10.1063/1.4984066.

[10] J. Zhang, M. Gecevicius, M. Beresna, P.G. Kazansky, Seemingly unlimited lifetime data storage in nanostructured glass, Phys. Rev. Lett. 112 (2014) 033901, https://doi.org/10.1103/PhysRevLett.112.033901.

[11] H. Wang, Y. Lei, L. Wang, M. Sakakura, Y. Yu, G. Shayeganrad, P.G. Kazansky, 100-Layer error-free 5D optical data storage by ultrafast laser nanostructuring in glass, Laser Photon. Rev. 16 (2022) 2100563, https://doi.org/10.1002/lpor.202100563.

[12] R. Osellame, G. Cerullo, R. Ramponi, Femtosecond Laser Micromachining: Photonic and Microfluidic Devices in Transparent Materials, Springer, 2012.

[13] S. Mihailov, D. Grobnic, C. Hnatovsky, R. Walker, P. Lu, D. Coulas, H. Ding, Extreme environment sensing using femtosecond laser-inscribed fiber Bragg gratings, Sensors 17 (2017) 2909, https://doi.org/10.3390/s17122909.

[14] D. Grobnic, C. Hnatovsky, S. Dedyulin, R.B. Walker, H. Ding, S.J. Mihailov, Fiber Bragg grating wavelength drift in long-term high temperature annealing, Sensors 21 (2021) 1454.

[15] J. Canning, Fibre gratings and devices for sensors and lasers, Laser Photon. Rev. 2 (2008) 275–289, https://doi.org/10.1002/lpor.200810010.

[16] B. Poumellec, I. Riant, C. Tessier-Lescourret, Precise life-time prediction using demarcation energy approximation for distributed activation energy reaction, J. Phys. Condens. Matter 18 (2006) 2199, https://doi.org/10.1088/0953-8984/18/7/009.

[17] R. Kashyap, Chapter 9 - measurement and characterization of gratings, in: R. Kashyap (Ed.), Fiber Bragg Gratings, Academic Press, San Diego, 1999, pp. 409–446.

[18] L. Maurin, N. Roussel, G. Laffont, Optimally temperature compensated FBG-based sensor dedicated to non-intrusive pipe internal pressure monitoring, Frontiers in Sensors 3 (2022), https://doi.org/10.3389/fsens.2022.835140.

[19] G. Laffont, R. Cotillard, N. Roussel, R. Desmarchelier, S. Rougeault, Temperature resistant fiber Bragg gratings for on-line and structural health monitoring of the next-generation of nuclear reactors, Sensors 18 (2018) 1791.

[20] Y. Corre, G. Laffont, C. Pocheau, R. Cotillard, J. Gaspar, N. Roussel, M. Firdaouss, J.-L. Gardarein, D. Guilhem, M. Missirlian, Integration of fiber Bragg grating temperature sensors in plasma facing components of the WEST tokamak, Rev. Sci. Instrum. 89 (2018), https://doi.org/10.1063/1.5024514.

[21] J.-B. Quelene, N. Salhi, R. Desmarcheliers, M.-C.P. Huy, R. Cotillard, S. Rougeault, D. Pohl, G. Laffont, Fiber Bragg Grating temperature monitoring of helicopter engine mechanical parts on an engine test bench, in: 27th International Conference on Optical Fiber Sensors, Optica Publishing Group, Alexandria, Virginia, 2022, pp. W4–W16.

[22] G. Adamovsky, J.R. Mackey, B.M. Floyd, K. Elam, M. Martinez, Development and performance verification of fiber optic temperature sensors in high temperature engine environments, 50th AIAA/ASME/SAE/ASEE Joint Propulsion Conference.

[23] F.J. Dutz, S. Boje, U. Orth, A.W. Koch, J. Roths, High-temperature profile monitoring in gas turbine exhaust-gas diffusors with six-point fiber-optic sensor array, International Journal of Turbomachinery, Propulsion and Power 5 (2020) 25.

[24] W. Tomboza, R. Cotillard, N. Roussel, M.C.P. Huy, G. Bouwmans, G. Laffont, Characterization of femtosecond laser micromachined fiber in-line pressure sensor for simultaneous measurement of high temperature and pressure, in: Optica Advanced Photonics Congress 2022, Optica Publishing Group, Maastricht,Limburg, 2022 BTh2A.3.

[25] J. He, B. Xu, X. Xu, C. Liao, Y. Wang, Review of femtosecond-laser-inscribed fiber Bragg gratings: fabrication technologies and sensing applications, Photonic Sensors 11 (2021) 203–226, https://doi.org/10.1007/s13320-021-0629-2.

[26] D.R. Alla, D.P. Neelakandan, F. Mumtaz, R.E. Gerald, L. Bartlett, R.J. O'Malley, J. D. Smith, J. Huang, Cascaded sapphire fiber Bragg gratings inscribed by femtosecond laser for molten steel studies, IEEE Trans. Instrum. Meas. 73 (2024) 1–8, https://doi.org/10.1109/TIM.2023.3335530.

[27] C. Bauer, M. Erber, G. Fuchs, T. Brügge, C. Hartmann, W. Volk, Analysis of the melting and solidification process of aluminum in a mirror furnace using Fiber-Bragg-Grating and numerical models, IOP Conf. Ser. Mater. Sci. Eng. 1281 (2023) 012063, https://doi.org/10.1088/1757-899X/1281/1/012063.

[28] S.I. Kim, H.Y. Jung, S. Yang, J. Yoon, H. Lee, W. Ryu, 3D Printing of a miniature turbine blade model with an embedded fibre Bragg grating sensor for high-temperature monitoring, Virtual Phys. Prototyp. 17 (2022) 156–169, https://doi.org/10.1080/17452759.2021.2017545.

[29] R. Richert, A. Blumen, Disorder Effects on Relaxational Processes, Springer Berlin, Heidelberg, 1994.

[30] T. Erdogan, V. Mizrahi, P.J. Lemaire, D. Monroe, Decay of UV-Induced Fiber Bragg Gratings, Conference on Optical Fiber Communication, Optica Publishing Group, San Jose, California, 1994, p. TuL4.

[31] S. Ishikawa, A. Inoue, M. Harumoto, T. Enomoto, H. Kanamori, Adequate aging condition for fiber Bragg grating based on simple power law model, OFC '98. Optical Fiber Communication Conference and Exhibit, in: Technical Digest. Conference Edition. 1998 OSA Technical Digest Series, vol. 2, IEEE Cat. No.98CH36177, 1998, pp. 183–184.

[32] J.C. Phillips, Microscopic theory of the Kohlrausch relaxation constant βK, J. Non-Cryst. Solids 172–174 (1994) 98–103, https://doi.org/10.1016/0022-3093(94)90421-9.

[33] W.A. Yager, The distribution of relaxation times in typical dielectrics, Physics 7 (1936) 434–450, https://doi.org/10.1063/1.1745355.

[34] V. Vand, A theory of the irreversible electrical resistance changes of metallic films evaporated in vacuum, Proc. Phys. Soc. 55 (1943) 222.

[35] W. Primak, Kinetics of processes distributed in activation energy, Phys. Rev. 100 (1955) 1677–1689, https://doi.org/10.1103/PhysRev.100.1677.

[36] P. Lemaire, Behavior of single mode MCVD fibers exposed to hydrogen, Proc. 10th ECOC (1984) 306–307.

[37] S. Kannan, P.J. Lemaire, J. Guo, M.J. LuValle, Reliability Predictions on Fiber Gratings through Alternate Methods, Bragg Gratings, Photosensitivity, and Poling in Glass Fibers and Waveguides: Applications and Fundamentals, Optica Publishing Group, Williamsburg, Virginia, 1997 BSuD.3.

[38] B. Poumellec, M. Lancry, Kinetics of thermally activated physical processes in disordered media, Fibers 3 (2015) 206–252, https://doi.org/10.3390/fib3030206.

[39] M. Lancry, B. Poumellec, S. Costes, J. Magné, Reliable lifetime prediction for passivated fiber Bragg gratings for telecommunication applications, Fibers 2 (2014) 92–107, https://doi.org/10.3390/fib2010092.

[40] Y. Wang, M. Lancry, M. Cavillon, B. Poumellec, Lifetime prediction of nanogratings inscribed by a femtosecond laser in silica glass, Opt Lett. 47 (2022) 1242–1245, https://doi.org/10.1364/OL.449486.

[41] A. Rudenko, J.P. Colombier, T.E. Itina, Nanopore-mediated ultrashort laser-induced formation and erasure of volume nanogratings in glass, Phys. Chem. Chem. Phys. 20 (2018) 5887–5899, https://doi.org/10.1039/c7cp07603g.

[42] M.S. Plesset, The dynamics of cavitation bubbles, J. Appl. Mech. 16 (1949) 277–282, https://doi.org/10.1115/1.4009975.

[43] Y. Wang, M. Cavillon, N. Ollier, B. Poumellec, M. Lancry, An overview of the thermal erasure mechanisms of femtosecond laser-induced nanogratings in silica glass, Phys. Status Solidi 218 (2021) 2100023, https://doi.org/10.1002/pssa.202100023.

[44] Y. Bellouard, E. Block, J. Squier, J. Gobet, Plasmon-less surface enhanced Raman spectra induced by self-organized networks of silica nanoparticles produced by femtosecond lasers, Opt Express 25 (2017) 9587–9594, https://doi.org/10.1364/OE.25.009587.

[45] Q. Xie, M. Cavillon, B. Poumellec, M. Lancry, Upper temperature limit for nanograting survival in oxide glasses, Appl. Opt. 62 (2023) 6794–6801, https://doi.org/10.1364/AO.496351.

[46] S. Lotarev, S. Fedotov, A. Lipatiev, M. Presnyakov, P. Kazansky, V. Sigaev, Light-driven nanoperiodical modulation of alkaline cation distribution inside sodium silicate glass, J. Non-Cryst. Solids 479 (2018) 49–54, https://doi.org/10.1016/j.jnoncrysol.2017.10.008.
[47] S.V. Lotarev, S.S. Fedotov, A.I. Kurina, A.S. Lipatiev, V.N. Sigaev, Ultrafast laser-induced nanogratings in sodium germanate glasses, Opt Lett. 44 (2019) 1564–1567, https://doi.org/10.1364/OL.44.001564.
[48] Y. Shimotsuma, S. Mori, Y. Nakanishii, E. Kim, M. Sakakura, K. Miura, Self-assembled glass/crystal periodic nanostructure in Al_2O_3-Dy_2O_3 binary glass, Appl. Phys. A 124 (2018) 82, https://doi.org/10.1007/s00339-017-1507-z.
[49] Y. Wang, S. Wei, M.R. Cicconi, Y. Tsuji, M. Shimizu, Y. Shimotsuma, K. Miura, G. D. Peng, D.R. Neuville, B. Poumellec, M. Lancry, Femtosecond laser direct writing in SiO2-Al2O3 binary glasses and thermal stability of Type II permanent modifications, J. Am. Ceram. Soc. 103 (2020) 4286–4294, https://doi.org/10.1111/jace.17164.
[50] J. Cao, M. Lancry, F. Brisset, L. Mazerolles, R. Saint-Martin, B. Poumellec, Femtosecond laser-induced crystallization in glasses: growth dynamics for orientable nanostructure and nanocrystallization, Cryst. Growth Des. 19 (2019) 2189–2205, https://doi.org/10.1021/acs.cgd.8b01802.
[51] M. Cavillon, Y. Wang, B. Poumellec, F. Brisset, M. Lancry, Erasure of nanopores in silicate glasses induced by femtosecond laser irradiation in the Type II regime, Appl. Phys. A 126 (2020) 876, https://doi.org/10.1007/s00339-020-04062-8.
[52] M. Born, E. Wolf, Principles of Optics: Electromagnetic Theory of Propagation, Interference and Diffraction of Light, Elsevier, 2013.
[53] T. Erdogan, V. Mizrahi, P.J. Lemaire, D. Monroe, Decay of ultraviolet-induced fiber Bragg gratings, J. Appl. Phys. 76 (1994) 73–80, https://doi.org/10.1063/1.357062.
[54] D. Razafimahatratra, P. Niay, M. Douay, B. Poumellec, I. Riant, Comparison of isochronal and isothermal decays of Bragg gratings written through continuous-wave exposure of an unloaded germanosilicate fiber, Appl. Opt. 39 (2000) 1924–1933, https://doi.org/10.1364/AO.39.001924.
[55] O. Deparis, D.L. Griscom, P. Mégret, M. Decréton, M. Blondel, Influence of the cladding thickness on the evolution of the NBOHC band in optical fibers exposed to gamma radiations, J. Non-Cryst. Solids 216 (1997) 124–128, https://doi.org/10.1016/S0022-3093(97)00123-3.
[56] Y. Mohanna, J.M. Saugrain, J.C. Rousseau, P. Ledoux, Relaxation of internal stresses in optical fibers, J. Lightwave Technol. 8 (1990) 1799–1802, https://doi.org/10.1109/50.62873.
[57] J.P. van den Brink, Master stress relaxation function of silica glasses, J. Non-Cryst. Solids 196 (1996) 210–215, https://doi.org/10.1016/0022-3093(95)00588-9.
[58] M.I. Ojovan, Viscosity and glass transition in amorphous oxides, Adv. Condens. Matter Phys. 2008 (2008) 1–23, https://doi.org/10.1155/2008/817829.
[59] J. Orenstein, M. Kastner, Photocurrent transient spectroscopy: measurement of the density of localized states in a-as_2Se_3, Phys. Rev. Lett. 46 (1981) 1421–1424, https://doi.org/10.1103/PhysRevLett.46.1421.
[60] A. Rudenko, J.-P. Colombier, S. Höhm, A. Rosenfeld, J. Krüger, J. Bonse, T.E. Itina, Spontaneous periodic ordering on the surface and in the bulk of dielectrics irradiated by ultrafast laser: a shared electromagnetic origin, Sci. Rep. 7 (2017), https://doi.org/10.1038/s41598-017-12502-4.
[61] K. Boyd, H. Ebendorff-Heidepriem, T.M. Monro, J. Munch, Surface tension and viscosity measurement of optical glasses using a scanning CO_2 laser, Opt. Mater. Express 2 (2012) 1101, https://doi.org/10.1364/ome.2.001101.
[62] Q. Xie, N. Shchedrina, M. Cavillon, B. Poumellec, M. Lancry, Nanoscale investigations of femtosecond laser induced nanogratings in optical glasses, Nanoscale Adv. (2024), https://doi.org/10.1039/D3NA00748K.
[63] V.A. Markel, Introduction to the Maxwell garnett approximation: tutorial, J. Opt. Soc. Am. 33 (2016) 1244–1256, https://doi.org/10.1364/JOSAA.33.001244.
[64] Y.I. Frenkel, Kinetic Theory of Liquids, Oxford University Press, Oxford UK, 1946.
[65] L.Y. Shao, J. Canning, T. Wang, K. Cook, H.Y. Tam, Viscosity of silica optical fibres characterized using regenerated gratings, Acta Mater. 61 (2013) 6071–6081, https://doi.org/10.1016/j.actamat.2013.06.049.
[66] S. Sakaguchi, S. Todoroki, Viscosity of silica core optical fiber, J. Non-Cryst. Solids 244 (1999) 232–237, https://doi.org/10.1016/S0022-3093(99)00019-8.
[67] G. Hetherington, The viscosity of vitreous silica, Phys. Chem. Glasses 5 (1964) 130–136.
[68] G. Urbain, Y. Bottinga, P. Richet, Viscosity of liquid silica, silicates and alumino-silicates, Geochem. Cosmochim. Acta 46 (1982) 1061–1072, https://doi.org/10.1016/0016-7037(82)90059-X.
[69] J.C. Mauro, Y. Yue, A.J. Ellison, P.K. Gupta, D.C. Allan, Viscosity of glass-forming liquids, Proc. Natl. Acad. Sci. USA 106 (2009) 19780–19784, https://doi.org/10.1073/pnas.0911705106.
[70] I. Avramov, Pressure dependence of viscosity of glassforming melts, J. Non-Cryst. Solids 262 (2000) 258–263, https://doi.org/10.1016/S0022-3093(99)00712-7.
[71] P. Hrma, A.A. Kruger, High-temperature viscosity of many-component glass melts, J. Non-Cryst. Solids 437 (2016) 17–25, https://doi.org/10.1016/j.jnoncrysol.2016.01.007.
[72] G. Tammann, W. Hesse, Die Abhängigkeit der Viscosität von der Temperatur bie unterkühlten Flüssigkeiten, Z. Anorg. Allg. Chem. 156 (1926) 245–257, https://doi.org/10.1002/zaac.19261560121.
[73] H. Vogel, The law of the relation between the viscosity of liquids and the temperature, Phys. Z. 22 (1921) 645–646.
[74] W.T. Laughlin, D.R. Uhlmann, Viscous flow in simple organic liquids, J. Phys. Chem. A 76 (1972) 2317–2325, https://doi.org/10.1021/j100660a023.
[75] E. Fontana, W. Plummer, A study of viscosity-temperature relationships in the GeO2 and SiO2 systems, Phys. Chem. Glasses 7 (1966) 139–146.
[76] J.D. Mackenzie, Viscosity-temperature relation for network liquids, J. Am. Ceram. Soc. 44 (1961) 598–601, https://doi.org/10.1111/j.1151-2916.1961.tb11665.x.
[77] K. Shirai, Interpretation of the apparent activation energy of glass transition, Journal of Physics Communications 5 (2021) 095013, https://doi.org/10.1088/2399-6528/ac24d7.
[78] C.M. Pépin, E. Block, R. Gaal, J. Nillon, C. Hoenninger, P. Gillet, Y. Bellouard, Silicon Formation in Bulk Silica through Femtosecond Laser Engraving, 2018 arXiv preprint arXiv:1806.10802.
[79] G. Adam, J.H. Gibbs, On the temperature dependence of cooperative relaxation properties in glass-forming liquids, J. Chem. Phys. 43 (1965) 139–146, https://doi.org/10.1063/1.1696442.
[80] L.M. Martinez, C.A. Angell, A thermodynamic connection to the fragility of glass-forming liquids, Nature 410 (2001) 663–667, https://doi.org/10.1038/35070517.

III.4 MODELING NANOGRATINGS ERASURE AT HIGH REPETITION RATE IN COMMERCIAL OPTICAL GLASSES

Modeling nanogratings erasure at high repetition rate in commercial optical glasses

QIONG XIE,[1] MAXIME CAVILLON,[1] AND MATTHIEU LANCRY[1*]

[1]*Institut de Chimie Moléculaire et des Matériaux d'Orsay (ICMMO), Université Paris-Saclay, CNRS, Orsay 91405, France*
**matthieu.lancry@universite-paris-saclay.fr*

Abstract: Volume nanogratings (NGs) imprinted by infrared femtosecond laser in commercial optical glasses take the form of orientable subwavelength birefringent nanostructures, being composed of an assembly of nanopores. The existence of NGs strongly depends on the laser parameters and glass composition. Therefore, in this work, we tentatively model the erasure threshold of NGs in a pulse energy - repetition rate processing window. For this purpose, we combine i) a heat diffusion model to simulate the thermal treatment experienced by the glass upon laser irradiation, and ii) the Rayleigh-Plesset equation to take into account the evolution of a nanopore size during laser processing. We first determine a criterion for nanopores erasure, falling within a typical characteristic time of few tens of ns, in which the cooling of the last laser pulse absorbed by the material is progressively cooled. Then, considering a multiple pulse regime and the dependence of the deposited pulse numbers on the thermal treatment, the modeled NGs erasure threshold follows the experimental trend. Finally, considering a steady state regime for various repetition rates, and adjusting the energy deposition (absorption coefficient or beam waist) as a function of the pulse energy, the NGs existence window can perfectly match the experimental values.

Keywords: Nanogratings; Nanopores; Erasure; Commercial glasses; energy deposition.

1. Introduction

Transparent materials, such as optical glasses, can undergo localized and in volume modifications using femtosecond laser direct writing (FLDW). Volume nanogratings (NGs), also referred to as Type II modifications in the literature [1], are one of the most interesting transformations one can imprint inside most oxide glasses. The arrangement of these subwavelength nanostructures can be controlled by light polarization state and orientation [2], yielding to a pseudo-periodic array of nanolayers. In most oxide glasses like ubiquitous SiO_2 or GeO_2, they usually take the form of porous nanolayers made of oblate nanopores whose sizes typically range within a few tens of nanometers. However, other types of NGs can be induced, made of alternating layers of crystalline and amorphous phases [3]. The porous NGs possess a significant birefringent optical response due to i) strong refractive index contrast from the nanolayers, and ii) associated significant stress [4], and can even result to optical chirality [5]. Consequently, these developments have gained interest in several applied areas such as birefringent optical devices, optics based on 3D geometric phase, reliable storage of optical data, microfluidics, structural health monitoring, or sensing at high temperatures [6, 7].

The formation of porous NGs by FLDW is suggested to originate through a plasma-mediated nanocavitation process, a "light-forced organization" [8]. Starting from some nanoscale inhomogeneities seeding the process at the femtosecond timescale, nanoplasma hot spots are formed, followed by a localized heat distribution due to electron-phonon energy transfers. Along the formation and erasure of NGs, the heat cooling profile (a temperature-time couple) assists this nanocavitation process to imprint NGs. This results in boundaries defining the existence of NGs under specific pulse energy, duration or repetition rate irradiation conditions [9].

In the literature, it was clearly reported in Ref. [10-12] that heat accumulation, arising when inter-pulse period is too short to remove the heat from the previously deposited pulses (i.e., at high repetition rate), limits or even hinders the formation of this nanoporous phase and thus nanogratings in various oxide glasses such as SiO_2, GeO_2, or B33 (Borofloat glass). In Ref. [12], it was found that above a fixed apparent power of 0.23 W, nanogratings cannot be observed. Later on, Rudenko et. al defined a NG formation threshold using a cavitation approach ($T_{cav}\approx2000$ K) in fused silica [13]. However the upper temperature also limits the NGs survival in oxide glasses [14]. If the temperature is too high, mechanisms including boiling, rapid nucleation and growth, or spinodal decomposition, may occur. Based on Rudenko et. al [13], when the Péclet number is above 1, typically corresponding to temperature higher than 3000 K for SiO_2, a rapid viscous growth rate condition yields to "unstable" nanopores. This approach was recently generalized to a wide range of oxide glasses. In a first approximation the estimated window of NGs existence within a pulse energy (E_p) – Repetition Rate (RR) landscape was defined between T_{max} ($\eta = 10^3$ Pa·s, the working point of the glass) and T_{soft} ($\eta = 10^{6.6}$ Pa·s, the softening point of the glass) [15]. The upper temperature limit of the NGs survival intimately relates to the temperature dependent glass viscosity. However, this is in fact a time dependent problem and this upper temperature depends on the heating conditions and the heating cooling profile [14].

In this paper, we first exploit a heat diffusion model combined with Rayleigh-Plesset (R-P) equation to simulate the evolution of nanopores compositing the NGs over time and temperature during a given laser cooling profile. We establish some objective criteria to determine the energy threshold corresponding to the collapse of the NGs processing window. Then, we consider a multipulse approach and the dependence of the heat accumulation at steady state for various repetition rates in the erasure of nanopores. We finally simulate the maximum deposited energy beyond which NGs erasure along the laser cooling profile for a wide range of commercial optical glasses in comparison to available experimental data.

2. Combines modeling approach

2.1 Modeling the temperature profile T(r,t)

The classical heat diffusion model is taken from [16, 17]. First, the heat deposited locally by the laser inside materials follows Fourier's law. As a first approximation we did not consider the geometrical changes of the focal zone (beam waist) by the pulse energy, for instance arising from self-focusing and electron plasma defocusing. Considering the spatial temperature distribution induced by fs laser irradiation in a static configuration (i.e., no beam scanning), the equation takes the following form: $\frac{\partial T(r,t)}{\partial t} - D_{th} \cdot \Delta T(r,t) = \frac{Q(r,t)}{\rho C_p}$ (Eq. 1). Here ρ is density, C_p is specific heat capacity, κ is the heat diffusivity and the thermal diffusivity can be written as $D_{th} = \frac{\kappa}{\rho C_p}$. Furthermore, r and t are the radial distance away from the focus center, and the laboratory time, respectively.

About the heat source $Q(r,t)$, we suppose the laser beam takes up a Gaussian shape as: $Q(r,t) = \frac{AE_p}{\pi^{\frac{3}{2}}\omega^3} \cdot e^{-\frac{r^2}{\omega^2}} \cdot f(t)$ (Eq. 2). Then we can use a Dirac comb to define $f(t) = \sum_0^{N_P} \delta(t - N_P \cdot \tau_P)$ and to consider the multipulse regime at various repetition rates *RR*. Here we define $\tau_P = \frac{1}{RR}$ as the pulse period, N_p is the number of the light pulse, E_p is the pulse energy. Finally, A is the absorbed fraction of the pulse energy, which was taken as independent of E_p and *RR* as a first hypothesis, but will be adjusted later on.

Therefore, the temperature rise can be expressed as follow $T(r,0) - T_{room} = \frac{1}{\rho C_p} \int_{pulse} Q(r,t).dt = T_0 \cdot e^{-\frac{r^2}{\omega^2}}$ where T_0 is maximum temperature at the focus region center, which can be simply written as $T_0 = \frac{AE_p}{\pi^{\frac{3}{2}}\rho C_p \omega^3}$. After hundreds of fs (i.e., the pulse duration), the heat source is null, and one can use the following expression demonstrated in Ref. [16]: $T(r,t) = T_0 \frac{\omega^3}{(\omega^2+4D_{th}\cdot t)^{\frac{3}{2}}} \cdot e^{-\frac{r^2}{(\omega^2+4D_{th}\cdot t)^2}} + T_{room}$ (Eq. 3). This equation describes the temperature distribution after one pulse irradiation. T_{room} is the ambient temperature taken herein as 20 °C. In this equation, $\omega^3 = \frac{\omega_{th}^2}{2} \cdot \frac{\omega_z}{2}$ where ω_z is the typical beam length along the laser propagation, z, taken as 30 µm based on experiments. ω_{th} is the beam waist defined as $\omega_{th} = \frac{2\lambda n}{\pi N_A}$; λ is the wavelength of the laser pulses (1030 nm); numerical aperture (N_A) is 0.6 for the laser beam; n is the refractive index of each oxide glass, taken at 20°C since it is weakly dependent on T.

2.2 Mutipulse approach and steady state condition

In the case of the absorption of N_p pulses by the glass material, we easily obtain the evolution of the distribution considering the linearity of the differential equation and making up the sum of the solution for one impulsion but shifted in time τ_P, the inter-pulse period [16]. In some conditions, this can result in a pulse-to-pulse heat accumulation, especially at high RR. It is thus necessary to define the steady state where the temperature distribution reaches saturation and this is related to the ratio $R_\tau = \frac{\tau_p}{\tau_d}$ between τ_p and the thermal diffusion time noted $\tau_d = \frac{\omega_{th}^2}{4D_{th}}$ [16].When R_τ values are large, corresponding to low RR, less N_p are needed to reach a steady state. The contribution of an increase of temperature induced by consecutive pulses overlapping in time (heat accumulation) is weak or even neglectable when $R_\tau > 10$ [16]. However, considering high RR values (low R_τ), this pulse-to-pulse temperature increase is significant, and accompanied by a larger N_p to reach steady state. Within our conditions for *RR* ranging from 1 to 10 000 kHz, we can estimate that the steady state can be effectively reach for N_p = 10 000 pulses for all investigated glasses [16].

2.3 Modeling nanopores erasure using Rayleigh-Plesset equation

Using the heat diffusion model, one can deduce the temperature profile $T(r,t)$ of the last pulse for a given set of laser parameters (E_p and RR). In the following, the temperature distribution $T(r,t)$ is taken at r = 0 µm, that is, at the center of the beam, where the temperature is the highest [17]. From that point, we combine such heat cooling profile $T(0,t)$ with the well-known Rayleigh-Plesset (R-P) equation to simulate the evolution of nanopores (their erasure), that are composing the NGs [18]. The R-P equation was initially suggested and employed by Rudenko et al. to model the evolution of a spherical bubble inside an incompressible Newtonian fluid, [19], and is expressed as: $\frac{\Delta P}{\rho} = R_{pore}\frac{d^2R_{pore}}{dt^2} + \frac{3}{2}\left(\frac{dR_{pore}}{dt}\right)^2 + \frac{4\eta(T)}{\rho R_{pore}}\frac{dR_{pore}}{dt} + \frac{2\sigma}{\rho R_{pore}}$ (Eq. 4)

Here, ΔP is the pressure difference (in Pa) between the inside of the nanopore (supposed spherical) and far away from it; ρ is the glass density (in kg·m^{-3}); R_{pore} the radius (in m) of the spherical nanopore; t is the cooling time (in s); $\eta(T)$

is the glass viscosity (in Pa·s), and σ is the surface energy (0.3 J m^{-2} for silica over a wide temperature range [20]). Note that the non-sphericity of the experimentally observed nanopores, which are oblate [8], does not change the physical interpretation and thus that nanopores are considered spherical. The viscosity and its dependence with respect to temperature can be taken into account in the model by using a Vogel-Tammann-Fulcher (VTF) law in the form $\log(\eta, Pa \cdot s) = A - 1 + \frac{B}{T-T_0}$. Initial conditions are R_{pore} (at t = 0) = R_{ini}, that is, the initial nanopore size before any heat treatment and $\frac{dR_{pore}}{dt} = 0$ m·s^{-1} at t = 0 s.

In our conditions, the second derivative and the square of the first derivative from the R-P equation have very small contributions numerically in our conditions and can be therefore neglected i.e., slow dynamics so no inertial pressure. ΔP is small enough and thus set to be null in the erasure case (taking the situation of an empty nanopore). As the glass viscosity η(T) and surface tension dictate the dynamics of the process, this gives the simplified R-P equation form [14]: $\frac{dR_{pore}}{dt} = \frac{d(R_{pore}-R_{ini})}{dt} = -\frac{\sigma}{2\eta}$ (Eq. 5).

To illustrate this purpose, we can observe in Fig. 1 a typical heating-cooling profile for a single pulse modeled in SiO_2 (black symbols) and the related nanopore erasure R_{pore} (t) for different values of R_{ini}. First, the equivalence of the two equations is demonstrated in Fig.1, showing a similar nanopore erasure rate using either Eq. 4 or Eq. 5. Secondly, the nanopore size diminution is the same considering different initial nanopore radius thus leading here to a full erasure of small nanopores while big ones are partially erased.

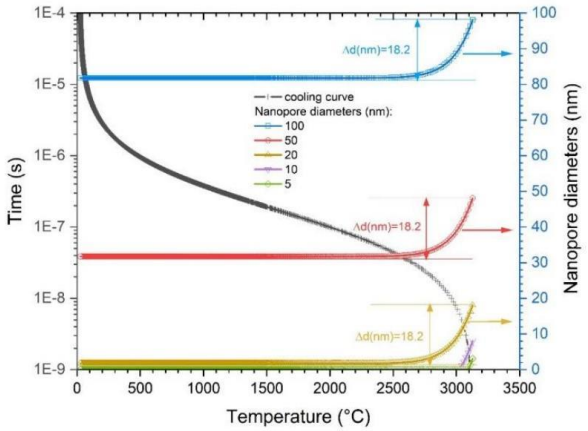

Fig. 1 Different nanopores diameters erased by the same heat cooling curve $T(0,t)$ in SuprasilCG glass using both the R-P equation (in solid line) and the simplified one (in circle symbol). The corresponding parameters in heat diffusion model are: ω_{th}= 1.58 µm; N_p= 1; A = 0.25; E_p = 1 µJ; SiO_2 glass.

3. Experimental data base and simulated

We use several commercial oxide glasses (Schott BK7, Borofloat 33 and AF32, Corning ULE, Eagle XG and 7059, Heraeus Suprasil CG and Marienfield Superior soda lime) to perform both experiments and the numerical simulations.

Table 1 Glass samples, molar composition, density, heat capacity, refractive index at 1030nm, diffusivity and viscosity parameters [14].

Glass Samples	Molar Composition	Density ρ (kg/m3)	Heat capacity Cp (J/(kg·K))	Refractive index n	Diffusity Dth (10^{-7})	Viscosity Parameters (A; B; T_0)[a]
BK7	69.13 SiO_2, 10.75 B_2O_3, 3.07 BaO, 10.40 Na_2O, 6.29 K_2O, others < 1	2510	858	1.5168	5.17	(-2.475; 4677; 527.8)
Soda lime	72.6 SiO_2, 13 Na_2O, 8.8 CaO, 4.3 MgO, 0.6 Al_2O_3, 0.3 K_2O, 0.2 SO_3, 0.1 Fe_2O_3	2500	750	1.52	5.33	(-1.741; 4309; 537.7)
Borofloat 33	81 SiO_2, 2 Al_2O_3, 13 B_2O_3, 4 Na_2O/K_2O	2230	830	1.4714	6.48	(-1.681; 6578; 384.8)
7059	63 SiO_2, 8.5 Al_2O_3, 16 B_2O_3, 12.5 BaO	2760	750	1.534	4.83	(-19.81; 34510; -140)
AF32	66.43 SiO_2, 11.28 Al_2O_3, 10.73 B_2O_3, 5.30 CaO, 4.63 MgO, 1.36 BaO, others < 1	2430	800	1.5099	5.97	(-4.062; 8876; 480.8)
Eagle XG	65.71 SiO_2, 11.10 Al_2O_3, 11.65 B_2O_3, 8.64 CaO, 2.28 MgO, others < 1	2380	768	1.5099	5.96	(-6.584; 13170; 319.4)
ULE	94.25 SiO_2, 5.75 TiO_2	2210	767	1.4828	7.14	(-21.47; 90920; -1365)
Suprasil CG	100 SiO_2	2200	703	1.444	8.92	(-9.5; 34200; -127)

[a]These parameters provides a value of $\log(\eta)$ with η in P (dPa.s), and T in Kelvin.

The thermal properties of the glasses are provided from the glass manufacturers and summarized in Table 1. Additionally, the viscosity parameters for VTF fit, namely (A, B and T_0) are also available in Table 1. After laser writing experiments described in Ref. [11], we have quantified the optical retardance (proportional to the birefringence). The presence of nanogratings was ascertained through polarization dependent form birefringence measurements and by direct observations using scanning electron microscopy in all glasses, which further allow to determine the typical pore size for each glass composition [21]. From that point, their NGs (Type II) processing window in a E_p-RR landscape have been reported in our previous work [11].

In the following, we first determine the criterion for determining the nanogratings erasure from the thermal modeling point of view. Then, we model nanopores erasure according to absorbed pulse energy at different RR. For each glass, we will first model the heating-cooling profile for a fixed absorption coefficient, and we consider various pulses numbers up to reaching the steady state. Finally in a second attempt, we introduce an adjustment within the model considering the absorption coefficient being function of the pulse number and thus on RR within our experimental conditions.

4. Results and discussion

Nanopores composing NGs are the key point here since they are at the origin of the ultimate nanogratings thermal stability. It is worth mentioning that other contributions can arise from point defects, stress fields, interlayers densification, or any kind of birefringent contribution [22], but this aspect goes beyond the framework of this study that is focused on the "ultimate" erasure of nanopores. As shown in the literature, nanopores typically erase within 30 min at ~1.1T_a where T_a stands for the glass annealing temperature (when log(η, Pa.s) = 12). However, we are willing to model to which extent these nanopores can survive to fs-laser direct writing in a E_p-*RR* landscape where temperatures exceed 2000°C [13].

4.1 Case of when $R_\tau > 10$

Let us first consider the case of most oxide glasses within which porous NGs (excluding partly crystallized ones) are imprinted. Once the oxide glass has been decomposed through a plasma-mediated nanocavitation process [8, 13], one can observe the nanopores few 100's of ps after the end of a pulse. From that point, there is a thermalization of the glass network, and nanopores can be partly erased along the subsequent heat cooling profile, until the next pulse through which they can be eventually regenerated, reshaped or even erased. Following this view, in a first example (Fig. 2) we will only consider the last pulse, i.e., the last cooling curve in our model, which corresponds to experimental conditions where R_τ is big enough (typ. >10) in such that there is no appreciable heat accumulation (e.g. $R_\tau = 140$ at 10 kHz in SiO_2). In Fig. 3 we will consider the multipulse regime that may lead to a heat accumulation thus affecting both the shape of the spatial heat distribution (that becomes Lorentzian [16] and the cooling curve T(t) as well). Note that for all glasses investigated, although the value of D_{th} (hence R_τ), can be slightly different, the reasoning remains the same.

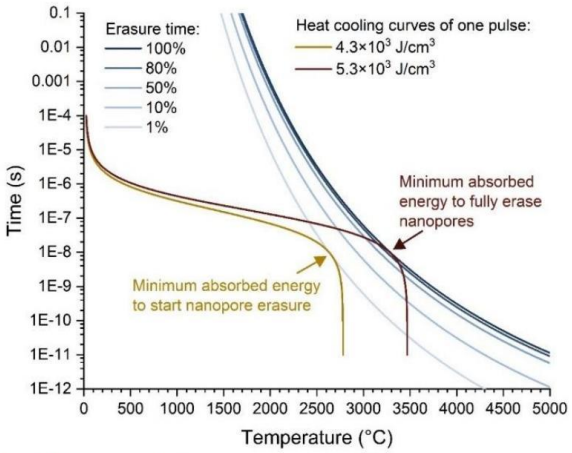

Fig. 2 The curves of the erasure time with different erasure percentage (nanopore diameter is 50 nm as an example) versus the heat cooling curves of one pulse with variable RR from 10 kHz to 1000 kHz for 1% and 100% erasure of the nanopore in SuprasilCG glass. The corresponding parameter in heat diffusion model: ω_{th} = 1.58 µm; N_p = 1; A = 0.05

However here, one first need to define an erasure criterion to compare modeling and experiments. So, we choose that the observable measurand, namely the optical retardance *R*, is no more measurable below our detection limit and estimated to 1 nm. Then we translate this criterion in term of nanopores size by means of the form birefringence model which makes the link between nanopores size, filling factor and the birefringence or retardance amplitude. So we define the P factor, $P = R_{pore}(t,T)/R_{ini}$, corresponding to the fraction of nanopore erasure, and expressed in percent. Typically, 80% erasure of the nanopore diameters corresponds to 99.99% erasure of the related optical retardance R.

In the following part, we take the situation of a 50 nm nanopore. Then using the simplified R-P equation, we can compute the time required to partly or fully erase such a nanopore along a given temperature profile T(r,t) taken at the center of the pulse, r = 0 µm. On the one hand, the erasure time of different P values can be calculated by the equation $\tau_e = \frac{2\eta R_{ini} P}{\sigma} = \frac{2\times 10^{A-1+\frac{B}{T-T_0}} \times R_{ini} \times P}{\sigma}$ [14]. As previously mentioned, here we keep σ term constant, which is a reasonable assumption for this work [30].

The results for various P values from 1 to 100% are summarized in Fig. 2 for silica (Suprasil CG). Whatever the chosen fraction P, the intuitive trend that the pore will collapse faster when brought to higher temperature is verified. Now, let us see on the graph the thermal cooling for a single pulse in silica glass which corresponds to the case

where R_τ is big enough so no heat accumulation is present (e.g. $R_\tau = 14$ for SuprasilCG at 100 kHz). These two heat cooling curves are calculated by the above-mentioned heat diffusion model. We thus let the heat cooling curves touch the curves of erasure time by adjusting the E_p. Note that the cooling curves of one pulse are shifted along T, but its temporal shape remains unchanged. The minimum absorbed energy to start erasing the nanopore (P = 1%) or fully erase it (P = 100%) can be deduced once the heat cooling curve and the erasure one touch each others. In Fig. 2, the minimum absorbed energy for P = 1% and P = 100% are 4.3×10^3 J/cm^3 and 5.3×10^3 J/cm^3, respectively. Since the results are provided for N_p = 1, the RR has no effect in this first simulation. The characteristic erasure times (initially defined in Ref. [14]) are typ. ~8 ns and ~10 ns for P = 1% and P = 100%, respectively.

4.2 The effect of the repetition rate when $R_\tau < 10$ (heat accumulation)

The objective now is to compute the value of the temperature T(r,t) when $N_p \gg 1$. We will show how the cooling profile changes with the RR according to heat accumulation (hence R_τ), i.e., when T at the end of the period cumulates with the T increase induced by the absorption of the next pulse. So, in the following curves, we will consider the situation where the steady state (typ. we chose $N_p = 10000$ in our conditions [16].) has been reached for a given practical number of pulses. Finally, as in previous case we will consider only the cooling profile of the last pulse at the center, since as the gaussian beam is moving away and the maximum temperature is then decreasing. To some extent, one possible view is that it takes more time to create a nanopore (multipulses) whereas a single pulse (i.e. here the last pulse) is enough to erase it.

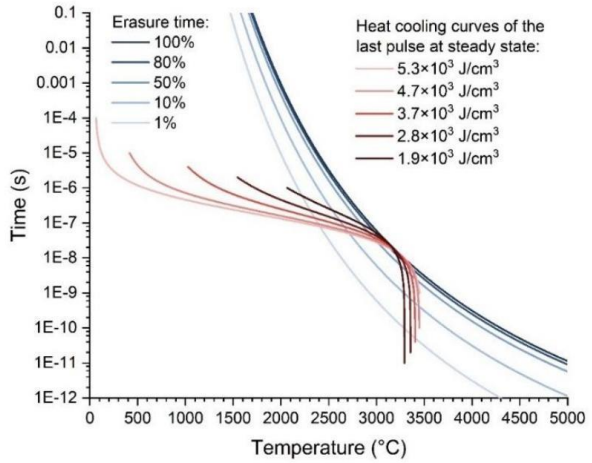

Fig. 3 The curves of the erasure time with different erasure percentage (initial nanopore diameter is set as 50 nm) versus the heat cooling curves of the last pulse with variable RR from 10 kHz to 1000 kHz for 100% erasure of the nanopore in Suprasil CG glass. The corresponding parameter in heat diffusion model: ω_{th} = 1.58 µm; at steady state [16].

Fig. 3 shows the heat cooling curves of the last pulse after the steady state regime is reached, for multiple RR values from 10 to 1000 kHz. In addition, we add the R-P erasure time curves for P = 100% (full erasure). First, one can see that minimum deposited energy necessary to fully erase a given nanopore ranges typ. from 2 up to 5×10^3 J/cm^3. Second, the shape of the heat cooling curves of the last pulse at steady state are different (e.g. the slope around the touching point) because of heat accumulation impacted by RR. Thirdly, the characteristic erasure time proportionally varies from ~10 ns to ~29 ns for 10 and 1000 kHz respectively.

One first comment is that this erasure time is much smaller than a typical diffusion time (~ 0.69 µs in SiO_2). This very short characteristic time arises from the cooling temperature profile where the temperature drastically decreases within a fraction of µs but the key driving force, the viscosity, varies itself in a log scale versus T. With such a characteristic time, it is shown that temperatures around 2700 °C and 3300°C are required to collapse the nanopore in SuprasilCG. Similarly, this erasure temperature remains quite similar whatever the RR and this is true for each glass. For example, it is around 3100 °C in Suprasil CG glass; 2870 °C in Borofloat33 glass; 2080 °C in AF32 glass; 1890 °C in Eagle XG glass; 1700 °C in BK7 glass; 1350 °C in 7059 glass. A second comment is that such calculations imply some very low viscosity values (i.e., high temperatures. So we can determine a viscosity "limit" of log(η, Pa.s) ~ -0.75 for nanopores erasure within such timescale. However, one must bear in mind that uncertainties can be quite large (typ. Δlog(η, Pa·s) ± 1) using viscosity fits instead of experimental data.

4.3 Comparison between experiments and modelling of nanopores erasure in the E_p-RR domain

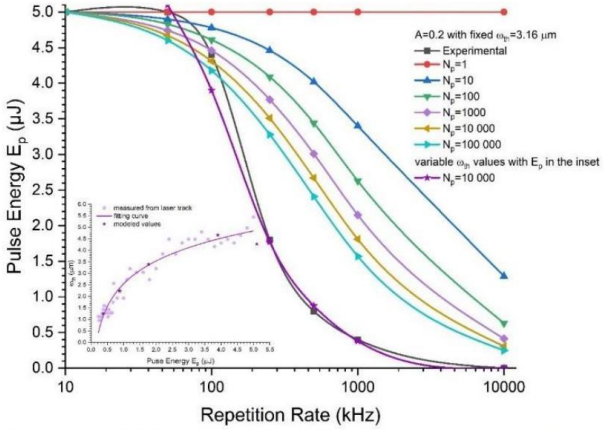

Fig. 4 The modeled and experimental E_p versus RR with variable N_p at A = 0.2 in Suprasil CG glass. N_p = 10 000 corresponds to the steady state. The inset shows the measured ω_{th} (dots) from the laser and ω_{th} values used for the modelling (stars symbols) versus experimental E_p.

In Fig. 4, the experimental curve of E_p versus RR is taken from Ref. [11], and corresponds to the upper threshold of the NGs window in SuprasilCG glass, for which there is no more form birefringence associated with a very low retardance (only residual stress). To set a value of the absorption coefficient *A* in these conditions, we use the experimental curve, at 10 kHz, where no heat accumulation is present. As mentioned above, the erasure criterion of the full erasure is around 80% erasure of the

nanopore diameter. In the following A was then fixed to 0.2 and the beam size ω_{th} was kept constant as well. When N_p=1, there is evidently no heat accumulation, and the modeled curve is thus flat according to RR. As N_p increases, the curves of modeled E_p versus RR start to drop in the high RR domain, getting closer to the experimental observations. Based on previous modeling, we can estimate that the temperature for P = 80% in this condition needs to reach around 3100 °C whatever RR and N_p. Ultimately when reaching the steady state (e.g. when N_p = 10000), the modeled curve exhibits a quite similar trend, but the match is still not perfect. The same result stands for all investigated chemical compositions. To refine a bit more the model in silica, we used a varying value of the beam waist ω_{th} according to the pulse energy E_p. We have thus measured the experimental beam size vs E_p within Type II regime and at low repetition rate, so we have no heat accumulation. The beam size was defined as the width over which we can effectively measure nanogratings by SEM as seen in the inset of Fig. 4. Following that experimental curve, we have then adjusted ω_{th} values used in the thermal model, at the steady state, to model the nanopores erasure energy. The resulting curve (purple line in Fig. 4) provides a quite good agreement with the experimental measurements.

To go one step further and generalize, one has introduced such dependence in the energy deposition in J/cm^3 according to the repetition rate for all glasses. Indeed, if A or ω_{th} are varied with respect to E_p at various RR (i.e., serving as an adjustment variable), a better match to the experimental conditions can be obtained. So, Figure 5 shows the curves of modeled E_p versus RR at steady state with variable A values in 8 commercial oxide glasses. For each curve, A was adjusted according to the experimental E_p at the corresponding RR. As expected, the modeled curves can be perfectly matched to the experimental ones. The overall modeled trend is that one need to increase the apparent absorption coefficient A when increasing RR.

This result is not obvious and there are few aspects to consider there. Indeed, one must keep in mind that behind this apparent parameter, there are in fact changes of both the E_p and the pulses number N_p that can both affect the energy deposition in different ways including a change of ω_{th}, which usually increases with E_p (see inset of Fig. 4).

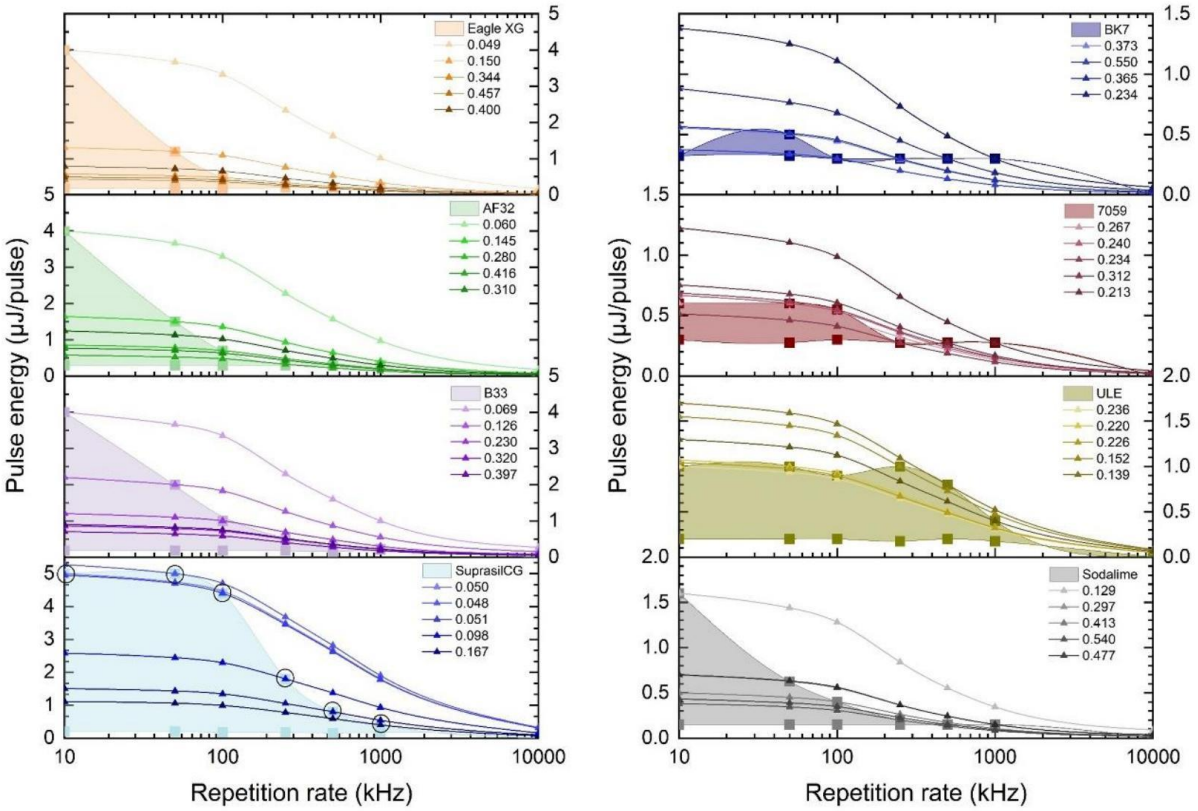

Fig. 5 The modeled and experimental E_p (for nanogratings erasure) versus RR at steady state in different oxide glasses. The values of absorption coefficients are written in each legend and decided by experimental E_p from 10 kHz to 500 kHz (e.g. 0.050→ 0.167 in Silica Suprasil CG). For each RR we have chosen the minimum absorption coefficient necessary to obtain nanopores full erasure at the corresponding experimental energy E_p.

i/ It is well known that the fraction of the incident energy effectively absorbed by the material is a function of the incident pulse energy, the pulse duration, and the material chemical composition. Absorption primarily occurs through nonlinear absorption namely multiphoton ionization and then avalanche occurs as shown by plasma measurements at short time scales [23, 24]. In addition, plasma reflection or scattering is also expected at high energies, thus reducing the effective absorption coefficient. Finally at higher energies, some intensity clamping further happen, e.g. 60 TW/cm^2 in similar experimental conditions [25]. The origin of the clamping is related to the shielding of the field on its way towards the focus by the generated plasma [26]. As a result, the absorption coefficient initially increases with E_p and then tends to saturate. In silica the absorption of a single laser pulse within the nanogratings regime range from about 2% to 25% depending on pulse energy and duration [27]. For example, at 500 kHz, 20% pulse energy was absorbed for pulse duration of 500 fs and an energy of 1uJ, a value typically in a reasonable agreement with our modeling.

ii/ A second point is to take into account the higher number of pulses seen by the material at high repetition rates. Indeed, in agreement with the literature, the measured thresholds decrease when the number of pulses increases. Such "incubation effects" were already observed nearly two decades ago by Schäffer [28] leading to a decrease in the modification threshold of various oxide glasses when increasing the number of pulses, but also in surface experiments [29, 30]. In the literature, it has been demonstrated [31] that the origin of such incubation can be attributed to i) the accumulation of point defects which results in a more efficient absorption when increasing N_p ii) it introduces new possibilities of energy deposition in the glass network, e.g. based on a coupling of electrons trapped in the lattice. This accumulation of points defects is proportional to the initial defect concentration (thus chemical composition), the increment in the number of pulses, and also depends on the number of atomic sites likely to be affected during the heat accumulation process. In the authors' view, this aspect is expected to play a rather minor role compared to the previous and following discussed contributions.

iii/ When considering the energy deposition in volume, not only the absorption coefficient but also the beam waist and its energy dependence are crucial information. At first self-focusing phenomenon occurs when the power of the laser beam is greater than the critical power (related to the nonlinear refractive index). Note that for tight focusing the lens-focusing is dominating and the Kerr nonlinearity could be partly neglected, and for loose focusing the self-focusing is dominating. The effective width at the focus in the material is given by Refs. [28, 32, 33] but this does not include the plasma defocusing effect which depends on the excited electron density. To quantitatively estimate the beam size evolution with E_p, one can use the width of Type II nanogratings since their nanostructure is achieved only by the laser light. In Lei et al. [34], the beam width increases already above 0.2 µJ although the excited electron density is of the order of $0.01.10^{21}$/cm^3. In silica, SEM micrographs reveal that for a beam size around 1.5 µm (0.6 NA focusing) at low energy, there is monotonous growth of the beam size and a trend to saturation resulting in a 3 µm width around 1µJ/pulse [35]. Based on our work [36-39], we note that the dependence of the beam waist with E_p is not very sensitive to the glass composition within silicate glasses family. So, the numerical modeling of nanopores erasure, which reveals an apparent increase of absorption coefficient at higher RR is not necessarily true. This is simply an "image" of the effective volume energy density that is necessary to erase nanopores in these conditions of E_p-RR. One should rather consider the changes of the beam waist, which is much smaller in the case of erasure threshold at high RR (i.e. erasure energy < 0.5 µJ) compared to low repetition rate (e.g. high energy of a few uJ/pulse). Such changes of the beam size by a factor 2 are more than enough to explain our observations. However, here the balance between Kerr self-focusing and plasma defocusing is determined by the effective pulse length undergoing ionization at nonlinear focus, which is difficult to predict without heavy computations, or robust knowledge of many parameters involved in the process, usually approximated, or simply ignored.

5. Conclusion

In this work, using a Fourier heat diffusion model combined with the Rayleigh-Plesset equation, we simulate the nanopore time-temperature evolution along the laser heat cooling profile. We show the modeled E_p versus *RR* curves at a steady state in 8 commercial oxide glasses. The full erasure of nanopores is defined by the "touching point" between the T(t) heat cooling profile and characteristic erasure time deduced from Rayleigh-Plesset equation. Additionally, we have observed that the temporal shape of the cooling curves of the last pulse at a steady state is dependent on *RR*, which can be attributed to heat accumulation. As the pulse number increases, the modeled curves of E_p versus *RR* become closer to experimental data for a fixed absorption coefficient. However, to obtain a perfect match with experimental data, the energy deposition was adjusted according to *RR* which could be likely attributed to changes in the beam waist with increasing energy due to plasma defocusing.

Funding: This research is funded by Agence Nationale de la Recherche (ANR), FLAG-IR Project, award number ANR-18-CE08-0004-01; and REFRACTEMP project, award number ANR-22-CE08-0001-01. Qiong Xie acknowledges the China Scholarship Council (CSC) for the funding of her PhD fellowship, NO.202007040018.

Disclosures: The authors declare no conflicts of interest.

6. References

[1] Y. Wang, S. Wei, M.R. Cicconi, Y. Tsuji, M. Shimizu, Y. Shimotsuma, K. Miura, G.D. Peng, D.R. Neuville, B. Poumellec, M. Lancry, Femtosecond laser direct writing in SiO2-Al2O3 binary glasses and thermal stability of Type II permanent modifications,

Journal of the American Ceramic Society, 103 (2020) 4286-4294. 10.1111/jace.17164.

[2] Y. Shimotsuma, P.G. Kazansky, J. Qiu, K. Hirao, Self-organized nanogratings in glass irradiated by ultrashort light pulses, Physical Review Letters, 91 (2003) 247405. 10.1103/PhysRevLett.91.247405.

[3] M. Cavillon, J. Cao, M. Vallet, F. Brisset, L. Mazerolles, B. Dkhil, M. Lancry, B. Poumellec, Thermal and Electron Plasma Effects on Phase Separation Dynamics Induced by Ultrashort Laser Pulses, Crystals, 12 (2022) 496. 10.3390/cryst12040496.

[4] E. Bricchi, B.G. Klappauf, P.G. Kazansky, Form birefringence and negative index change created by femtosecond direct writing in transparent materials, Optics Letters, 29 (2004) 119-121. 10.1364/OL.29.000119.

[5] J. Lu, J. Tian, B. Poumellec, E. Garcia-Caurel, R. Ossikovski, X. Zeng, M. Lancry, Tailoring chiral optical properties by femtosecond laser direct writing in silica, Light: Science & Applications, 12 (2023). 10.1038/s41377-023-01080-y.

[6] S. Mihailov, D. Grobnic, C. Hnatovsky, R. Walker, P. Lu, D. Coulas, H. Ding, Extreme Environment Sensing Using Femtosecond Laser-Inscribed Fiber Bragg Gratings, Sensors, 17 (2017) 2909. 10.3390/s17122909.

[7] M. Beresna, M. Gecevičius, P.G. Kazansky, Ultrafast laser direct writing and nanostructuring in transparent materials, Adv. Opt. Photon., 6 (2014) 293-339. 10.1364/AOP.6.000293.

[8] Q. Xie, N. Shchedrina, M. Cavillon, B. Poumellec, M. Lancry, Nanoscale investigations of femtosecond laser induced nanogratings in optical glasses, Nanoscale Advances, 6 (2024) 489-498. 10.1039/D3NA00748K.

[9] S. Richter, M. Heinrich, S. Döring, A. Tünnermann, S. Nolte, U. Peschel, Nanogratings in fused silica: Formation, control, and applications, J. Laser Appl., 24 (2012) 042008. 10.2351/1.4718561.

[10] M. Lancry, F. Zimmerman, R. Desmarchelier, J. Tian, F. Brisset, S. Nolte, B. Poumellec, Nanogratings formation in multicomponent silicate glasses, Applied Physics B, 122 (2016) 66.

[11] Q. Xie, M. Cavillon, D. Pugliese, D. Janner, B. Poumellec, M. Lancry, On the Formation of Nanogratings in Commercial Oxide Glasses by Femtosecond Laser Direct Writing, Nanomaterials, 12 (2022) 2986. 10.3390/nano12172986.

[12] S. Richter, M. Heinrich, S. Döring, A. Tünnermann, S. Nolte, U. Peschel, Nanogratings in fused silica: Formation, control, and applications, Journal of Laser Applications, 24 (2012) 042008. 10.2351/1.4718561.

[13] A. Rudenko, J.P. Colombier, T.E. Itina, Nanopore-mediated ultrashort laser-induced formation and erasure of volume nanogratings in glass, Phys Chem Chem Phys, 20 (2018) 5887-5899. 10.1039/c7cp07603g.

[14] Q. Xie, M. Cavillon, B. Poumellec, M. Lancry, Upper temperature limit for nanograting survival in oxide glasses, Applied Optics, 62 (2023) 6794-6801. 10.1364/AO.496351.

[15] Q. Xie, M. Cavillon, B. Poumellec, D. Pugliese, D. Janner, M. Lancry, Application and validation of a viscosity approach to the existence of nanogratings in oxide glasses, Optical Materials, 130 (2022) 112576. 10.1016/j.optmat.2022.112576.

[16] R. Que, M. Lancry, B. Poumellec, Usable Analytical Expressions for Temperature Distribution Induced by Ultrafast Laser Pulses in Dielectric Solids, Micromachines, 15 (2024) 196. 10.3390/mi15020196.

[17] M. Shimizu, M. Sakakura, M. Ohnishi, Y. Shimotsuma, T. Nakaya, K. Miura, K. Hirao, Mechanism of heat-modification inside a glass after irradiation with high-repetition rate femtosecond laser pulses, Journal of Applied Physics, 108 (2010) 073533. 10.1063/1.3483238.

[18] M.S. Plesset, The Dynamics of Cavitation Bubbles, Journal of Applied Mechanics, 16 (1949) 277-282. 10.1115/1.4009975.

[19] A. Rudenko, J.-P. Colombier, S. Höhm, A. Rosenfeld, J. Krüger, J. Bonse, T.E. Itina, Spontaneous periodic ordering on the surface and in the bulk of dielectrics irradiated by ultrafast laser: a shared electromagnetic origin, Scientific Reports, 7 (2017). 10.1038/s41598-017-12502-4.

[20] K. Boyd, H. Ebendorff-Heidepriem, T.M. Monro, J. Munch, Surface tension and viscosity measurement of optical glasses using a scanning CO_2 laser, Optical Materials Express, 2 (2012) 1101. 10.1364/ome.2.001101.

[21] H. Yao, Q. Xie, M. Cavillon, Y. Dai, M. Lancry, Materials roadmap for inscription of nanogratings inside transparent dielectrics using ultrafast lasers, Progress in Materials Science, 142 (2024) 101226. https://doi.org/10.1016/j.pmatsci.2023.101226.

[22] Y. Wang, M. Cavillon, N. Ollier, B. Poumellec, M. Lancry, An Overview of the Thermal Erasure Mechanisms of Femtosecond Laser-Induced Nanogratings in Silica Glass, physica status solidi (a), 218 (2021) 2100023. https://doi.org/10.1002/pssa.202100023.

[23] M. Lancry, N. Groothoff, B. Poumellec, S. Guizard, N. Fedorov, J. Canning, Time-resolved plasma measurements in Ge-doped silica exposed to infrared femtosecond laser, Physical Review B, 84 (2011) 245103.

[24] S. Guizard, S. Klimentov, A. Mouskeftaras, N. Fedorov, G. Geoffroy, G. Vilmart, Ultrafast Breakdown of dielectrics: Energy absorption mechanisms investigated by double pulse experiments, Applied Surface Science, 336 (2015) 206-211. https://doi.org/10.1016/j.apsusc.2014.11.036.

[25] J. Rolle, L. Bergé, G. Duchateau, S. Skupin, Filamentation of ultrashort laser pulses in silica glass and KDP crystals: A comparative study, Physical Review A, 90 (2014) 023834. 10.1103/PhysRevA.90.023834.

[26] A. Rudenko, J.V. Moloney, P. Polynkin, Ionization clamping in ultrafast optical breakdown of transparent solids, Physical Review Applied, 20 (2023) 064035. 10.1103/PhysRevApplied.20.064035.

[27] H. Wang, Y. Lei, L. Wang, M. Sakakura, Y. Yu, G. Shayeganrad, P.G. Kazansky, 100-Layer Error-Free 5D Optical Data Storage by Ultrafast Laser Nanostructuring in Glass, Laser & Photonics Reviews, 16 (2022) 2100563. 10.1002/lpor.202100563.

[28] C.B. Schaffer, A. Brodeur, E. Mazur, Laser-induced breakdown and damage in bulk transparent materials induced by tightly focused femtosecond laser pulses, Measurement Science and Technology, 12 (2001) 1784.

[29] M. Lenzner, J. Krüger, W. Kautek, F. Krausz, Incubation of laser ablation in fused silica with 5-fs pulses, Applied Physics A, 69 (1999) 465-466. 10.1007/s003390051034.

[30] D. Ashkenasi, M. Lorenz, R. Stoian, A. Rosenfeld, Surface damage threshold and structuring of dielectrics using femtosecond laser pulses: the role of incubation, Applied Surface Science, 150 (1999) 101-106. https://doi.org/10.1016/S0169-4332(99)00228-7.

[31] R. Stoian, Investigations of the dynamics of material removal in ultrashort pulsed laser ablation of dielectrics, Freien Universität Berli, 2000.

[32] J.H. Marburger, Self-focusing: Theory, Progress in Quantum Electronics, 4 (1975) 35-110. https://doi.org/10.1016/0079-6727(75)90003-8.

[33] J.B. Ashcom, R.R. Gattass, C.B. Schaffer, E. Mazur, Numerical aperture dependence of damage and supercontinuum generation from femtosecond laser pulses in bulk fused silica, Journal of the Optical Society of America B, 23 (2006) 2317-2322. 10.1364/JOSAB.23.002317.

[34] Y. Lei, Laser modification of materials at micro-and nanoscale for photonics and information technology, University of Southampton, 2023, pp. 199.

[35] R. Desmarchelier, B. Poumellec, F. Brisset, S. Mazerat, M. Lancry, In the heart of femtosecond laser induced nanogratings: from porous nanoplanes to form birefringence, World J. Nano Sci. and Eng., 5 (2015) 115-125.

[36] R. Que, M. Lancry, M. Cavillon, B. Poumellec, How to Cristallize a Glass with a Femtosecond Laser, Preprints, Preprints, 2024.

[37] M. Lancry, F. Zimmerman, R. Desmarchelier, J. Tian, F. Brisset, S. Nolte, B. Poumellec, Nanogratings formation in multicomponent silicate glasses, Appl. Phys. B, 122 (2016) 66. 10.1007/s00340-016-6337-8.

[38] J. Cao, M. Lancry, F. Brisset, L. Mazerolles, R. Saint-Martin, B. Poumellec, Femtosecond Laser-Induced Crystallization in Glasses: Growth Dynamics for Orientable Nanostructure and Nanocrystallization, Crystal Growth & Design, 19 (2019) 2189-2205. 10.1021/acs.cgd.8b01802.

[39] M. Lancry, R. Desmarchelier, K. Cook, B. Poumellec, J. Canning, Compact Birefringent Waveplates Photo-Induced in Silica by Femtosecond Laser, Micromachines, 5 (2014) 825-838.

III.5 CONCLUSION

This chapter presents the thermal stability of self-organized pores NGs imprinted by FLDW in 8 commercial glasses by isochronal annealing experiments. The erasure of NGs is attributed to the collapse of the nanopores and monitored by R measurements. The evolution of the R during isochronal annealing can theoretically predicted through the R-P equation. There is an excellent agreement between the experimental and predicted erasing temperatures, with discrepancies not more than typ. 50°C for all glasses investigated. The erasure of NGs in glass is intimately related to viscosity and the equation of the erasure time has been established using simplified R-P equation. It is used to theoretically predict the erasure of NGs in the context of any time–temperature process (e.g., thermal annealing, laser irradiation process, "any thermal treatment"). We found that the upper temperature limit under irradiation conditions corresponds to a temperature for which the glass viscosity value is log (η, Pa·s) ~ -0.75 in the hypothesis where we consider a characteristic time of 30 ns, or log (η, Pa·s) ~ 1 for a timescale of 1 µs, corresponding to a typical diffusion time. However, this temperature limit is lowered for much longer processes like isothermal / isochronal annealing where log (η, Pa·s) ~ 10.1.

By using the R-P equation and the VAREPA framework, we propose to predict the lifespan of nanogratings by coupling numerical modeling of optical retardance through accelerating thermal ageing. To build a so-called Master Curve, the modeled retardance is gathered based on the time-temperature annealing conditions. The erasure reaction constant rate k_0 of different oxide glasses can be deduced in simulation. The experimental data also can valid the master curve and the prediction is excellent at 50% erasure ratio. The physical interpretation of the k_0 and activation energy distribution has been provided, which is strongly related to the glass viscosity and its temperature dependence. And the log of the erasure constant rate, $\ln(k_0)$, was shown to linearly scale up together with the Angell's glass fragility, m.

Using a Fourier heat diffusion model combined with R-P equation, we simulate the nanopores time-temperature evolution undergone along the laser cooling profile. We show the curves of modeled E_p versus RR at steady state in 8 commercial oxide glasses. Here the full erasure of nanopores is defined by the "touching point" between the T(t) cooling curve and characteristic erasure time deduced from R-P. Also, we note that the temporal shape of the cooling curves of the last pulse at a steady state depends on repetition rate, which due to heat accumulation. For a fixed absorption coefficient, as pulse number increase, the modeled curves of E_p versus repetition rate are closer to experimental data. Following the experimental curve of ω_{th}-E_p, we adjusted ω_{th} values used in the thermal model at the steady state, to model the nanopores erasure energy, which provides a quite good agreement with the experimental measurements. Finally, considering a steady state regime for various repetition rates, and adjusting the energy deposition (absorption coefficient or beam waist) as a function of the pulse energy, the NGs existence window can perfectly match the experimental values.

Chapter IV. THE LINK OF NGS FORMATION WITH THE CHEMICAL COMPOSITION OF OPTICAL GLASSES

IV.1 INTRODUCTION

Volume NGs have been observed inside many transparent materials, especially glasses. NGs in SiO_2 glass can be created by partial oxide decomposition through a plasma-meditated nanocavitation process, and exhibit fascinating properties, including anisotropic light scattering and highly selective chemical etching. NGs formed by nanoporous self-organized structures were thought to be only observed in a handful of materials (mostly SiO_2-rich oxide glasses). Numerous results have already been reported on NGs in multicomponent glasses. But recent studies have revealed that glass chemical properties play a key role in the formation process of NGs. There are other kinds of nanogratings aside from porous NGs, which are composed of a partially crystalline nano-periodic structure. These structures are of interest for nonlinear optics related devices.

This chapter summarize the discovery of NGs in various chemical compositions of optical glasses, from silica and silicates to multicomponent glass compositions including alumino-silicates, heavy oxide glasses, sodium silicates or germanates, and commercial glasses. This work includes findings from previous chapters of this dissertation. The optical properties of formed NGs (NGs energy window, retardance, birefringence) can vary in great proportion with respect to glass composition. The mechanisms NGs formation induced in transparent materials are discussed, along with the effect of glass composition on characteristic features such as periodicity, nanopore size, filling factors (FF) and correlated "technological performances" according to chemical compositions. This chapter includes a paper published in Progress in Materials Science (IF=37.4), and I am the 2nd author and the corresponding author.

IV.2 MATERIALS ROADMAP FOR INSCRIPTION OF NANOGRATINGS INSIDE TRANSPARENT DIELECTRICS USING ULTRAFAST LASERS

Progress in Materials Science 142 (2024) 101226

Contents lists available at ScienceDirect

Progress in Materials Science

journal homepage: www.elsevier.com/locate/pmatsci

Materials roadmap for inscription of nanogratings inside transparent dielectrics using ultrafast lasers

Heng Yao [a,b], Qiong Xie [a,*], Maxime Cavillon [a], Ye Dai [b,*], Matthieu Lancry [a,*]

[a] Institut de Chimie Moléculaire et des Matériaux d'Orsay (ICMMO), Université Paris-Saclay, CNRS, Orsay 91400, France
[b] Department of Physics, Shanghai University, Shanghai 200444, China

ARTICLE INFO

Keywords:
Ultrafast laser
Femtosecond laser direct writing
Optical glasses
Glass materials
Volume nanogratings
Integrated optic applications
Birefringent devices
Multicomponent glasses
Silicate glasses

ABSTRACT

20 years ago, volume nanogratings were discovered in silica glass upon ultrafast laser irradiation. Since then, these extraordinary self-organised and birefringent structures have been observed in a wide range of transparent materials, including crystals and glasses. In the latter, the role of glass composition and chemistry drastically impact the overall nanostructuring, properties, and morphologies of the fabricated nanogratings, but there still is no global understanding of the origin of various observed discrepancies. Consequently, this work aims to provide a materials roadmap to stimulate the development and selection of glass materials for nanogratings imprinting, depending on the final application, and intends to comprehensively pinpoint the differences existing between glasses. A critical overview of the discovery of nanogratings in multicomponent glasses is presented from 2003 to 2023, and general aspects of the nanogratings formation mechanisms are provided. Then, principal nanograting characteristics are collected, summarized, and discussed (e.g., periodicity, nanopore size) along with useful "technical performances" (e.g., nanogratings energy window, maximum retardance, nanogratings power consumption) that are discussed in the light of chemical composition effects. Finally, a summary of the main optical applications based on nanogratings is given, such as birefringent or geometric phase optics, optical data storage, micro/nanofluidic devices, third harmonic generation and optical fiber sensors.

1. Introduction

Nearly three decades ago, the processing of transparent materials by ultrafast laser pulses has emerged as an excellent tool to induce on demand 2D/3D transformations with a high degree of freedom coupled to a high spatial precision [1–4]. These results in the possibility to imprint self-organized structures, voids, nanocrystals, and to perform 3D refractive index profiling depending on the laser writing conditions [5,6]. One of the most interesting and innovative effect found in the interaction of tightly focused femtosecond (fs) laser pulses with optical materials is the production of self-organised light-shaped nanostructures called nanogratings (NGs), also commonly referred as IR-fs Type II modifications [7,8]. A variety of photonic applications, taking advantage of this "light–forced nanostructuring" and associated properties have recently emerged, including birefringent elements, geometric phase optics, 5D optical storage, laser selective etching and optical fiber-based sensors for harsh environments [9–22] (see *section 4*).

These volume nanogratings can easily be observed using conventional electron microscopy techniques and an example is provided

* Corresponding authors.
E-mail addresses: qiong.xie@universite-paris-saclay.fr (Q. Xie), yedai@shu.edu.cn (Y. Dai), matthieu.lancry@universite-paris-saclay.fr (M. Lancry).

https://doi.org/10.1016/j.pmatsci.2023.101226
Received 24 May 2023; Received in revised form 23 November 2023; Accepted 6 December 2023
Available online 10 December 2023

in Fig. 1 (a) for ubiquitous silica (SiO_2) glass. In the focal volume of the irradiated region, arranged porous nanoplanes are typically observed with the latter being oriented perpendicular to the laser polarisation (*E*). These structures were first discovered in 2003 [23] and are composed of an assembly of disks [top of Fig. 1 (a)] measuring a few *μms* in diameter. Moreover, spatial plasma density and temperature distributions associated with their formation is exemplified in Fig. 1 (a), with peak maxima exceeding the silica glass decomposition limit [24].

NGs have been observed in many solid compounds, from adjustment of the laser parameters. There are several categories of NGs. The most popular one was primarily revealed in SiO_2 glass with an arrangement of nanoplanes populated by 10–30 nm oblate nanopores [23]. These nanopores are produced by partial oxide decomposition through a plasma-mediated nanocavitation [12,24]. The imprinted NGs are sensitive to laser polarization, giving rise to form birefringence leading to a large retardance (typ. > 200 nm), broadband exploitable anisotropic optical properties (e.g. a linear birefrigence up to 10^{-2}) [25] and extraordinary thermal stability (typ. many hours at 1000 °C) [26]. Moreover, the nanolayers exhibit alternatively high / low atomic densities (as illustrated in Fig. 1 (b) and thus higher / lower refractive indices (n_G versus n_{pl} respectively, see *section 3.3*). These anisotropic structures create fascinating properties, including anisotropic light scattering [16] and highly selective chemical etching [27]. Recent progress highlights that a fs laser beam (axially symmetric intensity distribution, linear polarized with orthogonal incidence) can break the glass symmetry and create optical chirality inside an achiral material through laser direct writing within NGs regime [28–33]. This concept shed light on a new approach for tailoring chiral optical properties such optical rotation and circular dichroism in three dimensional (3D) providing a wider landscape of laser manufacturing.

All the above mentioned optical properties have found practical use in 2D / 3D space variant birefringent optical devices [7], geometric phase optics [16], optical sensors for high temperature applications [34], long lifetime 5D optical memory [18],

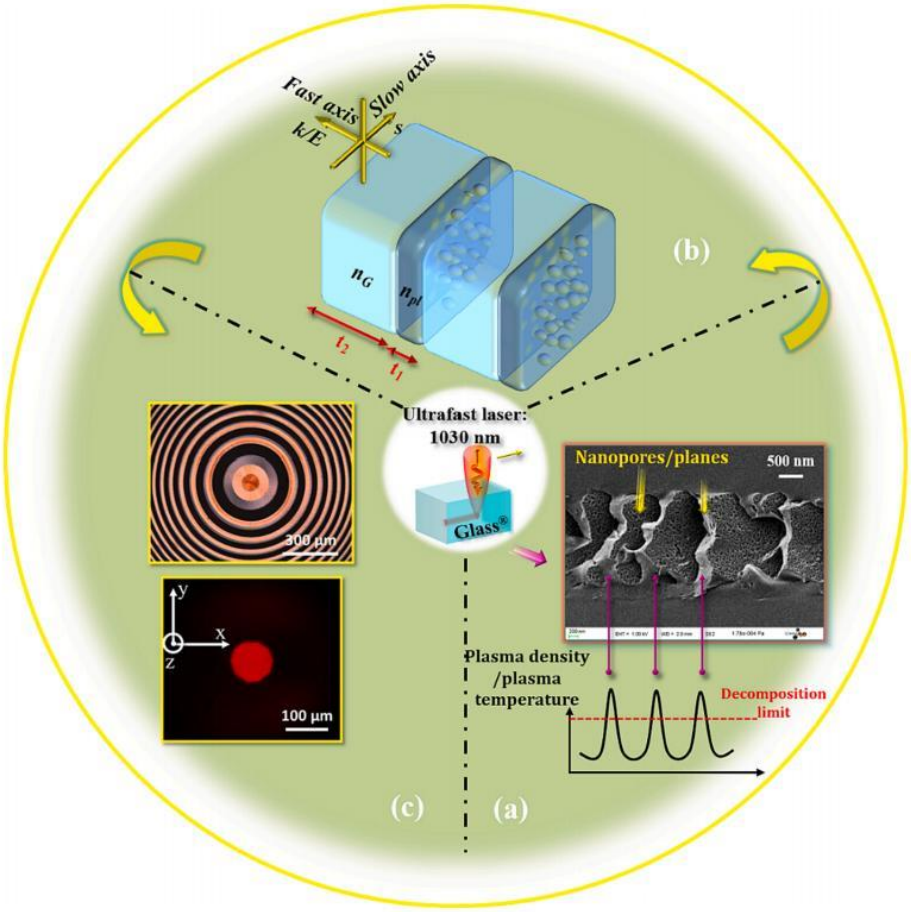

Fig. 1. (a) Top: internal structure of NGs induced by a fs-laser in SiO_2 and observed by scanning electron microscopy (SEM) imaging, where the nanoplanes are composed of nanopores; bottom: spatial distribution of plasma density and temperature with its peak maxima over the decomposition limit, adapted from Ref. [24]. (b) Sketch of fs-laser induced NGs in volume. The fast axis of the self-organised nanostructures is perpendicular to the self-organised nanoplanes with t_1 being the nanoplane thickness and t_2 the thickness between two consecutive nanoplanes. n_{pl} and n_G are the corresponding refractive indices of nanoplane and pristine glass, respectively, see section 3.3. E, s and k present respectively laser polarisation orientation, laser scanning and beam propagation directions. (c) Top: optical micrograph of fs-laser induced Fresnel zone plate in an 8% Ta_2O_5-BGG glass sample; bottom: image of the primary focus at 632 nm in 8% Ta_2O_5-BGG glass from Ref. [12].

microfluidics and lab-on-chips devices [27], and polarisation selective holography [35] (see *section 4*). An example of an optical component is shown in Fig. 1 (c) where a single-step birefringent Fresnel graded-index (GRIN) plate is fabricated with a 2 mm outer diameter inside a 8% Ta_2O_5-BGG glass (BaO-Ga_2O_3-GeO_2), an heavy oxide glass for mid-infrared (IR) photonics [12]. A phase retardation of 2π was easily reached and the typical primary focal spot is shown in the lower part of Fig. 1 (c).

Until recently, NGs formed by these nanoporous self-organised structures, as described for silica glass, were thought to be only observed in a handful of materials (mostly SiO_2-rich oxide glasses), restricting their use to the visible and near-IR optical spectrum. The effect of the physical properties of glass (melting temperature, thermal diffusivity, absorption, etc.) on the NGs formation process has been extensively investigated over the last decade and recently rationalised [36,37]. This clearly reveals that glass chemical properties, arising from their varying chemical compositions, play a key role in the formation process of NGs. To date, numerous results have already been reported on NGs in multicomponent glasses [38–42] as review in *section 2* but only a few systematic investigations have been performed [7,43].

Another kind of nanogratings exist aside from porous NGs, which are composed of a partially crystalline nano-periodic structure. For example, in Ref. [44], the authors reported form birefringence in lithium niobium silicate (LNS) glass after fs-laser irradiation which comprised of a periodical layering arrangement of nonlinear optical nanocrystals ($LiNbO_3$) with an amorphous phase (SiO_2). These structures are of interest for nonlinear optics related devices. In Ref. [45], other authors reported similar partially crystallised NGs in sodium germanate (SG) glasses for a wide range of Na_2O content (3 to 22 mol.%, the rest being GeO_2) and precipitation of $Na_2Ge_4O_9$ crystals embedded in the self-organised nanostructure was observed. Recently, regularly patterned crystal precipitation induced by ultrafast laser was shown in La_2O_3-Ta_2O_5-Nb_2O_5 (LTN) glass [46].

This paper aims to draw upon general trends linking NGs formation with the chemical composition of optical glasses. The discovery of NGs in various compositions is presented with an historical perspective, starting from the initial works in silica and silicates and moving to multicomponent glass compositions including alumino-silicates, heavy oxide glasses, sodium silicates or germanates, and commercial glasses. Optical properties of formed NGs (NGs energy window, retardance, birefringence) can vary in great proportion with respect to glass composition. Here, retardance equals $R = B \times L$ [47], where B is birefringence and L is the birefringent transformation thickness. In this work, we tentatively synthesize principal aspects of NGs observed from literature and induced in transparent materials, and we discuss their formation mechanisms in the light of the current state of the art. Key NGs characteristics such as periodicity, size of nanopores, filling factor (FF), and correlated "technological performances" are gathered and discussed according to

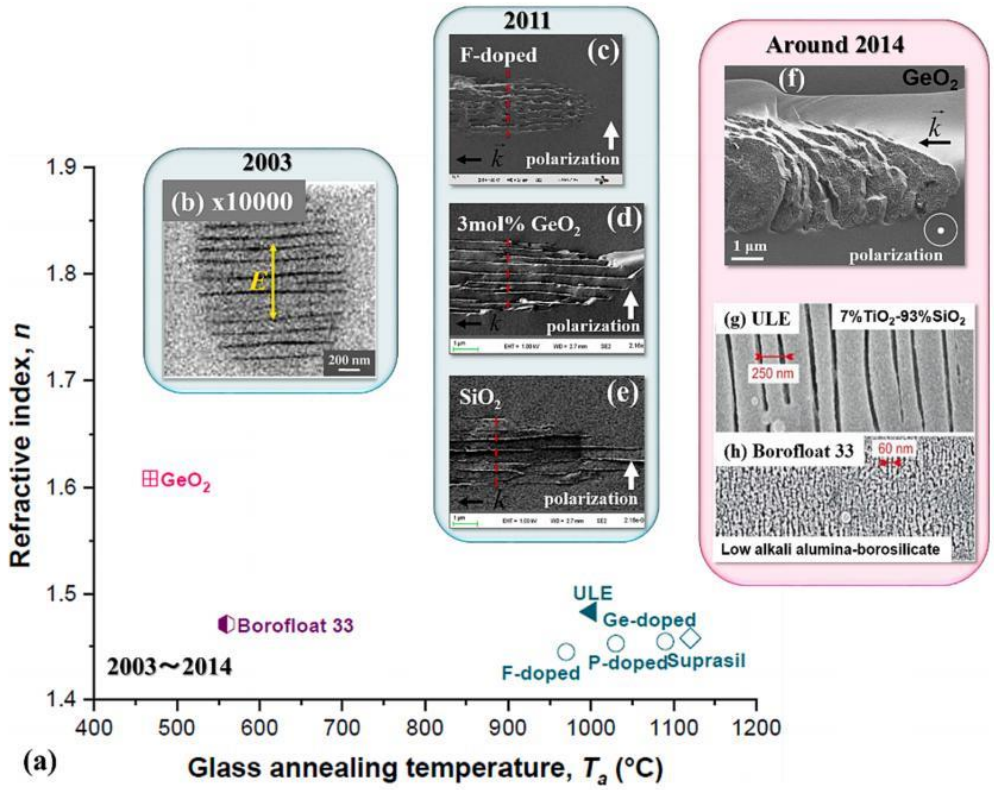

Fig. 2. Refractive index, n (measured at 550 nm) of various glasses as a function of glass annealing temperature, T_a (°C) for the observation of NGs (a) from 2003 to around 2014. (b) Backscattering electron micrograph of NGs in silica from 2003 [23]. (c) Field-emission gun scanning electron microscope (FEG-SEM) imaging of NGs in F-doped silicate glasses in 2011. (d) and (e) present respectively the images of FEG-SEM on NGs in 3 mol. % GeO_2 silicate and SiO_2 glasses in 2011. (f) and (g) (h) are respectively SEM micrographs from Ref. [43,56] and Ref. [50] around 2014.

the chemical composition. The latter are NGs fabrication energy window, maximum achieved optical retardance or related birefringence, energy consumption to imprint such nanostructures, laser scanning speed and thermal stability. Their evaluations are expected to drive forward glass design and laser parameter choices for industrial and laboratory uses.

2. Evolution of NGs discovered on the chemical composition

Silica-based glasses are the backbone for many of today's rapidly expanding photonics applications. There are various polymorphs such as quartz, trydimite or cristobalite leading to 3D assembling of SiO_4 tetrahedra, which is generally formed with a short-range order but has no order at a long distance. Any exception in the ≡Si-O-Si≡ sequence in silica can be considered as a point defect, e.g., SiE', NBOHC (Non-Bridging Oxygen Hole Centre) or ODC (Oxygen Deficient Centre). Moreover, glass doping using chemical elements such as alkali or alkaline earth modify the physical properties (density, glass transition temperature, thermal diffusivity etc.). Therefore, through doping or chemical composition change in oxide glasses is a key factor to be considered during the formation process of laser-induced transformations inside transparent materials, since it is governed by the direct coupling between light and matter leading to the spatial structuration of the free electron plasma. Indeed, NGs induced in volume by fs-laser were observed in several glasses or crystals among which we can cite doped silica [39–41] with F, P, Ge, Cl, OH elements, GeO_2 [43,48], SiO_2-GeO_2 [40], TiO_2-SiO_2 (ULE, Corning) [49,50], TeO_2 single crystal [51], Sapphire [52], Al_2O_3-Dy_2O_3 [53], LNS [44,54] and even multicomponent alumino-borosilicate [55] or BaO-GeO_2-Ga_2O_3 (BGG) glasses [12]. In this section, we present the findings of NGs, discovered in multiple series of chemical compositions over the last two decades since the discovery of NGs in 2003. For this purpose, we chose to represent the collected results from literature on a Refractive index – Glass annealing temperature plot. These two properties are both characteristic of glass families and key aspects for both the glass maker and user.

2.1. NGs discovered from 2003 to 2014

Since the first observation of NGs in fused silica by Shimotsuma et al. [23] in 2003 as illustrated in Fig. 2 (b), NGs have attracted great attention within the photonics research community. In fact, the most investigated transparent material for NGs was fused silica

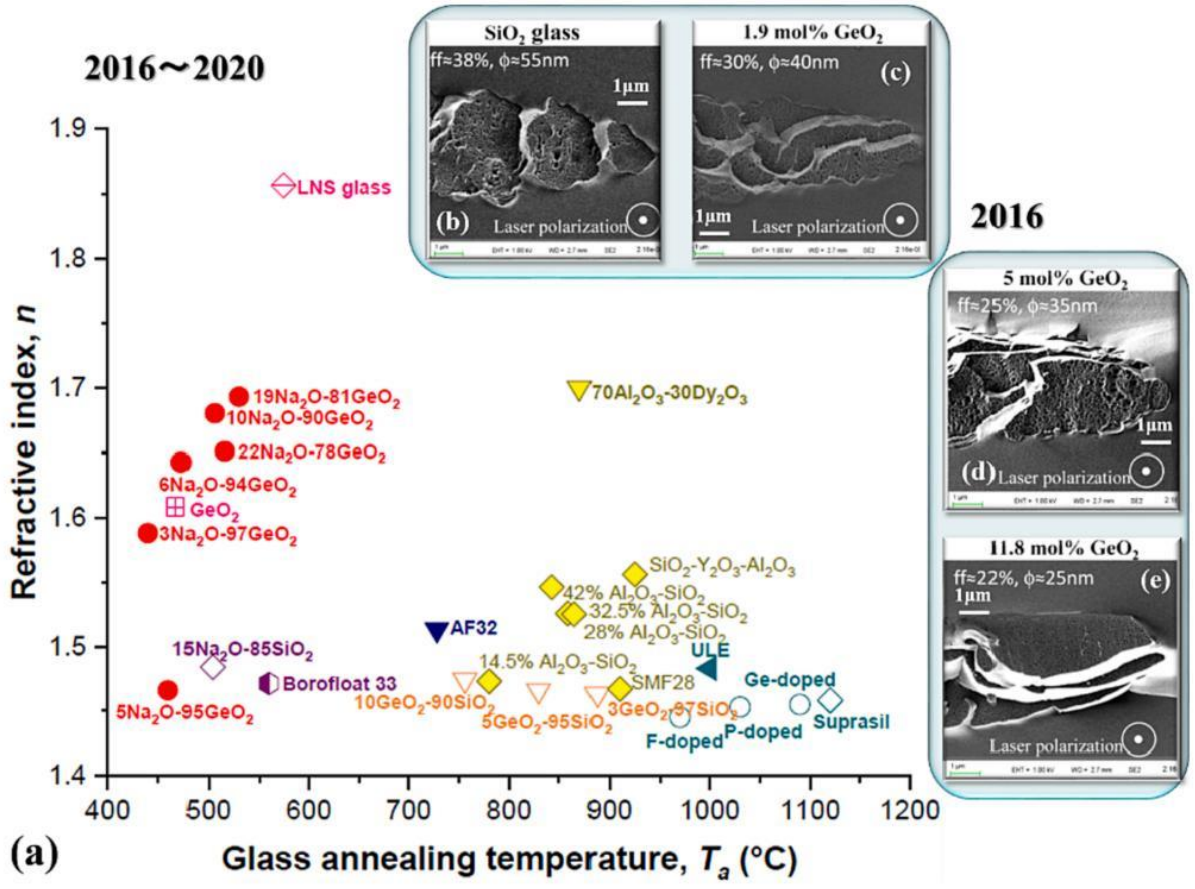

Fig. 3. Refractive index, n, measured at 550 nm, of various glasses as a function of glass annealing temperature, T_a (°C) for the observation of NGs in (a) 2016 ~ 2020. (b)-(e) are SEM micrographs of SiO_2, 1.9%, 5%, and 11.8% GeO_2 silicate glasses respectively from Ref. [40].

glass from 2003 to 2014 [24,57–59]. Additionally, NGs inside a few multicomponent glasses and glass systems were also investigated during this period by ultrafast laser irradiation as summarized in Fig. 2.

In 2011, Lancry et al. suggested that even a small amount of dopants can significantly affect the threshold of birefringence observation (a permanent linear birefringence) [39] in silica-doped glasses, e.g., the threshold to NGs formation in a 1.5 at% Ge-doped silica was almost two times lower (0.14 ± 0.05 μJ/pulse) compared to silica (0.31 μJ/pulse). On the other hand, the threshold in a 0.3 at% F-doped silica was higher compared to silica (1.20 ± 0.05 μJ/pulse). Finally, the addition of 0.3 at% of phosphorus into the 0.3 at % F-doped silica reduces the threshold from 1.20 to 0.25 ± 0.05 μJ/pulse. These differences are attributed to facilitated formation of point defects in Ge-doped silica glass by reduction process, where Ge can induce the creation of trapping centers. If P-doped silica followed a similar trend as the Ge-doped glass, F-doped silica glass was found to "harden" the glass against ionizing radiation [60]. Indeed, F-doping is known to reduce the concentration of defects and structural disorder [39] in the glass which may result in a challenging glass decomposition process (e.g., a more difficult seeding to induce decomposition) and thus a higher NGs formation threshold.

The dependence of glass decomposition on the bound energies was facilitated for Ge- and P-doping compared to F-doping. At that time, it was suggested that the presence of point defects was a key factor promoting NG formation. Indeed, doping chemical elements can directly control the concentration of defects. To correlate defect concentration with the final birefringence (B) of the NGs structure (measured through retardance), a relationship was proposed in Ref. [61] and takes the following form: $B = N \bullet \varepsilon \bullet [\mathrm{STE}]$. Here $[\mathrm{STE}] = \sigma \bullet I^k$ and N is the number of pulses, ε is the branching ratio, [STE] is the "self-trapped exciton" concentration, σ is the multiphoton absorption cross-section and k is the number of photons involved in the multiphoton ionisation (MPI) process. Furthermore, the role of viscosity, η, was initially suggested on the overall proposed mechanism and stating that $\frac{\eta(T_c)}{G(T_c)} = \delta t(T > T_c)$ where T_c is the "critical" temperature leading to the change in fictive temperature [62], η and G are respectively the viscosity and shear modulus. Such thermal effect can locally impact the "background material" density (densification or expansion depending on the composition) [62] but this can also lead to the erasure of the NGs themselves at high energies and repetition rates. Subsequently, NGs were gradually observed in Ultra Low Expansion (ULE, 7%TiO_2 - 93%SiO_2 in mol.%) and in Borofloat33 (81%SiO_2 - 13%B_2O_3 - 4%Na_2O / K_2O - 2%Al_2O_3 in mol. %, which was the first report of very short periodicity $\ll \Lambda/2n$, i.e. 60 nm) glasses by Richter et al. in 2013 [50] and in GeO_2 by Shimotsuma et al. in 2014 [56] as shown in Fig. 2 (g) (h) and (f) respectively.

2.2. NGs discovered from 2016 to 2020

Initially NGs were reported mainly inside anomalous glasses made of SiO_2 and slightly doped silica (typically 1.9 mol.% in GeO_2 or 7% TiO_2-93% SiO_2) or doped SiO_2 mentioned above, but not in most normal glasses (BK7, SnO_2-SiO_2, CaO-Na_2O-SiO_2 glass). However, in 2016 Lancry et al. [40] reported the observation of porous NGs in normal ones such as highly Ge-doped SiO_2 or GeO_2 glasses as illustrated in Fig. 3. This is a first step towards the rationalisation of several previous works from Refs. [50,56]. Here, the authors indicated that porosity FF and pore size decreased with increasing GeO_2 content, as illustrated in Fig. 3 (b)-(e). These two factors of prime importance for NGs, will be defined and discussed in *Section 3*. At that time, the nanopore formation mechanism was thought to be akin to the tensile stress assisted decomposition process [40].

In Ref. [43], Lancry et al. highlighted that chemical composition and heat accumulation (HA) are key factors in the formation / erasure process of NGs, affecting their characteristics such as FF, nanopore diameter (i.e., related to light scattering), optical retardance and thus birefringence. HA is a phenomenon that arises when the pulsed laser time period is in the order of magnitude or smaller than the thermal diffusion time, which leads to a temperature increase in the focal volume. These crucial factors (HA, FF, nanopore diameters, retardance or B) will be reviewed in the next section.

During the 2016–2020 period, there were a significant number of new observations not only in silicate glasses, but also in germanate and aluminate glasses as summarised in Fig. 3.

In 2016, Fedotov et al. [42] revealed that multicomponent silicate glasses with low glass annealing temperatures (T_a, corresponding to the viscosity $\eta = 10^{12.0}$ Pa·s [55], e.g., 1250 °C for silica glass, 717 °C for AF32 glass and 525 °C for Borofloat 33 glass) exhibit a narrow NGs processing window. For completeness, AF32 and Borofloat 33 glass compositions are respectively 11%B_2O_3 - 11%Al_2O_3 - 67%SiO_2 - 10%CaO / MgO and 13%B_2O_3 - 2%Al_2O_3 - 4% Na_2O / K_2O - 81%SiO_2. Similarly, when investigating NGs in GeO_2-SiO_2 glasses as exemplified in the insets for Fig. 3, both porosity FF and average pore size were found to significantly decrease with a progressive increase in GeO_2 content (from 1.9 mol.% to 11.8 mol.%) [40]. The NGs period, Λ, was also found to decrease. In contrast, the maximum optical retardance decreased when increasing the GeO_2 content. Furthermore, Zimmermann et al. reported in 2016 that the aspect ratio of nanopores (transversal to the laser propagation direction) was elevated by increasing the GeO_2 content in fused silica [63]. They also demonstrated that NGs periodicity and pore size decreased when increasing GeO_2 content in Ge-doped silica glass. According to these results they concluded that there is a strong decrease in periodicity which breaks the $\lambda/2n$ limit and challenged the nanoplasmonic model prediction [57]. This highlights the fact that glass chemical composition not only dictates nanopore morphology, but also their assembly into periodic NGs.

Later in 2017, Shimotsuma et al. [41] similarly reported form birefringence in silica glass with various anion dopants (OH, Cl and F) induced by fs-laser pulses. They found that higher birefringence can be induced in silica glass doped with higher Cl ion concentration due to shorter NGs periodicity, Λ (sample 100 ppm OH with Λ of 220 nm, 6300 ppm Cl with Λ of 204 nm and 9400 ppm F with Λ of 224 nm). This work clearly reflects the impact of anion doping on the properties of NGs, namely linear birefringence and NGs periodicity. Additionally, NGs imprinting was demonstrated in nanoporous silica (Vycor and sol–gel nanoporous silica) [64] showing a reduced formation threshold when increasing the initial nanoporosity, suggesting in such a way that glass free volume might be a precursor of

NGs formation rather than point defects.

Furthermore, another kind of NGs, i.e., $1/3Li_2O$-$1/3Nb_2O_5$-$1/3SiO_2$ (LNS) glass precipitating $LiNbO_3$ nanocrystals, was observed by Cao et al. [44] in 2016 and this will be discussed below in detail. Subsequently, Shimotsuma et al. [53] (in 2018) and Lotarev et al. [45] (in 2019) respectively reported on the similar NG structures with precipitation of crystals in Al_2O_3-Dy_2O_3 binary glass and Na_2O-GeO_2 binary glasses, i.e., $Dy_3Al_5O_{12}$ and $DyAlO_3$ crystals in Al_2O_3-Dy_2O_3 and $Na_2Ge_4O_9$ crystals in Na_2O-GeO_2 glasses. In fact, prior to 2019, Wang et al. [38] had already reported on the formation of NGs in a sodium germanate glass (5% Na_2O - 95%GeO_2 mol.%) in 2018 but without partial crystallisation. This further indicates the substantial impact of chemical composition on the formation of NGs.

In 2019, the possibility of writing NGs in sodium borosilicate glass (SBS) was demonstrated [65] with the molar composition of 68%SiO_2 - 27%B_2O_3 - 4%Na_2O, and 1%Al_2O_3. This composition falls down in the range of metastable liquidus, enabling the formation of a phase-separated structure by means of heat-treatment. Microregions with polarisation-sensitive birefringence are formed when 10^5 or more fs-laser pulses are deposited in the focal volume. The range of pulse energies enabling NGs formation, and the phase shift attained in birefringent regions rise by increasing numbers of writing pulses and the formation of NGs is accompanied by the chemical migration of sodium cations outside the laser-modified region. NGs inscription was demonstrated in binary sodium silicate glasses $xNa_2O(100\text{-}x)SiO_2$ (with x = 5, 15) and revealed the effect of nanoperiodical chemical differentiation inside NGs in 15%Na_2O - 85% SiO_2 glass with Na cations concentration near the nanoplanes [66]. Unlike in sodium silicate glasses, increasing Na_2O content to 10 mol.% was reported to prevent their formation in sodium germanate glass [38].

Later in 2020, nanoscale chemical migration was also observed along with formation of NGs inside Al_2O_3-SiO_2 binary glasses by Wang et al. [67]. They specifically reported on a higher thermal stability at the expense of a higher NGs formation threshold and lower retardance when increasing Al_2O_3 content. This was tentatively attributed to nanoscale phase separation and potentially to the formation of Mullite nanocrystals.

2.3. NGs discovered from 2020 to 2023

Over the 2020–2023 period, there was a trend towards systematic investigations of NGs in terms of the chemical composition. For example, the BGG glass family (BaO-Ga_2O_3-GeO_2) was investigated in 2022 as they involve useful compositions for targeted mid-IR optical applications. As shown in Fig. 4 (a), when these glasses are doped with Na, K, or La, no laser conditions were found to support NGs formation [68]. However, when Ta, Gd or Zn dopants were added, NGs could be imprinted quite easily [12,69]. Intriguingly, in 2022, Xie et al. [36] presented the existence of NGs in BK7 glass which revealed no nanostructures from SEM analysis in previous works (Refs. [42,50]). However, this was possible only for very specific conditions (< 100 kHz and for typ. 50,000 pulses/μm) and as shown from the SEM analysis in Fig. 4 (b)-(d). This suggests that NGs can be formed in any oxide glasses provided that 1) HA is prevented or moderate, and 2) the deposited fluence is sufficiently high. From this point, NGs formation was widely investigated inside

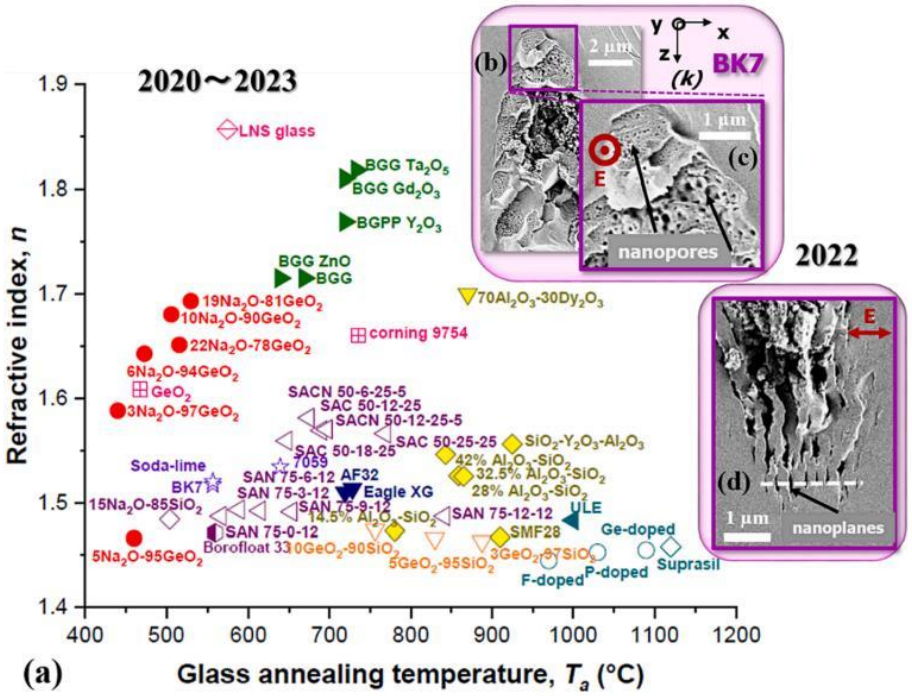

Fig. 4. Refractive index, *n*, measured at 550 nm, of various glasses as a function of glass annealing temperature, T_a (°C) for the observation of NGs in (a) 2020 - 2023. (b), (c) and (d) are illustrations of NGs observed in BK7 from SEM analysis with conditions: pulse duration = 800 fs, writing speed = 1 μm/s, *RR* = 25 kHz, E_p = 0.6 μJ, focal depth = 300 μm.

many other commercial glasses including soda-lime silicate, Corning 7059, Eagle XG as well as Corning 9754 glasses as reported by Xie et al. [37] and Delullier et al. [70]. In 2023, NGs were studied in the alumino-borosilicate family [55] i.e., alumino-silicate glasses including B_2O_3, Na_2O, and / or CaO on a large variation of proportion as shown in Fig. 4 (a) [36]. It further indicated the chemical composition and more specifically (Na_2O + CaO) / Al_2O_3 and B_2O_3 / Al_2O_3 molar ratios for NG formation. A lower B_2O_3/Al_2O_3 molar ratio and relatively high SiO_2 can result in a higher retardance response. Additionally, the Type II energy window was progressively reduced when increasing the molar ratio of (Na_2O + CaO)/Al_2O_3 and B_2O_3/Al_2O_3. Furthermore, NGs are also found in crystals with small bandgap such as Si, GaP, 4H-SiC, GaN, or GaAs crystals [71–74], and very recently in Ge-Sb-S chalcogenide glass [75], revealing for the first time the formation of NGs in non-oxide glasses.

2.4. Summary

To summarize there are various kinds of NGs. The first type is found in most oxide glasses like SiO_2 and was the first discovered. It is based on nanoporous layers made of ultrafast oxide decomposition. A second type on NGs is found in semiconductors (GaP [76] and Si [71]) and oxide crystals (Al_2O_3 [52] and TeO_2 [51]). The experimental observations mostly revealed arrangements of cracks, perpendicular to laser polarization. A third kind of NG is observed in quartz crystal through a periodic amorphization. This is likely due to local fluctuations of thermal effect induced by the electron plasma structure [77]. Finally, a fourth kind of NG corresponds to nano-periodic structures in glasses that are partially crystalline. For example, they were seen in 33%Li_2O - 33%Nb_2O_5 - 34%SiO_2

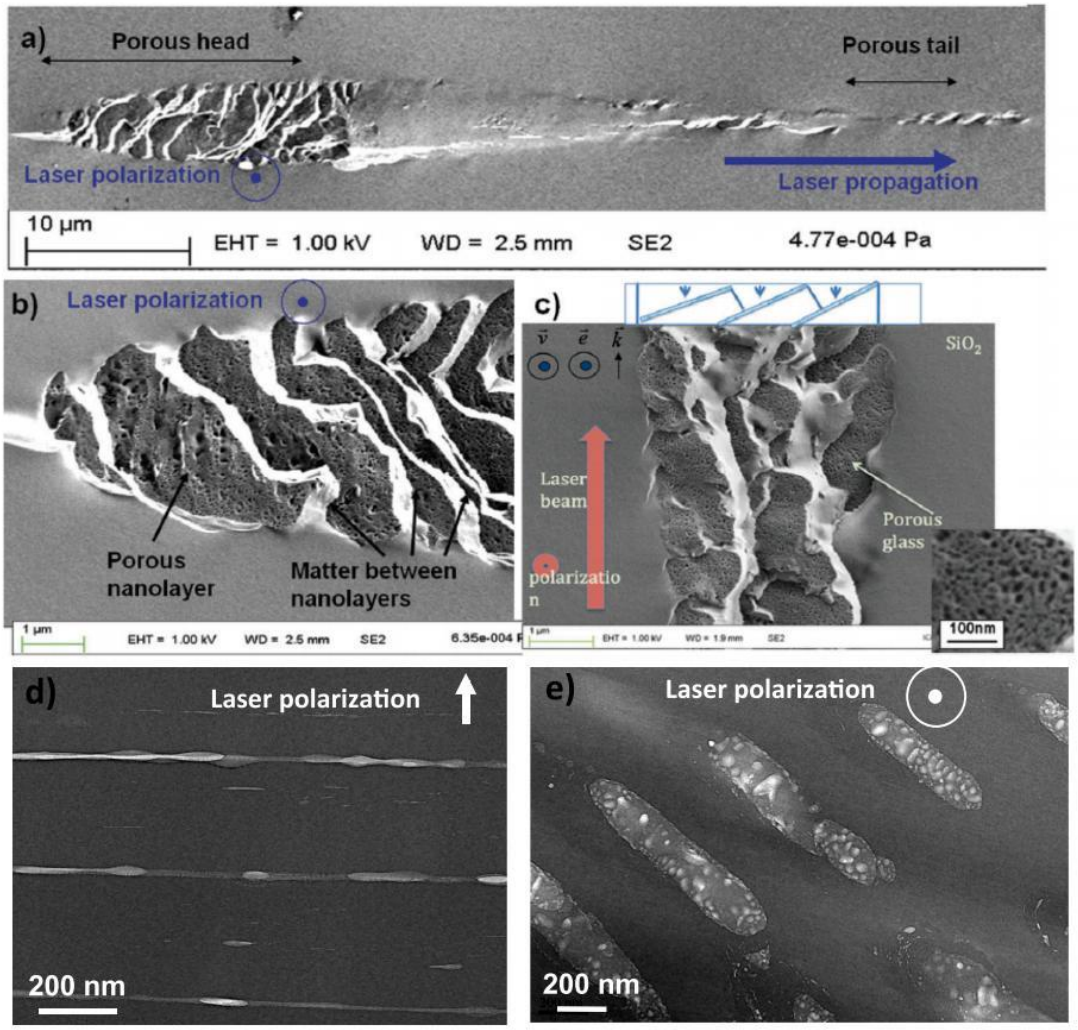

Fig. 5. SEM micrographs of laser track cross-sections, with a) the laser polarization parallel to the scanning direction; b) and c) are close-ups of the nanoporous regions. Micrographs extracted from Lancry et al. [24]. HR-TEM micrographs with laser polarization d) perpendicular to the scanning direction thus showing nanoplans made of "self-aligned" oblate nanopores and e) parallel to the scanning direction revealing internal structure of nanolayers made of nanopores. Laser parameters are: 1030 nm, 250 fs, 200 kHz, 200 µm/s, NA = 0.6, and 0.5 µJ/pulse.

(precipitating $LiNbO_3$ [54]), and (33%Li_2O - 33%Nb_2O_3 - (34-x)%SiO_2 - x%B_2O_3 non-congruent glasses [78]), in 20%Na_2O - 80%GeO_2 glasses (congruent glass composition for $Na_2Ge_4O_9$ [45]) and in 65%Al_2O_3 - 35%Dy_2O_3 glass (congruent glass composition for $Dy_3Al_5O_{12}$) [53]. In these glasses the observed NGs periodicity likely arises from an interplay between the glass constituents and multiphoton ionization. In the case of 20%Na_2O - 80%GeO_2 glasses, crystallization occurs mainly around the NGs area. In contrast, for 65%Al_2O_3 - 35%Dy_2O_3 glasses, crystallization is situated mostly inside the NGs region, but there are no details on its nanoscale distribution. As for Li_2O-Nb_2O_5-SiO_2 non-congruent glass, NGs are produced through an allotropic phase separation (i.e., $LiNbO_3$ nanocrystals in between SiO_2 thin lamellas) [54]. In such a glass, a thorough study [79] demonstrated that the induced plasma influences the spatial periodicity of the phase separation.

Very recently, Sakakura et al. [16] reported an intermediate regime of NGs, called "Type X" modification, which can be considered as randomly distributed anisotropic nanopores induced by ultrafast laser that exhibit ultralow scattering loss (99% transmission in the visible and > 90% transmission in the UV) compared to NGs (limited transmission when increasing the laser-induced layer). In parallel, Lei et al. [17] reported a systematic study with the comparison of photosensitivity characteristics (birefringence) among the nanolamella-like structure, Type X and NGs. These Type X modifications were then exploited for achieving 5D optical storage with high data capacity and long lifetime in fused silica [18].

3. Formation of nanogratings – self structuring and porosity

The historical perspective on NG presented above clearly shows that the most experimentally observed and investigated NGs are made of porous nanolayers. Therefore, in the following section, we principally discuss the mechanisms inherent to the formation of such NGs, by briefly summarizing the principal aspects and contributions.

3.1. First observations of NGs and their characteristics

At the nanoscale, Shimotsuma et al. [23] revealed NGs (around 20 nm in width, and with a periodicity from 140 to 320 nm) through back-scattered electron imaging corresponding to an atomic density contrast. Chemical analysis by Auger spectroscopy showed that it could correspond to oxygen depletion and related density modulation [23]. Hnatovsky et al. [80,81] reported nano-cracks and it was not clear if whether these NGs could be best described as highly modified regions of differing materials (e.g., through bond breaking accumulation) or as some nanovoids. Regardless of the precise mechanistic explanation of nanoplanes (nanoplasma [82], photon-plasmons interference [83], plasmon-polaritons [84] or complex self-organization similar to a Turing structure), it remained to determine the internal structure of these nanoplanes. Some authors observed cracks / fractures, others publications reported oxygen depletion. However, recent studies [24,85] using both transmission and scanning electron microscopy (TEM and SEM) techniques, revealed that NGs are made of an alternated assembly of "uniform" and porous glass layers as shown in Fig. 5. The interior of the NGs was made of "white areas" that, although having been irradiated, remained dense and even densified, while the parts that are nanoporous are the nanoplanes cleaved along their plane. At that time, formation of nanopores was attributed to SiO_2 decomposition into $SiO_{2(1-x)} + x \cdot O_2$ due to an electronic heating leading to an expulsion of ionized oxygen atoms [24] with a tensile stress mechanism [40,86–88] that was recently revisited as a nanocavitation process [45]. The oxygen atoms are thus found in the interstitial position and recombine to form oxygen molecules as confirmed by Raman spectroscopy [24]. The typical diameter of nanopores ranges from 10 to 50 nm. Asai et al. observed a similar feature in GeO_2 glass [89] providing again a clue of the suggested decomposition process in these oxide glasses. This nanoporosity has been confirmed recently by Richter et al. using small angle X-ray scattering [58,90] and they revealed the formation of elongated nanopores. In 2014 [91] and 2018 [92–94], the self-organization process was suggested to be seeded by nanoscale inhomogeneities such as voids and a nanocavitation mechanism was proposed.

In 2013, the formation of SiO_{2-x} nanocrystals within nanoplanes was reported [95], which could be in agreement with oxide decomposition [96]. In a second publication, the same group did not report nanocrystals but instead revealed that damaged nanoplanes contain randomly dispersed nanopores with a bimodal size distribution [97]. However, it appears that the use of HF etching degrades the quality of the observations. Recent work based on HR-TEM and STEM imaging techniques enabled to probe the intimate 3D nanostructure of fs imprinted NGs in silica [98]. An array of oblate nanopores can be observed (Fig. 5, d and e), which own a long axis both along $\boldsymbol{k}$ and perpendicularly to $\boldsymbol{E}$. The porous nanolayer thickness ranges from 6 to 30 nm, and their length, perpendicularly to the laser polarization, could reach typically few μms or more. Based on the reported mechanisms of the NGs formation in literature, imprinting of NGs is attributed to a plasma-mediated nanocavitation process with a spatial ordering due to scattered waves interference [91,99]. Several steps can be considered in such process.

3.2. Plasma spatial structuring mediated by a seeding process

A first requirement to the formation of NGs is the need of inhomogeneities in the dielectric constant to seed the process. These inhomogeneities (or seeds) could either be already present in the pristine glass or photo-induced by the first pulse(s). Following these first instants, spherical nanoplasmas would be formed, stimulated, and reinforced by plasma density or temperature. Over several pulses, they will evolve into oblate shaped nanoplasma due to field enhancement effect, in which the electric field of the laser light triggers an asymmetric growth [100]. This plasma-mediated process has been suggested early in the literature. For example, Taylor et al. [100] mentioned, in 2008, that the presence of defects or color centers might seed the plasma creating locally and easily ionized "nanospots" creating high plasma density. In this model, developed by Bhardwaj et al. [57], the period Λ of NGs was supposed to remain between λ/n and $\lambda/2n$ and a period initially independent of pulse energy. However, the NGs average period was observed to

decrease monotonously with the number of laser pulses [101,102], but also be a function of the chemical composition such as doped SiO_2 [50] or in multicomponent glasses [37,42] (this aspect will be discussed in the next section). This is clearly illustrated in Fig. 7 where we summarized the normalized period Λ/λ vs. refractive index reported in the overall literature including a wide range.

In 2014, Buschlinger et al. [91] modelled by Finite-Difference Time-Domain (FDTD) method the plasma spatial structuring, hence periodicity, induced by scattered wave interferences from existing inhomogeneities in glass. This creates high density plasma nanoplanes in an interference-like image by multiple scattered waves interference forming standing waves, which needs boundary conditions. For a circular polarization, the nanoplasma hot spots should remain symmetric, resulting in spherical nanopores like observed within Type X regime [16]. Then when considering a multi-pulses regime, there is an evolution of the oblate nanoplasmas into nanoplanes as shown in "post-mortem" experiments [102]. The lengths of the oblate voids, whose direction is perpendicular to ***E***, increase as the pulse number increases in agreement also with observations made in Type X regime [16]. In 2016 A. Rudenko et al. [103] developed a numerical model to explain the formation of periodic volume NGs from random inhomogeneities with varying concentration and laser parameters. The contribution of combined physical processes (e.g., the interference between the incident and the scattered waves, multiple scatterings, local field enhancement, and accumulation processes driven by multiphoton ionization) reinforces the formation of NGs. At this stage, the plasma of free electrons is roughly organized or structured, but this also corresponds to the end of the light pulse. Following that views we suggested that NGs are not self-organized or self-assembled through a diffusion–reaction mechanisms like Turing structures but rather "forced aligned" by the light pattern itself.

Circling back to the seeding process, in Ref. [91] the presence of nanovoids, being 0.6 nm on average diameter, are used to initiate / trigger the process. However, the nature of the seeding process is not yet fully elucidated. It could be i) point defects (e.g., self-trapped excitons, STE, or self-trapped holes, STH) which can facilitate electron excitation, ii) voids / bubbles / cavities generated by the first pulse(s) or iii) some glass free volume that is already "available" in the pristine glass. Indeed, glasses, and more specifically silica and silicates, exhibit short range order, with some n-membered rings creating well-known porosity at the sub-nm scale [104]. Such seeding should be facilitated in porous materials, which has been observed in nanoporous sol–gel silica for which a smaller number of pulses is needed to imprint NGs compared to dense silica [64]. From publications, short (typ. < 50 nm) but always oblate nanopores with a thickness much smaller than 5 nm appear dispersedly distributed, but sometimes starting to align along each other [98].

When increasing the number of pulses, a higher number of seeds is expected (e.g., some first nanopores or some STH). This in turn leads to additional scattering centers resulting in a smaller periodicity based on the scattered waves interference model suggested by Rudenko et al. [103] and in agreement with Zimmermann et al. [90] who reported a decrease of NGs period as highlight later in Fig. 7. According to the suggested "memory effect" involved in the mechanism of nonlinear ionization, new inhomogeneities are generated from pulse to pulse resulting in additional multiple scattering thus organizing the plasma distribution. As the pulse density increases, new plasma nanoplanes are generated "here and there" between the pre-existing ones following the light pattern. In this process it is worth mentioning that there are many "small size nanopores" between the long and well-arranged ones (see Fig. 5d) revealing the emergence, and growth, of new nanolayers like in Ref. [31]. The imprinted nanolayers are initially made of elongated nanopores that grow from pulse-to-pulse and merge resulting in new nanolayers. Finally, from pulse to pulse, this will lead to a reduction of the average spacing $\overline{\Lambda}$ of the nanogratings.

3.3. Energy transfer to the glass matrix and nanocavitation

The modification of transparent glasses with wide bandgap is rapidly induced within few fs through nonlinear effects including multiphoton, avalanche, or tunnelling electron ionization. The excited electrons composing the plasma will thus transfer their energy to the glass matrix through electron–phonon coupling and resulting in localized temperature hotspots and heterogeneities at the nanoscale. The low heat capacity of electrons allows them to be easily heated to extremely high temperatures, but the glass matrix (the lattice) initially remains "cold" due to the relatively long electron–phonon relaxation time (typically 10 ps in SiO_2). After this time, the lattice will finally heat up, by few 1000s of °C but this is a local effect. Indeed, after the free electron plasma energy is being transferred to the lattice, the spatial distribution of the temperature is quite like the plasma distribution itself because the timescale (< 1 ns) is too short to have some significant heat diffusion (on the order of the μs). In that sense this is a plasma-mediated process, and the temperature distribution is the image of plasma 3D nanostructuration [24].

A temperature difference, either established locally (nanoscale, between the nanoplasma hotspots and the background) or globally (at the focal volume level) would yield to a stress field, resulting in a local thermal expansion. During the time necessary for the heat to diffuse away, the silicon-oxygen bonds would elongate and the glass specific volume would expand within a time scale shorter than the characteristic acoustic relaxation time (typ. 500 ps in silica glass) [36] thus creating a moderate shock wave [105]. So at short time scale, there exist likely a localized nanostrain, which distributes ellipsoidally as a mirror image of the temperature map. This in turn will initiate the nanocavitation process at these specific locations. Indeed, a decrease of the local pressure would arise from the formation of a rarefaction zone behind the "shock wave" [106]. Once this tensile pressure develops between the "pore nuclei" and surrounding materials [24,107], nanopores will be imprinted at the image of the plasma ellipsoidal nanostructurating where start nanocavitation process.

Note that the resulting temperature increase inside the focal volume is a function of laser parameters, but typically is on the order of few 1000 °C [108,109]. If both thermal and stress confinement conditions are satisfied, which is the case for fs laser pulses deposited inside glass under most irradiation conditions, a tensile stress in the range of 100 MPa or more can yield to nanocavitation [36,37,109]. However, the imprinting of nanopores, hence nanogratings, is not only dependent on their appearance inside the glass under adequate experimental conditions, but also, they must withstand the thermal process induced by laser writing. This sets an upper temperature

limit beyond which the nanogratings would collapse / erase [110], precluding the imprinting of NGs, which can be modeled using for instance the Rayleigh-Plesset equation.

The main steps of the overall process are summarized in Fig. 6. It appears that the nanopores may not have the chance to grow from a spherical shape but rather an ellipsoid one, like the nanoplasma distribution itself for a linear polarization whereas a circular polarization would induce substantially spherical nanopores and thus no / low birefringence [111]. Following this view, the so-called Type X regime might be seen as the early birth of NGs formation mostly observed for a low number of pulses and low energy. These Type X modifications refer to oblate (for linear or elliptical polarization) nanopores with low birefringence and ultralow optical losses [16].

3.4. Beyond silica – porous NGs and partially crystallized NGs

Finally, the oxide glass decomposition and related formation of nanopores was observed in a wide range of oxide glasses [36,37,48,55,67,68,89], as mentioned in section 2, thus revealing that the formation of volume NGs is a general mechanism. In fact, while seeding may be of various kinds and proportion as a function of glass compositions, there will still be some seeds to trigger the process. Likewise, the nanocavitation process is in principle a global approach since all the glass compositions would experience a stress field upon heat deposition inside the focal volume and at the hotspot nanoscale. However, the existence of large electric field produced by mobility difference of oppositely charged carriers by light excitation open to consider that other effects may be at play such as electrostriction or inverse piezoelectricity [112]. This may also trigger strain fields and thus contribute to the nanocavitation process.

In the above mechanisms, NGs in silica and most oxide glasses are made of nanopores arranged in quite periodic nanolayers based on a nanocavitation process. This mechanism is coupled to electromagnetic waves through temperature modulations induced by electron plasma energy transfer to the lattice. There is a destabilization of the glass oxide (e.g. SiO_2) at the high electron density location where the light intensity is the largest but there is no chemical migration. In partly crystallized NGs, we suggest an alternative scenario to interpret the nanoscale chemical separation that is initiated before the crystallization. Indeed we suggest that the light "forced-organized" plasma imprints its spatial distribution on the chemical separation [113] that is driven by electrochemical potential gradient related to the various glass constituents [112]. At a short time scale, the excited electron density modulated in space (under light influence) is partly trapped into the glass network (e.g. in the form of STE, STH) and then further excited by the next pulse. NG structure is thus reinforced from pulse to pulse in agreement with the literature [102]. This plays a kind of memory effect in the plasma spatial distribution, which my imprint transformations on a time scale longer than the light pulse itself. However, while the initial excitation profile follows the light intensity pattern (e.g., induced by the above-mentioned scattered waves interference), this is no longer the case after several laser pulses. This implies that positive ions produced initially, and negative charges created though electron trapping do not own the same distribution, resulting in an electric field modulation along the direction of light polarization. Considering an excited electron density of 10^{19} e/cm^3, a classical calculation allows estimating a quite large electric field that could reach several kV per μm [114–116]. There are two aspects here: i) the involvement of the electric field in the phase separation and ii) the migration of species in an electric field. Indeed, as phase separation is guided by the gain in free energy and the partial relative permittivity of each species, the phase separation can be influenced by the electric field. Now considering the migration of non-ionic species such as SiO_2 "groups", one has to consider a complex forces introduced by the gradient of electrochemical potentials. Based on

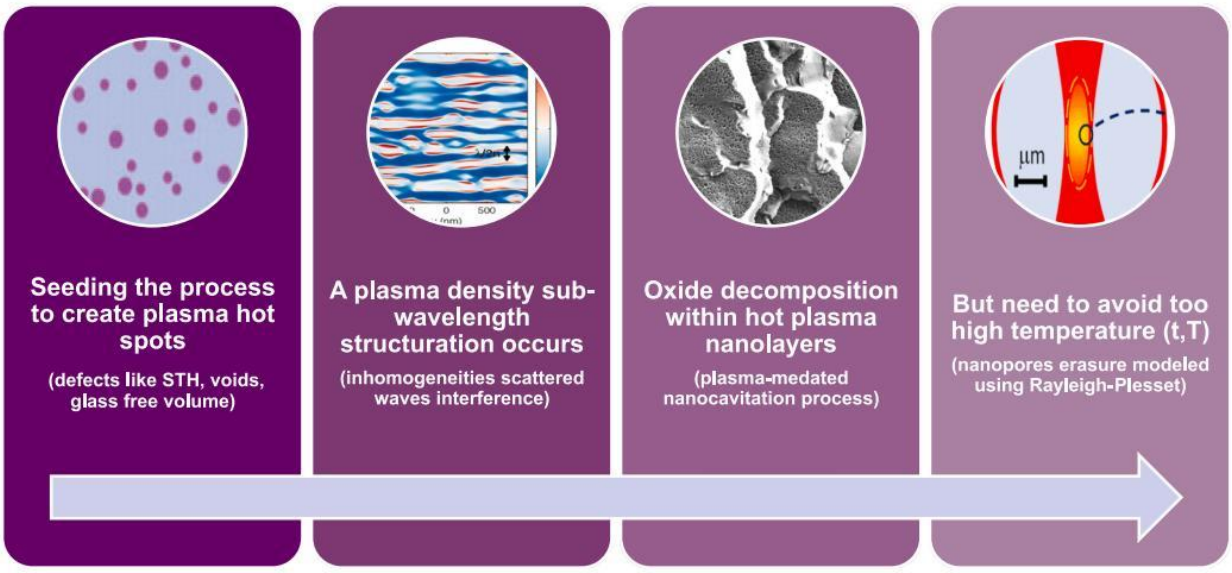

Fig. 6. Schematic overview of porous nanogratings formation mechanism in oxide glasses.

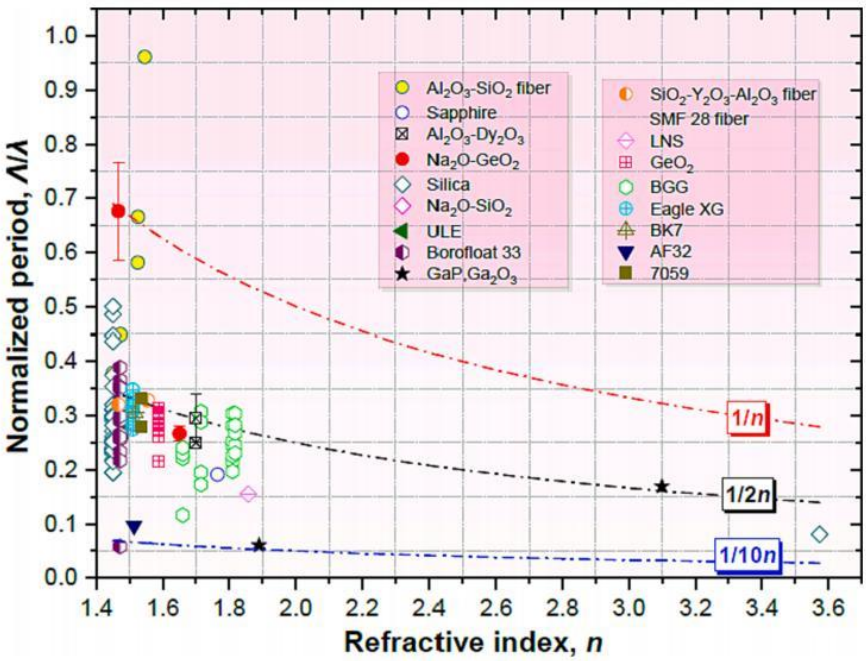

Fig. 7. Normalized period Λ/λ for sets of glasses including commercial glasses vs. refractive index, n, measured at 550 nm. The laser wavelength λ utilised in the various experiments was usually between 515 and 1030 nm.

theoretical calculations [112], this process can drive the nanoscale migration of silica that cumulates at the location of high electron density, i.e., where the electric field and the electric potential (in absolute value) are maximum. As a result, pure silica layers will develop as observed in LNS or LNSB glasses [54,79]. The "remaining glass is therefore poorer in silica, and ready for crystallization after enough time. Finally, the nanocrystallization is induced by the peripheral solid–solid crystallization. Following this view, there is an additional electrochemical force super-imposed to the thermal one (thermodynamical phase separation), leading to the formation of these partly crystallized NGs.

4. Influence of chemical composition on nanogratings properties and performances

From section 3, the formation of NGs is thought as a general mechanism that can operate in glass, although it is expected to take various forms and be a function of glass properties, essentially defined through its composition. Consequently, summarizing an understanding the effect of glass composition on the NGs, which is the motivation of this section, is of prime importance to encourage future development of glasses specifically designed for NGs imprinting.

4.1. Impact on nanogratings periodicity

In the literature, few publications have focused on NG periodicity, Λ. In accordance with the form birefringence model [117], a higher linear birefringence was demonstrated when the period is narrower (the maximum being predicted when Λ is equal to twice the nanolayer thickness) but this also brings an interesting prospective to the NGs formation mechanism itself. Indeed, in the model developed by Bhardwaj et al. [57], NGs periodicity is set between λ/n and $\lambda/2n$ where n was the refractive index of glass and λ was laser pump wavelength and a period initially independent of pulse energy. However, periodicity was shown to decrease continuously with the number of applied laser pulses [101,102]. Of Particular note, Rudenko et al. [103] conducted systematic modelling for the formation of NGs on the basis of inhomogeneity concentration, C_i, where $C_i = N/S$, N was the number of inhomogeneities in the laser-induced section, S. In this model, it was suggested that nanometer-sized inhomogeneities played an important role in the volume NG formation process and they were considered as seeds triggering the process. They also enhanced and improved the nanoplasma incubation process. Following the same concept due to the effect of local field enhancement suggested initially by Bhardwaj et al. [57], the free electrons excited by strong nonlinear photo-ionisation were easily generated near the equators of the inhomogeneities and then progressively grew into nanoplanes "self-organised" by scattered waves interference [91,103]. Here in Fig. 7, we present the results of normalized period vs. refractive index in a series of glasses including typical commercial glasses.

It can clearly be shown that in these glasses the period mostly falls below $\lambda/2n$ or more accurately in the $\lambda/10n < \Lambda < \lambda/2n$ range. The normalized period increases with the pulse energy in the BGG family, Borofloat 33, silica, and GeO_2 glasses. According to Ref. [103], the interference between multiple scattered waves from randomly distributed inhomogeneities strongly depends on inhomogeneity concentration, C_i. In the cited work, the authors defined the average distance between two initial inhomogeneities as $d =$

$1/\sqrt{C_i}$. For higher concentrations and if $\lambda/2n < d < \lambda/n$ ($0.05\% < C_i < 0.5\%$), the dominant period was close to λ/n due to the interference mechanism. However, for greater concentrations of inhomogeneities, the dominant period is close to $\lambda/2n$ and $\lambda/10n$ for even higher ones. Indeed, the authors deduced that the physical origin of subwavelength self-organised structures was related to the stationary wave photo-induced either by the interference of inhomogeneity-scattered waves and incident one for low-frequency nanogratings or by an interference of several scattered waves (from multiple inhomogeneities) for high-frequency nanogratings that own a 2x smaller periodicity. Consequently, distinct periodicity was obtained depending on the local inhomogeneity concentration due to the scattering behaviour. Moreover, multicomponent glasses such as BGG glasses, Eagle XG, 7059, Borofloat 33 glasses, etc., mostly showed a significant reduction in NGs periodicity, often breaking the limit of $\lambda/2n$. This was attributed to an increase of inhomogeneity concentration suggesting that some kinds of fluctuation in chemical composition at the nanoscale level are seeding the process. This theory needs further studies to be clarified. Overall, our results for NG periodicity tallied with [103] and [57]. In addition, Al_2O_3-SiO_2 fiber presented a wide range of normalized NGs periodicity, Λ/λ, from 0.375 to 0.961 (i.e., periods varying from 386 nm to 990 nm where the wavelength λ is 1030 nm). Many parameters can impact periodicity as mentioned above. The larger period, associated with higher Al_2O_3 content was attributed to both the larger refractive index but also to higher Type II threshold [67].

4.2. Impact on the oxide decomposition and observed nanoporosity

Continuing our investigation into NGs morphology, their principal features / characteristics, namely nanopore size and porosity FF, were both found to be key aspects of NGs in multicomponent glasses. In fact, nanopore shape is not limited to spheres but can be ellipsoidal or take the form of more complex shapes [16,58]. To compute optical retardance or birefringence from NGs, the refractive index inside and outside the nanoplanes must be known (respectively n_{pl} and n_G from Fig. 1 (b)). To estimate an effective refractive index for the porous nanoplane (n_{pl}), which is a pivotal term in the birefringent response of the NGs, one can use the Maxwell-Garnet equation [118]:

$$n_{pl} = \sqrt{n_G^2 \frac{n_G^2 + \frac{(1+2FF)}{3}(n_{\text{pore}}^2 - n_G^2)}{n_G^2 + \frac{(1-FF)}{3}(n_{\text{pore}}^2 - n_G^2)}} \quad (1)$$

Here, n_G is the refractive index from fused silica equal to 1.46 at 551 nm, and varies only little with respect to temperature (thermo-optic coefficient is $\sim 10^{-6}$ K^{-1} [119]). In this situation, n_G is kept constant both inside the porous nanoplanes (i.e., around the nanopores) and between the porous nanoplanes. As seen from Eq. (1), the refractive index of porous nanolayers is a function of the FF, itself being a function of the pore size and number (Fig. 8 (b)).

The evolution of nanopore diameter and FF inside various glasses is presented in Fig. 8 (a) and (b). Overall, the observed trend is related to the fact that a larger average nanopore size corresponds to a reduced nanopore density, i.e., the number of nanopores per unit of porous volume (excepted for the AF32 glass). Nanopore diameter in silica glass ranged from 26 nm to 39 nm as shown in Fig. 8 (a), and is a function of laser irradiation conditions. This diameter range is typically reduced compared to multicomponent glasses such as ULE glass (from 36 nm to 61 nm). Additionally, glasses with a higher SiO_2 content generally present a smaller nanopore diameter while nanopore diameter rises with an increasing amount of Al_2O_3, like in binary Al_2O_3-SiO_2 glass optical fiber cores [22] as emphasised in Fig. 8 (a). Furthermore, silica glass (such as Suprasil or Infrasil) presented higher FF than other glasses except for AF32. From these porosity measurements and NGs geometric parameters, one can evaluate form birefringence. In fact, this quantity was

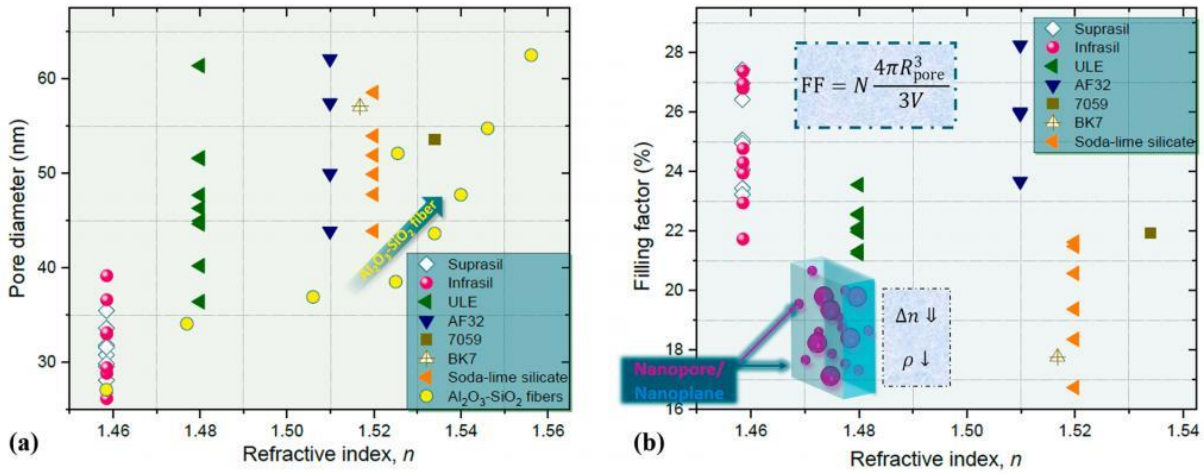

Fig. 8. (a) Average nanopore diameters for glasses, including Suprasil, Infrasil, ULE, AF32, 7059, BK7, soda-lime silicate and Al_2O_3-SiO_2 as a function of refractive index, n (measured at 550 nm). (b) Filling factor of these glasses as a function of refractive index, n (measured at 550 nm). FF is the filling factor, N is the number of nanopores (with an average nanopore radius R_{pore}) per unit volume V of the porous nanolayer. The inset is an exemple of a nanolayer with nanopores. Δn and ρ are refractive index variation and density, respectively.

correlated with refractive indices as well as nanolayer thickness t_1 and its periodicity Λ according to the following expression:

$$B = n_e - n_o = \sqrt{\frac{n_{pl}^2 n_G^2}{f_f n_G^2 + (1-f_f) n_{pl}^2}} - \sqrt{f_f n_{pl}^2 + (1-f_f) n_G^2} \quad (2)$$

where B is the form birefringence, n_e and n_o are respectively refractive indices of NGs along extraordinary and ordinary axes and f_f is equal to $t_1 / (t_1 + t_2)$ or t_1/Λ.

4.3. Impact on laser parameters processing window

Chemical composition can directly impact the formation of NGs [12,39,40], as denoted before. Here, we specifically show the effect of glass modifiers, in the form of alkali or alkaline earth elements, on the formation of NGs. This aspect is quantified by investigating the NGs window, as described from the recent work [37,55], and illustrated in Fig. 9. The NGs window is defined by keeping the all parameters constant, excepted pulse energy which is being varied while and monitoring the existence of NGs.

It is evident, from the above figure, that the width of the NGs windows are intrinsically linked with the amount of (alkali + alkaline earth). Note that the onset energy of NGs remained nearly constant (from 0.125 to 0.3 μJ) for all the glasses, while the closing energy is strongly decreased with a corresponding increase of alkali and / or alkaline earth elements. Firstly, Borofloat 33 presented the widest NGs window, i.e., from 0.175 to 2 μJ, which can be attributed to its highest absolute SiO_2 content (81 mol.% of SiO_2). It is worth pointing out that either ratio of (alkali + alkaline earth)/SiO_2 or (alkali + alkaline earth)/Al_2O_3 indicated a similar trend in the NGs window evolution, where Si, Al are generally the network formers. The addition of alkali and alkaline earth elements inside glasses can lead to strong structural changes due to the characteristics of network modifiers, such as bond breaking and even forming some "channels" as reported in Na_2O-containing glasses [120]. From Ref. [55], we depicted that alkali and alkaline earth atoms generally play the role of depolymerizing cations, i.e., breaking T-O-T linkages (T = Si or Al) and forming non-bridging ≡Si-O- bonds [121], further lowering the polymerization degree of the fundamental structural groups and hence impacting glass viscosity, which is a key factor to be considered during the NGs formation/erasure processing [36]. Moreover, Liu et al. [122] suggested the flow can correspond to the relative motion of larger molecular units, such as chains or sheets, due to the depolymerized network. Therefore, the network structure inside the glass will be more rigid and connected with decreasing the alkali and alkaline earth content, which probably improved the NGs formation [36]. Fernandez et al. [123] also indicated that the ratio of (alkali + alkaline earth)/Al_2O_3 mostly affected the viscosity of the glass, and that the maximum value was reached as the ratio of (alkali + alkaline earth)/Al_2O_3 was equal to 1, which can be explained by a Al playing the role of a charge compensator. This was the case of SAN 75–12-12 glass which possessed the widest NGs window in the alumino-borosilicate family glasses, as in Fig. 9 (b).

Interestingly, we note that there exists two irradiated glasses with significantly different NGs windows while presenting the same ratio of (alkali + alkaline earth)/Al_2O_3 (equal to 2), i.e., SAN 75–6-12 and SAC 50–12-25, as shown in Fig. 9 (b). Na-doped alumino-borosilicate glass, namely SAN 75–6-12, showed a nearly 2 times broader NGs window than the Ca-doped one, namely SAC 50–12-25. This apparent contradictory observation is attributed to the higher silica content in SAN 75–6-12 relative to SAC 50–12-25 (75 mol.% versus 50 mol.%).

From previous works, the existence domain of nanopores, hence NGs, could be anticipated from an approach based on viscosity-based arguments [36,94]. To further highlight this aspect and provide an example, the viscosity profiles versus temperature is first presented in Fig. 10 (a). The data were obtained from the SciGlass software and they were subsequently fitted using the Vogel-Fulcher-

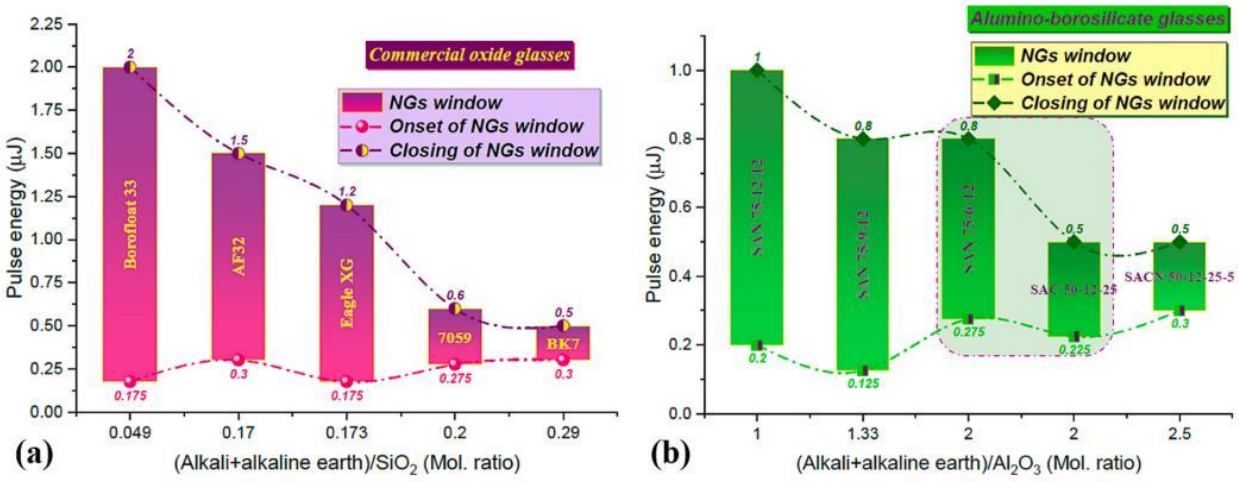

Fig. 9. Type II processing window in a series of glass samples, taking the pulse energy as the varying parameter, and as a function of, (a) (alkali + alkaline earth)/SiO_2 ratio at RR = 50 kHz and (b) (alkali + alkaline earth)/Al_2O_3 ratio at RR = 100 kHz, from Ref. [37] and Ref. [55], respectively. The ratios are calculated from the molar glass composition. Experimental parameters are: 1030 nm, NA = 0.6, 800 fs.

Tammann (VFT) equation [124].

The domain of NGs existence was predicted by taking into account two boundaries [36] in terms of viscosity, which can then be translated into two limiting temperatures. The lower limit corresponds to the temperature, T_{min} for which the viscosity value (η) is situated at nearly ~$10^{6.6}$ Pa·s. This corresponds to T_{soft}, i.e., glass softening temperature, at which nanocavitation in the glass can occur thus forming nanopores that compose the NGs. Meanwhile, the upper temperature limit, $T_{max} = T_{working}$, namely, working temperature (η~10^{3} Pa·s.), corresponds to either the unstable hydrodynamic growth or the collapse of the nanopores, resulting in the erasure of the nanopores, hence the NGs nanostructuring. Note that this upper limit is a time dependent problem, and it depends on the considered time. For example when considering a characteristic time ~ 30 ns corresponding to the case of a laser heating–cooling profile, hence the viscosity "limit" is log(η, Pa·s) ~ -0.75 as discussed in Ref. [110]. The presented upper and lower temperature limits are presented in Fig. 10 (a). In addition, it is worth mentioning that the viscosity value of $10^{12.0}$ Pa·s, as in Fig. 10 (a), corresponds to the annealing temperature of glass and is given for the completeness. Then, the temperature interval, ΔT, of each glass was obtained according to the approach mentioned above and was reported on the x-axis of Fig. 10 (b). The normalized Type II energy window of the glasses, including alumino-borosilicate family glasses (from SAN 75–0-12 to SACN 50–12-25–5) and commercial oxide glasses (from Suprasil CG to Soda-lime silicate), were reported in y-axis of Fig. 10 (b). Here, the Type II energy window of each glass was normalized to SiO_2 (i.e., Suprasil CG, set equal to 1). The latter window is be defined as: $(E_{max(glass)} - E_{min(glass)})/(E_{max} - E_{min})$ where $E_{max(glass)}$ and $E_{min(glass)}$ respectively represent the maximum and minimum energy for which NG is detected (using polarized optical microscopy) in a given glass sample. The E_{max} and E_{min} are similarly defined, but specific to the SiO_2 glass (as per the normalization). This energy window is clearly correlated with the previously defined ΔT and scales with it. The window gradually increases in the following order: SAN 75–12-12 > SAN 75–6-12 > SAC 50–25-25 > SAC 50–12-25 > SAN 75–0-12 ≈ SAN 75–3-12 > SACN 50–12-25–5. Overall, this trend is valid for a wide range of glass compositions, and the monotonous increase of the windows with respect to exhibit a slope of 0.0015 °C^{-1}, excepted for SiO_2, Suprasil CG, which indicated the widest NGs window and slightly depart from this trend. The temperature dependence of the glass viscosity is therefore of prime importance in the formation of NGs. Moreover, from a general view and as depicted above, glasses containing a relatively high alkali and alkaline earth content relative to Si favor a low network connectivity, hence a large amount of non-bridging oxygens [114,123]. They tend to lower the glass viscosity, like in the case of SAN 75–12-12 and SAC 50–12-25. More specifically, this is likely related to the viscosity of these glasses that strongly varies with respect to temperature (so called "short glasses").

From above, the dependency of NGs existence window on the chemical composition was reviewed and rationalized through a viscosity approach. A direct consequence of this review section is to demonstrate that NGs can be achieved in most, if not any, glasses. However, the processing windows can be drastically different, and a systematic analysis must be undertaken to find the adequate conditions for which NGs can survive the laser-irradiation process. For example, recently sub-surface formation of nanopores was revealed to be possible under specific conditions in telluride or chalcogenide glasses [75,125], a great progress towards nanogratings writing in any kind of optical materials.

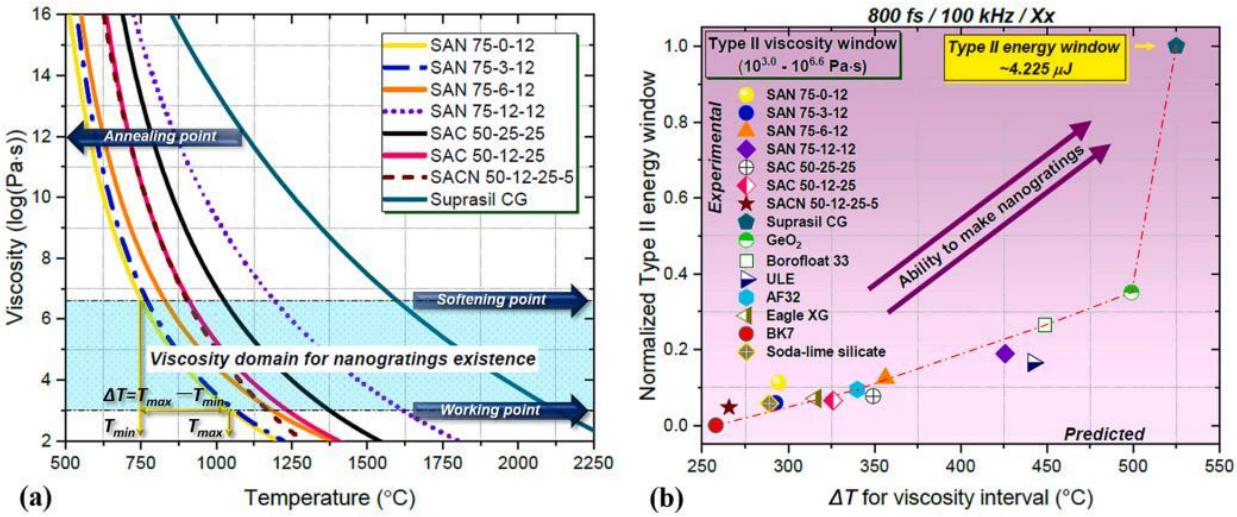

Fig. 10. (a) Viscosity versus temperature for various alumino-borosilicates and SiO_2 (Suprasil CG, taken as a reference) glasses, along with an estimated temperature domain of NGs existence from T_{min} ($\eta = 10^{6.6}$ Pa·s, namely, softening temperature) to T_{max} ($\eta = 10^{3.0}$ Pa·s, working temperature). (b) Normalized Type II energy window as a function of the temperature interval (i.e., $\Delta T = T_{max} - T_{min}$) for various alumino-borosilicate and commercial glasses. The x axis involves the predicted results of temperature interval extracted from (a), while the y axis are the experimental results, from Ref. [55].

4.4. Impact on maximum NGs retardance and underlying birefringence

As previously introduced, the prominent characteristic of NGs lies in its anisotropic optical property corresponding to linear birefringence. The photonic components studied in this field are directly or indirectly related to birefringence, hence retardance ($B \times L$) which originates from the variation in phase when light passes the birefringent transparent imprinted transformations with the thickness, L.

In the following section, we will compare the typical retardance and the corresponding birefringence for standard and comparable writing conditions (1030 nm, 200–300 fs, 100 kHz, 0.1 mm/s, NA = 0.6). According to the literature [37], maximum measured retardance arising from NGs induced in SiO_2 (252 nm) and GeO_2 (292 nm) glasses generally present higher values compared to other glasses, including commercial multicomponent glasses as illustrated in Fig. 11 (a). By comparing these commercial glasses, we show that glasses doped with alkali (K or Na) or alkaline earth (Ca or Mg) exhibited lower retardance values: Borofloat 33 (190 nm), Eagle XG (135 nm), soda-lime silicate (119 nm), AF32 (99 nm), 7059 (94 nm). The higher the alkali or alkaline earth content, the lower the retardance as found in [38]. Moreover, ULE glass exhibits higher retardance (232 nm) than other commercial glasses which can be explained by the absence of alkali or alkaline earths and higher SiO_2 concentration.

As for aluminosilicate glasses (such as $42Al_2O_3$-$58SiO_2$ (mol.%)) employed as a core material in optical fibers, they interestingly exhibit lower retardance values (63 nm) relative to silica-rich glass, e.g. SMF 28 fiber (122 nm). However, this value employed in optical fibers is sufficient for most of the targeted applications such as fiber Bragg grating sensors or optical devices based on Rayleigh backscattering [22].

Furthermore, IR-dedicated glasses including the BGG family, demonstrate high retardance compared to most other oxide glasses and can be applied in a wider range of optical applications due to a characterised transparency window up to 6 μm [36,126]. The maximum retardance of 192 nm can be found in 8% Ta_2O_5-BGG which was comparable with the "model glass" SiO_2 or GeO_2. Ref-BGG glass was also investigated for comparative purpose and presented the maximum retardance of 114 nm although this was lower than other doped BGG glasses. We sketched the principle ofo optical retardance in the inset of Fig. 11 (a).

Following the equation of optical retardance, birefringence values for these glasses can be calculated and the results are displayed in Fig. 11 (b). As an illustration of the periodic nanostructure observed in NGs using SEM imaging, a cleaved sample cross-section of the fs laser-modified region is shown in Fig. 11 (b). It corresponds to an 8% ZnO-BGG bulk glass with a birefringence value of 1.11×10^{-2} at a laser energy of 1.2 μJ. Firstly, 8% ZnO-BGG [69] presented the highest birefringence (2.88×10^{-2}) and broadest birefringence window (from 5.20×10^{-3} up to 2.88×10^{-2}) relative to the other glasses. The sample labelled Ref-BGG in Fig. 11 (b) possessed slightly higher birefringence than SiO_2 and GeO_2 and 8% Ta_2O_5-BGG exhibited comparative birefringence, again with respect to SiO_2 and GeO_2. Similarly, the BGG glasses all presented very high refractive indices relative to conventional glasses (SiO_2, GeO_2, or Corning 9754). Importantly, transparent dielectrics with high refractive indices generally possesse a prominent value in optical application (e.g., dispersion coefficient, Abbe number) which are intimately correlated to index and constitute a key parameter for evaluating the choices of optical glasses. Our results demonstrated the potential of these glasses for index-contrast devices such as Fresnel zone plates or polarisation gratings in near-/mid-IR range. Indeed, soda-lime silicates also exhibit superior birefringence values and birefringence window (from 6.14×10^{-3} up to 1.85×10^{-2}) as presented in Fig. 11 (b). A strong dependency between retardance / birefringence and chemical composition was observed.

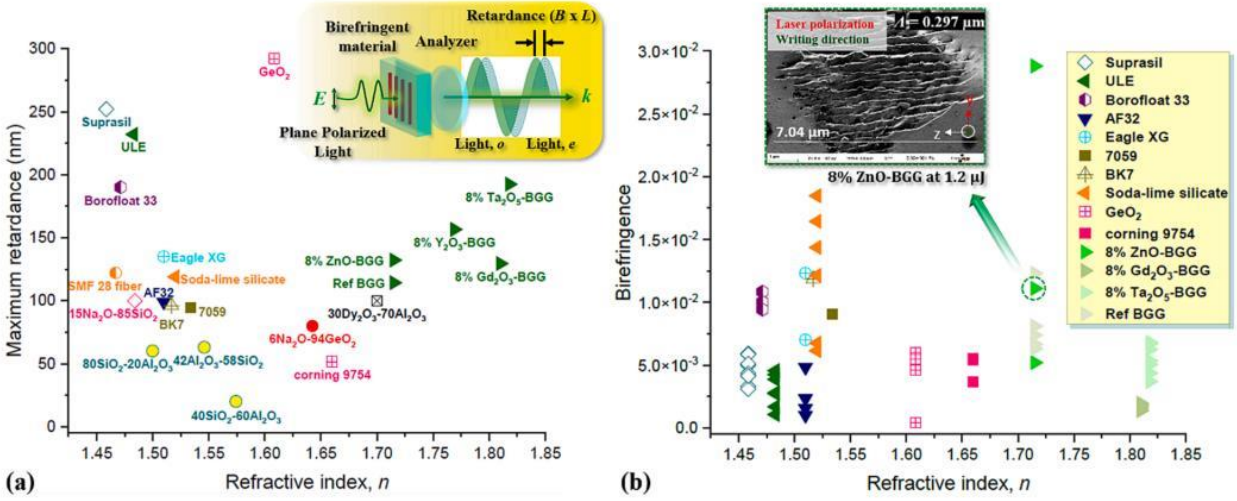

Fig. 11. (a) Typical retardance as a function of refractive index, n (measured at 550 nm) for these studied glasses and with commercial glasses. The inset of (a) is the sketch of principle to the optical retardance. E and k are respectively electric field and wave vector. (b) Birefringence as a function of refractive index, n in the studied glasses including commercial glasses. Inset of (b) FEG-SEM micrographs of the cleaved laser track cross section for a 8% ZnO-BGG glass. Laser polarisation orientation is along y, and laser scanning direction along x. (For interpretation of the references to color in this figure legend, the reader is referred to the web version of this article.)

4.5. Impact on NGs related optical performances

The presence of alkali and alkaline earth cations can affect NGs formation in glass [114,123]. In order to tentatively summarize the relative "performances" of all investigated glasses influenced by chemical composition and identify "best performers" with respect to NGs making, three parameters as a function of the refractive index were employed: 1) the writing speed, which represented the potential for writing a high quantity optical components thus unlocking industrial potential, 2) the maximum retardance which was a key parameter for birefringent applications, and 3) the energy consumption in μJ/nm (laser energy in μJ used to write one unit of retardance expressed in nm). The results are summarised in Fig. 12.

From this graph, it can be clearly seen that Suprasil (i.e. SiO_2) was found to reach the greatest retardance value (252 nm) with the highest writing speed (1 mm/s) and the lowest energy consumption (0.6 μJ/nm). For Suprasil, ULE and GeO_2 glasses, NGs could be induced with higher retardance values and writing speeds (ULE: 232 nm and 0.1 mm/s; GeO_2: 292 nm and 0.05 mm/s) as well as lower energy consumption (ULE: 6.9 μJ/nm; GeO_2: 1.79 μJ/nm). Borofloat33 and 8%Ta_2O_5 - BGG glass both exhibited relatively good performance, i.e. high retardance values (Borofloat33: 190 nm; 8%Ta_2O_5 - BGG: 193 nm), moderate speeds (Borofloat 33: 0.05 mm/s; 8% Ta_2O_5-BGG: 0.01 mm/s) and energy consumption (Borofloat 33: 8.4 μJ/nm; 8% Ta_2O_5-BGG: 36.4 μJ/nm). Moreover, SACN 50–6-25–5 glass demonstrated very low retardance (55 nm) and required low speed (0.01 mm/s) due to high alkali and alkaline earth concentration (25%CaO + 5%Na_2O in mol.%) as well as moderately high B_2O_3 content (14 mol.%) which is detrimental to NGs formation. Indeed, maximum retardance consistently decreased as Al_2O_3 content progressively reduced within alumino-borosilicate, as observed in the SAC glass family (SAC 50–25-25, SAC 50–18-25 and SAC 50–12-25, SACN 50–6-25–5). Moreover, BK7 and 7059 glasses possessed relatively low retardances values (BK7: 96 nm; 7059: 94 nm) and low writing speed (0.001 mm/s), this with high energy consumption (BK7: 286.0 μJ/nm; 7059: 251.7 μJ/nm). As for Eagle XG, alumino-borosilicate family (including SAN 75–0-12, SAN 75–3-12, SAN 75–6-12, SAN 75–9-12, SAN 75–12-12, SAC 50–25-25, SAC 50–12-25, SAC 50–18-25) and BGG family (including 8%Y_2O_3 - BGG, 8%Gd_2O_3 - BGG, BGG, 8%ZnO - BGG) glasses, they exhibited relatively high optical retardance values (from 86 nm for SAN 75–6-12 to 165 nm for SAN 75–9-12) at moderate speeds and energy consumption (0.01 mm/s, energy consumption from 1.6 μJ/nm for 8%Y_2O_3 - BGG to 155 μJ/nm for 8%Gd_2O_3 - BGG). Moreover, other irradiated samples reported in the literature have been added in Fig. 12. The 15%Na_2O - 85%SiO_2, 30%Dy_2O_3 - 70%Al_2O_3 and 6%Na_2O - 94%GeO_2 samples exhibited a moderate retardance value (100 nm) but had very high energy consumption and low writing speeds, e.g., 15%Na_2O - 85%SiO_2: 10^4 μJ/nm and 0.02 μm/s. In addition, even if writing speed was quite high for 80%SiO_2 - 20%Al_2O_3 and 40%SiO_2 - 60%Al_2O_3, they exhibited low retardance with relatively high-energy consumption. Overall, we can globally deduce from these results that much more energy consumption was required for NGs formation by increasing the content of alkali and alkaline earth cations.

Furthermore, the glass refractive index, *n*, is a key application property. Here, LNS, BGG family (BaO-Ga_2O_3-GeO_2), 30%Dy_2O_3 - 70%Al_2O_3, 6%Na_2O - 94%GeO_2 and Corning 9754 glasses exhibited the highest refractive indices relative to other glasses which was

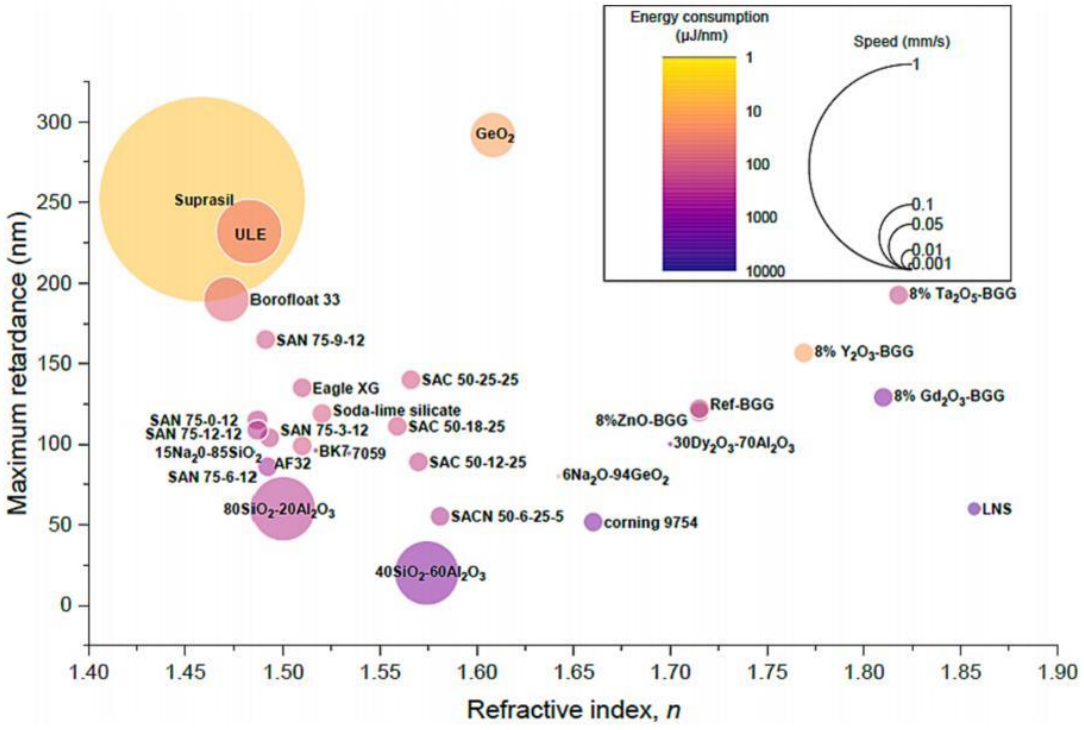

Fig. 12. Bubble plot of maximum retardance induced by fs-laser in glass as a function of refractive index, n (both measured at 550 nm) for the studied glasses. Na_2O-SiO_2 and Na_2O-GeO_2 samples were extracted from [66] and [40] respectively.

mostly attributed to their higher molecular mass. Moreover, the importance of the Na_2O-CaO-SiO_2 system is widely known and has been used extensively [124]. Alumino-borosilicate glasses doped with Na_2O and CaO, which could demonstrate similar universalism to Na_2O-CaO-SiO_2, presented moderately high optical retardance ranges and moderate writing speed, energy consumption and refractive index ranges (from 1.487 for SAN 75–0-12 and SAN 75–12-12 to 1.591 for SACN 50–6-25–5) compared to SiO_2, GeO_2 and other commercial glasses. This further confirmed the potential of alumino-borosilicate glasses when applied to the field of optics. Finally, SiO_2 and GeO_2, which are strong network formers and fourfold coordinated glasses, were always the best candidates to unlock industrial potential due to their excellent characteristics as deduced above.

4.6. Impact on nanogratings thermal stability

The thermal stability of NGs is a hot topic since many optical devices are exposed to moderate, or harsh environments especially under high temperature conditions such as temperature optical sensors. In order to appropriately evaluate the industrial potential of NGs induced by fs-laser inside transparent materials, we reviewed the temperature related to the full erasure of optical retardance (or refractive index changes for Type I modifications) as a function of glass annealing temperatures (°C) as shown in Fig. 13. The glass annealing temperature (i.e. the temperature at which the viscosity is log(η, Pa•s) = 12.0.) is correlated to the erasure of these nanostructured and related birefringence (proportional to the measured optical retardance). Generally, the higher the glass annealing temperature, the more stable are the imprinted optical properties. The full erasure of optical retardance is indeed a key aspect for evaluating the abilities of materials to withstand harsh environments (such as ultra-high temperature, eventually coupled to extreme radiation [127]) in industrial applications.

Overall, from Fig. 13 we can see that the temperature corresponding to the erasure of optical retardance increased linearly (as the short, dashed line in Fig. 13) with rising glass annealing temperature for most investigated glasses. They included silicate, germanate

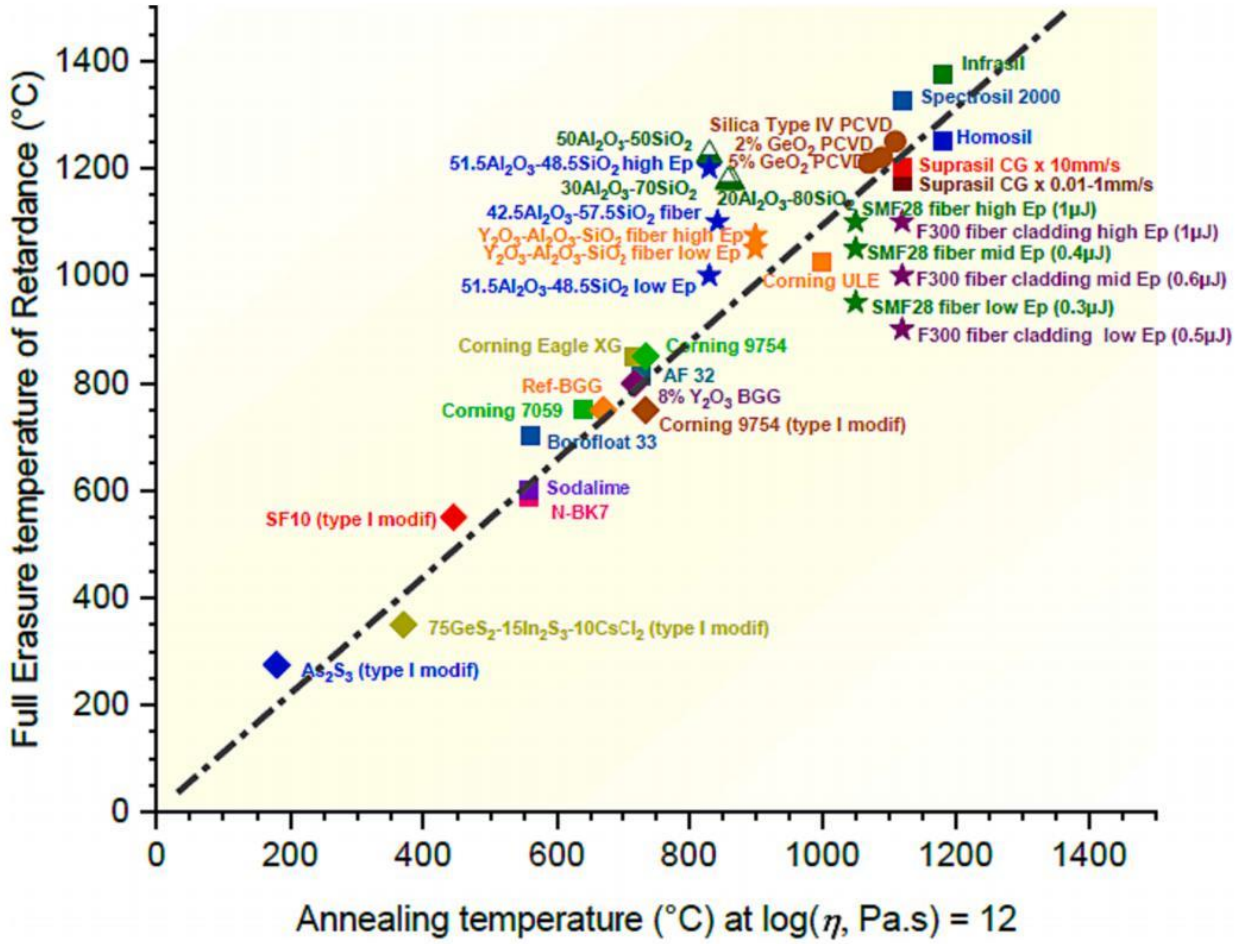

Fig. 13. Temperature relative to the full erasure of optical retardance as a function of glass annealing temperature (°C). The annealing temperature is correlated with viscosity at log(η, Pa • s) = 12.0. Values taken from Refs. [6,12,21,22,36,37,67,70,128,129]. Stars are for fiber materials wheras others symbols are for bulk glasses. All measurements were obtained based on 30 min step isochronal annealing and performed at room temperature.

or aluminate glasses such as Borofloat33, BGG, Corning 9754, 30%Al_2O_3 - 70%SiO_2, 51.5%Al_2O_3 - 48.5%SiO_2, Y_2O_3 - Al_2O_3 - SiO_2 fibers, ULE, SMF-28 fibers, GeO_2 - SiO_2 and SiO_2 (including Suprasil, Infrasil, Spectrosil, Homosil) glasses. Up to date Infrasil (SiO_2 containing low OH and Cl) and N-BK7 glasses demonstrated the best and the lowest thermal stabilities in the glasses studied (Type II) respectively. For sake of comparison, we added some mid-IR dedicated glasses such as heavy oxide (SF10) and chalcogenide glasses namely As_2S_3 and GeS_2, but they all correspond to Type I optical modifications.

Moreover, NGs induced by higher laser energies present higher thermal stability such as SMF-28 fibers core, SiO_2 fiber cladding or 51.5% Al_2O_3-48.5% SiO_2 in most glass compositions as highlighted in Fig. 13. In addition, NGs induced by a high writing speed (e.g. SuprasilCG at 10 mm/s compared to that at 0.01 – 1 mm/s) presented slightly higher thermal stability which can be attributed to a larger nanopore size [102].

Of particular interest are the results of the Al_2O_3 - SiO_2 glass family, where the experimental thermal stability of NGs deviated from the linear relationship between T_a and erasure. This could be related to the characteristics of Al_2O_3 (e.g. Al_2O_3 possess a higher melting point (2054 °C) than SiO_2 (1723 °C)) and the possibility to create nanoscale phase separation including Mullite nanocrystals [67]. Also, chemical composition may play an important role in terms of affecting the thermal stability of materials compared to other factors like laser parameters. We can see that the full erasure temperature of the photo-induced retardance increased from 1175 °C up to 1225 °C (increment of 4.3%) while Al_2O_3 content increased from 20% up to 50% in the Al_2O_3 - SiO_2 glass. In addition, other approaches based on the control of laser parameters can improve thermal stability. Typically, when increasing laser pulse energy, the erasure temperature was higher by 22% in F300 fiber cladding. Similar observations can be made when increasing the laser scanning speed while the increment remains quite limited to a few % in Suprasil CG glass. Therefore, chemical composition is the primary key factor to be considered from the results in Fig. 13 with regard to the thermal stability of NGs, which further validates their potential for industrial applications. The results provide useful information of optical component designers to select an adequate glass (and its viscosity profile) when considering high temperature operations, or simply thermal ageing considerations. However one must keep in mind that an "erasure temperature" relates to a kinetics problem (time–temperature couple) [129]. We can thus define different "high temperature limits" depending on the operating conditions: i) short times (minutes, seconds) in fire alarms and some kind of structural health monitoring, ii) long times (years' timescale) for sodium cooled nuclear reactors, metal recycling, airplanes or process monitoring, and iii) laser writing timescale in either repetitive or cumulative regimes, for which either average temperature and cooling profiles are dissimilar.

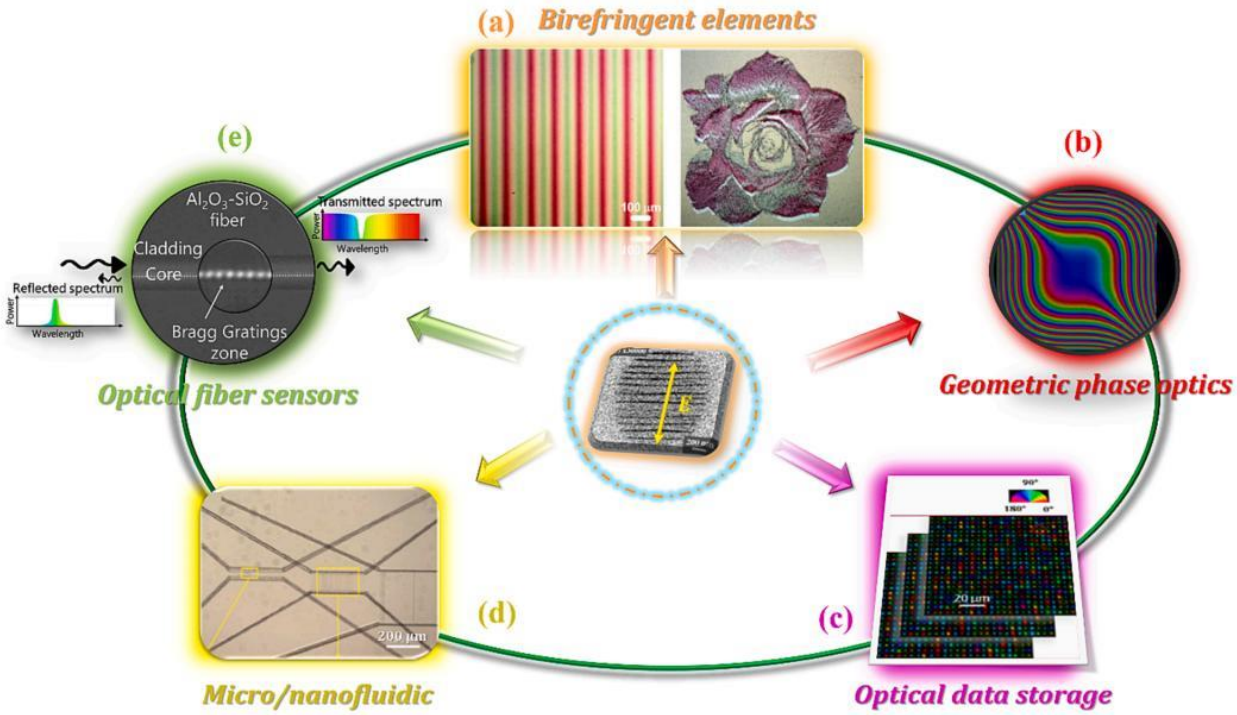

Fig. 14. The optical applications based on nanogratings. (a) Birefringent element: polarisation diffraction gratings from Ref. [9]. The left: colouration of birefringent structure under crossed polarizers with an optical retarder added. The right: birefringent rose printed in SiO_2 glass by ultrafast laser pulses. (b) Geometric phase optics: microscopy image of the 2D Airy beam converter in quantitative birefringence microscopy image from Ref. [13]. (c) Optical data storage: schematic diagram of 5D optical data storage using femtosecond laser writing from Ref. [18]. (d) Micro/nanofluidic: top-view optical micrograph of the fabricated 3D nanofluidic device for DNA analysis from Ref. [20]. (e) Fiber Bragg gratings inscribed in the molten core of Al_2O_3-SiO_2 fiber using a point-by-point technique from Ref. [22].

5. Applications of ultrafast laser-induced nanogratings

Up to now, NGs were revealed within a wide range of optical glasses, hinting at distinct potential applications due to the unique physical and chemical properties for each optical material. Indeed, one main purpose of the current investigations on NGs is to apply these sub-wavelength periodic nanostructures into optics or integrated micro-optics [86,130–132] with various functionalities by ultrafast laser. Over the two decades, various types of applications based on NGs including birefringent optical elements, 3D geometric phase optics, 5D optical data storage, highly selective etching or optical fibers based on sensors resistant to harsh environment were successively achieved in [9–22] as summarised in Fig. 14.

5.1. Birefringent optical elements

Several types of birefringent components employing self-organised NGs have been demonstrated, like a polarisation diffractive grating (PDG), waveplates, polarisation rotators. In 2010, Beresna et al. [9] first presented PDG based on self-organised nanostructures due to intriguing prospective functions, including azimuthal and radial polarisation converters [133], beam splitters [134,135] and rotated waveplates [136]. Indeed, the polarisation and phase of the incident light with fixed polarisation can be periodically modulated in space while this incident beam propagates through the PDG, which can be applied for security masking as shown in Fig. 14 (a). In 2011, they subsequently fabricated a spatially variant birefringent element based on NGs, called “S” waveplate. Here, “S” stands for “superstructured” and this can generally be explained as follows: an azimuthally or radially polarised vortex with its orbital angular momentum $l = 1$ or -1 can be divided into two configurations: one circularly polarised beam with orbital angular momentum $l = 2$ or -2; and the other with a plane front [10,137]. These integrated NG-based optical devices imprinted in transparent matters provide a new thread towards complex 3D space variant birefringent based devices and also integrated birefringent micro-optics in bulk glasses or fibers.

As a recent example, in 2023 Lu et al. [28–33] delivered a fundamentally novel idea to transfer the chirality of structured polarised chiral light beam to optical materials via fs laser direct writing. Experimentally, they combine a polarization distribution control of the fs laser beam by a 2D space variant birefringent waveplate and an axicon focusing technique to generate a 3D chiral Bessel beam with the linear polarization orientation rotating along the optical path in the Bessel core: an innovative 3D structured polarization [14]. This is a kind of “helical polarized” beam and can directly imprint “twisted nanograting” structures in oxide glasses. Such a twisted nanograting owns strong circular optical properties (optical rotation and circular dichroism) due to its inherent chiral distribution in 3D, which confirms the chirality transfer from light to matter.

5.2. 3D geometric phase optics

The recent advances in flat optics have challenged the limitations of conventional optics by implementing ultra-thin planar elements that instead of relying on optical path differences manipulate light waves via optical resonators with spatially varying phase response. In principle, the phase profiles of nearly any optical components including lenses, gratings, vortex phase plates, as well as elements capable of bending light in unusual ways could be designed based on gradient metasurfaces, referred to as geometric-phase (Pancharatnam-Berry phase) optical elements. Theoretically any phase pattern can be achieved by means of geometric-phase optics with high efficiencies and transparency. Following this view, the light phase tuned by geometric phase optics through anisotropic media is of great interest in to design functional devices that can be integrated into the systems such as high-power lasers, high-resolution microscopy, optical communication systems, polarization sensitive imaging, and consumer electronics. The ability of ultra-short laser pulses to imprint localized birefringent structures has thus been successfully exploited to demonstrate several optical elements operating on geometric phase effect with ultralow losses [16,138]. Indeed fs-laser induced NGs can be exploited as geometric phase regulators, due to their features of tunable birefrigence orientation and the related optical retardance. As far back as 2002, Bricchi et al. [11] demonstrated strongly birefringent Fresnel zone plates within silica glasses, which are attractive because of their unique focusing abilities and compactness. Recently, we also presented Fresnel zone plates based on NGs written in a mid-IR BGG glass [12]. Besides, in 2014, Gecevičius et al. [13] fabricated Airy beam [139] converters based on fs-laser-inscribed space variant birefringent structures, as in Fig. 14 (b). Moreover, a spontaneous "self-detachment" of a fiber-like structure was demonstrated in their study, by using this beam converter, enabling the fabrication of glass cantilevers in an alternative way. In 2017, vortex half-wave retarder generating optical vortex with a tunable orbital angular momentum and computer-generated holograms with a phase gradient close to π rad/μm, were fabricated [138].

5.3. Optical data storage

Nowadays, digital data storage is immensely on-demand due to the exponentially increasing amount of data in this era of information explosion. Magnetisation-based storages such as hard disk drivers and magnetic tapes have been developed but exhibit the drawbacks such as low energy efficiency and lifetime as well as longer access latency and degradation over time and/or temperature [140]. The durability of DNA-based data storage is restricted despite presenting a capacity of hundreds of terabytes per gram [141]. Now, 5D optical data storage (3 spatial coordinates with 2 degrees of freedom namely slow axis direction and optical retardance) reveals the potential for practical applications based on anisotropic nanostructures photo-induced by fs-laser pulses. The first demonstration of 5D optical image storage (e.g. a small world map) [15] associated to almost "unlimited" data-storage lifetime [59] with high recording speed and high capacity showcased the considerable feasibility and superiority of such optical data storage based

on femtosecond laser direct writing.

Recently, Sakakura et al. [16] reported an intermediate regime of NGs, called "Type X" modification which can be considered as randomly distributed anisotropic nanopores induced by ultrafast laser able to demonstrate ultralow scattering loss (99% transmission in visible light and higher than 90% transmission in UV light) compared to NGs (limited transmission when increasing the laser-induced layer). In this mechanism, the small nanopores diameters that are quite randomly arranged result in a decrease of the Rayleigh scattering, and thus low optical losses, offering exciting prospects for applications. For example, these Type X modifications were exploited for achieving a 5D optical storage with high data capacity and long lifetime in fused silica [18] or to imprint ultralow loss 3D geometric phase optics [16]. In parallel, Lei et al. [17] reported systematically research about the comparison of photosensitivity characteristics (birefringence) among these nanolamellae-like structures, both within Type X and NGs regimes. 5 GB digital data was inscribed in 120 mm × 2.4 mm across 50 layers from the bottom to top and the data writing speed was 225 kB/s at the imprinting rate 6×10^5 voxels/s with nearly 100% readout accuracy. More recently, Wang et al. [18] achieved 5D optical storage with high data capacity and long lifetime, based on Type X modification in fused silica as illustrated in Fig. 14 (c). They presented 5D optical data storage of "The Hitchhiker's Guide to the Galaxy" written in 100 layers in fused silica, which can represent transmission higher than 99% in the visible range. The readout accuracy can reach 100% for the 100th layer while removing the background using a dedicated algorithm.

5.4. Laser selective etching

The physico-chimical stability of fused silica could be modified by ultrafast laser due to the ultrahigh transient intensities (several TW/cm^2) resulting in the decomposition of the glass network structure (bound energy). This action will lead to laser selective etching, due to the unique characteristics of NGs (periodically alternative nanolayers containing nanopores and defects centers). That is to say, laser-induced structures can be easily removed by strong acidic or basic solution while leaving the pristine region much less affected with a etching ratio that can reach 10000. This technique is generally applied to bio-chemical reagents or lab-on-chip devices [142–144] due to itsresolution in micro scale. In 2006, Hnatovsky et al. [19] selectively etched NG-based micro-channels. Another example in 2013, Liao et al. [20] subsequently achieved fabrication of nanofluidic channels [27] (transverse width less than 50 nm) based on NGs under fs-laser irradiation. This technique could be used in DNA analysis as shown in Fig. 14 (d). Recently, a 3D model hand of fused silica (3 cm × 2.7 cm × 1.1 cm) was demonstrated [145] with the blood vessel system encapsulated inside the model hand. Although this demonstrator was not directly based on selective-etched NGs, it still opened a new era for applications of novel lab-on-chip and biochip devices, which can be used for in-depth understanding of human diseases.

5.5. Optical fibers-based sensors for harsh environment

With the development of the optical industry, optical fibers and laser imprinted optical waveguides with various characteristics are more and more developed [132,146–149]. Optical fibers can generally be classified according to the various doping of chemical elements, e.g. F-doped Fiber or Ge-doped Fiber that are the most usual ones. NGs are mostly applied in optical fiber based sensors due to their unique anisotropic optical characteristics and very high thermal stability [26,150]. Recently, Wei et al. [21] investigated the thermal stability of Type II modifications (NGs) of fiber Bragg gratings (FBGs) [34,127,151–155] under fs-laser irradiation, in various conventional glass systems, including different Cl-/OH-doped silica glasses, GeO_2-SiO_2 binary glass and Ti- and B-doped commercial glasses. Such FBGs (or their assembly into Fabry-Perot cavity) are very attractive and can be applied to pressure and temperature monitoring in airplane engines and in the next generation sodium cooled nuclear reactors. In some of these works, it is indicated that Ge-doped silica glass can exhibit higher optical retardance values and high thermal stability. Intriguingly, in 2021 Wang et al. [156] described in details the inscription of NGs in silica fiber cores to obtain sensors resistant to harsh environment. Low insertion loss (1 dB. m^{-1}) and high-temperature performance (tested at 1000 °C over 5 days) were demonstrated. Also, this type of optical sensor was exploited in radiation environments in the Massachusetts Institute of Technology Nuclear Research Reactor (MITR). This paper presented NGs-based fiber sensors, which were prime optical devices and applied to extreme environments. More recently, Wang et al. [22] studied the writing kinetics and thermal stability of laser-induced oriented nanostructures over a temperature range from 20 °C to 1200 °C inside the cores of sapphire (Al_2O_3) and YAG (yttrium aluminium garnet) derived silicate optical fibers, as in Fig. 14 (e). They suggested that optical sensors revealed high-temperature sensitivity and stability, e.g., those based on Rayleigh backscattering or fiber Bragg grating sensors, when imprinted in these nonconventional Al_2O_3 based fibers. They believed this technique to be a promising large-scale platform for the next generation of harsh environment sensing optical devices.

5.6. Third-order nonlinear optics control and supervision

Diffraction of ultrashort pulses such as fs pulses by Bragg Gratings can produce nonlinear optical effects. The first report on this aspect was that volume Bragg gratings led to a diffraction phenomenon, i.e., third harmonic generation through Cherenkov radiation (an interference of third-order nonlinear polarization between incident and diffracted lights) [157]. Siiman et al. elucidated complementarily three conditions for generating third harmonic via volume Bragg grating due to the different grating plane azimuths [158]. In parallel, and similarly to Bragg gratings, NGs revealed the generation of intense ultraviolet emission using infrared light, which was confirmed as third harmonic [159]. Then, a similar phenomenon was reported by Grigutis et al. [160], that is, conical third harmonic emission originating from filament-induced NGs. The authors indicated that conical third harmonic generation created during supercontinuum generation is a noncollinear phase-matched four-wave mixing process involving the reciprocal lattice vector.

Recently, the same group further confirmed the previously mentioned point of view (i.e., phase-matching scenario) by using various near-IR driving wavelengths [161]. In fact, third harmonic generation is the most generic third-order nonlinear effect due to the very high fluence of light filament and can be utilized for *in situ* imaging of laser-affected zones inside glass. Moreover, it can be generated by sharp discontinuities in refractive indices and thus interfaces [162]. In general, the interface can be identified via the randomly distributed nanopores/nanogratings/cracks in laser-irradiated regions. More recently, Bernard et al. [162] performed a systematical investigation of third harmonic generation upon three laser-induced modifications, i.e., "Type X", "NGs" and "hot spot" and indicated that full-field polarisation-resolved third harmonic generation could be feedback signal for discriminating various states of matters in laser-affected zones and can be exploited to control nanogratings and laser-enhanced etching selectivity.

6. Conclusions

In this review, we firstly presented the timeline of nanostructures (nanogratings and Type X) discovered in various transparent materials from 2003 to date (as of 2023). Nanogratings were revealed within a wide range of optical glasses but mostly in oxide glasses. To further understand the impact of chemical composition on nanogratings, the characteristics inherent to their internal structures including normalized periodicity, nanopore size and filling factor, were closely reviewed. Additionally, the useful performance-related optical properties of these nanogratings were discussed such as their energy processing window, maximum retardance and birefringence as well as correlated "technological performances" including energy consumption (μJ/nm), laser scanning speed, and thermal stability. These results could provide a useful roadmap in the fabrication and design of optical glasses to induce nanogratings with targeted properties. Indeed over the last 20 years, various applications were successively proposed [9–22], which include: birefringent optical elements (e.g. polarisation diffractive grating (PDG) [9] with functions of polarisation convertors [133] and beam splitters [134,135] or "S" waveplate [10,137]); 3D geometric phase optics (like Fresnel zone plates [11,12], Airy beam [139] convertors [13] or polarisation-shaped Bessel beam [14]); optical data storage [18] and other demonstrators [15–17]); selective etching (for instance, micro channels in 2006 [19], nanofluidic channels towards DNA analysis [20]); or optical fibers based sensors resistant to harsh environment such as fiber Bragg gratings (FBGs) for high power laser applications [21], optical sensors resistant to high temperature [22] or radiative environment [156].

CRediT authorship contribution statement

Heng Yao: Data curation, Writing – original draft. **Qiong Xie:** Data curation, Methodology. **Maxime Cavillon:** Writing – review & editing. **Ye Dai:** . **Matthieu Lancry:** Conceptualization, Funding acquisition, Methodology, Supervision, Validation.

Declaration of competing interest

The authors declare that they have no known competing financial interests or personal relationships that could have appeared to influence the work reported in this paper.

Data availability

Data will be made available on request.

Acknowledgements

National Natural Science Foundation of China (12274280, 11774220); Agence Nationale de la Recherche, FLAG-IR Project (ANR-18-CE08-0004-01) and REFRACTEMP project (ANR-22-CE08-0001-01); Science and Technology Innovation Plan of Shanghai Science and Technology Commission (20JC1415700); The China Scholarship Council (CSC) Project (No. 202206890050).

References

[1] Stoian R, Colombier JP. Advances in ultrafast laser structuring of materials at the nanoscale. Nanophotonics 2020;9(16):4665–88.
[2] Stoian R. Volume photoinscription of glasses: three-dimensional micro- and nanostructuring with ultrashort laser pulses. Appl Phys A 2020;126(6):438.
[3] Tan D, Sharafudeen KN, Yue Y, Qiu J. Femtosecond laser induced phenomena in transparent solid materials: Fundamentals and applications. Prog Mater Sci 2016;76:154–228.
[4] Malinauskas M, Žukauskas A, Hasegawa S, Hayasaki Y, Mizeikis V, Buividas R, et al. Ultrafast laser processing of materials: from science to industry. Light Sci Appl 2016;5(8):e16133–.
[5] Poumellec B, Lancry M, Chahid-Erraji A, Kazansky PG. Modification thresholds in femtosecond laser processing of pure silica: review of dependencies on laser parameters [Invited]. Opt Mater Express 2011;1(4):766–82.
[6] Wang Y, Cavillon M, Ollier N, Poumellec B, Lancry M. An Overview of the Thermal Erasure Mechanisms of Femtosecond Laser-Induced Nanogratings in Silica Glass. Phys Status Solidi A 2021;218(12):2100023.
[7] Beresna M, Gecevičius M, Kazansky PG. Ultrafast laser direct writing and nanostructuring in transparent materials. Adv Opt Photon 2014;6(3):293–339.
[8] Zhang B, Liu X, Qiu J. Single femtosecond laser beam induced nanogratings in transparent media - Mechanisms and applications. J Materiomics 2019;5(1):1–14.
[9] Beresna M, Kazansky PG. Polarization diffraction grating produced by femtosecond laser nanostructuring in glass. Opt Lett 2010;35(10):1662–4.
[10] Beresna M, Gecevičius M, Kazansky PG, Gertus T. Radially polarized optical vortex converter created by femtosecond laser nanostructuring of glass. Appl Phys Lett 2011;98(20):201101.

[11] Bricchi E, Mills JD, Kazansky PG, Klappauf BG, Baumberg JJ. Birefringent Fresnel zone plates in silica fabricated by femtosecond laser machining. Opt Lett 2002;27(24):2200–2.
[12] Yao H, Zaiter R, Cavillon M, Delullier P, Lu B, Cardinal T, et al. Formation of nanogratings driven by ultrafast laser irradiation in mid-IR heavy oxide glasses. Ceram Int 2022;48(21):31363–9.
[13] Gecevičius M, Beresna M, Drevinskas R, Kazansky PG. Airy beams generated by ultrafast laser-imprinted space-variant nanostructures in glass. Opt Lett 2014; 39(24):6791–4.
[14] Hassan M, Lu J, Sapaly B, Lancry M, Courvoisier F. Polarization shaping of a femtosecond Bessel beam to control birefringence writing in silica. Fiber Lasers and Glass Photonics: Materials through Applications III, Proc. SPIE 2022:PC1214209.
[15] Shimotsuma Y, Sakakura M, Kazansky PG, Beresna M, Qiu J, Miura K, et al. Ultrafast manipulation of self-assembled form birefringence in glass. Adv Mater 2010;22(36):4039–43.
[16] Sakakura M, Lei Y, Wang L, Yu YH, Kazansky PG. Ultralow-loss geometric phase and polarization shaping by ultrafast laser writing in silica glass. Light Sci Appl 2020;9:15.
[17] Lei Y, Sakakura M, Wang L, Yu Y, Wang H, Shayeganrad G, et al. High speed ultrafast laser anisotropic nanostructuring by energy deposition control via near-field enhancement. Optica 2021;8(11):1365–71.
[18] Wang H, Lei Y, Wang L, Sakakura M, Yu Y, Shayeganrad G, et al. 100-layer error-free 5D optical data storage by ultrafast laser nanostructuring in glass. Laser Photonics Rev 2022;16(4):2100563.
[19] Hnatovsky C, Taylor RS, Simova E, Rajeev PP, Rayner DM, Bhardwaj VR, et al. Fabrication of microchannels in glass using focused femtosecond laser radiation and selective chemical etching. Appl Phys A 2006;84(1–2):47–61.
[20] Liao Y, Cheng Y, Liu C, Song J, He F, Shen Y, et al. Direct laser writing of sub-50 nm nanofluidic channels buried in glass for three-dimensional micro-nanofluidic integration. Lab Chip 2013;13(8):1626.
[21] Wei SE, Wang Y, Yao H, Cavillon M, Poumellec B, Peng GD, et al. Thermal Stability of Type II Modifications by IR Femtosecond Laser in Silica-based Glasses. Sensors 2020;20(3):762.
[22] Wang Y, Cavillon M, Ballato J, Hawkins T, Elsmann T, Rothhardt M, et al. 3D Laser Engineering of Molten Core Optical Fibers: Toward a New Generation of Harsh Environment Sensing Devices. Adv Opt Mater 2022;10(18):2200379.
[23] Shimotsuma Y, Kazansky PG, Qiu J, Hirao K. Self-organized nanogratings in glass irradiated by ultrashort light pulses. Phys Rev Lett 2003;91(24):247405.
[24] Lancry M, Poumellec B, Canning J, Cook K, Poulin JC, Brisset F. Ultrafast nanoporous silica formation driven by femtosecond laser irradiation. Laser Photon Rev 2013;7(6):953–62.
[25] Beresna M, Gecevičius M, Lancry M, Poumellec B, Kazansky PG. Broadband anisotropy of femtosecond laser induced nanogratings in fused silica. Appl Phys Lett 2013;103(13):131903.
[26] Bricchi E, Kazansky PG. Extraordinary stability of anisotropic femtosecond direct-written structures embedded in silica glass. Appl Phys Lett 2006;88(11): 111119.
[27] Bellouard Y, Said A, Dugan M, Bado P. Fabrication of high-aspect ratio, micro-fluidic channels and tunnels using femtosecond laser pulses and chemical etching. Opt Express 2004;12(10):2120–9.
[28] Poumellec B, Lancry M, Desmarchelier R, Herve E, Bourguignon B. Parity violation in chiral structure creation under femtosecond laser irradiation in silica glass? Light Sci Appl 2016;5(11):e16178.
[29] Tian J, Lancry M, Yoo SH, Garcia-Caurel E, Ossikovski R, Poumellec B. Study of femtosecond laser-induced circular optical properties in silica by Mueller matrix spectropolarimetry. Opt Lett 2017;42(20):4103–6.
[30] Tian J, Li R, Yoo SH, Poumellec B, Garcia-Caurel E, Ossikovski R, et al. Spectral dependence of femtosecond laser induced circular optical properties in silica. OSA Continuum 2019;2(4):1233–41.
[31] Lu J, Tian J, Poumellec B, Garcia-Caurel E, Ossikovski R, Zeng X, et al. Tailoring chiral optical properties by femtosecond laser direct writing in silica. Light Sci Appl 2023;12(1):46.
[32] Lu J, Garcia-Caurel E, Ossikovski R, Courvoisier F, Zeng X, Poumellec B, et al. Femtosecond laser direct writing multilayer chiral waveplates with minimal linear birefringence. Opt Lett 2023;48(2):271–4.
[33] Lu J, Hassan M, Courvoisier F, Garcia-Caurel E, Brisset F, Ossikovski R, et al. 3D structured Bessel beam polarization and its application to imprint chiral optical properties in silica. APL Photon 2023;8(6):060801.
[34] Mihailov SJ, Grobnic D, Hnatovsky C, Walker RB, Lu P, Coulas D, et al. Extreme Environment Sensing Using Femtosecond Laser-Inscribed Fiber Bragg Gratings. Sensors 2017;17(12):2909.
[35] Cai W, Libertun AR, Piestun R. Polarization selective computer-generated holograms realized in glass by femtosecond laser induced nanogratings. Opt Express 2006;14:3785–91.
[36] Xie Q, Cavillon M, Poumellec B, Pugliese D, Janner D, Lancry M. Application and validation of a viscosity approach to the existence of nanogratings in oxide glasses. Opt Mater 2022;130:112576.
[37] Xie Q, Cavillon M, Pugliese D, Janner D, Poumellec B, Lancry M. On the formation of nanogratings in commercial oxide glasses by femtosecond laser direct writing. Nanomaterials 2022;12(17):2986.
[38] Wang J, Liu X, Dai Y, Wang Z, Qiu J. Effect of sodium oxide content on the formation of nanogratings in germanate glass by a femtosecond laser. Opt Express 2018;26(10):12761–8.
[39] Lancry M, Poumellec B, Chahid-Erraji A, Beresna M, Kazansky PG. Dependence of the femtosecond laser refractive index change thresholds on the chemical composition of doped-silica glasses. Opt Mater Express 2011;1(4):711–23.
[40] Lancry M, Canning J, Cook K, Heili M, Neuville DR, Poumellec B. Nanoscale femtosecond laser milling and control of nanoporosity in the normal and anomalous regimes of GeO_2-SiO_2 glasses. Opt Mater Express 2016;6(2):321–30.
[41] Shimotsuma Y, Kubota S, Murata A, Kurita T, Sakakura M, Miura K, et al. Tunability of form birefringence induced by femtosecond laser irradiation in anion-doped silica glass. J Am Ceram Soc 2017;100(9):3912–9.
[42] Fedotov SS, Drevinskas R, Lotarev SV, Lipatiev AS, Beresna M, Čerkauskaitė A, et al. Direct writing of birefringent elements by ultrafast laser nanostructuring in multicomponent glass. Appl Phys Lett 2016;108(7):071905.
[43] Lancry M, Zimmerman F, Desmarchelier R, Tian J, Brisset F, Nolte S, et al. Nanogratings formation in multicomponent silicate glasses. Appl Phys B 2016;122 (3):66.
[44] Cao J, Mazerolles L, Lancry M, Solas D, Brisset F, Poumellec B. Form birefringence induced in multicomponent glass by femtosecond laser direct writing. Opt Lett 2016;41(12):2739–42.
[45] Lotarev SV, Fedotov SS, Kurina AI, Lipatiev AS, Sigaev VN. Ultrafast laser-induced nanogratings in sodium germanate glasses. Opt Lett 2019;44(7):1564–7.
[46] Zhang B, Tan D, Wang Z, Liu X, Xu B, Gu M, et al. Self-organized phase-transition lithography for all-inorganic photonic textures. Light Sci Appl 2021;10(1):93.
[47] Tian J, Yao H, Cavillon M, Garcia-Caurel E, Ossikovski R, Stchakovsky M, et al. A comparison between nanogratings-based and stress-engineered waveplates written by femtosecond laser in silica. Micromachines 2020;11(2):131.
[48] Zhang F, Zhang H, Dong G, Qiu J. Embedded nanogratings in germanium dioxide glass induced by femtosecond laser direct writing. J Opt Soc Am B 2014;31 (4):860–4.
[49] Cavillon M, Wang Y, Poumellec B, Brisset F, Lancry M. Erasure of nanopores in silicate glasses induced by femtosecond laser irradiation in the Type II regime. Appl Phys A 2020;126(11):876.
[50] Richter S, Miese C, Döring S, Zimmermann F, Withford MJ, Tünnermann A, et al. Laser induced nanogratings beyond fused silica - periodic nanostructures in borosilicate glasses and ULE™. Opt Mater Express 2013;3(8):1161–6.
[51] Shimotsuma Y, Hirao K, Qiu J, Kazansky PG. Nano-modification inside transparent materials by femtosecond laser single beam. Mod Phys Lett B 2005;19(5): 225–38.

[52] Zhai Q, Ma H, Lin X, Li Y, Yin W, Tang X, et al. Evolution of self-organized nanograting from the pre-induced nanocrack-assisted plasma–laser coupling in sapphire. Appl Phys B 2021;127(5):74.
[53] Shimotsuma Y, Mori S, Nakanishii Y, Kim E, Sakakura M, Miura K. Self-assembled glass/crystal periodic nanostructure in Al_2O_3-Dy_2O_3 binary glass. Appl Phys A 2018;124(1):82.
[54] Cao J, Mazerolles L, Lancry M, Brisset F, Poumellec B. Modifications in lithium niobium silicate glass by femtosecond laser direct writing: morphology, crystallization, and nanostructure. J Opt Soc Am B 2016;34(1):160–8.
[55] Yao H, Xie Q, Cavillon M, Neuville DR, Pugliese D, Janner D, et al. Volume nanogratings inscribed by ultrafast IR laser in alumino-borosilicate glasses. Opt Express 2023;31(10):15449–60.
[56] Shimotsuma Y, Asai T, Sakakura M, Miura K. Femtosecond-laser Nanostructuring in Glass. J Laser Micro/Nanoen 2014;9(1):31–6.
[57] Bhardwaj VR, Simova E, Rajeev PP, Hnatovsky C, Taylor RS, Rayner DM, et al. Optically produced arrays of planar nanostructures inside fused silica. Phys Rev Lett 2006;96(5):057404.
[58] Richter S, Plech A, Steinert M, Heinrich M, Döring S, Zimmermann F, et al. On the fundamental structure of femtosecond laser-induced nanogratings. Laser Photonics Rev 2012;6(6):787–92.
[59] Zhang J, Gecevicius M, Beresna M, Kazansky PG. Seemingly unlimited lifetime data storage in nanostructured glass. Phys Rev Lett 2014;112(3):033901.
[60] Sanada K, Shamoto N, Inada K. Radiation resistance of fluorine-doped silica-core fibers. J Non-Cryst Solids 1994;179:339–44.
[61] Richter S, Jia F, Heinrich M, Döring S, Peschel U, Tünnermann A, et al. The role of self-trapped excitons and defects in the formation of nanogratings in fused silica. Opt Lett 2012;37:482–4.
[62] Lancry M, Régnier E, Poumellec B. Fictive temperature in silica-based glasses and its application to optical fiber manufacturing. Prog Mater Sci 2012;57(1):63–94.
[63] Zimmermann F, Lancry M, Plech A, Richter S, Babu BH, Poumellec B, et al. Femtosecond laser written nanostructures in Ge-doped glasses. Opt Lett 2016;41(6):1161–4.
[64] Cerkauskaite A, Drevinskas R, Rybaltovskii AO, Kazansky PG. Ultrafast laser-induced birefringence in various porosity silica glasses: from fused silica to aerogel. Opt Express 2017;25(7):8011–21.
[65] Lotarev SV, Lipatiev AS, Fedotov SS, Mikhailov AA, Sigaev VN. Laser Writing of Polarization-Sensitive Birefringence in Sodium-Borosilicate Glass. Glass Ceram 2019;76:85–8.
[66] Lotarev SV, Fedotov SS, Lipatiev AS, Presnyakov M, Kazansky PG, Sigaev VN. Light-driven nanoperiodical modulation of alkaline cation distribution inside sodium silicate glass. J Non-Cryst Solids 2018;479:49–54.
[67] Wang Y, Wei S, Cicconi MR, Tsuji Y, Shimizu M, Shimotsuma Y, et al. Femtosecond laser direct writing in SiO2-Al2O3 binary glasses and thermal stability of Type II permanent modifications. J Am Ceram Soc 2020;103(8):4286–94.
[68] Yao H, Zaiter R, Cavillon M, Sapaly B, Calzavara F, Delullier P, et al. Photosensitivity of barium germano-gallate glasses under femtosecond laser direct writing for Mid-IR applications. Ceram Int 2021;47(24):34235–41.
[69] Zaiter R, Lancry M, Fargues A, Adamietz F, Dussauze M, Rodriguez V, et al. Optical and structural characterization of femtosecond laser written micro-structures in germanate glass. Sci Rep 2023;13(1):11050.
[70] Delullier P, Calvez L, Druart G, De La Barrière F, Humbert C, Poumellec B, et al. Photosensitivity of Infrared Glasses under Femtosecond Laser Direct Writing for mid-IR Applications. Appl Sci 2022;12(17):8813.
[71] Mori M, Shimotsuma Y, Sei T, Sakakura M, Miura K, Udono H. Tailoring thermoelectric properties of nanostructured crystal silicon fabricated by infrared femtosecond laser direct writing. Phys Status Solidi (a) 2015;212(4):715–21.
[72] Sei T, Shimotsuma Y, Sakakura M, Miura K. Self-assembled Nanostructures inside Indirect Bandgap Semiconductor by Using IR Femtosecond Double-pulses. J Laser Micro/Nanoen 2016;11:76–80.
[73] Kim E, Shimotsuma Y, Sakakura M, Miura K. Nano Periodic Structure Formation in 4H–SiC Crystal Using Femtosecond Laser Double-Pulses. J Superhard Mater + 2018;40(4):259–66.
[74] Shimotsuma Y, Sei T, Sakakura M, Miura K, Udono H. Nanostructuring in Indirect Band-gap Semiconductor Using IR Femtosecond Double Pulses. J Laser Micro/Nanoen 2016;11(1):35–40.
[75] Torun G, Yadav A, Richardson KA, Bellouard Y. Ultrafast Laser Direct-Writing of Self-Organized Microstructures in Ge-Sb-S Chalcogenide Glass. Front Phys 2022;10:883319.
[76] Shimotsuma Y, Nakanishi Y, Skakura M, Miura K. Self-assembled periodic nanostructures embedded in wide bandgap semiconductor. Conference on Lasers and Electro-Optics Pacific Rim. Singapore: Optica Publishing Group; 2017.
[77] Zhang F, Nie Z, Huang H, Ma L, Tang H, Hao M, et al. Self-assembled three-dimensional periodic micro-nano structures in bulk quartz crystal induced by femtosecond laser pulses. Opt Express 2019;27(5):6442–50.
[78] Muzi E, Cavillon M, Lancry M, Brisset F, Sapaly B, Janner D, et al. Polarization-oriented LiNbO3 nanocrystals by femtosecond laser irradiation in LiO_2–Nb_2O_5–SiO_2–B_2O_3 glasses. Opt Mater Express 2021;11(4):1313–20.
[79] Cavillon M, Cao J, Vallet M, Brisset F, Mazerolles L, Dkhil B, et al. Thermal and Electron Plasma Effects on Phase Separation Dynamics Induced by Ultrashort Laser Pulses. Crystals 2022;12(4):496.
[80] Hnatovsky C, Taylor RS, Rajeev PP, Simova E, Bhardwaj VR, Rayner DM, et al. Pulse duration dependence of femtosecond-laser-fabricated nanogratings in fused silica. Appl Phys Lett 2005;87(1):014104.
[81] Hnatovsky C, Taylor RS, Simova E, Bhardwaj VR, Rayner DM, Corkum PB. Polarization-selective etching in femtosecond laser-assisted microfluidic channel fabrication in fused silica. Opt Lett 2005;30:1867–9.
[82] Rajeev PP, Gertsvolf M, Hnatovsky C, Simova E, Taylor RS, Corkum PB, et al. Transient nanoplasmonics inside dielectrics. J Phys B At Mol Opt Phys 2007;40(11).
[83] Kazansky PG, Yang W, Bricchi E, Bovatsek J, Arai A, Shimotsuma Y, et al. "Quill" writing with ultrashort light pulses in transparent materials. Appl Phys Lett 2007;90(15):151120.
[84] Beresna M, Gecevičius M, Kazansky PG, Taylor T, Kavokin AV. Exciton mediated self-organization in glass driven by ultrashort light pulses. Appl Phys Lett 2012;101(5):053120.
[85] Canning J, Lancry M, Cook K, Weickman A, Brisset F, Poumellec B. Anatomy of a femtosecond laser processed silica waveguide [Invited]. Opt Mater Express 2011;1(5):998–1008.
[86] Bellouard Y, Champion A, McMillen B, Mukherjee S, Thomson RR, Pépin C, et al. Stress-state manipulation in fused silica via femtosecond laser irradiation. Optica 2016;3(12):1285–93.
[87] Champion A, Bellouard Y. Direct volume variation measurements in fused silica specimens exposed to femtosecond laser. Opt Mater Express 2012;2(6):789–98.
[88] Champion A, Beresna M, Kazansky P, Bellouard Y. Stress distribution around femtosecond laser affected zones: effect of nanogratings orientation. Opt Express 2013;21(21):24942–51.
[89] Asai T, Shimotsuma Y, Kurita T, Murata A, Kubota S, Sakakura M, et al. Systematic Control of Structural Changes in GeO2 Glass Induced by Femtosecond Laser Direct Writing. J Am Ceram Soc 2015;98(5):1471–7.
[90] Zimmermann F, Plech A, Richter S, Tünnermann A, Nolte S. Ultrashort laser pulse induced nanogratings in borosilicate glass. Appl Phys Lett 2014;104(21):211107.
[91] Buschlinger R, Nolte S, Peschel U. Self-organized pattern formation in laser-induced multiphoton ionization. Phys Rev B 2014;89(18):184306.
[92] Rudenko A, Colombier JP, Hohm S, Rosenfeld A, Kruger J, Bonse J, et al. Spontaneous periodic ordering on the surface and in the bulk of dielectrics irradiated by ultrafast laser: a shared electromagnetic origin. Sci Rep 2017;7(1):12306.

[93] Rudenko A, Ma H, Veiko VP, Colombier JP, Itina TE. On the role of nanopore formation and evolution in multi-pulse laser nanostructuring of glasses. Appl Phys A 2018;124(1):63.
[94] Rudenko A, Colombier JP, Itina TE. Nanopore-mediated ultrashort laser-induced formation and erasure of volume nanogratings in glass. Phys Chem Chem Phys 2018;20(8):5887–99.
[95] Oliveira V, Sharma SP, Herrero P, Vilar R. Transformations induced in bulk amorphous silica by ultrafast laser direct writing. Opt Lett 2013;38:4950–3.
[96] Pépin CM, Block E, Gaal R, Nillon J, Hoenninger C, Gillet P, et al. Silicon formation in bulk silica through femtosecond laser engraving. arXiv:1806.10802 2018.
[97] Sharma SP, Oliveira V, Herrero P, Vilar R. Internal structure of the nanogratings generated inside bulk fused silica by ultrafast laser direct writing. J Appl Phys 2014;116(5):053106.
[98] Xie Q, Shchedrina N, Cavillon M, Poumellec B, Lancry M. Nanoscale investigations of femtosecond laser induced nanogratings in optical glasses. Nanoscale Advances (Accepted, DOI: 10.1039/D3NA00748K) 2023.
[99] Rudenko A, Colombier JP, Itina TE, Stoian R. Genesis of Nanogratings in Silica Bulk via Multipulse Interplay of Ultrafast Photo-Excitation and Hydrodynamics. Adv Opt Mater 2021;9(20):2100973.
[100] Taylor RS, Hnatovsky C, Simova E. Applications of femtosecond laser induced self-organized planar nanocracks inside fused silica glass. Laser Photonics Rev 2008;2(1–2):26–46.
[101] Zimmermann F, Plech A, Richter S, Tünnermann A, Nolte S. The onset of ultrashort pulse-induced nanogratings. Laser Photonics Rev 2016;10(2):327–34.
[102] Desmarchelier R, Poumellec B, Brisset F, Mazerat S, Lancry M. In the Heart of Femtosecond Laser Induced Nanogratings: From Porous Nanoplanes to Form Birefringence. World J Nano Sci Eng 2015;05(04):115–25.
[103] Rudenko A, Colombier JP, Itina TE. From random inhomogeneities to periodic nanostructures induced in bulk silica by ultrashort laser. Phys Rev B 2016;93(7):075427.
[104] Doremus RH. Glass Science. Wiley; 1973.
[105] Mouskeftaras A, Koritsoglou O, Duchateau G, Utéza O. From femtosecond laser-induced plasma formation inside glass to stress wave generation and propagation: Experiments and modelling. Lasers and Electro-Optics/Europe (CLEO/Europe 2023) and European Quantum Electronics Conference (EQEC 2023), Technical Digest Series (Optica Publishing Group, 2023), 2023.
[106] Radhakrishnan A, Gateau J, Vlugter P, Bellouard Y. Femtosecond laser-shockwave induced densification in fused silica. Opt Mater Express 2022;12(7):2886–98.
[107] Vlugter P, Bellouard Y. Elastic properties of self-organized nanogratings produced by femtosecond laser exposure of fused silica. Phys Rev Materials 2020;4(2):023607.
[108] Yoshino T, Ozeki Y, Matsumoto M, Itoh K. In situ Micro-Raman Investigation of Spatio-Temporal Evolution of Heat in Ultrafast Laser Microprocessing of Glass. Jpn J Appl Phys 2012;51(10R):102403.
[109] Rudenko A. Numerical study of ultrashort laser-induced periodic nanostructure formation in dielectric materials. Sciences Ingénierie et Santé: Université de Lyon, France; 2017.
[110] Xie Q, Cavillon M, Poumellec B, Lancry M. Upper temperature limit for nanograting survival in oxide glasses. Appl Opt 2023;62(25):6794–801.
[111] Lei Y, Shayeganrad G, Wang H, Sakakura M, Yu Y, Wang L, et al. Efficient ultrafast laser writing with elliptical polarization. Light Sci Appl 2023;12(1):74.
[112] Poumellec B, Cavillon M, Lancry M. Electrostatic Interpretation of Phase Separation Induced by Femtosecond Laser Light in Glass. Crystals 2023;13(3):393.
[113] Fernandez TT, Siegel J, Hoyo J, Sotillo B, Fernandez P, Solis J. Controlling plasma distributions as driving forces for ion migration during fs laser writing. J Phys D Appl Phys 2015;48(15):155101.
[114] Fernandez TT, Sakakura M, Eaton SM, Sotillo B, Siegel J, Solis J, et al. Bespoke photonic devices using ultrafast laser driven ion migration in glasses. Prog Mater Sci 2018;94:68–113.
[115] Couairon A, Sudrie L, Franco M, Prade B, Mysyrowicz A. Filamentation and damage in fused silica induced by tightly focused femtosecond laser pulses. Phys Rev B 2005;71(12):125435.
[116] Huang F, Si J, Chen T, Shen T, Shi M, Hou X. Temporal-spatial dynamics of electronic plasma in femtosecond laser induced damage. Opt Express 2021;29(10):14658–67.
[117] Emoto A, Nishi M, Okada M, Manabe S, Matsui S, Kawatsuki N, et al. Form birefringence in intrinsic birefringent media possessing a subwavelength structure. Appl Opt 2010;49:4355–61.
[118] Markel VA. Introduction to the Maxwell Garnett approximation: tutorial. J Opt Soc Am A Opt Image Sci Vis 2016;33(7):1244–56.
[119] Weber MJ. Handbook of Optical Materials. London: CRC Press; 2003.
[120] Henderson GS, Stebbins JF. The short-range order (SRO) and structure. Rev Mineral Geochem 2022;87(1):1–53.
[121] Neuville DR, Cormier LMassiot D. Al coordination and speciation in calcium aluminosilicate glasses: Effects of composition determined by 27Al MQ-MAS NMR and Raman spectroscopy. Chem Geol 2006;229(1-3):173-185.
[122] Liu SB, Stebbins JF, Schneider E, Pines A. Diffusive motion in alkali silicate melts: An NMR study at high temperature. Geochim Cosmochim Acta 1988;52(2):527–38.
[123] Fernandez TT, Gross S, Privat K, Johnston B, Withford M. Designer Glasses—Future of Photonic Device Platforms. Adv Funct Mater 2021;32(3):2103103.
[124] Neuville DR. Viscosity, structure and mixing in (Ca, Na) silicate melts. Chem Geol 2006;229(1–3):28–41.
[125] Torun G, Kishi T, Bellouard Y. Direct-write laser-induced self-organization and metallization beyond the focal volume in tellurite glass. Phys Rev Materials 2021;5(5):055201.
[126] Bayya S, Sanghera J, Aggarwal I. Optical transmission of BGG glass material. United States US 7285509 B2, 23 October 2007.
[127] Zaghloul MAS, Wang M, Huang S, Hnatovsky C, Grobnic D, Mihailov S, et al. Radiation resistant fiber Bragg grating in random air-line fibers for sensing applications in nuclear reactor cores. Opt Express 2018;26(9):11775–86.
[128] Cavillon M, Lancry M, Poumellec B, Wang Y, Canning J, Cook K, et al. Overview of high temperature fibre Bragg gratings and potential improvement using highly doped aluminosilicate glass optical fibres. J Phys Photonics 2019;1(4):042001.
[129] Wang Y, Lancry M, Cavillon M, Poumellec B. Lifetime prediction of nanogratings inscribed by a femtosecond laser in silica glass. Opt Lett 2022;47(5):1242–5.
[130] Marshall GD, Politi A, Matthews JCF, Dekker P, Ams M, Withford MJ, et al. Laser written waveguide photonic quantum circuits. Opt Express 2009;17(15):12546–54.
[131] Ams M, Marshall GD, Dekker P, Piper JA, Withford MJ. Ultrafast laser written active devices. Laser Photon Rev 2009;3(6):535–44.
[132] Smelser CW, Mihailov SJ, Grobnic D. Formation of Type I-IR and Type II-IR gratings with an ultrafast IR laser and a phase mask. Opt Express 2005;13(14):5377–86.
[133] Niv A, Biener G, Kleiner V, Hasman E. Formation of linearly polarized light with axial symmetry by use of space-variant subwavelength gratings. Opt Lett 2003;28(7):510–2.
[134] Hasman E, Ze B, Niv A, Biener G, Kleiner V. Polarization beam-splitters and optical switches based on space-variant computer-generated subwavelength quasi-periodic structures. Opt Commun 2002;209(1–3):45–54.
[135] Cariñe J, Cañas G, Skrzypczyk P, Šupić I, Guerrero N, Garcia T, et al. Multi-core fiber integrated multi-port beam splitters for quantum information processing. Optica 2020;7(5):542–50.
[136] Corrielli G, Crespi A, Geremia R, Ramponi R, Sansoni L, Santinelli A, et al. Rotated waveplates in integrated waveguide optics. Nat Commun 2014;5:4249.
[137] Beresna M, Gecevičius M, Kazansky PG. Polarization sensitive elements fabricated by femtosecond laser nanostructuring of glass [Invited]. Opt Mater Express 2011;1(4):783–95.
[138] Drevinskas R, Kazansky PG. High-performance geometric phase elements in silica glass. APL Photonics 2017;2(6):066104.
[139] Gris-Sánchez I, Van Ras D, Birks TA. The Airy fiber: an optical fiber that guides light diffracted by a circular aperture. Optica 2016;3(3):270–6.
[140] Gu M, Li X, Cao Y. Optical storage arrays: a perspective for future big data storage. Light Sci Appl 2014;3(5):e177–.

[141] Church GM, Gao Y, Kosuri S. Next-Generation Digital Information Storage in DNA. Science 2012;337(6102):1628.
[142] Schaap A, Rohrlack T, Bellouard Y. Optical classification of algae species with a glass lab-on-a-chip. Lab Chip 2012;12(8):1527.
[143] Vazquez RM, Osellame R, Nolli D, Dongre C, van den Vlekkert H, Ramponi R, et al. Integration of femtosecond laser written optical waveguides in a lab-on-chip. Lab Chip 2009;9(1):91–6.
[144] Sima F, Sugioka K, Vázquez RM, Osellame R, Kelemen L, Ormos P. Three-dimensional femtosecond laser processing for lab-on-a-chip applications. Nanophotonics 2018;7(3):613–34.
[145] Lin Z, Xu J, Song Y, Li X, Wang P, Chu W, et al. Freeform Microfluidic Networks Encapsulated in Laser-Printed 3D Macroscale Glass Objects. Adv Mater Technol 2020;5(2):1900989.
[146] Eaton SM, Herman PR. Passive Photonic Devices in Glass. R. Osellame, G. Cerullo and R. Ramponi Femtosecond Laser Micromachining. Topics in Applied Physics 2012. Springer, Berlin, Heidelberg.
[147] Nolte S, Will M, Burghoff J, Tuennermann A. Femtosecond waveguide writing: a new avenue to three-dimensional integrated optics. Appl Phys A 2003;77(1):109–11.
[148] Shah L, Arai AY, Eaton SM, Herman PR. Waveguide writing in fused silica with a femtosecond fiber laser at 522 nm and 1 MHz repetition rate. Opt Express 2005;13(6):1999–2006.
[149] Eaton SM, Ng ML, Osellame R, Herman PR. High refractive index contrast in fused silica waveguides by tightly focused, high-repetition rate femtosecond laser. J Non-Cryst Solids 2011;357(11–13):2387–91.
[150] Grobnic D, Smelser CW, Mihailov SJ, Walker RB. Long-term thermal stability tests at 1000 °C of silica fibre Bragg gratings made with ultrafast laser radiation. Meas Sci Technol 2006;17(5):1009–13.
[151] Zhang H, Eaton SM, Herman PR. Single-step writing of Bragg grating waveguides in fused silica with an externally modulated femtosecond fiber laser. Opt Lett 2007;32(17):2559–61.
[152] Mihailov SJ. Fiber Bragg grating sensors for harsh environments. Sensors 2012;12(2):1898–918.
[153] Grobnic D, Mihailov SJ, Smelser CW, Ding H. Sapphire Fiber Bragg Grating Sensor Made Using Femtosecond Laser Radiation for Ultrahigh Temperature Applications. IEEE Photonic Tech L 2004;16(11):2505–7.
[154] Jewart CM, Wang Q, Canning J, Grobnic D, Mihailov SJ, Chen KP. Ultrafast femtosecond-laser-induced fiber Bragg gratings in air-hole microstructured fibers for high-temperature pressure sensing. Opt Lett 2010;35(9):1443–5.
[155] Hnatovsky C, Grobnic D, Coulas D, Barnes M, Mihailov SJ. Self-organized nanostructure formation during femtosecond-laser inscription of fiber Bragg gratings. Opt Lett 2017;42(3):399–402.
[156] Wang M, Zhao K, Wu J, Li Y, Yang Y, Huang S, et al. Femtosecond laser fabrication of nanograting-based distributed fiber sensors for extreme environmental applications. Int J Extrem Manuf 2021;3(2):025401.
[157] Juodkazis S, Gaižauskas E, Jarutis V, Reif J, Matsuo S, Misawa H. Optical third harmonic generation during femtosecond pulse diffraction in a Bragg grating. J Phys D Appl Phys 2006;39(1):50–3.
[158] Siiman LA, Lumeau J, Canioni L, Glebov LB. Non-collinear generation of third harmonic of IR ultrashort laser pulses by PTR glass volume Bragg gratings. Opt Express 2009;17(5):3564–73.
[159] Cheng G, Mishchik K, Mauclair C, Audouard E, Stoian R. Ultrafast laser photoinscription of polarization sensitive devices in bulk silica glass. Opt Express 2009;17(12):9515–25.
[160] Grigutis R, Jukna V, Navickas M, Tamošauskas G, Staliunas K, Dubietis A. Conical third harmonic generation from volume nanogratings induced by filamentation of femtosecond pulses in transparent bulk materials. Opt Express 2021;29(24):40633–42.
[161] Grigutis R, Jukna V, Tamošauskas G, Dubietis A. Broadband conical third harmonic generation in femtosecond filament-modified fused silica. Opt Lett 2023;48(2):506–9.
[162] Bernard O, Kraxner A, Boukhayma A, Squier JA, Enz C, Bellouard Y. Third-harmonic generation monitoring of femtosecond-laser-induced in-volume functional modifications. Optica 2023;10(6):774–82.

IV.3 Conclusion

This chapter reviews the impact of chemical composition on nanogratings and their characteristics to their internal structures including normalized periodicity, nanopore size and filling factor. Useful performance-related optical properties of these nanogratings, such as their energy processing window, maximum retardance and birefringence as well as correlated “technological performances” including energy consumption (µJ/nm), laser scanning speed, and thermal stability. This collection of experimental work provides a materials roadmap to stimulate the development and selection of glass materials for nanogratings imprinting, depending on the final application, and intends to comprehensively pinpoint the differences existing between glasses.

GENERAL CONCLUSION

Today's advanced femtosecond laser systems offer a myriad of material interactions in glass and glass-containing media, with perhaps the most striking effect being related to 3D refractive index complex tuning (positive or negative index changes; isotropic or anisotropic) depending on both the laser parameters [20] and the material chemical composition [9]. Over last decade, other properties induced by laser irradiation in glass have also been unveiled, like chirality [219, 220], non-reciprocal writing [68, 158, 221, 222], oxidation-reduction and cluster structuring [223, 224], and chemical rearrangement with a sub-wavelength resolution [9, 13]. Furthermore, 3D internal structuring in transparent glasses by fs-laser brings unprecedented functionalities, attracting remarkable interest from many sectors of both the scientific and industrial communities including working on ultrafast light-matter interactions, micromachining, and micro- and integrated optics. The technology allows fabricating any tailored optical element with sub-µm thicknesses, while being printed in a single step procedure. Therefore, no molding nor polishing are required, as opposed to optical elements fabricated by conventional means. The manufacturing does not need expensive clean rooms in contrast to lithography, which also is limited to 2D transformations. The same technology can be exploited for planar waveguide or fiber-based optics, free space optics and micro-optics fabrication. The high-performance birefringent and geometric phase elements imprinted in silica-based glasses by FLDW have demonstrated the potential of this technique for designing functional devices that can be integrated into complex photonic systems such as optical data storage, high-power lasers, high resolution microscopy, optical communication systems, polarization sensitive imaging, optofluidic platforms, optomechanical devices, optical sensors and even consumer electronics. This framework was the basis of this dissertation work.

This PhD project started with the study of 3D photo-imprinting of anisotropic optical properties in transparent inorganic glasses using femtosecond laser light. In the first stage, we shed light on the importance of glass composition under laser irradiation, along with laser parameters associated. Among the findings to highlight, we established what laser parameter values are the most adequate to induce nanogratings in both commercial and "laboratory-made" glasses in collaboration with academic partners. Then, in the second stage of this work, we studied fs-laser irradiation on several commercial optical glasses and focused on investigating anisotropies in the optical properties namely the linear birefringence and its thermal stability. One objective was to provide a roadmap to produce optical sensors in a high-temperature regime by mastering NGs formation, their thermal stability and lifetime in operating conditions. The central idea of this PhD was to comprehend the interplay between the chemical composition (e.g., introduction of TiO_2, B_2O_3 or Al_2O_3 inside a silica glass together with charges compensators such as Na, K or Ca) and the nanostructure itself (periodicity, nanopores size and filling factor, …). In fact, this work systematically studies, through several approaches, the writing and erasing mechanisms of nanogratings as a

function of pulse energy, repetition rate, polarization orientation, and oxide glasses chemical composition.

Key results are summarized as follow:

1) We investigated areas of glass compositions based on the presence of SiO_2, GeO_2, B_2O_3, TiO_2, Al_2O_3, CaO and Na_2O. The nanogratings existence is evaluated through their polarization dependent birefringence, along with the laser pulse energy-repetition rate (E_p-RR) landscape. The processing window of NGs is narrow when the alkali and alkali earth and boron elements amount with respect to glass network formers (Si, Al or Ge element) content increases.

2) We demonstrated the effect of laser writing parameters (repetition rate, energy, writing speed and polarization orientation) on the NG properties (periodicity, porosity size and filling factor) in a wide range of commercial oxide glasses.

3) We investigated and discussed the underlying mechanisms at the origin of nanogratings formation in glasses. The formation of the ''self-organized'' porous NGs in oxide glasses was investigated by SEM, HR-TEM and STEM. From this in depth electron microscopy analysis, oblate nanopores were found to populate some array of non-continuous nanoplanes, which grow perpendicularly to the laser polarization direction and along the laser propagation direction. Some tiny elongated nanopores were also found between the long and fully-grown nanoplanes. These nanopores will grow and merge in a multipulse regime, resulting in a pulse-to-pulse decrease of the averaged periodicity much below $\lambda/2n$ as reviewed. The plasma-mediated nanocavitation model discussed the formation of these "light forced-organized" (rather than self-organized) sub-wavelength NGs in a multipulse view.

4) The form birefringence, due to the self-organization of nanopores in a layered nanostructure, is found to play a key role in the ultimate thermal stability of the fs laser-induced nanogratings. For all glass compositions, the viscosity and glass annealing temperature (T_a) appears strongly related to the "ultimate" thermal stability of the birefringence i.e., the higher viscosity the higher full erasure temperature. We provide insights on the effect of viscosity on the existence of NGs, supported by experimental evidences and theoretical ones (Rayleigh-plesset (R-P) equation), applied to predict the NGs possessing window. The pressure and thermal confinement conditions are considered in this approach. The NGs domain is bound between two limits: i) a low temperature one, the viscosity at ~$10^{6.6}$ Pa·s, corresponding to a cavitation mechanism, ii) a high temperature one the viscosity value typically around ~$10^{3.0}$ Pa·s, for which the pores experience either growth or collapse, leading to a disappearance of the NG structure. There is a high correlation between the temperature interval from the viscosity curve and the NGs processing window landscape in different commercial glasses and a series of alumino-borosilicate glasses.

5) We exploit the Rayleigh–Plesset (R–P) equation to simulate, and compared to

experimental results, the thermal stability of nanopores and resulting form birefringence. This provides insights into the temperature range at which the nanopores would ultimately collapse and simulate the erasure process of the nanopores/nanogratings during the thermal annealing.

6) By coupling Rayleigh–Plesset (R–P) equation and a model of laser-induced heat effects, we can tentatively mimic and explain the erasure kinetic of nanogratings according to laser parameters (repetition rate and energy). There is a close dependence between the material parameters, and in particular the T dependence of the viscosity and the formation of nanogratings, hence associated anisotropic optical properties. The equation of the erasure time has been established using simplified R-P equation. It is used to theoretically predict the erasure of NGs in the context of any time–temperature process (e.g., thermal annealing, laser irradiation process, "any thermal treatment"). We found that the upper temperature limit under irradiation conditions corresponds to a temperature for which the glass viscosity value is log (η, Pa·s) ~ -0.75 in the hypothesis where we consider a characteristic time of 30 ns, or log (η, Pa·s) ~ 1 for a timescale of 1 µs, corresponding to a typical diffusion time. However, this temperature limit is lowered for much longer processes like isothermal / isochronal annealing where log (η, Pa·s) ~ 10.1.

7) Finally, a framework is developed for lifetime and passivation determination of birefringence (or average index changes) associated to nanogratings. This framework is based on demarcation energy approximation and the existence of a master curve. The theoretical master curve is then validated using accelerated aging experiments under specific conditions. Then due to the distributed nature of activation energies, it is possible to increase the nanogratings stability by erasing the less stable part to extend the lifetime i.e., a so-called passivation process.

With these in hands, we can envision to develop optical glasses (bulk or fiber geometries) or select commercial ones dedicated to the creation of anisotropic optical properties in various spectral ranges, from UV to mid-IR but also for applications in a high-temperature regime where lifetime control and is mandatory.

FUTURE WORK AND PERSPECTIVES

Towards a new paradigm – To go beyond a simple energy deposition mechanism to develop forces

Understanding how a material behaves at the nanoscale under intense laser excitation is crucial for advancing future laser processing technologies. Mechanical, thermal, optical, structural and compositional properties of materials could be tailored for optical data storage, micro/nano fluidic devices, novel alloy formation, catalytic, sensor applications, etc. Light polarization is an effective parameter for controlling energy delivery in laser structuring of surfaces and volumes. However, it is possible to go far

beyond a simple deposition of laser energy in the matter. A classical effect of a light beam is a thermal effect (laser cutting, melting) instead of developing forces after non-linear energetic excitation of the transparent matter by intense laser light. Deeper investigations of NG structural changes and mechanisms using nanoscale techniques such as nano IR and nano Raman to investigate structural changes at a 10 nm scale using vibrational spectroscopy, nano XPEEM (X-ray photoelectron emission microscopy), elemental analysis using HR-TEM EELS (Electron Energy Loss Spectroscopy), EFM to check the presence of space charge field, especially at short time scales (ps-ns). From an engineering point of view, temporal shaping, such as few pulses and GHz burst machining for enhancing NGs linear writing speed combined with the control of nanoscale porosity in glasses to favour their formation, while spatial shaping, such as extended or multi-focus can be used for enhancing writing speed in volume. Combining with spatial pulse shaping (e.g. truncated Airy, truncated Bessel beams etc.) should enhance the spatial uniformity of NGs and reduce overall optical losses. In addition, one should develop a few-cycle ultrafast pulses processing that may result in an "avalanche-free mode for a more efficient and highly localized energy deposition, a more efficient manipulation of spatial-temporal coupling and a better control of NGs seeding process.

What one can imagine with a sub-picosecond laser nowadays can also be realized more clearly with a truly femtosecond one appearing on the market in the next few years. The time for a half period in the IR at a wavelength of 1 μm is 1.7fs! In that case, opposite charges can be more easily separated. Ultimately, we will pave the way to materials science by sub-cycle laser pulses. In the future, we will use them to show that it is a general possibility in transparent materials. We intend to challenge the proposed theory by simulation work, i.e., to show that the forces and torques are large enough to compute the electric field and the induced mechanical field, to show we can imprint twisted NGs and figure out the appropriate laser parameters to use. These future works will increase our knowledge of non-linear action involving the interaction of intense and ultrashort laser light with matter. This new knowledge will apply to any structuration of optical functionalization of dielectric materials in adjacent fields of integrated optics and solid-state chemistry.

Exploring vectorial aspects of light matter interaction process

The experimental results reported bring evidence of a polarization-affected light-matter interaction process. One fascinating prospect is to combine the time and spatial distribution of the light's polarization, intensity, and phase inside a dielectric material. By doing so, it will become possible to efficiently control the non-linear force distribution and orientation in the excited solid state (e.g., the induced plasma) and, thus, the final effect in the matter, exerting mechanical actions in the matter in addition to the thermal effect. This is possible only for significant intensity and short pulse durations when electrons can be excited in delocalized states independently of the ionic motion.

The proposed ideas boil down to the following sentence: match the processing tool (i.e. laser and its spatial-temporal shaping) to a given task. For instance, an exciting

result would be creating complex NGs by combining several laser beams. Laser beams, i.e., circularly polarized or optical vortices, carry the spin and orbital angular momentum (SAM and OAM). These experiments help answer the starting question of whether SAM and OAM are equivalent concerning light absorption. Another example is Bessel beams, which allow the fabrication of high aspect ratio structures. Indeed, NG imprinting can be explored to generate known laser beams such as Bessel, Hermite-Gaussian, and Laguerre-Gaussian modes and to enable engineering of both the intensity and the polarization distribution at the focus of the beam. Among particular vector beams are a class of solutions to the vector wave equation defined by a spatially varying direction of polarization. Cylindrical vector beams obey axial symmetry, such as radial and azimuthal polarization. Vector beams are of interest because of their unique focusing properties, which allow a significant amount of control over the electric field shape near the focus, including the potential for tighter focusing than regular beams. We will develop novel birefringent optical elements and expand our knowledge on ultrafast laser beam focus control under tight focusing. For instance, a radially polarized laser beam focused with a high NA objective will exhibit a solid longitudinal electric field, which could even accelerate charged particles. These possibilities of focal spot polarization engineering can benefit both anisotropic circulars and nonlinear effects imprinting in glasses.

Exploring other glass systems – oriented crystallization

NGs are composed of nanopores or nanocrystals and amorphous phase separation. Compared to nanopores, nanocrystals process more properties, e.g., photoluminescence, high thermal stability, and second harmonic generation (SHG). For instance, the photoluminescence property of nanocrystals is useful in multi-dimentional information encoding and as microscale LEDs inside glass or solid. We also expect to point out that crystallographic structure is controllable by playing with the electromagnetic field's morphology in the beam's focal volume focused inside a transparent glass. For instance, concerning the precipitation of chiral crystals from suitable glasses, we expect to get racemic nanocrystal assemblies when the beam is axis-symmetric while getting enantiomeric excesses when the beam is not axis-symmetric. The latter may lead to the controlled generation of circular optical properties. At the same time, we expect the orientation of the induced optical properties to be controllable with the orientation of the vector properties of light (polarization, gradients of intensity and phase). Results in this direction will represent a step forward in understanding the non-linear interaction of light with glasses. In that way, we will abandon the classical view in elaboration chemistry that the laser is only an energy source for a new paradigm in which light can shape matter at the microscopic level in many ways.

Towards applications

Besides the fundamental interest in these NGs, the ability to control the birefringence slow/fast axis and even to induce circular optical properties lead to the engineering of unique integrated optical devices with 3D spatially varying birefringence

and refractive index changes. NGs have drawn attention to applications/fields, including birefringent optical devices, 3D geometric phase optics, optical data storage, microfluidic, structural health monitoring, and high-temperature sensing.

However, intrinsic parameters (period, rotation in 3D, nanoporosity) of femtosecond laser-induced NGs are still not fully controlled. We are convinced that those spatiotemporal beam distortions are new parameters in this process. An ongoing major problem is to quantitatively establish the role played by each one of the laser parameters. In addition, the light scattering losses and stress accumulation must be reduced. The ability to manipulate them would open possibilities for engineering the optical properties of a given material. As a result, we will be able to develop birefringent-based devices operating in a broad spectral range, including super-achromatic components, which are very important for applications ranging from polarimetry, spectroscopy, attosecond pulse generation, THz, military and domotics applications. Furthermore, this will allow us to control the phase and polarization of the light locally and effectively replace costly equipment such as spatial light modulators.

From one perspective, we propose to specifically apply this 3D manufacturing technique for the fabrication of compact and low-cost optical components in Vis and near-IR transparent materials like SiO2 glasses. Additionally, we plan to extend our results in the UV range and towards the IR, i.e. mid-IR, using heavy oxide glass materials and later in the far IR using non-oxide glasses like fluorides and chalcogenides. NG formation inside polymers is another exciting area that has yet to be explored. Indeed, in mid and far-IR instrumentation, there is a need for miniaturized, weight and low-cost optical systems for civil (domotics, smartphone, automobile) but also security and military applications (vehicle steering, survey, weapons guidance, unmasking, countermeasure identification). The constraints on the size and weight of optical systems are so demanding that traditional optical systems with a single optical axis are reaching their limits. Therefore, breakthroughs in optical design have been proposed to develop bio-inspired multichannel architectures and integrate optical functions using planar optical components. In addition, the possibility of making 3D direct shaping using femtosecond lasers enlarges the panel of optical functions we could encode into a small device.

From Industry perspective

From the very beginning, the industrial community working in FLDW has strongly been influenced by the development of ultrafast laser systems, which are, in fact, the critical part of the ultrafast laser direct writing setup. For example, the initial demonstration of waveguide writing was implemented after introducing Ti: Sapphire laser systems with high operation stability. Thus, future trends in this field should also be determined by the evolution of femtosecond laser systems. We can already see that high average power femtosecond laser systems operating at more than 100 W reached industrial-scale applications, where requirements are raised for quality and to increase the processing speed. Several commercial systems based on compact and reliable fibre

lasers were introduced for two-photon polymerization and glass processing. The flexibility of this technique in terms of materials and its ability to implement 3D geometries with subwavelength precision turned it into an ideal low-cost platform for rapid prototyping, which was explored in the fields of microfluidics and quantum optics. However, for industrial applications, implementing parallel processing or at least increasing the volumetric writing speed in ultrafast laser direct writing is crucial. Commonly, even nJ laser pulses can modify the material; however, conventional focusing techniques do not allow exploration of the whole power capacity of a laser system. Adding adaptive optics elements into the laser direct writing system has already demonstrated the potential of process parallelization, increasing writing speed (lineic, surface and volumetric), and reducing production cost.

We also propose to investigate the ability to induce high retardance of up l/2 at 5 mm but also writing NGs at high speeds (Typ. >10cm/s) to unlock the industrial potential of this direct writing technique. Recently, 'Type X', spherical or flattened nanopores NGs, can be imprinted in silica with high speed and ultralow loss in high transmission, promising for the polarization multiplexed data storage with high capacity and ultralong lifetime even at high temperature. For instance, 735 GB per 127 mm disk data capacity can be in 72 kB/s writing speed. This writing speed can be achieved as several MB/s using a multi-channel experimental setup.

APPENDIX – EXPERIMENTAL DETAILS

Appendix 1- Femtosecond laser direct writing (FLDW) system

We mostly used a femtosecond fibre laser writing system for the work described in this thesis. The femtosecond fibre laser system used for the fabrication of our samples in bulk fused silica consists of a directly diode-pumped Ytterbium fibre laser (Satsuma HP from Amplitude Systèmes), with a centre wavelength of 1030 nm and variable repetition rates from 10 kHz to 2 MHz. The key characteristics of this system are summarized in Fig. A - 1. It is equipped with a pulse picker (acoustic-optic modulator), which reduces the repetition rate to a single pulse if needed. The average power is fixed to 10 W, which allows reaching up to 73 to 25 J/pulse at 400 kHz or 10 J/pulse at 1 MHz.

	Laser Parameters		Unit	Target		Measurement	
				400 kHz	2000 kHz	400 kHz	2000 kHz
IR	Energy per pulse		*µJ*	≥ 25	≥ 5	26.5	27
	Average power		*W*	≥ 10	≥ 10	11.1	11.3
	Center wavelength		nm	1030 +/- 5		1032.1	1032.2
	Bandwidth FWHM			≤ 10		8.6	8.9
	Pulse duration		*fs*	< 500		220	240
	Pulse energy over 12h	*Average*	*µJ*	> 25	> 5	27.8	-
		RMS	*%*	< 2		0.08	
	Polarization ratio		-	> 100:1		625:1	
	M^2	M^2x	-	< 1.30		1.10	
		M^2y				1.07	
	Beam diameter	W_0x	*mm*	2 +/- 0.5		1.53	
		W_0y				1.50	
	Beam ellipticity		*%*	< 13%		1.9	
	Astigmatism			< 50%		27.8	
	Waist ellipticity			< 13%		0.1	

Fig. A - 1 Certificate of Conformance (CoC) of the Satsuma HP Laser used in this PhD work. Graph adapted from our group work in thesis [225].

After amplification and compression, the pulse width is typ. 250 fs full width at half maximum (FWHM). Note that the intra-cavity distance between the chirped gratings is adjustable using a motorized translation stage to optimize the compression of the pulses according to the repetition rate provided by the laser. An example of an autocorrelation function measurement performed on typical 1030nm output pulses is shown in Fig. A - 2, where the experimental data was fitted to a Lorentzian function in order to determine an autocorrelation FWHM value of 341 fs. This value corresponds to an absolute pulse width of 221 fs in optimal conditions and before the focusing lens. The spatial chirp (wavelength vs position) was measured around 0.54nm/mm along the x-axis and 0.02 nm/mm along the y-axis.

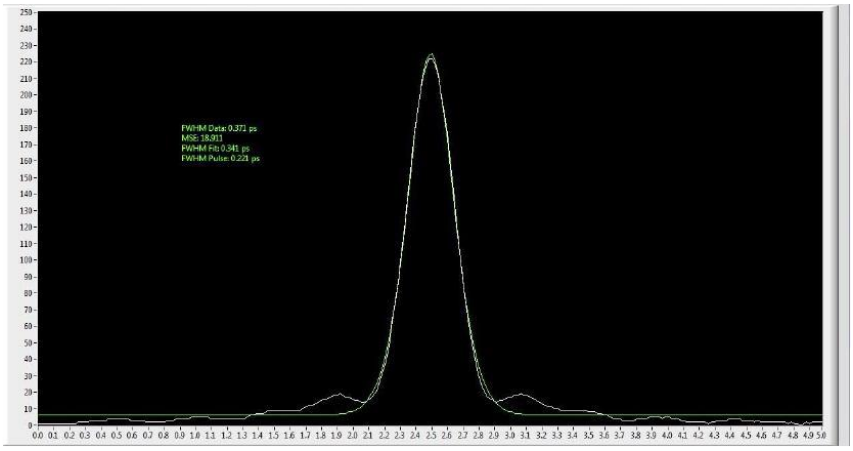

Fig. A - 2 Measurements of the laser temporal pulse profile using an optical autocorrelator (x axis is expressed in ps, y axis is a power in arbitrary units). Graph adapted from our group work in thesis [225].

The laser is linearly polarized horizontally (parallel to the optical table) and perpendicular to the z-axis (Fig. A - 3). The computer-controlled half waveplate (Newport SR50CC rotation stage) and the Glan-Laser polarizer provide a way of tuning the beam power while guaranteeing the linear polarization of the laser, which is fixed horizontally at this point (along the x-axis and thus parallel the ideal plane of the laser compressor). The laser path can then be selected between two alternatives, the acoustic-optic modulator (AOM) path and the non-AOM path.

The AOM is also computer-controlled by a digital RF driver signal and is optimized to create one first-order diffraction beam with an adjustable diffraction efficiency from 0 up to 100% of the total power of the input beam. In some cases, this configuration serves as a fast on/off switch for the laser beam and can reliably operate at frequencies up to 2 MHz with the current setup. At this point in the fabrication setup of Fig. A - 3, the laser wavelength is 1030 nm, and the pulse width is typ. 250 fs with a variable repetition rate ranging from 10 kHz to 2 MHz and the possibility of AOM modulation (typ. 100 kHz and down to single pulse) and an additional shutter for synchronization.

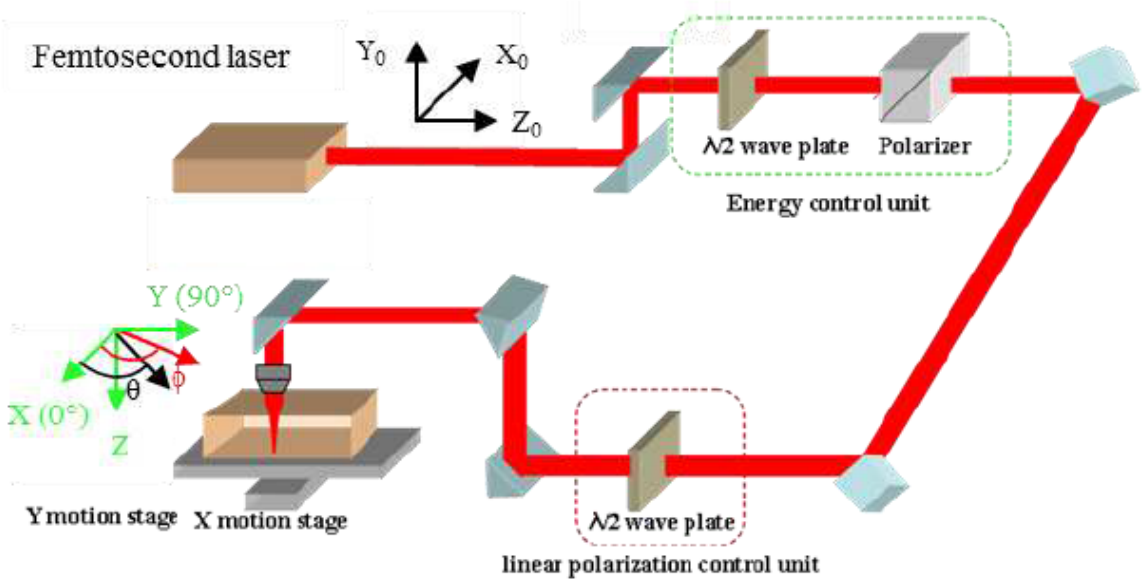

Fig. A - 3 Schematic diagram of the femtosecond laser direct writing (FLDW) setup used at ICMMO laboratory. Graph adapted from our group work in thesis [225].

The laser beam is then aligned inside the target delivery system described in

Fig. A - 4 and focused into the silica glass sample that is mounted in the computer-controlled motion XY-stages (one-XY200HA from Newport) having a minimum resolution of 50 nm, a bidirectional repeatability of 90 nm and a speed up to 200mm/s. The computer-controlled Zstage (Newport UTS100CC) positions the laser spot typically at 300 µm below the surface of the glass substrate. Aspheric lenses with numerical apertures (NAs) ranging from 0.16 NA to 0.65 NA were used to create spot sizes with diameters ranging from 4.5 µm to 1.1 µm (e.g. 1.3 µm for 0.55 NA). The diameter is calculated at $1/e^2$ of the maximum intensity $\omega_0 = \frac{M^2\lambda}{\pi N_A}$, where ω_0 is the spot radius for the infrared 1030 nm wavelength, considering a typical beam quality of $M^2<1.1$, and assuming a Gaussian distribution.
The additional motorized half-waveplate pictured in the diagram of

Fig. A - 4 further permits the control of any linear polarization state in between at the sample position. This waveplate is mounted on a fast belt-driven rotation stage (Newport URB100CC) with a typical speed of 720°/s. Using this freedom to control the laser polarization and the laser power together with the XYZ motion control, it is possible to have the polarization of the laser beam oriented parallel or perpendicular, or even oriented at an arbitrary azimuth with the laser scanning direction in the glass sample.

Fig. A - 4 illustrates that the laser is focused into a fused silica sample, and a laser-written line is formed by scanning the sample through the laser spot. The geometry shown in

Fig. A - 4 also illustrates the orientation of the birefringence proper polarization axis of the waveguide modes, which are formed by the orthogonal directions: Vertical, V, and Horizontal, H, defined with respect to the optical table.

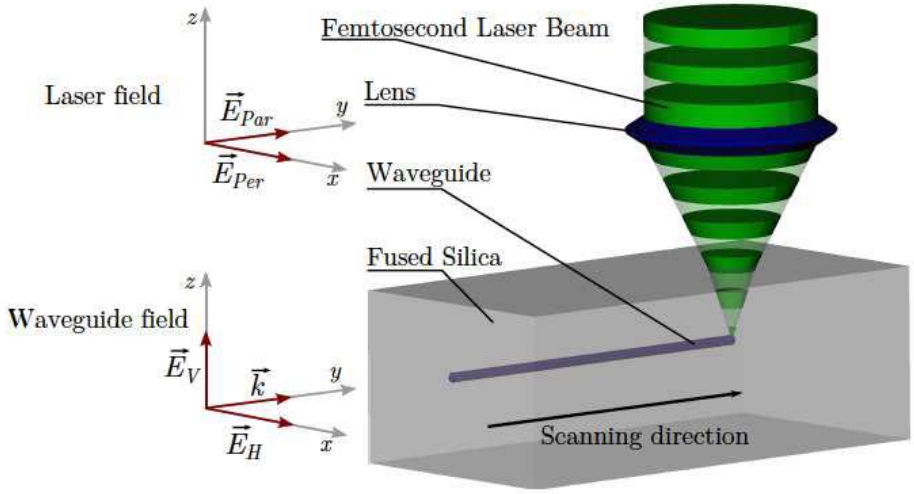

Fig. A - 4 Schematic diagram of the laser lines (waveguide like) fabrication where E_{par} and E_{per} represent the parallel and perpendicular polarizations of the writing laser. The scanning direction was fixed along Y-axis. For E_{par} (Yy writing configuration), we have the nanogratings form birefringence optical fast axis along y whereas slow axis is along x. For E_{per} case (Yx writing configuration), we have optical fast axis along x whereas slow axis is along y. Graph adapted from Ref. [226].

All motorized components are connected to a computer via an XPS - 8-axis controller from Newport. The control interface is made from the GOL3D software, the schematic description of which is shown in Fig. A - 5. This software is designed to centralize the control of the assembly elements and control the translation plates where the sample is positioned. This makes it possible to perform complex writing paths at a constant speed, such as a spiral or sets of objects in 3D. The write speed is an important parameter to consider because it influences the pulse accumulation on the laser trace. It is, therefore, necessary to remain identical throughout the trajectory by optimizing the writing algorithm and the writing synchronization with the shutter.

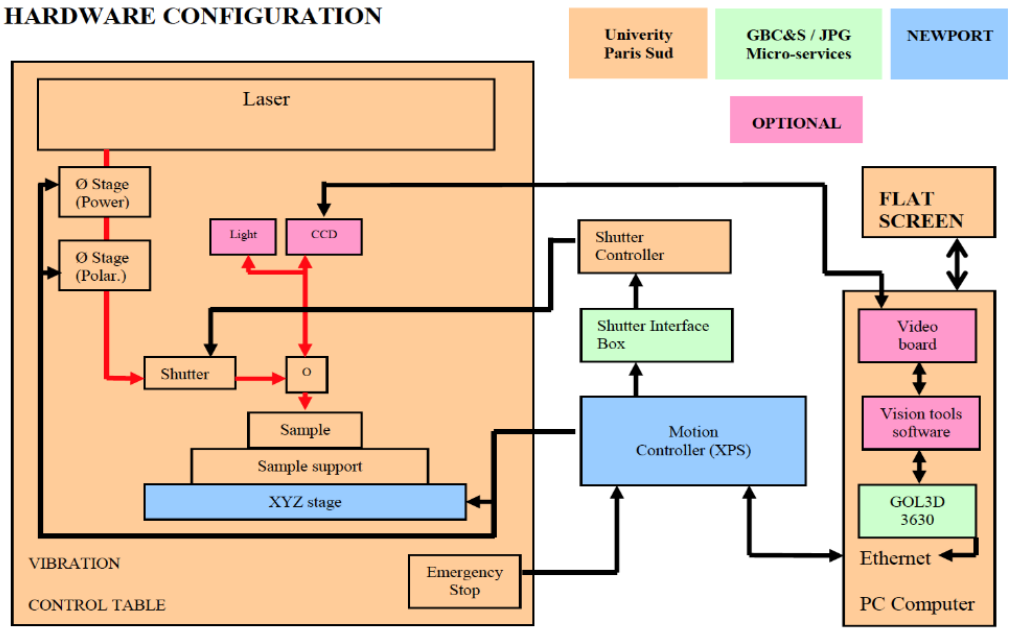

Fig. A - 5 Schematic diagram of the hardware configuration related to our direct writing software "GOL3D". Graph adapted from our group work in thesis [225].

Appendix 2- The de Sénarmont Compensator

This compensator coupled a high-precision quarter waveplate with a 180 rotating analyzer to provide retardation measurements in the visible range. As described by the Olympus resource centres (Polarized Light Microscopy - The de Sénarmont Compensator | Olympus LS (olympus-lifescience.com)), the principle behind the "de Sénarmont" compensation technique rests on the fact that the elliptically (or circularly) polarized light electric vector emerging from the specimen is superimposed upon the circular polarization vector introduced by the quarter waveplate to yield plane (linearly) polarized light having a vibration azimuth different from that of the polarizer. The effect occurs because the quarter waveplate produces linearly polarized light from elliptically or circularly polarized light that is incident on the crystal surface. The azimuth of the linear polarized light emerging from the compensator is a direct function of the optical path difference induced by the specimen. By rotating the analyzer until the specimen is extinct (dark), the azimuth of the vibration produced by the compensator can be ascertained along with the optical path difference introduced by the specimen. The rotation angle of the analyzer at extinction is equal to one-half of the full phase shift between the orthogonal (ordinary and extraordinary) wavefronts passing through the specimen. Therefore, the relative retardation (in nm) is described by the following equation (for monochromatic light at 546 nm): $R = (546 \times \theta)/180$, where θ is the rotation angle of the analyzer and R is the relative retardation or optical path difference.

Appendix 3- The datasheet of the commercial glasses

7059: 7059 / 7059F | Low alkali barium-borosilicate glass (pgo-online.com)

AF32: &AF 32® eco | Alkali-free glass for semiconductor & MEMS (pgo-online.com)

BK7: N-BK7 | Optical borosilicate-crown glass from SCHOTT | BK 7 (pgo-online.com)

ULE : ULE® Ultra Low Expansion Titanium Silicate glass (pgo-online.com)

Eagle XG : EAGLE XG® | Alkali-free boro-alumino-silicate glass (pgo-online.com)

Borofloat 33 : BOROFLOAT® 33 | Borosilicate glass from SCHOTT (pgo-online.com)

Sodalime (Microscope slide) :Technical Information - Paul Marienfeld (marienfeld-superior.com)

Suprasil CG : Heraeus Conamic | Heraeus Conamic - Suprasil® (heraeus-conamic.com)

PUBLICATION LIST

Journal papers

1. Xie Q., Cavillon M., Poumellec B., Lancry M. Lifespan prediction procedure of volume nanogratings imprinted by femtosecond laser in optical glasses. Ceramics International. **2024**. https://doi.org/10.1016/j.ceramint.2024.03.153.
2. Xie, Q., Shchedrina, N., Cavillon, M., Poumellec, B., Lancry, M. Nanoscale investigations of femtosecond laser induced nanogratings in optical glasses, Nanoscale Adv. **2024**, 6, 489-498. http://dx.doi.org/10.1039/D3NA00748K
3. Yao, H., Xie, Q., Cavillon, M., Dai, Y., Lancry, M. Materials roadmap for inscription of nanogratings inside transparent dielectrics using ultrafast lasers. Prog. Mater. Sci. **2024**, *142*, 101226. https://doi.org/https://doi.org/10.1016/j.pmatsci.2023.101226
4. Xie, Q., Cavillon, M., Poumellec, B., Lancry, M. Upper temperature limit for nanograting survival in oxide glasses. *Appl. Opt.* **2023**, *62*, 6794-6801. https://dx.doi.org/10.1364/AO.496351
5. Yao, H., Xie, Q., Cavillon, M., Neuville, D. R., Pugliese, D., Janner, D., Dai, Y., Poumellec, B., Lancry, M. Volume nanogratings inscribed by ultrafast IR laser in alumino-borosilicate glasses. *Opt. Express* **2023**, *31*. https://dx.doi.org/10.1364/oe.488249
6. Xie, Q., Cavillon, M., Pugliese, D., Janner, D., Poumellec, B., Lancry, M. On the Formation of Nanogratings in Commercial Oxide Glasses by Femtosecond Laser Direct Writing. *Nanomaterials* **2022**, *12*, 2986. https://dx.doi.org/10.3390/nano12172986
7. Xie, Q.; Cavillon, M.; Poumellec, B.; Pugliese, D.; Janner, D.; Lancry, M. Application and validation of a viscosity approach to the existence of nanogratings in oxide glasses. *Opt. Mater.* **2022**, *130*, 112576.

https://dx.doi.org/10.1016/j.optmat.2022.112576

International conference proceedings

1. Xie, Q., Cavillon, M., Poumellec, B., Pugliese, D., Janner, D., Lancry, M. On the existence of nanogratings in commercial oxide glasses. In Proceedings of the Optica Advanced Photonics Congress 2022, Maastricht, Limburg, 2022/07/24, **2022**; p. BM3A.2. ISBN: 978-1-957171-16-6. https://doi.org/10.1364/BGPPM.2022.BM3A.2
2. Cavillon, M., Xie, Q., Ktafi, I., Kong, J., Ari, J., Poumellec, B., Shimotsuma, Y., Hawkins, T., Ballato, J., Lancry, M. (**2024**). *Thermal stability of nanogratings in oxide glasses: a route to overcome silica* (Vol. 12875). SPIE. https://doi.org/10.1117/12.2691346
3. Xie, Q., Cavillon, M., Lancry, M. ICG Annual Meeting **2023** Abstract, 'On the erasure of femtosecond laser imprinted nanogratings in optical glasses'.

International conferences

1. Optica Advanced Photonics Congress **2022**, Bragg Gratings, Photosensitivity and Poling in Glass Waveguides and Materials 2022, Maastricht, Limburg Netherlands, 24–28 July 2022, oral presentation, On the existence of nanogratings in commercial oxide glasses (optica.org)
2. ICG Annual Meeting **2023**, 12-15 November 2023, Hangzhou, China, oral presentation, 'On the erasure of femtosecond laser imprinted nanogratings in optical glasses'.

Summer school

14th ICG Montpellier Summer School **2023**, 2-7 July 2023, Montpellier.

REFERENCES

1. A. Forbes, "Structured Light from Lasers," Laser Photonics Rev. **13**, 1900140 (2019).
2. M. Sakakura, Y. Lei, L. Wang, Y. H. Yu, and P. G. Kazansky, "Ultralow-loss geometric phase and polarization shaping by ultrafast laser writing in silica glass," Light Sci. Appl. **9**, 15 (2020).
3. G. Berglund, A. Wisniowiecki, J. Gawedzinski, B. Applegate, and T. S. Tkaczyk, "Additive manufacturing for the development of optical/photonic systems and components," Optica **9**, 623-638 (2022).
4. J. Carcreff, F. Cheviré, E. Galdo, R. Lebullenger, A. Gautier, J.-L. Adam, D. Le Coq, L. Brilland, R. Chahal, G. Renversez, and J. Troles, *Elaboration of chalcogenide*

microstructured optical fibers preform by 3D additive manufacturing, SPIE OPTO (SPIE, 2021), Vol. 11682.
5. E. Baudet, Y. Ledemi, P. Larochelle, S. Morency, and Y. Messaddeq, "3D-printing of arsenic sulfide chalcogenide glasses," Opt. Mater. Express **9**, 2307-2317 (2019).
6. R. Stoian and J.-P. Colombier, "Advances in ultrafast laser structuring of materials at the nanoscale," Nanophotonics **9**, 4665-4688 (2020).
7. R. Stoian, "Volume photoinscription of glasses: three-dimensional micro- and nanostructuring with ultrashort laser pulses," Appl. Phys. A **126**, 438 (2020).
8. R. Osellame, G. Cerullo, and R. Ramponi, *Femtosecond laser micromachining: photonic and microfluidic devices in transparent materials* (Springer, 2012), Vol. 123.
9. H. Yao, Q. Xie, M. Cavillon, Y. Dai, and M. Lancry, "Materials roadmap for inscription of nanogratings inside transparent dielectrics using ultrafast lasers," Prog. Mater Sci. **142**, 101226 (2024).
10. R. Drevinskas, M. Beresna, J. Zhang, A. G. Kazanskii, and P. G. Kazansky, "Ultrafast Laser-Induced Metasurfaces for Geometric Phase Manipulation," Adv. Opt. Mater. **5**, 1600575 (2017).
11. A. Arbabi, Y. Horie, M. Bagheri, and A. Faraon, "Dielectric metasurfaces for complete control of phase and polarization with subwavelength spatial resolution and high transmission," Nature Nanotechnology **10**, 937-943 (2015).
12. M. Lancry, R. Desmarchelier, K. Cook, B. Poumellec, and J. Canning, "Compact Birefringent Waveplates Photo-Induced in Silica by Femtosecond Laser," Micromachines **5**, 825-838 (2014).
13. Y. Shimotsuma, P. G. Kazansky, J. R. Qiu, and K. Hirao, "Self-organized nanogratings in glass irradiated by ultrashort light pulses," Phys. Rev. Lett. **91**, 247405 (2003).
14. Q. Xie, N. Shchedrina, M. Cavillon, B. Poumellec, and M. Lancry, "Nanoscale investigations of femtosecond laser induced nanogratings in optical glasses," Nanoscale Advances (2024).
15. M. Lancry, B. Poumellec, J. Canning, K. Cook, J.-C. Poulin, and F. Brisset, "Ultrafast nanoporous silica formation driven by femtosecond laser irradiation," Laser and Photonics Reviews **7**, 953-962 (2013).
16. Q. Xie, M. Cavillon, B. Poumellec, D. Pugliese, D. Janner, and M. Lancry, "Application and validation of a viscosity approach to the existence of nanogratings in oxide glasses," Opt. Mater. **130**, 112576 (2022).
17. A. Rudenko, J.-P. Colombier, and T. E. Itina, "From random inhomogeneities to periodic nanostructures induced in bulk silica by ultrashort laser," Phys. Rev. B **93**, 075427 (2016).
18. E. Bricchi and P. G. Kazansky, "Extraordinary stability of anisotropic femtosecond direct-written structures embedded in silica glass," Appl. Phys. Lett. **88**(2006).
19. Q. Xie, M. Cavillon, B. Poumellec, and M. Lancry, "Upper temperature limit for nanograting survival in oxide glasses," Appl. Opt. **62**, 6794-6801 (2023).
20. B. Poumellec, M. Lancry, A. Chahid-Erraji, and P. Kazansky, "Modification

thresholds in femtosecond laser processing of pure silica: review of dependencies on laser parameters [Invited]," Opt. Mater. Express **1**, 766-782 (2011).
21. Q. Xie, M. Cavillon, D. Pugliese, D. Janner, B. Poumellec, and M. Lancry, "On the Formation of Nanogratings in Commercial Oxide Glasses by Femtosecond Laser Direct Writing," Nanomaterials **12**, 2986 (2022).
22. H. Yao, Q. Xie, M. Cavillon, D. R. Neuville, D. Pugliese, D. Janner, Y. Dai, B. Poumellec, and M. Lancry, "Volume nanogratings inscribed by ultrafast IR laser in alumino-borosilicate glasses," Opt. Express **31**(2023).
23. Q. Xie, M. Cavillon, B. Poumellec, and M. Lancry, "Lifespan prediction procedure of volume nanogratings imprinted by femtosecond laser in optical glasses," Ceram. Int. **50**, 20303-20312 (2024).
24. G. W. Arnold and W. D. Compton, "Radiation effects in silica at low temperatures.," Phys. Rev. **116**, 802-811 (1959).
25. W. Primak and R. Kampwirth, "The radiation compaction of vitreous silica.," J. Appl. Phys. **39**, 5651-5658 (1968).
26. M. Rajaram, T.-E. Tsai, and E. J. Friebele, "Radiation-Induced Surface Deformation in Low-Thermal-Expansion Glasses and Glass-Ceramics," Advanced Ceramic Materials **3**, 598-600 (1988).
27. D. Barbier, M. Green, and S. J. Madden, "Waveguide fabrication for integrated optics by electron beam irradiation of silica.," J. Lightwave Technol. **9**, 715-720 (1991).
28. T. A. Dellin, D. A. Tichenor, and E. H. Barsis, "Volume, index-of-refraction, and stress changes in electron-irradiation vitreous silica," Applied Physics **48**, 1131 (1977).
29. R. R. A. Syms, T. J. Tate, and M. F. Grant, "Reduction of propagation loss in silica-on-silicon channel waveguides formed by electron beam irradiation," Electronics Letters **30**, 1480-1481 (1994).
30. L. Lichtenstein, M. Heyde, and H.-J. Freund, "Atomic Arrangement in Two-Dimensional Silica: From Crystalline to Vitreous Structures," The Journal of Physical Chemistry C **116**, 20426-20432 (2012).
31. B. E. Warren, "Summary of work on atomic arrangement in glass," American Ceramic Society **24**, 256-261 (1941).
32. F. Liebau, "Structural chemistry of silicates," (1985).
33. A. C. Wright, "The structure of vitreous silica: what have we learned from 60 years of diffraction studies?," Journal of Non-Crystalline Solids **179**, 84-115 (1994).
34. M. Lancry, E. Régnier, and B. Poumellec, "Fictive temperature in silica-based glasses and its application to optical fiber manufacturing," Prog. Mater Sci. **57**, 63-94 (2012).
35. J. Arndt, "Densification of glasses of the system TiO sub 2-SiO sub 2 by very high-static pressures," Phys. Chem. Glasses **24**, 104-110 (1983).
36. S. M. Stishov and S. V. Popova, "New dense polymorphic modification of silica," Geokhimiya **10**, 837-839 (1961).

37. D. L. Griscom, "The natures of point defects in amorphous silicon dioxide," in *Defects in SiO2 and Related Dielectrics: Science and Technology*, L. S. a. D. L. G. G. Pacchioni, ed. (2000), pp. 117-159.
38. D. L. Griscom, "Optical Properties and Structure of Defects in Silica Glass: Optical Materials," J. Ceram. Soc. Jpn. **99**, 923-942 (1991).
39. J. Garapon, "Etude théorique des défauts déficients en oxygène dans la silice pure ou dopée.," Docteur en Sciences (Université de Paris Sud, 2001).
40. L. N. Skuja, "Optically active oxygen-deficiency-related centers in amorphous silicon dioxide.," Journal of Non-Crystalline Solids **239**, 16-48 (1998).
41. L. Skuja, *Optical properties of defects in silica,* Pacchioni, G., Skuja, L., Griscom, D. ed., Defect in SiO2 and related dielectrics : Science and Technology (Kluwer Academic, Dirdrecht, Netherlands, 2000).
42. A. N. Trukhin, H. J. Fitting, T. Barfels, and A. von Czarnowski, "Cathodoluminescence and IR absorption of oxygen deficient silica - influence of hydrogen treatment.," Radiation effects and defects in solids. **149**, 61-68 (1999).
43. W. H. Zachariasen, "THE ATOMIC ARRANGEMENT IN GLASS," Journal of the American Chemical Society **54**, 3841-3851 (1932).
44. B. E. Warren, "X-Ray Diffraction of Vitreous Silica," Zeitschrift für Kristallographie - Crystalline Materials **86**, 349-358 (1933).
45. C. Calahoo and L. Wondraczek, "Ionic glasses: Structure, properties and classification," Journal of Non-Crystalline Solids: X **8**, 100054 (2020).
46. A. K. Varshneya and J. C. Mauro, "Chapter 9 - The viscosity of glass," in *Fundamentals of Inorganic Glasses (Third Edition)*, A. K. Varshneya and J. C. Mauro, eds. (Elsevier, 2019), pp. 215-251.
47. U. Fotheringham, "Viscosity of Glass and Glass-Forming Melts," in *Springer Handbook of Glass*, J. D. Musgraves, J. Hu, and L. Calvez, eds. (Springer International Publishing, Cham, 2019), pp. 79-112.
48. Y. I. Frenkel, *Kinetic Theory of Liquids* (Oxford University Press, Oxford UK, 1946).
49. G. S. Fulcher, "ANALYSIS OF RECENT MEASUREMENTS OF THE VISCOSITY OF GLASSES," J. Am. Ceram. Soc. **8**, 339-355 (1925).
50. H. Vogel, "The law of the relation between the viscosity of liquids and the temperature," Phys. Z **22**, 645-646 (1921).
51. G. Tammann and W. Hesse, "Die Abhängigkeit der Viscosität von der Temperatur bie unterkühlten Flüssigkeiten," Z. Anorg. Allg. Chem. **156**, 245-257 (1926).
52. G. Adam and J. H. Gibbs, "On the Temperature Dependence of Cooperative Relaxation Properties in Glass - Forming Liquids," The Journal of Chemical Physics **43**, 139-146 (1965).
53. R. W. Boyd, *Nonlinear optics* (Academic Press, 3 edition (April 11, 2008), 1992).
54. Y. R. Shen, *The principles of nonlinear optics* (Wiley, 1984).
55. G. P. Agrawal, ed., *Non-linear effects in optical fibers.* (Academic Press, San Diego., 1989).

56. Y. R. Shen, "Recent Advances in nonlinear optics," Review of modern physics **48**, 1-32 (1976).
57. J. Toulouse, "Optical nonlinearities in fibers: review, recent examples, and systems applications," Lightwave Technology, Journal of **23**, 3625-3641 (2005).
58. L. Sudrie, "Propagation non-linéaire des impulsions laser femtosecondes dans la silice.," Docteur en Sciences, Optique (Université de Paris Sud XI Orsay, 2002).
59. A. Čerkauskaitė, "Ultrafast laser nanostructuring for photonics and information technology," (UNIVERSITY OF SOUTHAMPTON, 2018).
60. A. Couairon and A. Mysyrowicz, "Femtosecond filamentation in transparent media," Physics reports **441**, 47-189 (2007).
61. S. S. Mao, F. Quere, S. Guizard, X. Mao, R. E. Russo, G. Petite, and P. Martin, "Dynamics of femtosecond laser interactions with dielectrics," Appl. Phys. A-Mater. **79**, 1695-1709 (2004).
62. C. Schaffer, J. García, and E. Mazur, "Bulk heating of transparent materials using a high-repetition-rate femtosecond laser," Applied Physics A: Materials Science & Processing **76**, 351-354 (2003).
63. S. M. Eaton, H. Zhang, P. R. Herman, F. Yoshino, L. Shah, J. Bovatsek, and A. Y. Arai, "Heat accumulation effects in femtosecond laser-written waveguides with variable repetition rate.," Opt. Express **13**, 4708-4716 (2005).
64. Y. Bellouard, A. Champion, B. McMillen, S. Mukherjee, R. R. Thomson, C. Pépin, P. Gillet, and Y. Cheng, "Stress-state manipulation in fused silica via femtosecond laser irradiation," Optica **3**, 1285-1293 (2016).
65. A. Champion, M. Beresna, P. Kazansky, and Y. Bellouard, "Stress distribution around femtosecond laser affected zones: effect of nanogratings orientation," Opt. Express **21**, 24942-24951 (2013).
66. F. Dürr, H. Limberger, R. Salathe´, F. Hindle, M. Douay, E. Fertein, and C. Przygodzki, "Tomographic measurement of femtosecond-laser induced stress changes in optical fibers," Appl. Phys. Lett. **84**, 4983-4985 (2004).
67. V. Bhardwaj, P. Corkum, D. Rayner, C. Hnatovsky, E. Simova, and R. Taylor, "Stress in femtosecond-laser-written waveguides in fused silica," Opt. Lett. **29**, 1312-1314 (2004).
68. B. Poumellec, L. Sudrie, M. Franco, B. Prade, and A. Mysyrowicz, "Femtosecond laser irradiation stress induced in pure silica," Opt. Express **11**, 1070-1079 (2003).
69. S. Guizard, P. Martin, G. Petite, P. d'Oliveira, and P. Meynadier, "Time-resolved study of laser-induced colour centres in SiO_2," J. Phys.: Condens. Matter **8**, 1281 (1996).
70. K. Mishchik, C. d'Amico, P. K. Velpula, C. Mauclair, A. Boukenter, Y. Ouerdane, and R. Stoian, "Ultrafast laser induced electronic and structural modifications in bulk fused silica," J. Appl. Phys. **114**, 133502 (2013).
71. K. Mishchik, "Ultrafast laser-induced modification of optical glasses: a spectroscopy insight into the microscopic mechanisms," 2012).
72. K. Itoh, W. Watanabe, S. Nolte, and C. B. Schaffer, "Ultrafast processes for bulk modification of transparent materials.," MRS Bull. **31**, 620-625 (2006).

73. C. B. Schaffer, A. Brodeur, and M. E., "Laser-induced breakdown and damage in bulk transparent materials induced by tighly focused femtosecond laser pulses.," Measurement Science Technology **12**, 1784-1794 (2001).
74. R. Stoian, "Volume photoinscription of glasses: three-dimensional micro-and nanostructuring with ultrashort laser pulses," Applied physics. A, Materials science & processing **126**(2020).
75. A. Rudenko, J.-P. Colombier, and T. E. Itina, "Nanopore-mediated ultrashort laser-induced formation and erasure of volume nanogratings in glass," Physical Chemistry Chemical Physics **20**, 5887-5899 (2018).
76. F. Quéré, S. Guizard, and P. Martin, "Time-resolved study of laser-induced breakdown in dielectrics," EPL (Europhysics Letters) **56**, 138 (2001).
77. M. Lancry, N. Groothoff, B. Poumellec, S. Guizard, N. Fedorov, and J. Canning, "Time-resolved plasma measurements in Ge-doped silica exposed to infrared femtosecond laser," Physical Review B **84**, 245103 (2011).
78. A. Mouskeftaras, S. Guizard, N. Fedorov, and S. Klimentov, "Mechanisms of femtosecond laser ablation of dielectrics revealed by double pump–probe experiment," Appl. Phys. A **110**, 709-715 (2013).
79. M. Lenzner, J. Krüger, S. Sartania, Z. Cheng, C. Spielmann, G. Mourou, W. Kautek, and F. Krausz, "Femtosecond optical breakdown in dielectrics," Phys. Rev. Lett. **80**, 4076 (1998).
80. B. C. Stuart, M. D. Feit, S. Herman, A. Rubenchik, B. Shore, and M. Perry, "Nanosecond-to-femtosecond laser-induced breakdown in dielectrics," Physical review B **53**, 1749 (1996).
81. T. E. Itina and N. Shcheblanov, "Electronic excitation in femtosecond laser interactions with wide-band-gap materials," Appl. Phys. A **98**, 769-775 (2010).
82. P. Rajeev, M. Gertsvolf, P. Corkum, and D. Rayner, "Field dependent avalanche ionization rates in dielectrics," Phys. Rev. Lett. **102**, 83001 (2009).
83. A. Wasiela, G. Ascarelli, and Y. Merle d'Aubigné, "Détection optique de la résonance électronique de l'exciton autopiégé dans les halogénures alcalins ; observation d'un croisement de niveaux," J. Phys. France **35**, 466 (1974).
84. K. Miura, J. Qiu, H. Inouye, T. Mitsuyu, and K. Hirao, "Photowritten optical waveguides in various glasses with ultrashort pulse laser," Appl. Phys. Lett. **71**, 3329-3331 (1997).
85. L. Sudrie, M. Franco, B. Prade, and A. Mysyrowicz, "Writing of permanent birefringent microlayers in bulk fused silica with femtosecond laser pulses," Opt. Commun. **171**, 279-284 (1999).
86. C. Hnatovsky, J. R. Taylor, P. P. Rajeev, E. Simova, V. R. Bhardwaj, D. M. Rayner, and P. B. Corkum, "Pulse duration dependence of femtosecond-laser fabricated nanogratings in fused silica.," Appl. Phys. Lett. **87**, 14104-14101/14103 (2005).
87. S. Juodkazis, K. Nishimura, S. Tanaka, H. Misawa, E. G. Gamaly, B. Luther-Davies, L. Hallo, P. Nicolai, and V. T. Tikhonchuk, "Laser-induced microexplosion confined in the bulk of a sapphire crystal: evidence of multimegabar pressures," Phys. Rev. Lett. **96**, 166101-166101 (2006).

88. J. W. Chan, T. R. Huser, S. H. Risbud, J. S. Hayden, and D. M. Krol, "Waveguide fabrication in phosphate glasses using femtosecond laser pulses," Appl. Phys. Lett. **82**, 2371-2373 (2003).
89. J. Siegel, J. Fernández-Navarro, A. García-Navarro, V. Diez-Blanco, O. Sanz, J. Solis, F. Vega, and J. Armengol, "Waveguide structures in heavy metal oxide glass written with femtosecond laser pulses above the critical self-focusing threshold," Appl. Phys. Lett. **86**, 121109 (2005).
90. F. Vega, J. Armengol, V. Diez-Blanco, J. Siegel, J. Solis, B. Barcones, A. Perez-Rodriguez, and P. Loza-Alvarez, "Mechanisms of refractive index modification during femtosecond laser writing of waveguides in alkaline lead-oxide silicate glass," Appl. Phys. Lett. **87**, 021109 (2005).
91. A. Zoubir, C. Lopez, M. Richardson, and K. Richardson, "Femtosecond laser fabrication of tubular waveguides in poly(methyl methacrylate)," Opt. Lett. **29**, 1840-1842 (2004).
92. H. S. Carslaw and J. C. Jaeger, *Conduction of heat in solids* (Clarendon press, 1992).
93. C. B. Schäffer, "Interaction of femtosecond laser pulses with transparent materials," Ph.D. Thesis (Harvard, 2001).
94. M. Lenzner, J. Krüger, W. Kautek, and F. Krausz, "Incubation of laser ablation in fused silica with 5-fs pulses," Appl. Phys. A **69**, 465-466 (1999).
95. D. Ashkenasi, M. Lorenz, R. Stoian, and A. Rosenfeld, "Surface damage threshold and structuring of dielectrics using femtosecond laser pulses: the role of incubation," Appl. Surf. Sci. **150**, 101-106 (1999).
96. R. Stoian, *Investigations of the dynamics of material removal in ultrashort pulsed laser ablation of dielectrics* (2000).
97. A. M. Streltsov and N. F. Borrelli, "Study of femtosecond-laser-written waveguides in glasses," J. Opt. Soc. Am. B **19**, 2496-2504 (2002).
98. F. Zimmermann, M. Lancry, A. Plech, S. Richter, T. Ullsperger, B. Poumellec, A. Tünnermann, and S. Nolte, "Ultrashort Pulse Laser Processing of Silica at High Repetition Rates—from Network Change to Residual Strain," Int. J. Appl. Glass Sci. (2016).
99. T. Yoshino, Y. Ozeki, M. Matsumoto, and K. Itoh, "In situ micro-raman investigation of spatio-temporal evolution of heat in ultrafast laser microprocessing of glass," Jpn. J. Appl. Phys. **51**, 102403 (2012).
100. L. Shah, A. Arai, S. Eaton, and P. Herman, "Waveguide writing in fused silica with a femtosecond fiber laser at 522 nm and 1 MHz repetition rate," Opt. Express **13**, 1999-2006 (2005).
101. R. Osellame, N. Chiodo, V. Maselli, A. Yin, M. Zavelani-Rossi, G. Cerullo, P. Laporta, L. Aiello, S. De Nicola, P. Ferraro, A. Finizio, and G. Pierattini, "Optical properties of waveguides written by a 26 MHz stretched cavity Ti:sapphire femtosecond oscillator," Opt. Express **13**, 612-620 (2005).
102. M. Royon, E. Marin, S. Girard, A. Boukenter, Y. Ouerdane, and R. Stoian, "X-ray preconditioning for enhancing refractive index contrast in femtosecond laser photoinscription of embedded waveguides in pure silica," Opt. Mater. Express **9**,

65-74 (2019).
103. M. Lancry and B. Poumellec, "UV laser processing and multiphoton absorption processes in optical telecommunication fiber materials," Physics Reports **523**, 207-229 (2013).
104. E. Bricchi and P. G. Kazansky, "Extraordinary stability of anisotropic femtosecond direct-written structures embedded in silica glass," Appl. Phys. Lett. **88**, 2-4 (2006).
105. D. Grobnic, C. W. Smelser, S. J. Mihailov, and R. B. Walker, "Long-term thermal stability tests at 1000°C of silica fibre Bragg gratings made with ultrafast laser radiation," Meas. Sci. Technol. **17**, 1009 (2006).
106. E. Bricchi, B. G. Klappauf, and P. G. Kazansky, "Form birefringence and negative index change created by femtosecond direct writing in transparent materials," Opt. Lett. **29**, 119-121 (2004).
107. E. Bricchi, J. D. Mills, P. G. Kazansky, and B. G. Klappauf, "Birefringent Fresnel zone plates in silica fabricated by femtosecond laser machining.," Opt. Lett. **27**, 2200-2202 (2002).
108. E. N. Glezer, M. Milosavljevic, L. Huang, R. J. Finlay, T. H. Her, J. P. Callan, and E. Mazur, "Three-dimensional optical storage inside transparentmaterials," Opt. Lett. **21**, 2023-2025 (1996).
109. S. Onda, W. Watanabe, K. Yamada, K. Itoh, and J. Nishii, "Study of filamentary damage in synthesized silica induced by chirped femtosecond laser pulses," JOSA B **22**, 2437-2443 (2005).
110. J. B. Ashcom, R. R. Gatlass, C. B. CSchaffer, and E. Mazur, "Numerical aperture dependence of damage and supercontinuum generation from femtosecond laser pulses in bulk fused silica.," Journal of Optical Society of America B **23**, 2317-2322 (2006).
111. D. Von der Linde and H. Schüler, "Breakdown threshold and plasma formation in femtosecond laser–solid interaction," JOSA B **13**, 216-222 (1996).
112. S. Nemoto, "Waist shift of a Gaussian beam by plane dielectric interfaces," Appl. Opt. **27**, 1833-1839 (1988).
113. A. Marcinkevičius, V. Mizeikis, S. Juodkazis, S. Matsuo, and H. Misawa, "Effect of refractive index-mismatch on laser microfabrication in silica glass," Appl. Phys. A **76**, 257-260 (2003).
114. R. D. Simmonds, P. S. Salter, A. Jesacher, and M. J. Booth, "Three dimensional laser microfabrication in diamond using a dual adaptive optics system," Opt. Express **19**, 24122-24128 (2011).
115. A. M. Streltsov and N. F. Borelli, "Fabrication and analysis of a directional coupler written in glass by nanojoule femtosecond laser pulses.," Opt. Lett. **26**, 42-43 (2001).
116. C. Schaffer and E. Mazur, "Micromachining using ultrashort pulses from a laser oscillator," Optics & Photonics News **12**, 20-23 (2001).
117. C. B. Schaffer and E. Mazur, "Micromachining using Ultrashort Pulses from a Laser Oscillator," in *Optics and Photonics News* (2001), pp. 21–23.

118. A. Couairon, L. Sudrie, M. Franco, B. Prade, and A. Mysyrowicz, "Filamentation and damage in fused silica induced by tightly focused femtosecond laser pulses," Physical Review B **71**, 125435 (2005).
119. J. W. Chan, T. R. Huser, S. H. Risbud, and D. M. Krol, "Modification of the fused silica glass network associated with waveguide fabrication using femtosecond laser pulses," Appl. Phys. A-Mater. **76**, 367-372 (2003).
120. R. Brückner, "Properties and structure of vitreous silica. I," Journal of Non-Crystalline Solids **5**, 123-175 (1970).
121. M. Sakakura, M. Shimizu, Y. Shimotsuma, K. Miura, and K. Hirao, "Temperature distribution and modification mechanism inside glass with heat accumulation during 250kHz irradiation of femtosecond laser pulses," Appl. Phys. Lett. **93**, 231112-231112-231113 (2008).
122. K. Hirao and K. Miura, "Writing waveguides and gratings in silica and related materials by a femtosecond laser.," Journal of Non-Crystalline Solids **239**, 91-95 (1998).
123. A. Saliminia, R. Vallée, and S. L. Chin, "Waveguide writing in silica glass with femtosecond pulses from an optical parametric amplifier at 1.5um," Opt. Commun. **256**, 422-427 (2005).
124. M. Lancry, B. Poumellec, A. Chahid-Erraji, M. Beresna, and P. Kazansky, "Dependence of the femtosecond laser refractive index change thresholds on the chemical composition of doped-silica glasses," Opt. Mater. Express **1**, 711-723 (2011).
125. L. Bressel, D. de Ligny, C. Sonneville, V. Martinez, V. Mizeikis, R. Buividas, and S. Juodkazis, "Femtosecond laser induced density changes in GeO2 and SiO2 glasses: fictive temperature effect."
126. J. W. Chan, T. Huser, S. Risbud, and D. M. Krol, "Structural changes in fused silica after exposure to focused femtosecond laser pulses.," Opt. Lett. **26**, 1726-1728 (2001).
127. K. M. Davis, K. Miura, N. Sugimoto, and K. Hirao, "Writing waveguides in glass with a femtosecond laser.," Opt. Lett. **21**, 1729-1731 (1996).
128. M. Bernasconi, "Ab-initio molecular dynamics simulation of amorphous silica surface.," in *Defects in $Si0_2$ and related dielectrics: Science and Technology.*, L. S. a. D. L. G. G. Pacchioni, ed. (Kluwer, Dordrecht, 2000).
129. S. Nolte, M. Will, B. Chichkov, and A. Tuennermann, *Waveguides produced by ultrashort laser pulses inside glasses and crystals*, High-Power Lasers and Applications (SPIE, 2002), Vol. 4637.
130. O. Efimov, L. Glebov, K. Richardson, E. Van Stryland, T. Cardinal, S. Park, M. Couzi, and J. Brunéel, "Waveguide writing in chalcogenide glasses by a train of femtosecond laser pulses," Opt. Mater. **17**, 379-386 (2001).
131. G. Petite, P. Daguzan, S. Guizard, and P. Martin, "Ultrafast processes in laser irradiated wide bandgap insulators," Appl. Surf. Sci. **109–110**, 36-42 (1997).
132. M. Royon, "Ingénierie de verres de silice: influence de pré-traitements sur la variation d'indice de réfraction de guides d'ondes photo-inscrits par laser

femtoseconde," 2018).
133. C. Hnatovsky, R. S. Taylor, E. Simova, P. P. Rajeev, D. M. Rayner, V. R. Bhardwaj, and P. B. Corkum, "Fabrication of microchannels in glass using focused femtosecond laser radiation and selective chemical etching," Appl. Phys. A **84**, 47-61 (2006).
134. J. Canning, M. Lancry, K. Cook, A. Weickman, F. Brisset, and B. Poumellec, "Anatomy of a femtosecond laser processed silica waveguide [Invited]," Opt. Mater. Express **1**, 998-1008 (2011).
135. R. Fleischer, P. Price, and R. Walker, "Solid-state track detectors: Applications to nuclear science and geophysics," Annu. Rev. Nucl. Sci. **15**, 1-28 (1965).
136. C. Schaffer, A. Brodeur, N. Nishimura, and E. Mazur, "Laser-induced microexplosions in transparent materials: microstructuring with nanojoules," Proceedings of SPIE **3616**, 143 (1999).
137. R. Stoian, K. Mishchik, G. Cheng, C. Mauclair, C. D'Amico, J.-P. Colombier, and M. Zamfirescu, "Investigation and control of ultrafast laser-induced isotropic and anisotropic nanoscale-modulated index patterns in bulk fused silica," Opt. Mater. Express **3**, 1755-1768 (2013).
138. E. N. Glezer and E. Mazur, "Ultrafast-laser driven micro-explosions in transparent materials," Appl. Phys. Lett. **71**, 882-884 (1997).
139. S. Juodkazis, H. Misawa, T. Hashimoto, E. G. Gamaly, and B. Luther-Davies, "Laser-induced microexplosion confined in a bulk of silica: Formation of nanovoids," Appl. Phys. Lett. **88**, 201909 (2006).
140. A. Mermillod-Blondin, J. Bonse, A. Rosenfeld, I. V. Hertel, Y. P. Meshcheryakov, N. M. Bulgakova, E. Audouard, and R. Stoian, "Dynamics of femtosecond laser induced voidlike structures in fused silica," Appl. Phys. Lett. **94**, 041911 (2009).
141. M. Birnbaum, "Semiconductor surface damage produced by ruby lasers," J. Appl. Phys. **36**, 3688 (1965).
142. J. Bonse, J. Krüger, S. Höhm, and A. Rosenfeld, "Femtosecond laser-induced periodic surface structures," Journal of Laser Applications **24**, 042006 (2012).
143. Z. Guosheng, P. Fauchet, and A. Siegman, "Growth of spontaneous periodic surface structures on solids during laser illumination," Physical Review B **26**, 5366 (1982).
144. H. Van Driel, J. Sipe, and J. F. Young, "Laser-induced periodic surface structure on solids: a universal phenomenon," Phys. Rev. Lett. **49**, 1955 (1982).
145. R. Nemanich, D. Biegelsen, and W. Hawkins, "Aligned, coexisting liquid and solid regions in laser-annealed Si," Physical Review B **27**, 7817 (1983).
146. J. Bonse, S. Baudach, J. Krüger, W. Kautek, and M. Lenzner, "Femtosecond laser ablation of silicon–modification thresholds and morphology," Appl. Phys. A **74**, 19-25 (2002).
147. A. Siegman and P. Fauchet, "Stimulated Wood's anomalies on laser-illuminated surfaces," IEEE J. Quantum Electron. **22**, 1384-1403 (1986).
148. A. Borowiec and H. Haugen, "Subwavelength ripple formation on the surfaces of compound semiconductors irradiated with femtosecond laser pulses," Appl.

Phys. Lett. **82**, 4462-4464 (2003).
149. N. Yasumaru, K. Miyazaki, and J. Kiuchi, "Femtosecond-laser-induced nanostructure formed on hard thin films of TiN and DLC," Appl. Phys. A **76**, 983-985 (2003).
150. B. Gaković, M. Trtica, D. Batani, T. Desai, P. Panjan, and D. Vasiljević-Radović, "Surface modification of titanium nitride film by a picosecond Nd: YAG laser," Journal of Optics A: Pure and Applied Optics **9**, S76 (2007).
151. J. Bonse, A. Rosenfeld, and J. Krüger, "On the role of surface plasmon polaritons in the formation of laser-induced periodic surface structures upon irradiation of silicon by femtosecond-laser pulses," J. Appl. Phys. **106**, 104910 (2009).
152. J. Bonse, S. Höhm, S. V. Kirner, A. Rosenfeld, and J. Krüger, "Laser-induced periodic surface structures—A scientific evergreen," IEEE Journal of selected topics in quantum electronics **23**(2016).
153. R. Buividas, M. Mikutis, and S. Juodkazis, "Surface and bulk structuring of materials by ripples with long and short laser pulses: Recent advances," Prog. Quant. Electron. **38**, 119-156 (2014).
154. J. Bonse, M. Munz, and H. Sturm, "Structure formation on the surface of indium phosphide irradiated by femtosecond laser pulses," J. Appl. Phys. **97**, 013538 (2005).
155. J. Bonse and J. Krüger, "Pulse number dependence of laser-induced periodic surface structures for femtosecond laser irradiation of silicon," J. Appl. Phys. **108**, 034903 (2010).
156. S. Sundaram and E. Mazur, "Inducing and probing non-thermal transitions in semiconductors using femtosecond laser pulses," Nature materials **1**, 217-224 (2002).
157. P. G. Kazansky, H. Inouye, T. Mitsuyu, K. Miura, J. Qiu, K. Hirao, and F. Starrost, "Anomalous anisotropic light scattering in Ge-doped silica glass," Phys. Rev. Lett. **82**, 2199-2202 (1999).
158. B. Poumellec, M. Lancry, J. C. Poulin, and S. Ani-Joseph, "Non reciprocal writing and chirality in femtosecond laser irradiated silica," Opt. Express **16**, 18354-18361 (2008).
159. A. Paleari, E. Franchina, N. Chiodini, and A. Lairia, "SnO_2 nanoparticles in silica: nanosized tools for femtosecond-laser.," Appl. Phys. Lett. **88**, 131912-131911/131913 (2006).
160. M. Born and E. Wolf, *Principles of optics: electromagnetic theory of propagation, interference and diffraction of light* (CUP Archive, 1999).
161. Y. Shimotsuma, M. Sakakura, P. G. Kazanksky, M. Beresna, J. Qiu, K. Miura, and K. Hirao, "Ultrafast Manipulation of Self-Assembled Form Birefringence in Glass," Adv. Mater. **22**, 4039-4043 (2010).
162. E. Bricchi, "Femtosecond laser micro-machining and consequent self-assembled nano-structures in transparent materials," (2005).
163. M. Gecevičius, "Polarization sensitive optical elements by ultrafast laser nanostructuring of glass," (University of Southampton, 2015).

164. C. Gu and P. Yeh, "Form birefringence dispersion in periodic layered media," Opt. Lett. **21**, 504-506 (1996).
165. V. Bhardwaj, E. Simova, P. Rajeev, C. Hnatovsky, R. Taylor, D. Rayner, and P. Corkum, "Optically produced arrays of planar nanostructures inside fused silica," Phys. Rev. Lett. **96**, 57404 (2006).
166. F. Liang, R. Vallée, and S. L. Chin, "Mechanism of nanograting formation on the surface of fused silica," Opt. Express **20**, 4389-4396 (2012).
167. M. Beresna, M. Gecevičius, P. G. Kazansky, T. Taylor, and A. V. Kavokin, "Exciton mediated self-organization in glass driven by ultrashort light pulses," Appl. Phys. Lett. **101**, 053120 (2012).
168. A. Rudenko, J.-P. Colombier, and T. E. Itina, "From random inhomogeneities to periodic nanostructures induced in bulk silica by ultrashort laser," Physical Review B **93**, 075427 (2016).
169. F. Zimmermann, A. Plech, S. Richter, A. Tünnermann, and S. Nolte, "The onset of ultrashort pulse - induced nanogratings," Laser Photonics Rev. **10**, 327-334 (2016).
170. Y. Liao, W. Pan, Y. Cui, L. Qiao, Y. Bellouard, K. Sugioka, and Y. Cheng, "Formation of in-volume nanogratings with sub-100-nm periods in glass by femtosecond laser irradiation," Opt. Lett. **40**, 3623-3626 (2015).
171. Y. Liao, J. Ni, L. Qiao, M. Huang, Y. Bellouard, K. Sugioka, and Y. Cheng, "High-fidelity visualization of formation of volume nanogratings in porous glass by femtosecond laser irradiation," Optica **2**, 329-334 (2015).
172. Y. Liao, Y. Shen, L. Qiao, D. Chen, Y. Cheng, K. Sugioka, and K. Midorikawa, "Femtosecond laser nanostructuring in porous glass with sub-50 nm feature sizes," Opt. Lett. **38**, 187-189 (2013).
173. P. G. Kazansky, E. Bricchi, Y. Shimotsuma, and K. Hirao, "Self-assembled nanostructures and two-plasmon decay in femtosecond processing of transparent materials," in *2007 Conference on Lasers and Electro-Optics (CLEO)*, (IEEE, 2007), 1-2.
174. P. Martin, S. Guizard, P. Daguzan, G. Petite, P. D'Oliveira, P. Meynadier, and M. Perdrix, "Subpicosecond study of carrier trapping dynamics in wide-band-gap crystals," Physical Review B **55**, 5799-5810 (1997).
175. F. Zimmermann, "Ultrashort pulse induced nanostructures in transparent materials," 2017).
176. S. Richter, A. Plech, M. Steinert, M. Heinrich, S. Doering, F. Zimmermann, U. Peschel, E. B. Kley, A. Tunnermann, and S. Nolte, "On the fundamental structure of femtosecond laser-induced nanogratings," Laser Photonics Rev. **6**, 787-792 (2012).
177. R. Taylor, C. Hnatovsky, and E. Simova, "Applications of femtosecond laser induced self - organized planar nanocracks inside fused silica glass," Laser Photonics Rev. **2**, 26-46 (2008).
178. P. Rajeev, M. Gertsvolf, C. Hnatovsky, E. Simova, R. Taylor, P. Corkum, D. Rayner, and V. Bhardwaj, "Transient nanoplasmonics inside dielectrics," J. Phys. B: At.,

Mol. Opt. Phys. **40**, S273 (2007).
179. M. Lancry, J. Canning, K. Cook, M. Heili, D. Neuville, and B. Poumellec, "Nanoscale femtosecond laser milling and control of nanoporosity in the normal and anomalous regimes of GeO2-SiO2 glasses," Opt. Mater. Express **6**, 321-330 (2016).
180. F. Zimmermann, M. Lancry, A. Plech, S. Richter, B. H. Babu, B. Poumellec, A. Tünnermann, and S. Nolte, "Femtosecond laser written nanostructures in Ge-doped glasses," Opt. Lett. **41**, 1161-1164 (2016).
181. F. Zimmermann, A. Plech, S. Richter, A. Tunnermann, and S. Nolte, "Ultrashort laser pulse induced nanogratings in borosilicate glass," Appl. Phys. Lett. **104**, 211107 (2014).
182. M. Beresna, M. Gecevičius, M. Lancry, B. Poumellec, and P. Kazansky, "Broadband anisotropy of femtosecond laser induced nanogratings in fused silica," Appl. Phys. Lett. **103**, 131903 (2013).
183. H. C. Guo, H. B. Jiang, Y. Fang, C. Peng, H. Yang, Y. Li, and Q. H. Gong, "The pulse duration dependence of femtosecond laser induced refractive index modulation in fused silica," Journal of Optics a-Pure and Applied Optics **6**, 787-790 (2004).
184. S. Richter, M. Heinrich, S. Döring, A. Tünnermann, S. Nolte, and U. Peschel, "Nanogratings in fused silica: Formation, control, and applications," Journal of Laser Applications **24**, 042008(042001)-042008(042008) (2012).
185. M. Lancry, F. Zimmerman, R. Desmarchelier, J. Tian, F. Brisset, S. Nolte, and B. Poumellec, "Nanogratings formation in multicomponent silicate glasses," Appl. Phys. B **122**, 66 (2016).
186. M. Beresna, "Polarization engineering with ultrafast laser writing in transparent media," (Southampton, 2012).
187. S. Richter, F. Jia, M. Heinrich, S. Döring, U. Peschel, A. Tünnermann, and S. Nolte, "The role of self-trapped excitons and defects in the formation of nanogratings in fused silica," Opt. Lett. **37**, 482-484 (2012).
188. Y. Shimotsuma, K. Miura, and H. Kazuyuki, "Nanomodification of Glass Using fs Laser," Int. J. Appl. Glass Sci. **4**, 182-191 (2013).
189. M. Lancry and B. Poumellec, "Femtosecond Laser Direct Writing in P, Ge Doped Silica Glasses: Time Resolved Plasma Measurements," Femtosecond Laser Microfabrication (2009).
190. A. Cerkauskaite, R. Drevinskas, A. O. Rybaltovskii, and P. G. Kazansky, "Ultrafast laser-induced birefringence in various porosity silica glasses: from fused silica to aerogel," Opt. Express **25**, 8011-8021 (2017).
191. R. Desmarchelier, B. Poumellec, F. Brisset, S. Mazerat, and M. Lancry, "In the heart of femtosecond laser induced nanogratings: from porous nanoplanes to form birefringence," World J. Nano Sci. and Eng. **5**, 115-125 (2015).
192. M. Lancry, F. Brisset, and B. Poumellec, "In the heart of nanogratings made up during femtosecond laser irradiation," in *Advanced Photonics & Renewable Energy*, OSA Technical Digest (CD) (Optica Publishing Group, 2010), BWC3.
193. T. Asai, Y. Shimotsuma, T. Kurita, A. Murata, S. Kubota, M. Sakakura, K. Miura, F.

Brisset, B. Poumellec, and M. Lancry, "Systematic Control of Structural Changes in GeO2 Glass Induced by Femtosecond Laser Direct Writing," J. Am. Ceram. Soc. **98**, 1471-1477 (2015).
194. F. Zhang, H. Zhang, G. Dong, and J. Qiu, "Embedded nanogratings in germanium dioxide glass induced by femtosecond laser direct writing," J. Opt. Soc. Am. B **31**, 860-864 (2014).
195. Y. Shimotsuma, A. Taiga, M. Sakakura, and K. Miura, "Femtosecond-laser Nanostructuring in Glass," Journal of Laser Micro/Nanoengineering **9**(2014).
196. S. Richter, C. Miese, S. Döring, F. Zimmermann, M. J. Withford, A. Tünnermann, and S. Nolte, "Laser induced nanogratings beyond fused silica - periodic nanostructures in borosilicate glasses and ULE™," Opt. Mater. Express **3**, 1161-1166 (2013).
197. Y. SHIMOTSUMA, K. HIRAO, J. QIU, and P. G. KAZANSKY, "NANO-MODIFICATION INSIDE TRANSPARENT MATERIALS BY FEMTOSECOND LASER SINGLE BEAM," Mod. Phys. Lett. B **19**, 225-238 (2005).
198. Q. Zhai, H. Ma, X. Lin, Y. Li, W. Yin, X. Tang, X. Zeng, and Y. Dai, "Evolution of self-organized nanograting from the pre-induced nanocrack-assisted plasma–laser coupling in sapphire," Appl. Phys. B **127**, 74 (2021).
199. Y. Shimotsuma, S. Mori, Y. Nakanishii, E. Kim, M. Sakakura, and K. Miura, "Self-assembled glass/crystal periodic nanostructure in Al_2O_3-Dy_2O_3 binary glass," Appl. Phys. A **124**, 82 (2018).
200. J. Cao, L. Mazerolles, M. Lancry, F. Brisset, and B. Poumellec, "Modifications in lithium niobium silicate glass by femtosecond laser direct writing: morphology, crystallization, and nanostructure," J. Opt. Soc. Am. B **34**, 160-168 (2017).
201. M. Ahn, A. Sarracino, A. Ansari, B. Torralva, S. Yalisove, and J. Phillips, *Unique material modifications of Ga2O3 enabled by ultrafast laser irradiation*, SPIE OPTO (SPIE, 2020), Vol. 11281.
202. Y. Nakanishi, Y. Shimotsuma, M. Sakakura, M. Shimizu, and K. Miura, "Formation mechanism of self-assembled polarization-dependent periodic nanostructures in β-Ga2O3," in *Laser-based Micro- and Nanoprocessing XII,* U. Klotzbach, K. Washio, and R. Kling, eds. (SPIE, San Francisco, California, United States, 2018).
203. H. Yao, R. Zaiter, M. Cavillon, P. Delullier, B. Lu, T. Cardinal, Y. Dai, B. Poumellec, and M. Lancry, "Formation of nanogratings driven by ultrafast laser irradiation in mid-IR heavy oxide glasses," Ceram. Int. **48**, 31363-31369 (2022).
204. Y. Wang, M. Cavillon, J. Ballato, T. Hawkins, T. Elsmann, M. Rothhardt, R. Desmarchelier, G. Laffont, B. Poumellec, and M. Lancry, "3D Laser Engineering of Molten Core Optical Fibers: Toward a New Generation of Harsh Environment Sensing Devices," Adv. Opt. Mater. **10**, 2200379 (2022).
205. Y. Wang, S. Wei, M. R. Cicconi, Y. Tsuji, M. Shimizu, Y. Shimotsuma, K. Miura, G. D. Peng, D. R. Neuville, B. Poumellec, and M. Lancry, "Femtosecond laser direct writing in SiO2 – Al2O3 binary glasses and thermal stability of Type II permanent modifications," J. Am. Ceram. Soc. **103**, 4286-4294 (2020).
206. Y. Shimotsuma, Y. Nakanishi, M. Skakura, and K. Miura, "Self-assembled periodic

nanostructures embedded in wide bandgap semiconductor," in *2017 Conference on Lasers and Electro-Optics Pacific Rim (CLEO-PR)*, 2017), 1-3.
207. S. Fedotov, A. Lipatiev, T. Lipateva, S. Lotarev, E. Mel'Nikov, and V. Sigaev, "Femtosecond laser‐induced birefringent microdomains in sodium‐borate glass for highly secure data storage," J. Am. Ceram. Soc. **104**, 4297-4303 (2021).
208. S. Lotarev, S. Fedotov, A. Lipatiev, M. Presnyakov, P. Kazansky, and V. Sigaev, "Light-driven nanoperiodical modulation of alkaline cation distribution inside sodium silicate glass," J. Non-Cryst. Solids **479**, 49–54 (2018).
209. S. S. Fedotov, A. S. Lipat'ev, S. V. Lotarev, and V. N. Sigaev, "Local Formation of Birefringent Structures in Alkali-Silicate Glass by Femtosecond Laser Beam," Glass Ceram. **74**, 227-229 (2017).
210. J. Wang, X. Liu, Y. Dai, Z. Wang, and J. Qiu, "Effect of sodium oxide content on the formation of nanogratings in germanate glass by a femtosecond laser," Opt. Express **26**, 12761-12768 (2018).
211. S. V. Lotarev, S. S. Fedotov, A. I. Kurina, A. S. Lipatiev, and V. N. Sigaev, "Ultrafast laser-induced nanogratings in sodium germanate glasses," Opt. Lett. **44**, 1564-1567 (2019).
212. A. Rudenko, J. P. Colombier, and T. E. Itina, "Nanopore-mediated ultrashort laser-induced formation and erasure of volume nanogratings in glass," Phys. Chem. Chem. Phys. **20**, 5887-5899 (2018).
213. P. P. Rajeev, M. Gertsvolf, C. Hnatovsky, E. Simova, R. S. Taylor, P. B. Corkum, D. M. Rayner, and V. R. Bhardwaj, "Transient nanoplasmonics inside dielectrics," J. Phys. B: At., Mol. Opt. Phys. **40**, S273 (2007).
214. H. Cang, A. Labno, C. Lu, X. Yin, M. Liu, C. Gladden, Y. Liu, and X. Zhang, "Probing the electromagnetic field of a 15-nanometre hotspot by single molecule imaging," Nature **469**, 385-388 (2011).
215. F. T. Zhang, Z. G. Nie, H. X. Huang, L. Ma, H. Tang, M. M. Hao, and J. R. Qiu, "Self-assembled three-dimensional periodic micro-nano structures in bulk quartz crystal induced by femtosecond laser pulses," Opt. Express **27**, 6442-6450 (2019).
216. E. Muzi, M. Cavillon, M. Lancry, F. Brisset, B. Sapaly, D. Janner, and B. Poumellec, "Polarization-oriented LiNbO3 nanocrystals by femtosecond laser irradiation in LiO2–Nb2O5–SiO2–B2O3 glasses," Opt. Mater. Express **11**, 1313-1320 (2021).
217. M. Cavillon, J. Cao, M. Vallet, F. Brisset, L. Mazerolles, B. Dkhil, M. Lancry, and B. Poumellec, "Thermal and Electron Plasma Effects on Phase Separation Dynamics Induced by Ultrashort Laser Pulses," Crystals **12**, 496 (2022).
218. B. Poumellec, M. Cavillon, and M. Lancry, "Electrostatic Interpretation of Phase Separation Induced by Femtosecond Laser Light in Glass," Crystals **13**, 393 (2023).
219. B. Poumellec, M. Lancry, R. Desmarchelier, E. Hervé, and B. Bourguignon, "Parity violation in chiral structure creation under femtosecond laser irradiation in silica glass?," Light: Sci. Appl. **5**, e16178-e16178 (2016).
220. J. Lu, J. Tian, B. Poumellec, E. Garcia-Caurel, R. Ossikovski, X. Zeng, and M. Lancry,

"Tailoring chiral optical properties by femtosecond laser direct writing in silica," Light: Sci. Appl. **12**(2023).
221. W. Yang, P. G. Kazansky, and Y. P. Svirko, "Non-reciprocal ultrafast laser writing," Nat. photonics **2**, 99-104 (2008).
222. P. G. Kazansky, W. Yang, E. Bricchi, J. Bovatsek, A. Arai, Y. Shimotsuma, K. Miura, and K. Hirao, ""Quill" writing with ultrashort light pulses in transparent materials," Appl. Phys. Lett. **90**(2007).
223. S. Qu, J. Qiu, C. Zhao, X. Jiang, H. Zeng, C. Zhu, and K. Hirao, "Metal nanoparticle precipitation in periodic arrays in Au2O-doped glass by two interfered femtosecond laser pulses," Appl. Phys. Lett. **84**, 2046-2048 (2004).
224. A. Podlipensky, A. Abdolvand, G. Seifert, and H. Graener, "Femtosecond laser assisted production of dichroitic 3D structures in composite glass containing Ag nanoparticles," Appl. Phys. A-Mater. **80**, 1647-1652 (2005).
225. J. Tian, "Femtosecond laser direct writing of circular optical properties in silica glass," 2020).
226. L. A. Fernandes, J. R. Grenier, P. R. Herman, J. S. Aitchison, and P. V. S. Marques, "Femtosecond laser writing of waveguide retarders in fused silica for polarization control in optical circuits," Opt. Express **19**, 18294-18301 (2011).

SYNTHESE EN FRANÇAIS

La photonique subit actuellement une transition vers une plus grande intégration de composants optiques ainsi qu'une transition exploitant des techniques d'écriture directe avec des faisceaux structurés [1]. Des composants compacts et légers sont nécessaires pour les applications de soins de santé, de transport d'information ou encore les applications spatiales. Simultanément, la mise en forme complexe de l'amplitude, de la phase et de la polarisation des faisceaux est cruciale pour un nombre croissant d'applications et en sciences fondamentales (optique quantique, biophotonique, impulsions attosecondes, traitement des matériaux par laser). Par conséquent, la photonique de nouvelle génération a besoin d'une technique de fabrication pour imprimer « à la demande » des composants optiques arbitraires pour la mise en forme des faisceaux. Idéalement, ces optiques seraient plates, fines, présentant de faibles pertes optiques, un seuil de dommage élevé et un faible coût. Les outils conventionnels de mise en forme de la lumière ont des capacités limitées : les modulateurs spatiaux de lumière sont volumineux, coûteux, offrent un changement de phase limité (typiquement 3π à 800 nm) et exploitent un axe de polarisation unique. Les éléments optiques diffractifs ne peuvent pas offrir une mise en forme de polarisation. Les métasurfaces spatiales [2]permettent un contrôle total du champ lumineux de sortie, mais les processus lithographiques sont longs, en plusieurs étapes, nécessitent des processus coûteux et polluants tandis que la couche finale nm est fragile.

Les méthodes d'écriture directe 3D pour la photonique : des publications récentes sur la fabrication 3D d'optiques démontrent l'attrait de ce sujet dans le monde entier. De nombreuses méthodes rappelées dans la Réf. [3]permettent la fabrication 3D d'éléments optiques. Parmi ces différentes techniques on retrouve les techniques de dépôt, l'impression jet d'encre, la stéréolithographie et la polymérisation 2 photons (2PP) par laser femtoseconde. Cependant, les optiques réalisées par ces procédés ont une résolution modérée (jusqu'à 0,1 µm en 2PP) et avec des rugosités de surface diverses (pouvant descendre jusqu'à 10 nm en 2PP ou en jet d'encre). Parmi ces méthodes, l'impression 2PP ou le jet d'encre peut être utilisée pour produire des optiques de qualité suffisamment élevée pour l'imagerie. Cependant, ces technologies en sont encore à leurs débuts et le plus souvent portées par quelques startups (PRINTOPTIX, Vadient Optics, Luxexcel, ADDOPTICS). Une des limites de ces technologies est le domaine spectral d'application qui est souvent limité au domaine visible. Des stratégies d'impression 3D avec des verres infrarouges au chalcogénure sont étudiées dans le contexte académique [4, 5] mais le niveau de rugosité est actuellement proche des techniques de dépôt de polymères, si bien que cette approche permet de réaliser par moulage des préformes utilisées pour l'optique finale. De plus, aucune de ces techniques n'est capable de contrôler la polarisation de la lumière.

L’écriture directe par laser femtoseconde: Même si l'approche de texturation et de structuration 3D par un laser femtoseconde ne peut être considérée à strictement parler comme un procédé de fabrication 3D d'optiques, la possibilité d'agir dans le volume d'un substrat optique (de forme quelconque) permet envisager de fabriquer des fonctions optiques dans un domaine inaccessible aux concepteurs optiques. C'est une méthode polyvalente compatible avec une large gamme de matériaux (oxydes, fluorures, chalcogénures) et donc dans plusieurs bandes spectrales, notamment du visible jusqu'à l'infrarouge thermique. Il permet à la fois une modification des propriétés optiques du matériau en volume et une structuration en surface. Cette méthode permet également d'envisager des matériaux optiques présentant de très bonnes propriétés mécaniques qui ne sont ni usinables par diamant ni moulables. Cette méthode est bien établie dans le domaine académique [6-8]. D'un intérêt particulier, les nanoréseaux photo-induits par laser fs peuvent être utilisés pour former, en principe, n'importe quelle optique.

Les optiques plates imprimées par laser fs est une solution de grande envergure. Avec des impulsions laser fs, des nanoréseaux peuvent être formés à l'intérieur de la plupart des verres dans un régime laser multi-impulsions [9]. Ces structures sont sub-longueur d'onde, périodiques (typiquement 100-300 nm) et fortement biréfringentes. Une caractéristique clé est que leur amplitude et leur direction peuvent être contrôlées respectivement par le dépôt d'énergie et la direction de polarisation de la lumière. Par conséquent, l’écriture directe au laser femtoseconde ouvre de grandes perspectives pour fabriquer n’importe quel composant optique. Il a été exploité pour démontrer la fabrication d'optiques biréfringentes variantes spatiales 3D (faisceaux vectoriels, réseaux de plaques micro-ondes) ainsi que d'éléments optiques fonctionnant sur une phase géométrique 3D (lentille, réseau) [2, 10, 11]. En parallèle, les progrès récents dans le domaine de l’optique planaire ont remis en question les limites de l’optique conventionnelle. Le profil de phase de presque tous les composants optiques, y compris les lentilles, les réseaux, les prismes, les lames de phase à vortex, ainsi que les éléments capables de courber la lumière de manière inhabituelle, peuvent être conçus à l'aide d’une phase géométrique 3D i.e. une phase dite de Pancharatnam-Berry. Théoriquement, n'importe quel motif de phase peut être obtenu au moyen d'une optique à phase géométrique avec des rendements atteignant jusqu'à 100 %. De plus, la possibilité d'imprimer une réponse de phase anisotrope (biréfringence) variant spatialement permettra la mise en forme de faisceaux lumineux structurés en polarisation (transversale et longitudinale) comme des faisceaux vectoriels cylindriques ou plus généralement des faisceaux de Poincaré. Cependant, et malgré des réalisations passionnantes, leur développement est freiné par des performances relativement faibles (vitesse d'écriture > 10 h/cm2, transmission de 70 % (peut être améliorée dans le cadre du régime de type X [2], densité de phase de 0,25 rad/µm [10] et une retardance limitée à qq 100’s nm par couche [12]) résultant principalement du manque de contrôle des processus d'interaction laser-matière. De ce fait, cette technologie d’écriture directe est bien étudiée dans le milieu académique en raison de ses avantages incontestables mais reste peu exploitée à l'heure actuelle au niveau

industriel.

Dans ce contexte, comprendre l'interaction de la matière avec les impulsions laser femtoseconde permettra d'évaluer le potentiel industriel qu'offre cette nouvelle méthode d'écriture directe. Certains aspects de l'interaction lumière-matière sont fondamentalement nouveaux. La physique sous-jacente est le comportement du plasma électronique en présence d'un support ionique et d'une onde lumineuse. Ici, les états solide et plasma coexistent pendant une fraction de picoseconde. De plus, la matière et la lumière interagissent pour produire une organisation structurée de la densité du plasma. Les problèmes fondamentaux sont de décrire avec précision la structuration du plasma d'électrons libres produit à la fin de l'ionisation multiphotonique (transition à travers le gap de l'isolant transparent). Ici le solide intervient comme source d'électrons. Sa microstructure organise le plasma en cohérence avec celle du faisceau lumineux. Puis, après l'impulsion, cette distribution de densité électronique est « imprimée » en piégeant les électrons dans le solide, et elle peut être utilisée comme « source » par l'impulsion suivante assurant ainsi un effet mémoire. Dans cette opération, le solide n'est pas détruit ; il reste en dessous du seuil de vaporisation, il se restructure dans le champ de force créé par le laser. On peut donc imaginer l'orientation du matériau, d'imprimer des nano/microstructures orientées comme des eutectiques directionnellement solidifiés. C'est une nouvelle physique. Mais pour la chimie aussi, il y a de nouveaux aspects car les processus impliquent des états très excités, qui sont en grande partie hors équilibre. Il est donc nécessaire de remettre en question certaines idées précédentes. Par exemple, les connaissances sur l'effet des impuretés, des défauts ponctuels ou des états facilement ionisables restent très limitées. Des champs de force et pas seulement des champs d'énergie sont également produits. Leur maîtrise ouvre la porte à une science de modification des matériaux par laser. C'est l'objet des travaux menés aujourd'hui par le groupe MAP de l'ICMMO et dans le cadre de cette thèse.

En particulier, une découverte principale constitue la base de cette thèse de doctorat. Il s'agit de la découverte de nanoréseaux auto-organisés dans SiO2 (périodicité de 100 à 400 nm persistant sur la plage du mm, y compris des nanocouches aussi fines que 10 à 30 nm), qui sont en fait les plus petites structures jamais créées par la lumière [13, 14]. Selon les auteurs, ces nanoréseaux résulteraient d'une modulation de la composition chimique (probablement la redistribution de l'oxygène) et cela serait lié aux ondes de densité stationnaires dans le plasma produites par l'interférence entre des ondes diffusées par des fluctuations de la constante diélectrique à l'échelle nanométrique. Notre groupe a révélé que les nanoréseaux sont en fait un assemblage de couches nanoporeuses dû à la décomposition d'oxydes [15] qui aurait été suggéré comme provenant d'un processus de nanocavitation assisté par contrainte [16, 17]. Ces structures, également appelées modifications de type II dans la littérature, sont à l'origine d'autres phénomènes expérimentaux inhabituels comme une réponse de biréfringence linéaire élevée (jusqu'à -10-2), une luminescence polarisée, une diffusion anisotrope de la lumière, un fort « dichroïsme » linéaire, un changement d'indice

négatif, des propriétés optiques chirales et une stabilité thermique extraordinaire (jusqu'à 150 heures à 1000°C) [18-20].

Ces observations expérimentales laissent plusieurs questions ouvertes qui devraient être abordées pour permettre des applications fiables. Comment maîtriser de telles structures et les propriétés qui en résultent, et par conséquent comment les utiliser efficacement ? Le défi de cette thèse était d'améliorer notre compréhension de l'interaction du laser femtoseconde avec les verres optiques, afin de contrôler les propriétés optiques anisotropes globales (signe, amplitude, orientation, pertes) dans des matériaux solides transparents à l'aide d'un procédé à grande vitesse et à faible coût ainsi qu'une technologie idéalement respectueuse de l'environnement et durable pour les applications optiques. En conséquence, le cœur de ce travail de thèse vise à caractériser et comprendre les transformations induites par laser dans une large gamme de verres d'oxydes, leurs types et changements structurels. Un intérêt clé est de mieux comprendre les mécanismes à l'origine de la formation des nanoréseaux et les propriétés optiques anisotropes associées. La maîtrise de ce type de photosensibilité permettra d'évaluer correctement le potentiel de cette technique d'écriture directe et d'exploiter pleinement les atouts de ce régime d'interaction. Cela libérera le potentiel industriel vers des applications fiables basées sur des propriétés optiques anisotropes linéaires et/ou circulaires.

Les nanoréseaux (NG) imprimés par écriture directe au laser femtoseconde à l'intérieur des verres sont donc des nanostructures extraordinaires avec des domaines d'application tels que l'optique, la microfluidique, le stockage de données optiques, les capteurs, etc. Sur la base du cette thèse, l'origine des NG et l'état des connaissances associé ont été largement discuté dans le premier et le dernier chapitre. Dans cette thèse, nous nous concentrons ensuite sur l'étude du rôle de la composition du verre sur leur formation. Nous étudions la fenêtre de type II (NG) dans un paysage de taux de répétition d'énergie d'impulsion (Ep-RR) à l'intérieur de 9 verres d'oxyde commerciaux, SiO_2 (SuprasilCG), GeO_2, silicate de titane (ULE), aluminoborosilicate alcalin libre/faible (verres Schott AF32 et Borofloat33), aluminoborosilicates (Eagle XG et 7059), borosilicate alcalin (BK7) et un verre sodocalcique en utilisant des paramètres laser similaires. Le retardance des NG est mesurée par microscopie optique en lumière polarisée. La microscopie électronique à balayage est utilisée pour confirmer la nature poreuse des nanocouches composant les NG. Nous discutons ensuite de l'impact de la viscosité du verre sur la formation de NG, propriété clé à prendre en compte. Le domaine d'existence des NG est défini à l'aide d'un modèle de viscosité dans des conditions de confinement thermique et de pression, étayé par des preuves expérimentales et théoriques (équation de Rayleigh-plesset (R-P)), puis appliqué afin de prédire la fenêtre d'existence des NG. La limite inférieure correspond à la formation de NG par nanocavitation et est définie comme la température pour laquelle la viscosité du verre atteint environ 106,6 Pa·s. La limite supérieure concerne l'effacement des NG par « l'effondrement » des nanopores et est définie comme la température à laquelle la viscosité atteint 103,0 Pa·s. Les fenêtres expérimentales sont en accord avec

les hypothèses développés à travers cette approche basée sur la viscosité des verres. Lorsque le rapport éléments alcalins et alcalino-terreux / formateurs de réseau vitreux (élément Si, Al ou Ge) augmente, la fenêtre des NG se rétrécit. Le dopage des éléments alcalins et alcalino-terreux dans les verres silicatés diminue la fenêtre des NG car la présence d'éléments mobiles comme le sodium ou encore la présence de compensateur de charge (e.g. dans les verres SiO2-Al2O3) sont étroitement liés à la viscosité du verre. Ensuite, nous analysons la nanostructure interne des NG et leur formation à l'intérieur du verre de silice via des techniques SEM, microscopie électronique à transmission par balayage (STEM), microscopie électronique à transmission à haute résolution (HRTEM) et microscopie à force atomique (AFM). À partir des images, il apparait que des nanopores de forme oblate peuplent un ensemble de nanoplans non continus, qui se développent perpendiculairement à la direction de polarisation du laser et le long de la direction de propagation du laser. De minuscules nanopores allongés ont également été découverts entre les nanoplans longs et pleinement développés. Ces nanopores se développeront et fusionneront dans un régime multi-impulsions, ce qui entraînera une diminution d'impulsion en impulsion de la périodicité moyenne bien inférieure à λ/2n. Le modèle de « nanocavitation médiée par le plasma » est discuté afin d'expliquer la formation de ces NG sub-longueur d'onde qui sont «organisés de manière forcée par la lumière» (plutôt qu'auto-organisés) dans un régime multi-impulsionnel.

L'étude de la stabilité thermique des nanoréseaux est utile pour les applications de dispositifs optiques à haute température, en particulier pour les concepteurs afin de prédire l'évolution dans leurs conditions de travail (température et durée). Lors des recuits thermiques, le retardance ou biréfringence linéaire sont progressivement effacées, caractéristique de l'effacement des NG. Nous étudions la stabilité thermique des NG dans 8 verres d'oxyde commerciaux (Schott BK7, Borofloat 33, AF32, Corning ULE, Eagle XG, 7059, Heraeus Suprasil CG et un verre sodo-calcique) lors d'expériences de recuits thermiques isochrones (pas de temps = 30 min). La température supérieure d'effacement des NG peut être enregistrée au cours de l'évolution du R à mesure que la température augmente. L'évolution du R au cours du recuit isochrone peut théoriquement être prédite grâce à l'équation Rayleigh-Plesset. Il existe un excellent accord entre les températures d'effacement expérimentales et prévues, avec des écarts ne dépassant pas 50°C pour tous les verres étudiés. L'effacement des NG dans le verre est intimement lié à la viscosité et l'expression du temps caractéristique d'effacement a été établie à l'aide de l'équation R-P simplifiée. Il est utilisé pour prédire théoriquement l'effacement des NG dans le contexte de tout processus temps-température (par exemple, recuit thermique, processus d'irradiation laser, « tout traitement thermique »). Nous avons constaté que la limite supérieure de température dans les conditions d'irradiation correspond à une température pour laquelle la valeur de la viscosité du verre est log (η, Pa·s) ~ -0,75 dans l'hypothèse où l'on considère un temps caractéristique de 30 ns, soit log (η, Pa·s) ~ 1 pour une échelle de temps de 1 µs, correspondant au temps typique de diffusion de la chaleur. Cependant, cette limite de température est abaissée pour des processus beaucoup plus longs comme le recuit

isotherme/isochrone où log (η, Pa·s) ~ 10. Le couple temps et température doit être pris en compte dans l'effacement des NG puisqu'il s'agit d'un problème de cinétique, et une relation entre les deux dans un contexte d'effacement des NG est ainsi établie. Ensuite, nous exploitons et adaptons le formalisme VAREPA pour prédire la durée de vie des NG dans ces 8 verres d'oxydes commerciaux. En utilisant l'équation de Rayleigh-Plesset et VAREPA, nous proposons de prédire la durée de vie des NG. Pour construire ce que l'on appelle la « courbe maitresse », le retard modélisé est collecté en fonction des conditions de recuit temps-température. La constante de vitesse de la réaction d'effacement, k0, de différents verres d'oxyde peut ainsi être déduite en simulation. Les données expérimentales peuvent également valider l'existence d'une courbe maitresse et la prédiction est excellente avec un taux d'effacement donné. L'interprétation physique du k0 et de la distribution de l'énergie d'activation sous-jacente a été développé, montrant un lien direct avec la viscosité du verre et sa dépendance à la température. Enfin il a été démontré que le ln(k0), augmentait linéairement avec la fragilité du verre d'Angell, m.

Ensuite nous développons un modèle de diffusion de chaleur combiné à l'équation R-P pour simuler l'évolution temps-température des nanopores le long du profil de refroidissement thermique du laser. Nous montrons les courbes de Ep versus RR modélisées à l'état stationnaire dans 8 verres d'oxyde commerciaux. Ici, l'effacement complet des nanopores est défini par le « point de contact » entre la courbe de refroidissement T(t) et le temps d'effacement caractéristique des nanopores déduit de R-P. Nous notons également que la forme temporelle des courbes de refroidissement de la dernière impulsion à l'état stationnaire dépend du taux de répétition, dû à l'accumulation de chaleur qui intervient à haute cadence. Pour un coefficient d'absorption fixe, à mesure que le nombre d'impulsions augmente, les courbes modélisées Ep en fonction du taux de répétition se rapprochent des données expérimentales. Cependant, pour obtenir une correspondance parfaite avec les données expérimentales, le dépôt d'énergie a été ajusté en fonction du RR, ce qui a été fait en prenant en compte l'évolution du waist du faisceau laser qui augmente avec l'énergie.

Enfin nous examinons l'impact de la composition chimique sur les nanoréseaux et leurs caractéristiques sur leurs structures internes, notamment la périodicité, la taille des nanopores et le facteur de remplissage des nanoplans poreux. Les propriétés optiques utiles sont ensuite étudiées et comparées, telles que leur fenêtre de traitement énergétique, leur retardance et leur biréfringence maximale, ainsi que les « performances technologiques » corrélées, notamment la consommation d'énergie (µJ/nm), la vitesse de balayage laser et la stabilité thermique. Cette collection de travaux expérimentaux fournit une feuille de route des matériaux pour stimuler le développement et la sélection de matériaux pour l'impression des nanoréseaux, en fonction de l'application finale, et vise à identifier de manière exhaustive les différences existantes entre ces verres.

En termes de perspectives, il sera crucial de continuer à comprendre comment ces matériaux se comportent à l'échelle nanométrique sous une intense excitation laser pour faire progresser les futures technologies de traitement par laser. Les propriétés mécaniques, thermiques, optiques, structurelles et compositionnelles des matériaux pourraient être adaptées au stockage de données optiques, aux dispositifs micro/nano fluidiques, à la formation de nouveaux alliages, aux applications catalytiques, aux capteurs, etc. La polarisation de la lumière est un paramètre efficace pour contrôler l'apport d'énergie dans la structuration laser des surfaces et des volumes. Il est cependant possible d'aller bien au-delà d'un simple dépôt d'énergie laser dans la matière conduisant à des effets thermiques conventionnels (découpe laser, fusion) mais il est possible de développer des forces après une excitation énergétique non linéaire. Des recherches plus approfondies sur les changements structurels et les mécanismes du NG à l'aide de techniques à l'échelle nanométrique telles que le nano IR et le nano Raman pour étudier les changements structurels à l'échelle de 10 nm à l'aide de la spectroscopie vibrationnelle, du nano XPEEM (microscopie à émission photoélectronique à rayons X), de l'analyse élémentaire à l'aide de HR-TEM EELS (Electron Energy Loss Spectroscopy), EFM pour vérifier la présence d'un champ de charge d'espace, en particulier à des échelles de temps courtes (ps-ns). D'un point de vue technique, la mise en forme temporelle, telle que quelques impulsions et l'usinage en rafale de GHz pour améliorer la vitesse d'écriture linéaire des NG, combinée au contrôle de la porosité à l'échelle nanométrique des verres pour favoriser leur formation, tandis que la mise en forme spatiale, telle qu'une mise au point étendue ou multifocale, peut être utilisé pour améliorer la vitesse d'écriture en volume. La combinaison avec la mise en forme d'impulsions spatiales (par exemple, faisceaux d'Airy tronqués, de Bessel tronqués, etc.) devrait améliorer l'uniformité spatiale des NG et réduire les pertes optiques globales. De plus, il faudrait développer un traitement d'impulsions ultrarapides en quelques cycles qui pourrait aboutir à un « mode sans avalanche pour un dépôt d'énergie plus efficace et hautement localisé, une manipulation plus efficace du couplage spatio-temporel et un meilleur contrôle du processus d'ensemencement des NG ».

Ce que l'on peut imaginer aujourd'hui avec un laser subpicoseconde peut également être réalisé plus clairement avec un laser « véritablement femtoseconde » qui apparaîtra sur le marché dans les prochaines années. Le temps nécessaire pour une demi-période dans l'IR à une longueur d'onde de 1 µm est de 1,7 fs ! Dans ce cas, les charges opposées peuvent être plus facilement séparées. A terme, nous ouvrirons la voie à la science des matériaux grâce aux impulsions laser sous-cycle. À l'avenir, nous les utiliserons pour montrer que c'est une possibilité générale dans les matériaux transparents. Nous avons l'intention de remettre en question la théorie proposée par des travaux de simulation, c'est-à-dire de montrer que les forces et les couples sont suffisamment importants pour calculer le champ électrique et le champ mécanique induit, de montrer que nous pouvons imprimer des NG « tordus » et déterminer les paramètres laser appropriés à utiliser. Ces futurs travaux augmenteront nos connaissances sur l'action non linéaire impliquant l'interaction d'une lumière laser

intense et ultracourte avec la matière. Ces nouvelles connaissances s'appliqueront à toute structuration de fonctionnalisation optique de matériaux diélectriques dans les domaines adjacents de l'optique intégrée et de la chimie du solide. Les résultats expérimentaux rapportés mettent en évidence un processus d'interaction lumière-matière affecté par la polarisation. Une perspective fascinante consiste à combiner la distribution temporelle et spatiale de la polarisation, de l'intensité et de la phase de la lumière à l'intérieur d'un matériau diélectrique. Ce faisant, il deviendra possible de contrôler efficacement la distribution et l'orientation des forces non linéaires dans l'état solide excité (par exemple le plasma induit) et, ainsi, l'effet final dans la matière, en exerçant en plus des actions mécaniques dans la matière en plus des effets thermiques. Ceci n'est possible que pour des intensités significatives et des durées d'impulsion ultracourtes, lorsque les électrons peuvent être excités dans des états délocalisés indépendamment du mouvement ionique.

Les idées proposées se résument à la phrase suivante : adapter l'outil de traitement (c'est-à-dire le laser et sa mise en forme spatio-temporelle) à une tâche donnée. Par exemple, un résultat passionnant serait de créer des NG complexes en combinant plusieurs faisceaux laser. Les faisceaux laser, c'est-à-dire les vortex optiques ou à polarisation circulaire, transportent le spin et le moment cinétique orbital (SAM et OAM). Ces expériences aident à répondre à une question de départ de savoir si SAM et OAM sont équivalents en ce qui concerne l'absorption de la lumière. Un autre exemple est celui des faisceaux de Bessel, qui permettent la fabrication de structures « très allongées ». En effet, l'empreinte NG peut être explorée pour générer des faisceaux laser connus tels que les modes Bessel, Hermite-Gaussien et Laguerre-Gaussien et pour permettre l'ingénierie de l'intensité et de la distribution de polarisation au foyer du faisceau. Parmi les faisceaux vectoriels particuliers, on trouve une classe de solutions à l'équation des ondes vectorielles définie par une direction de polarisation variable dans l'espace. Les faisceaux vectoriels cylindriques obéissent à une symétrie axiale, telle que la polarisation radiale et azimutale. Les faisceaux vectoriels sont intéressants en raison de leurs propriétés de focalisation uniques, qui permettent un contrôle important sur la forme du champ électrique à proximité du foyer, y compris la possibilité d'une focalisation plus précise que les faisceaux ordinaires. Nous développerons de nouveaux éléments optiques biréfringents et élargirons nos connaissances sur le contrôle ultrarapide de la focalisation du faisceau laser sous focalisation étroite. Par exemple, un faisceau laser polarisé radialement focalisé avec un objectif à NA élevée présentera un champ électrique longitudinal solide, qui pourrait même accélérer des particules chargées. Ces possibilités d'ingénierie de polarisation de point focal peuvent bénéficier à la fois à l'impression d'effets circulaires anisotropes et non linéaires dans les verres.

References:

1. A. Forbes, "Structured Light from Lasers," Laser Photonics Rev. 13, 1900140

(2019).
2. M. Sakakura, et al., "Ultralow-loss geometric phase and polarization shaping by ultrafast laser writing in silica glass," Light Sci. Appl. 9, 15 (2020).
3. G. Berglund, et al., "Additive manufacturing for the development of optical/photonic systems and components," Optica 9, 623-638 (2022).
4. J. Carcreff, et al., Elaboration of chalcogenide microstructured optical fibers preform by 3D additive manufacturing, SPIE OPTO (SPIE, 2021), Vol. 11682.
5. E. Baudet, et al., "3D-printing of arsenic sulfide chalcogenide glasses," Opt. Mater. Express 9, 2307-2317 (2019).
6. R. Stoian and J.-P. Colombier, "Advances in ultrafast laser structuring of materials at the nanoscale," Nanophotonics 9, 4665-4688 (2020).
7. R. Stoian, "Volume photoinscription of glasses: three-dimensional micro- and nanostructuring with ultrashort laser pulses," Appl. Phys. A 126, 438 (2020).
8. R. Osellame, et al., Femtosecond laser micromachining: photonic and microfluidic devices in transparent materials (Springer, 2012), Vol. 123.
9. H. Yao, et al., "Materials roadmap for inscription of nanogratings inside transparent dielectrics using ultrafast lasers," Prog. Mater Sci. 142, 101226 (2024).
10. R. Drevinskas, et al., "Ultrafast Laser-Induced Metasurfaces for Geometric Phase Manipulation," Adv. Opt. Mater. 5, 1600575 (2017).
11. A. Arbabi, et al., "Dielectric metasurfaces for complete control of phase and polarization with subwavelength spatial resolution and high transmission," Nature Nanotechnology 10, 937-943 (2015).
12. M. Lancry, et al., "Compact Birefringent Waveplates Photo-Induced in Silica by Femtosecond Laser," Micromachines 5, 825-838 (2014).
13. Y. Shimotsuma, et al., "Self-organized nanogratings in glass irradiated by ultrashort light pulses," Phys. Rev. Lett. 91, 247405 (2003).
14. Q. Xie, et al., "Nanoscale investigations of femtosecond laser induced nanogratings in optical glasses," Nanoscale Advances (2024).
15. M. Lancry, et al., "Ultrafast nanoporous silica formation driven by femtosecond laser irradiation," Laser and Photonics Reviews 7, 953-962 (2013).
16. Q. Xie, et al., "Application and validation of a viscosity approach to the existence of nanogratings in oxide glasses," Opt. Mater. 130, 112576 (2022).
17. A. Rudenko, et al., "From random inhomogeneities to periodic nanostructures induced in bulk silica by ultrashort laser," Phys. Rev. B 93, 075427 (2016).
18. E. Bricchi and P. G. Kazansky, "Extraordinary stability of anisotropic femtosecond direct-written structures embedded in silica glass," Appl. Phys. Lett. 88(2006).
19. Q. Xie, et al., "Upper temperature limit for nanograting survival in oxide glasses," Appl. Opt. 62, 6794-6801 (2023).
20. B. Poumellec, et al., "Modification thresholds in femtosecond laser processing of pure silica: review of dependencies on laser parameters [Invited]," Opt. Mater. Express 1, 766-782 (2011).